A STUDY OF SELF-SUSTAINING

THIN-FILMS AS A MEANS OF FUSION PLASMA

IMPURITY AND WALL EROSION CONTROL

A THESIS
Presented to
The Faculty of the Division
of Graduate Studies

By

A.   Bruce DeWald, Jr.

In Partial Fullfillment
of the Requirements for the Degree
of Doctor of Philosophy
in the   School of Nuclear Engineering

Georgia Institute of Technology

November 12, 1984

Thesis

"A Study of Secondary Ion-Emitting, Self-Sustaining Thin Films as a Means of Fusion Plasma Impurity and Wall Erosion Control"

Approved: 11|12|84

Dr. Weston M. Stacey, Jr., Chairman

Dr. R. Glenn Bateman

Dr. Alan R. Kraus

Dr. Joseph D. Clement

Dr. John L. Carden

TABLE OF CONTENTS

ACKNOWLEDGEMENTS

I would like to thank Alan Krauss and Dieter Gruen of Argonne National Laboratory for suggesting the thesis topic and for providing the motivation for tackling the varied aspects of the thesis research. Thanks goes to Bill Stacey of Georgia Tech as my thesis advisor for providing the directional support and the political clout necessary to accomplish certain aspects of the thesis research. I am indebted to Al Bailey of Georgia Tech and to the rest of the "guys" at Argonne, especially Mike Pellin, Charlie Young, Manfred Kaminsky, Jeff Brooks, and Nghi Lam, all of whom provided technical insight and guidance. I would further like to thank John Carden, Joseph Clement, and Glenn Bateman for being a part of my thesis reading committee along with Alan Krauss and Bill Stacey.

On a more personal note, I am not sure if my "working" sanity would have been maintained without my office buddies: Bob Morris (a pro at filling garters -- oh yes those teeth!) and Mike Valentine (the up and coming protege). Of course without the emotional support of my wife (Dolores), my parents, and my sister, the inner drive to forge ahead would have been lacking. Finally, I would like to thank my wife for playing the role of editor, graphics specialist, and data "reducer" all of which sped the thesis project to its ultimate finality.

LIST OF ILLUSTRATIONS

SUMMARY

A simulation of self-sustaining (low-Z) "thin-films" as a means of fusion plasma impurity and wall erosion control has been performed through the development and/or extension of potential sheath, sputtering mechanics, and metal-surface kinetic models. Angular impact behaviour determined from the potential sheath model as a function of plasma-edge conditions provides the parameterization necessary for calculating thin-film alloy sputtering yields. The sputtering yields and damage profile behaviour resulting from the sputtering mechanics model for heterogeneous alloys provide the athermal driving force characteristics necessary for modeling the metal-surface kinetics of thin-film systems. The coupling of athermal and thermal phenomena establishes the framework for investigating the ability of thin-film systems to sustain themselves in an irradiation environment.

The application of the sheath, sputtering, and metal-surface kinetic models assumes a "worst case" scenario of a potential field in the presence of a grazing magnetic angle with the fusion conditions of edge densities greater than $O(10^{18} m^{-3})$ and edge temperatures less than $\sim O(10^{2} eV)$. Potential sheath calculations predict that low-Z ions impact at angles closely coinciding with the magnetic angle, while high-Z ions may be assumed to impact normally for magnetic

angles of 80 degrees or less. If the low-Z secondary-ion fraction exceeds 50%, low-Z self-sustaining thin-film systems are potentially advantageous in comparison to elemental surfaces due to reduced sputter erosion. For one such system, a Cu-Li alloy, the kinetic modeling is predictive of a self-sustaining Li thin-film, if the Li secondary-ion fraction approaches 90%. Comparison of the kinetic modeling to experiment for the Cu-Li alloy suggests that preferential sputtering is not the sole determinant of the equilibrium surface composition for mass-disparitive alloying elements.

CHAPTER I

Introduction

The notion of a magnetically confined plasma suggests that charged particle motion along field lines is constrained within a predefined physical space in isolation from disruptive forces and/or physical material boundaries. Ideal confinement further implies that no outflux of charged particles normal to the control surface enveloping the plasma is possible. However, for real plasmas, transport mechanisms such as collisions, plasma turbulence, instabilities, and particle drifts act to drive particle fluxes across constraining magnetic flux surfaces.[1,2] Thus, a plasma does not exist in isolation, rather its characteristics are modified by the encompassing environment. In a fusion device, the enveloping boundary is defined by a material surface commonly referred to as the first-wall, limiter (mechanical or magnetic), and any other major material surfaces in contact with the plasma.

Charge-exchange neutrals associated with edge recycling, plasma ions and electrons intersecting limiters/divertors, energetic fusion alphas, and ions resulting from neutral beam injection are among the various sources of particle fluxes incident on materials facing a fusion plasma. These fluxes

may cause the release of surface atoms and/or absorbates (e.g., oxygen, sulfur, carbon) via the processes of sputtering, arcing, desorption, and blistering. If the impurities penetrate the plasma edge, possible deleterious effects include changes in the temperature and current profiles, leading to MHD instabilites [3-6] and/or a limitation on the maximum achievable ion flux density due to a fixed β-limit.[3] Perhaps more importantly, small impurity concentrations on the order of 10^{-4} -10^{-1} produce enhanced radiative power losses which may prevent thermonuclear conditions from being obtained or sustained (Figure 1.1).[3,4,7-10] Radiative processes, if dominant as a power loss mechanism, limit plasma discharge duration and are evident especially for nondiverted tokamak operation where radiation losses in ASDEX [6], Doublet-III [8], T-12 [11], and DITE [10] accounted for 50-80% of the total energy loss. The allowable impurity concentration is dependent upon the charge state, Z, since the radiative power loss mechanisms of bremsstrahlung, line radiation, and recombination are approximately proportional to Z^2, Z^4, and Z^6, respectively.[2]

1.1 Impurity/Erosion Mechanism/Control Review

The various sources of plasma impurities having an
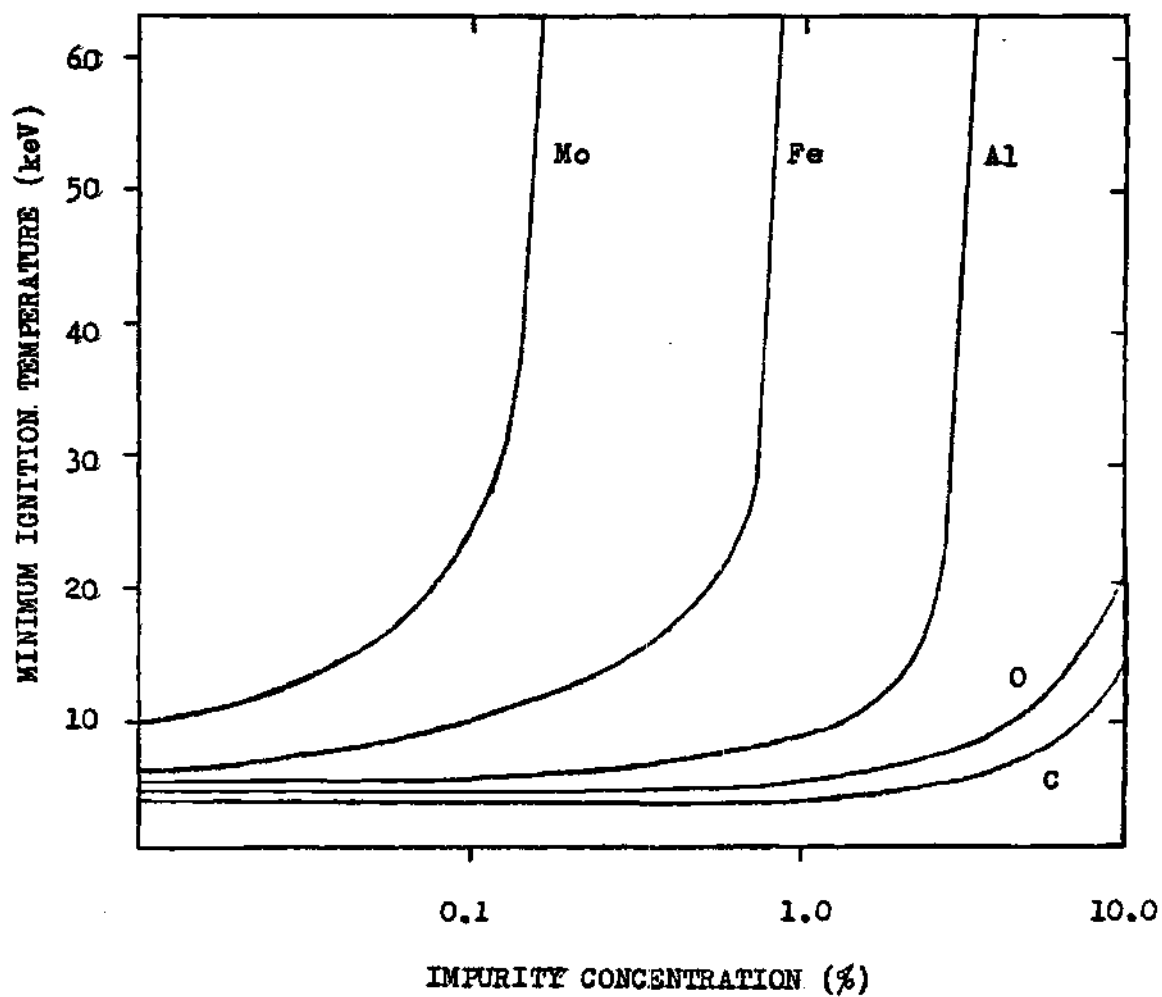
Figure 1.1   Minimum Tokamak Ignition Temperature
Versus Plasma Impurity Concentration

impact on non-disruptive tokamak operations can be diminished by a judicious assessment of wall conditioning, material specification, and adjustment of the plasma-edge conditions (density and temperature) in conjunction with an active impurity scheme (pumped limiter or magnetic divertor). As a brief review of the constraints and conditions necessary for plasma impurity reduction and/or wall erosion control (given in more detail elsewhere [12-14]), a number of the more important aspects are summarized below.

Through the use of wall conditioning defined to include degreasing, polishing, vacuum baking, and discharge cleaning, the following observations have been made.

(a) Elimination of surface protrusions, asperities, and adsorbed contaminants reduces the initial arcing frequency by two to three orders of magnitude for a given set of plasma parameters [3,15-17] and inhibits the development cone formation associated with sputtering.[18,19] Also, chunk emission due to neutron sputtering of fabrication asperities can be avoided by proper surface preparation.[20,21]

(b) High temperature baking and various wet-chemical and physical treatments of the torus and vacuum components act to prevent the thermal desorption of surface contaminants due to simple plasma heating. Furthermore, the initial conditioning of the tokamak vessel via argon sputtering followed by the periodic application of discharge cleaning methods (e.g., Taylor DC, electron cyclotron resonance (ECR-DC), and AC)

lessens the probability of near-surface adsorbates and volatile oxides from being desorbed (or sputtered) by ion-impact.[3,22-25]

Material specification defined to include elemental composition, porosity, hardness, and operating temperature influences the plasma impurity sources such that:

(a) Avoidance of materials having a low melting point and low thermal conductivity (hence, high arcing erosion rates) in favor of refractory metals or various proposed tokamak materials such as stainless steels, titanium, and copper increases arcing resistance.[26-28]

(b) Selection of metals whose associated oxides are easily reducible to H_2O will insure that discharge cleaning removes the near-surface passivation oxide layer (if any), preventing subsequent ion-impact desorption during tokamak operation.[22,23,29]

(c) For poor to moderate confinement of energetic fusion alphas (a condition of experimental reactors, but not expected in power reactors), the use of sintered materials (high porosity) e.g., beryllium and aluminum, reduces the blistering probability by as much as three orders of magnitude.[30]

(d) Because the sputtering threshold energy is inversely proportional to atomic number, high-Z element surfaces, as opposed to low-Z element surfaces, will suppress plasma contamination and wall erosion via physical sputtering at low

plasma-edge temperatures (<50 eV).[31] However, if plasma-edge temperatures $\sim O(10^2$ eV) are necessary from a plasma-physics point of view, then low-Z element surfaces must be employed in light of the excessive radiation losses and self-sputtering yields associated with high-Z elements.

Adjustment of the plasma-edge parameters, either at the first-wall and/or at the limiter/divertor plates, may substantially reduce erosion rates.

(a) In future tokamaks (demos or power reactors) where "hotter and denser" plasma conditions will be necessary to sustain fusion ignition requirements, arcing may occur regardless of the exposed material composition and condition if the plasma-edge density exceeds 10^{13} cm^{-3} .[14]

(b) Low edge temperatures and high edge densities may provide a buffer zone between the surface material of the first-wall and an energetic source of charge-exchange neutrals or an energetic recirculating ion-flux.[13,30] However, such a buffer zone results in larger incident surface fluxes (at least an order of magnitude greater than the plasma diffusion flux) which may act to increase erosion rates if the particle energies exceed the sputtering threshold.

(c) Low edge temperatures at the limiter/divertor plate proportionally decrease the sheath potential and, in turn, substantially reduce material surface erosion rates via sputtering.[31]

(d) Low edge temperatures may lower the chemical activities enough to permit the use of a material such as graphite which undergoes hydrocarbon formation (chemical sputtering).[32]

A summary, then, of the impurity/erosion control factors leads to the following general conclusions. On the basis of wall conditioning alone, the desorption and neutron sputtering mechanisms have a negligible impact on plasma contamination. The combination of material specification and wall conditioning in association with the appropiate plasma-edge parameters substantially reduces the seriousness of arcing, blistering, and chemical erosion. However, physical sputtering remains as probably the most critical impurity and material life-limiting phenomenon confronting the analysis and design of most envisoned tokamak devices. Only in a regime as proposed for the Phase-I INTOR divertor plate [33] (high density and low temperature, 20 eV) can the effects of physical sputtering be diminshed for conventional materials. If such a regime is unattainable due to plasma physics contraints, low-Z materials must be applied to all surfaces exposed to the plasma. However, low-Z elements tend to possess poor thermal and mechanical properties, thus, necessitating their use in a coating (thin-film) form on a higher-Z structural substrate. Conceptually then, coatings provide the means to preserve the substrate conditions of tensile strength, thermal conductivity, high melting point,

and swelling resistance while reducing the detrimental impurity/erosion effects via physical sputtering.

Conventional coatings have been applied to substrates by vapor deposition or bonding techniques. One life-limiting aspect of these coatings has been lack of mechanical integrity of the coating-substrate interface (adhesion layer) under thermal shock/cycling and irradiation induced gas build-up. Mechanical instability via exfoliation, blistering, and micro-crack formation [34-37] or from the redeposition process associated with erosion and recycling [38] has lead to the observed failure for a number of coating types. Another problematic aspect of deposited/bonded coatings is the preferential erosion of various surfaces within the plasma environment (e.g., limiter, divertor, probes), requiring an in-situ replenishment scheme.

Rather than seeking solutions to the interfacial/replenishment problems of distinct coating/substrate systems, another approach is to develop alloys that produce self-healing low-Z coatings under induced radiation/thermal segregation. The concept of a self-sustaining thin-film requires the identification of alloy component systems in which the stringent conditions of thermal mismatch and gas accumulation are avoided at the interface. Furthermore, good thermal contact at the interface demands that the coating not buildup to some arbitrary thickness; hence, the coating thickness must be

self-limiting as well as self-sustaining.

Experimental data [39] and initial scoping calculations [40] indicate that for incident light-ions with energies below 1 keV more than 95% of all sputtered atoms originate from the uppermost atomic layer. Hence, a self-sustaining monolayer ("thin-film") may be sufficient in preventing the structural substrate from being sputtered. Indeed, the experimental data [39] in conjunction with preliminary calculations [40] show a significant reduction in the substrate sputtering yield for an atomic overlayer/substrate system. However, accompanying a reduction in the erosion of the "underlying" substrate is the substitutional sputtering erosion of the overlayer. If the overlayer consists of low-Z material and has an "acceptable" sputter-erosion yield, then it not only provides a means of wall erosion control but also a means of plasma-impurity control through lower radiation losses.

An extension of the self-sustaining overlayer concept is to select alloys in which the segregating solute sputters primarily as an ion. Scoping calculations show that in the presence of a plasma sheath potential (limiter/divertor), secondary-ions have a small probability of escaping into the plasma via overcoming the retarding potential.[41,42] Also, secondary-ions emanating from the first-wall and/or limiter/divertor are redeposited without entering the plasma as a result of the deflection produced by a magnetic field.

The return of secondary-ions via a sheath potential or magnetic-field deflection is exhibited in Figure 1.2.

For most elements, except the alkali metals and alkaline earths, the charged fraction of the sputtering yield is less than one percent.[43] The sputtered ion yield (secondary-ion emission) of the alkali metals is on the order of 90%.[43] Hence, an alkali-metal covered surface may provide the means to reduce substrate sputtering and substantially diminish overlayer sputtering altogether. An initial experimental attempt to study an alkali-metal system has been accomplished by analyzing the behaviour of a deposited monolayer of potassium on molydenum.[39] The application of a negative bias to the K/Mo system to simulate a negative sheath potential shows a significant reduction in the sputtering yield (Figure 1.3). Sputtering of the potassium is not eliminated since the secondary-ion fraction for the K/Mo system is equal experimentally to 60%.[39]

1.2 Thesis Proposal and Scope

The objective of the current research (thesis) is to determine the needs and to develop a framework (mechanics) for analyzing mono-layer "thin-films" as a means of fusion plasma-impurity and wall erosion control. The investigation into the proposition of self-sustaining low-Z and/or

First Wall

M⁺

Toroidal Magnetic Field Line

M⁰

Plasma Particle

Plasma Edge

M⁺

PLASMA

Limiter

~ -100 ev Plasma Sheath Potential
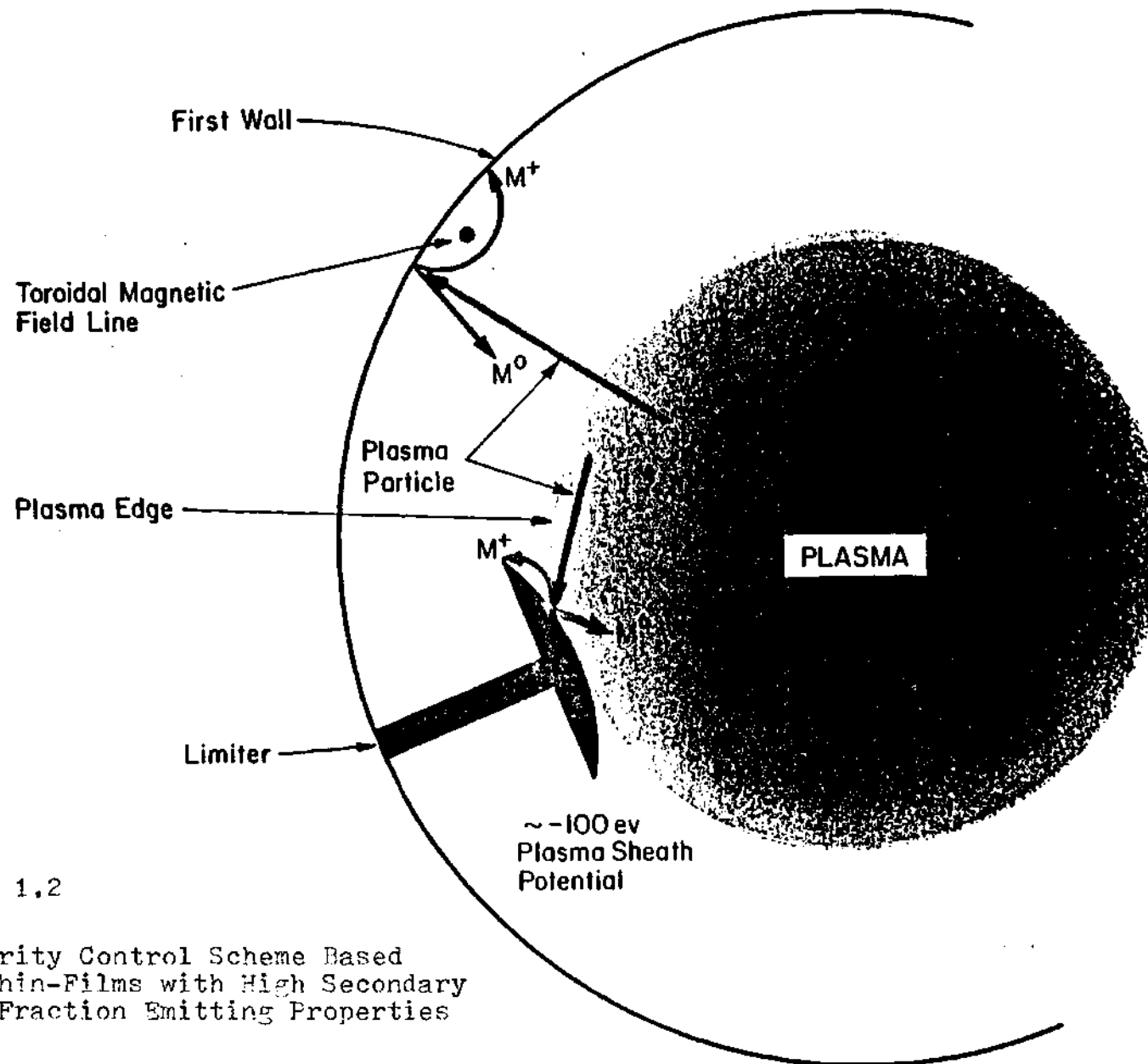
Figure 1.2

Impurity Control Scheme Based on Thin-Films with High Secondary Ion-Fraction Emitting Properties
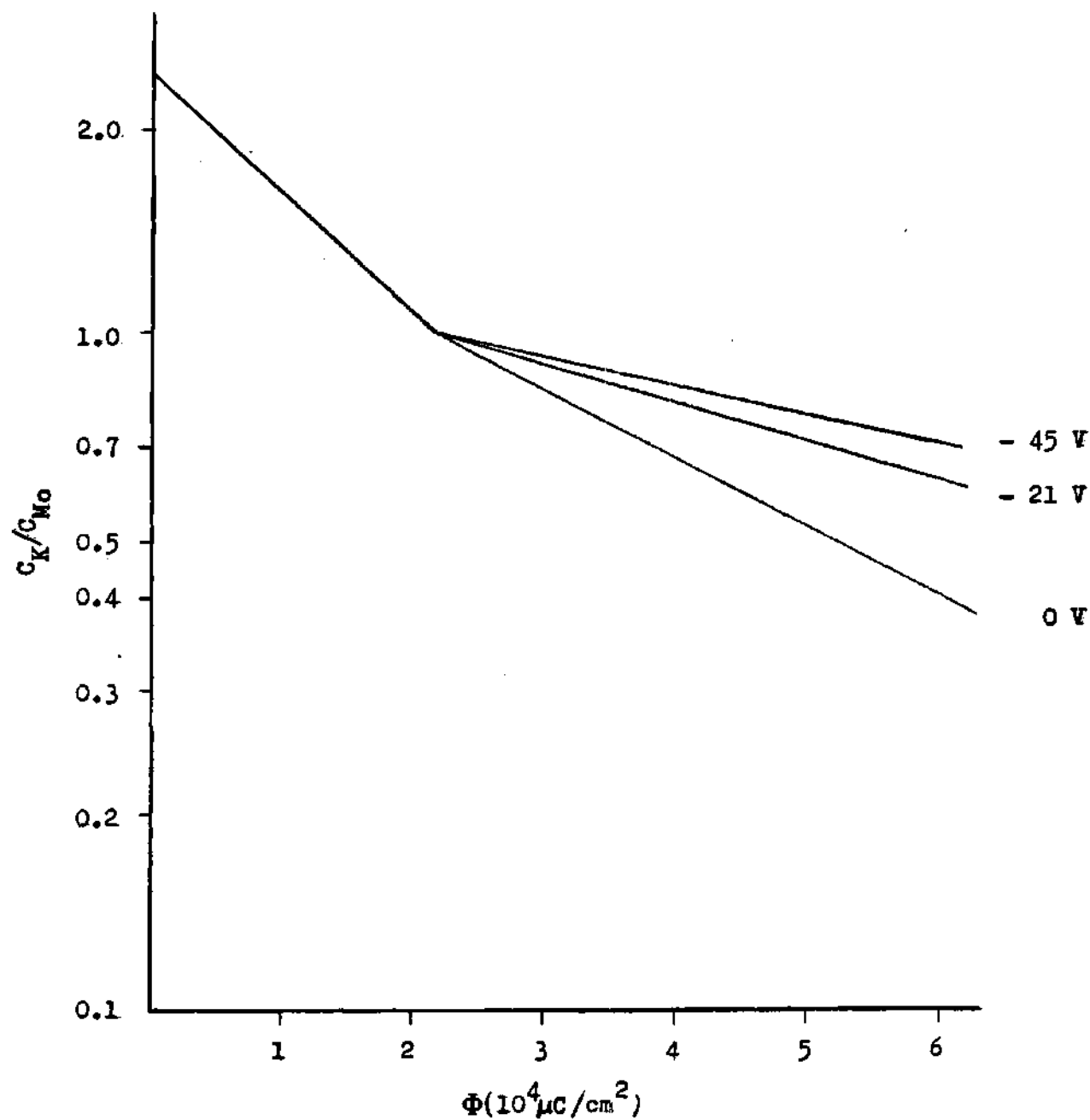
Figure 1.3   Relative Potassium to Molydenum Surface
            Concentration (C_K/C_{Mo}) as a Function of
            1 keV He+ Fluence

secondary-ion emitting monolayers must account for plasma-edge phenomena, physical sputtering, and metal-surface kinetics of an irradiated solid.

Limitations of the plasma-edge characteristics (e.g., density and temperature) are determined by the most severe erosion conditions. Within a tokamak, the limiter/divertor present the most extreme erosion due to the predominance of heavy-ion sputtering. Current proposed limiter/divertor materials provide no means of achieving edge-temperatures in excess of 50 eV for acceptable erosion rates. At the first-wall, the sputter-erosion is predominately due to light-ions since the sputtered material from the first-wall more severly affects the limiter/divertor as impurities are carried to these sites. Because light-ion sputtering is orders of magnitude less than heavy-ion sputtering and because light-ion sputtering does not directly result in "runaway" erosion (sputtering cascades resulting from sputtering yields exceeding unity), the physics of the plasma-wall interaction is not the limiting criterion on the material in contact with the plasma. impurites are carried to these sites.

The modeling of the plasma-edge "in contact" with the limiter/divertor plate has been reduced to investigating the kinetic behaviour of the potential sheath for a magnetized plasma. The angle of projectile impact with respect to the plate surface in the presence of a sheath potential is not

well known as a function of plasma-edge temperature and/or plasma-edge density. Erosion is strongly dependent upon the impact angle; hence, if the potential advantages of thin-film systems over conventional materials are to be evaluated, a comprehensive analysis requires the impact angle dependence upon the material species. Furthermore, material characteristics that may affect the potential sheath due to secondary emission must be surveyed in terms of relative importance. A kinetic potential sheath model for an arbitrary magnetic field is developed in order to consider a number of the impact and secondary-emission characteristics within the limiter/divertor region.

The wall-erosion protection provided by a self-sustaining monolayer requires a fundamental knowledge of sputtering and damage processes within the near-surface region of irradiated materials. The energy deposition profile within the target material as a result of light/heavy-ion impact is directly proportional to the sputtering yield and the damage incurred. Projectile impact angle and impact energy in conjunction with the spatial concentrations of the material determine the energy deposition characteristics. A sputtering mechanics model has been developed to simulate the collision cascade processes for a multi-component, multi-layer (heterogeneous) material.

While erosion yields provide a means of determining a static shielding factor for protective thin-film coverage,

the time evolution of a proposed self-sustaining "coating" under plasma-edge irradiation and fusion material conditions determines the overall feasibility of such systems. The athermal processes of sputter erosion and displacement mixing coupled to the thermal processes of atom-defect migration within the alloy are modeled to investigate the solute replenishment at the alloy surface. The kinetic evolution of the alloy composition is functionally dependent upon the energy deposition characteristics of the impacting projectiles which, in turn, are dependent upon the impact angle and energy quantities. Hence, in a heuristic fashion, the viability of the thin-film concept is dependent upon the coupling of the plasma-edge characterisitics to the metal kinetics of the limiter/divertor surface.

The mechanics/kinetics developed to investigayte thin-film systems is general enough (or can be generalized) to model any number of proposed limiter/divertor alloy surfaces. For the current research, the modeling is restricted to three alloy systems, specifically, Cu-Li, V-Al, and W-Be. The solvents Cu, V, and W in conjunction with their respective alloying elements have the bulk properties required by fusion reactor material constraints of tensile strength, thermal conductivity, relatively low radiation induced activity, swelling resistance, and a sufficiently high melting point. Preliminary segregation calculations, considering thermal aspects only, are suggestive that a

protective solute coating (Li, Al, or Be) can be maintained at fusion reactor operating temperatures. A 100% concentration of the low-Z solute can be obtained for solute concentrations as low as 4% for solvent metal temperatures less than 500°C. Of the three systems, the Cu-Li alloy has been analyzed more extensively than the V-Al and W-Be alloys since experimental work on the Cu-Li alloy has coincided with the general modeling developed during the current research effort. As a result, experimental data have been available to test the validity of the model results, alter the physics as necessary, and to provide physical insights into sputtering and alloy (atom-defect) kinetics. The model simulation of the Cu-Li alloy includes plasma-edge, sputter-erosion, and metal kinetic considerations, while the study of the V-Al and the W-Be alloys includes plasma-edge and erosion considerations alone. All investigations performed are based upon a philosophical premise of known physics and parameters, rather than extrapolating to "what if" scenarios, simply due to the vast number of "unknowns" for the alloys studied.

As a final addendum, the research is not limited in scope to modeling various physical effects, rather importance is placed on identifying a number of other pertinent effects (not modeled) to provide a framework for future research and to provide the bounds necessary for drawing the general conclusions herein.

1.3 Relevant Mechanics/Kinetics Review

As a direct result of an ion/electron plasma coming in contact with an electrically insulated plate (limiter/divertor) a negative potential at the plate surface with respect to the plasma is formed.[44-47] Briefly, the potential formation scenario begins with the pre-equilibrium condition of the plate surface at the plasma potential. Due to the higher thermal velocities of electrons as compared to ions, the electron current to the plate is greater than the ion current resulting in a negative charge buildup. Equilibrium occurs when the net current to the plate vanishes. The resulting negative potential has the general characteristics of (1) repulsion of all electrons, except those that have kinetic energies sufficient to overcome the retarding potential, (2) acceleration of ions due an attracting potential, and (3) a potential "drop" in close proximity to the plate due to Debye shielding. Debye shielding provides a screening layer (otherwise known as a sheath) between the plasma and the plate. Within the plasma where potential changes are small relative to kinetic electron temperature, temporal potentials vanish due to the simple redistribution of the electrons.

The physical characteristics of sheath potentials have been extensively analyzed employing both kinetic and fluid concepts, where the magnetic field is assumed parallel to the

metal surface normal; i.e., magnetic field effects on the potential and particle behaviour can be neglected. The emphasis of magnetic field-free studies has been to investigate the effects of electron and ion temperature, flow velocity conditions, secondary charged-particle emission, charge state, mass, and reflection upon the the sheath potential magnitude and profile (for a general review see ref. [48]). While these investigations have yielded qualitative information important in predicting general sheath trends expected in fusion reactor applications, in reality the sheath potential region is not free of magnetic forces. At a limiter or a poloidal divertor plate, where it is necessary to spread the incident heat flux over a surface area as large as possible, the magnetic field must thus intersect the surface at oblique angles. The effects of a nonnormal magnetic field angle upon the sheath potential magnitude and the particle motion, specifically surface impact quantities (e.g., impact angle and energy) may directly affect the plasma-edge conditions and the surface material considerations.

Limited research efforts have been conducted in describing the magnetic field effects on the various sheath potential phenomena: most notably, work performed by Lambroise and Rubenstein [49] (probe theory), Daybelge and Bein [50] (exact particle dynamics for grazing magnetic angles),and Chodura [51] (a coupling of fluid presheath

mechanics to sheath kinetics). Daybelge and Bein concluded that the effect of the magnetic field angle on the potential magnitude is inconsequential, while Chodura observed a "weak" dependence of the potential magnitude on the magnetic angle, especially at grazing angles. Of more importance though, the inclusion of a magnetic angle may increase the pitch angle of the particle orbit away from the surface normal and along the direction of the magnetic axis.[49,51] Most fusion design analyses have assumed that the potential sheath will always force charged particles to impact normally, regardless of the magnetic angle. If indeed plasma ions impact at nonnormal angles of incidence, the erosion yields will increase subsequently and, perhaps, become intolerable for many proposed fusion reactor materials. Investigations performed to study the effects of impact quantities have been limited in scope and, as yet, the functional dependence upon particle mass, plasma-edge density, and plasma-edge temperature versus magnetic angle is lacking.

Physical sputtering is defined by those processes which lead to the ejection of atomic particles from a solid surface (under projectile bombardment) due to the momentum transfer of slowing down energetic ions and/or neutrals. "Classic" Sigmund theory [52] was the first extensive mathematical treatment of the relevant phenomena associated with sputtering mechanics and is based on the solution to the general Boltzmann transport equation. Under the assumption

of random slowing down in an infinite medium, exact solutions are obtained in the asymptotic limit where the scattering energy is much greater than the energy of sublimation. The theory is accurate to within a factor of two (compared to experimental yields) for heavy-ion sputtering over the energy range 10^2-10^5 eV [52,53], whereas, for light-ion sputtering, only qualitative agreement is possible (an order of magnitude inaccuracy). Extensions of Sigmund theory consider the anisotropy of the momentum density of the collision cascade [54], the threshold effects for cascade initiation [55], and the exact numerical solution to the Boltzmann equation for a finite medium using the discrete-ordinates ANISN computer code.[56] As a result, the energy and angular distributions of sputtered particles are correctly determined within a factor of two [54], light-ion sputtering is better approximated [55], and the yield as a function of projectile energy and angle for a finite medium can be accurately determined if the material interaction cross-sections are known.[56]

Sputtering models based on either Monte Carlo techniques or empirical relationships have matched successfully with experimental data benchmarks. Of the Monte Carlo models, the MARLOWE [57] and TRIM [58] computer codes have attained the widest acceptability to fusion applications. These codes are based upon an atomistic approach to the collision sequences which may lead to a sputtering event. Calculations employing

either MARLOWE or TRIM produce correct sputtering yields (with the proper adjustment of material parameters) as a function of incident energy and angle regardless of the projectile-target combination.

Of the several proposed empirical models, two of the most commonly used approaches have been formulated by D.L. Smith et al. [59,60] and J. Roth et al. [61,62]. A better empirical approach is a hybrid of these models [14] such that $Y(E,\theta)=R(E)S(\theta)$, where the sputtering yield as a function of energy and angle, $Y(E,\theta)$, is equal to the product of the normal incidence Roth yield, $R(E)$, and the angular dependent Smith multiplier, $S(\theta)$

Determination of a sputtering mechanics framework best suited for the modeling of irradiated alloy systems was based on a process of review and elimination of the above models taking into consideration experimental accuracy, computational expediency, and availabilty of model parameters. The empirical approaches immediately present themselves as unacceptable due to the inherent assumption of material homogeneity. Classic analytical Sigmund theory (plus recent modifications) predict, at best, sputtering yields within 50-100% of experimental data. The numerical Boltzmann transport treatment (ANISN), while relatively accurate, requires a knowledge of complex alloy cross-sections. For the alloy systems under study (where experimental data is lacking), material cross-sections are

not readily available.

The Monte Carlo codes present the best means and versatility for predicting the sputtering yields over a large range of incident energies and angles for heteorgeneous alloy systems. MARLOWE while more physically accurate than TRIM due to its inclusion of the exact lattice geometry as opposed to an amorphous structure, is extremely time consuming. Also, a detailed knowledge of the lattice behaviour of the alloy systems is not well established. The TRIM code, thus, presents itself as the most flexible and expedient framework in which to model multi-component, multi-layer (concentration gradient) materials.

A brief synopsis of atom-defect kinetics and of other relevant atom-defect phenomena is presented in Chapter 4 of the thesis. The importance of each metal kinetic mechanism (thermal and athermal) upon solute diffusion and segregation is discussed and subsequently analyzed with respect to the Cu-Li alloy.

CHAPTER II

Derivation of the Sheath Model

2.1 Introduction

Particle quantities such as the projectile angle/energy of impact and resultant sputtering yield require a kinetic treatment as opposed to a fluid treatment of the plasma-wall transition layer. Specifically, a model (partially analogous to the kinetic treatment proposed by Chodura [51]) is developed to characterize a strong electric space-charge potential defined by boundary conditions found at the limiter/divertor. Within the specified spatial domain, the mean-free-path collision and ionization distance, λ_{mfp}, is assumed to be much greater than the plasma-edge scale length. Because the sheath development region scales similarily to the plasma-edge scale length, electron, ion, atom, and molecule collision processes may be ignored.

Briefly, the model is defined as a "box" or control surface through which plasma-edge ions flow assuming upstream velocity conditions. At time $t=0^+$, a metal partition is inserted to simulate the charge-buildup (if any) at the limiter/divertor surface. The resultant transient electric-field is used to step the primary particle

trajectories through time until convergence of an electrostatic potential is obtained. In lieu of experimental data, secondary particle models and trends, whenever available, are employed so that these effects on the potential magnitude and potential profile may be investigated.

2.2 Plasma Sheath Geometry

Resolution of the magnetized sheath model geometry into four distinct regions - the plasma, "presheath," sheath, and wall (metal surface) - is depicted by Figure 2.1. The plasma state is assumed to depend only on the x'-coordinate perpendicular to the wall; i.e., particle densities and fluxes, force fields, and the wall surface are infinite and uniform in the $y'z'$ plane. The electric field (if any) is parallel to the x'-direction and is equal to the negative gradient of the potential such that $\vec{E}(x') = -\vec{\nabla}\phi(x')$, while the magnetic field is at an angle, ψ, with respect to x' such that $\vec{B} = B(x',y')$.

The plasma is assumed to be an infinite source of primary electrons and ions with the additional constraint of time independent particle fluxes across the plasma-edge boundary in the direction of the wall. Hence, the plasma-edge distribution functions are decoupled from
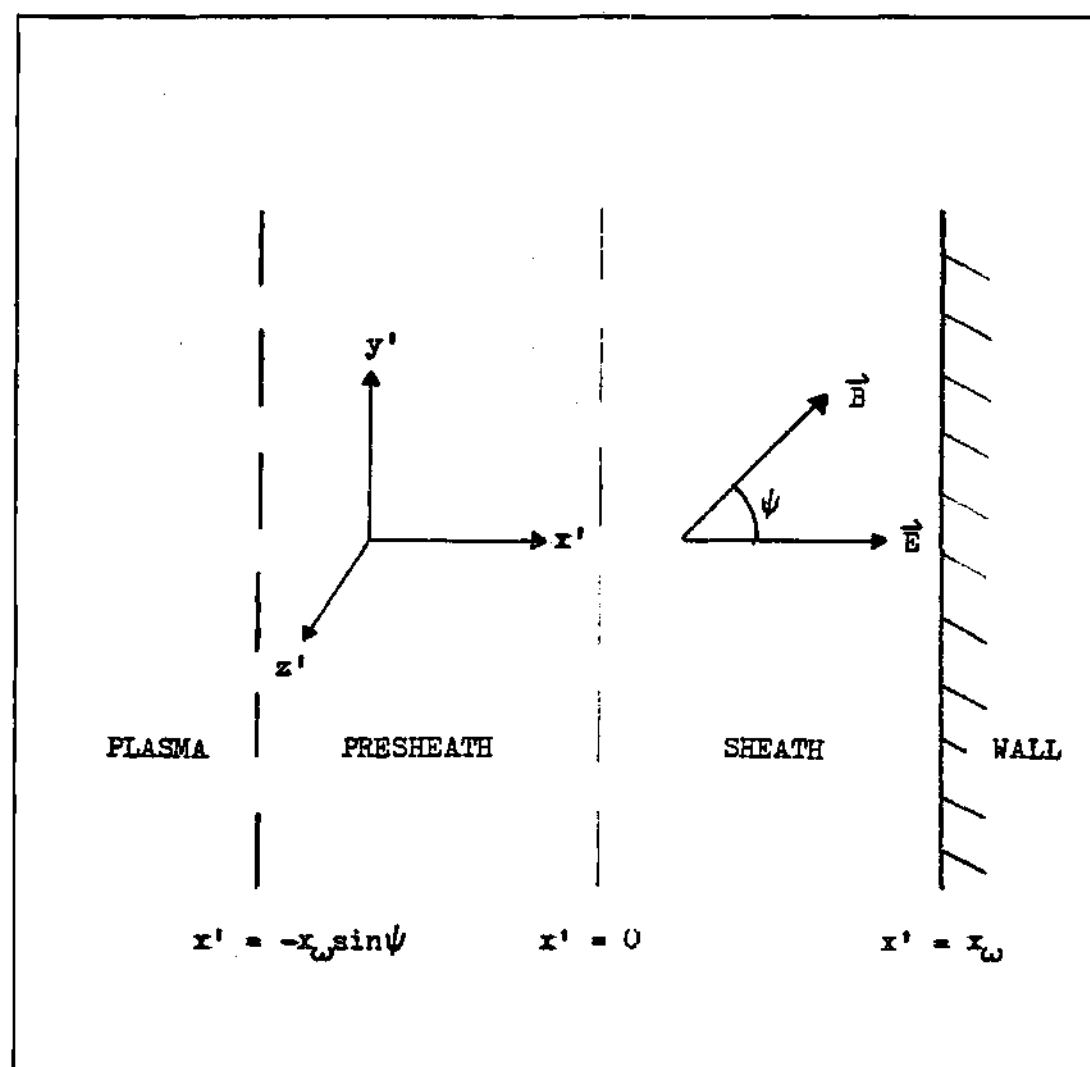
Figure 2.1   Magnetized Sheath Model Geometry

plasma-wall interaction effects that could otherwise alter the primary charged-particle distributions during the profile evolution of the sheath potential. While such a coupling may be important in specifying the form and the structure of the plasma (hence, the potential itself) near a metal surface [63], the necessity of including collision and ionization processes to simulate a coupling has been deemed beyond the scope of the current research (collisionless modeling). Furthermore, within the geometrical framework defined, the plasma-edge boundary distributions are representative of the "plasma presheath." These distributions must then reflect the streaming (acceleration) conditions due to the long-range plasma electric field set-up by the electron pressure gradient.

Particle fluxes streaming from the plasma into the "presheath" (better known as the magnetic presheath) traverse parallel along a uniform magnetic field, $\vec{\nabla B}=0$. Neglecting the gradient of the magnetic field over the sheath region as a second-order effect is justified when compared to strong first-order effects of the electric sheath and Lorentz forces. The mathematical construct of a "presheath" is justified due to the necessity of ion-flux conservation across the boundary $x'=0$. When the angle of the magnetic field, ψ, is nonzero, primary ions streaming into the sheath may re-enter the "presheath" region due to their gyromotion. Thus, the size of the presheath is proportional to the ion

gyroradius and the magnetic angle. Within the defined presheath, the electric field (if any) is "weak" such that relative quasineutrality is assumed and $\nabla\phi \sim 0$ over the presheath thickness.

In Chodura's analysis of the transistion layer, the presheath does not exist solely as a feature of flux conservation, rather the presheath potential relative to upstream conditions is determined by using a two-fluid model for ions and electrons.[51] Solving the continuity and momentum equations with the proper closure conditions, the space-charge with the presheath can be found. Chodura couples the fluid presheath potential to the sheath potential at $x'=0$ by insuring an equivalent space-charge at the presheath-sheath boundary.

The sheath region is characterized by a strong electric-field (at least one to two orders of magnitude greater than the presheath field) and scales according to the Debye length, λ_D, as defined by the conditions at $x'=0$. The Debye length is that distance over which particle-particle, i.e. space-charge effects dominate. A sheath width of $x'=10\lambda_D$ appears sufficient to model the potential profile, $\phi(x')$.

It is assumed that the wall is fully absorptive to primary electron and ion fluxes. Secondary electron and ion fluxes as well as reflected primary-ion fluxes are modeled as a function of the primary particle and wall material

characteristics. Non-uniformities in the wall surface have been ignored.

2.3 Particle Trajectory Model

The kinetic equations describing the primary and secondary particle trajectories during the temporal development of the sheath potential are given by Newton's and Poisson's equations:

$$m_k \frac{d\vec{v}}{dt} = q_k \left(\vec{E} + \vec{v} \times \vec{B} \right) \tag{2.3.1}$$

$$\nabla \cdot \vec{E} = \frac{|e|}{\varepsilon_o} \left(n_i - n_e \right) \tag{2.3.2}$$

where k designates the particle species, m the particle mass, and $\vec{v}$ the particle velocity vector. The ion and electron space-charge densities (n_i and n_e, respectively) are defined as the zeroth moment of the distribution function:

$$n_k (x') = \int f_k (x', v') \, d^3v' \tag{2.3.3}$$

where $f_k (x',v')$ is the 6-D position-velocity distribution function of species k.

The particle charge, q_k, is defined as

$$q_k = \overline{Z}_k e \qquad\qquad (2.3.4)$$

such that $Z=-1$ for electrons, $Z=1$ for reflected and secondary emitted ions, and $Z=\overline{Z}(T_e)$, the average plasma-edge primary ionic state.   Primary ions emanating from the plasma have a charge state representative of coronal equilibrium (strongly temperature dependent), while the recycled ion wall flux which originates from within the plasma-wall transistion region (scrape-off layer) fails to coronally equilibrate.[64] These charge states are only weakly dependent upon the plasma-edge parmaters and for most impurites are well approximated by $Z=3\pm1$.[64] Justification for singly-ionized reflection and secondary emission is discussed later in sections 2.8 and 2.9, respectively.

Newton's equation of motion for each particle is solved by using a second-order accurate, numerical implicit scheme [65] that insures the properties of time reversibility and energy conservation within a conservative field of force. Violation of these properties would erroneously result in the numerical generation of entropy.   The implicit scheme of the position and velocity coordinates is given by

$$\dot{v}_h = \left(v_h^{i+1} - v_h^i\right)/\Delta t \qquad (2.3.5)$$

$$v_h = \left(v_h^{i+1} + v_h^i\right)/2 \qquad (2.3.6)$$

$$h^{i+1} = h^i + \Delta t \left(v_h^{i+1} + v_h^i\right)/2 \qquad (2.3.7)$$

where i corresponds to the ith time increment, Δt, and h is the Cartesian space coordinate (x,y,z).

For calculational simplicity, the geometry of particle motion is chosen along the guiding center axis where $\vec{B}=B_o\hat{n}_x$ (Figure 2.2). Newton's force balance components for the $\dot{v}_h$ terms are given by

$$\dot{v}_x = \frac{q}{m} E_x \qquad (2.3.8a)$$

$$\dot{v}_y = \frac{q}{m}\left(E_y + v_z B_o\right) \qquad (2.3.8b)$$
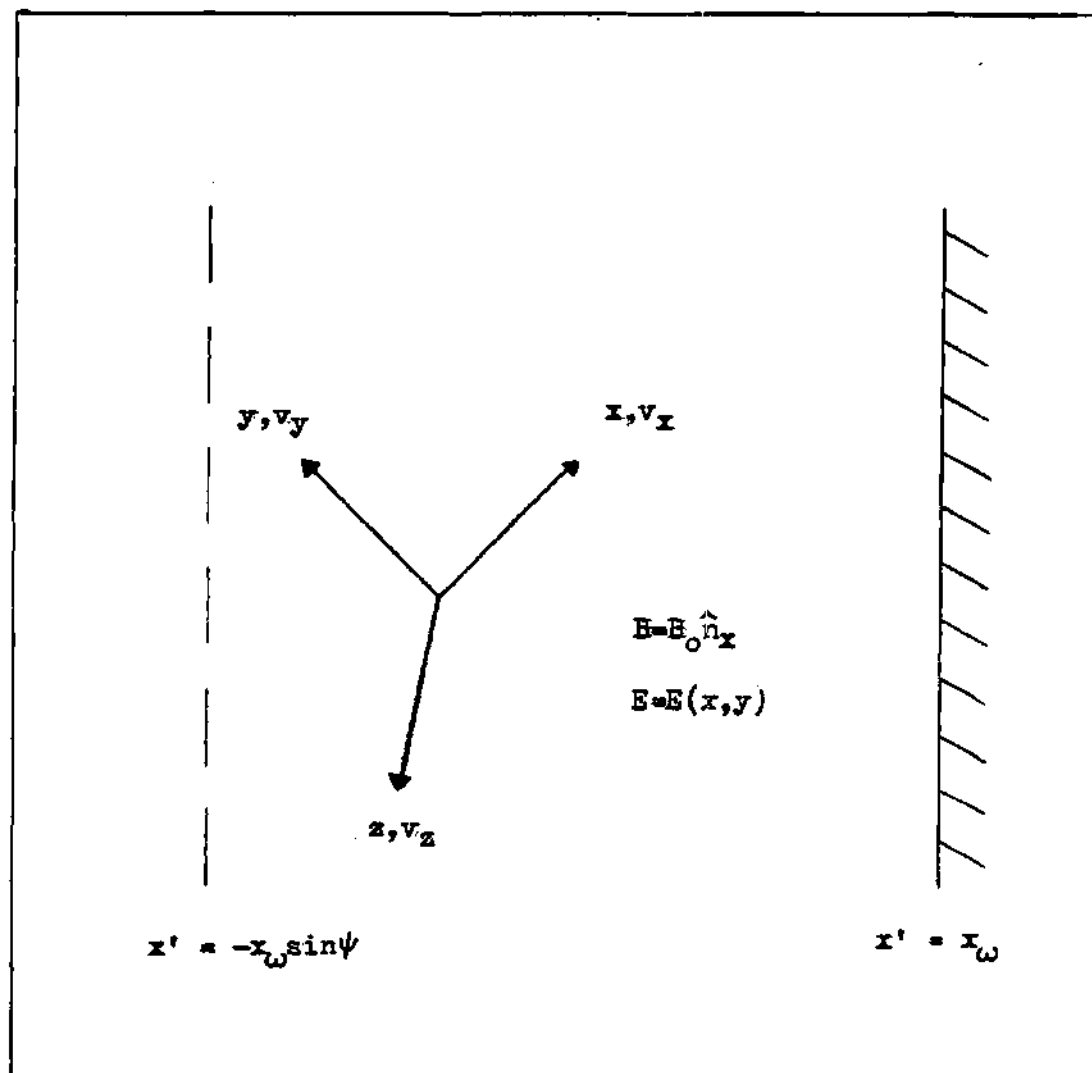
Figure 2.2 Particle Motion Geometry

$$\dot{V}_z = - \frac{q}{m} v_y B_o \qquad (2.3.8c)$$

Substitutions of equation 2.3.5 and 2.3.6 into these equations yields

$$V_x^{i+1} - V_x^i = \frac{q \Delta t}{m} E_x \qquad (2.3.9a)$$

$$V_y^{i+1} - V_y^i = q \frac{\Delta t}{m} \left\{ E_y + \frac{B_o}{2} \left(v_z^{i+1} + v_z^i \right) \right\} \qquad (2.3.9b)$$

$$V_z^{i+1} - V_z^i = -q \frac{\Delta t}{m} \frac{B_o}{2} \left\{ v_y^{i+1} + v_y^i \right\} \qquad (2.3.9c)$$

Rearrangement of these equations leads to the final result that

$$V_x^{i+1} = V_x^i + \frac{2c}{B_o} E_x \qquad (2.3.10a)$$

$$V_y^{i+1} = \frac{1}{1+c^2}\left\{\left(1-c^2\right)v_y^i + \frac{2c}{B_o}E_y + 2cv_z^i\right\} \qquad (2.3.10b)$$

$$V_z^{i+1} = \frac{1}{1+c^2}\left\{\left(1-c^2\right)v_z^i - \frac{2c^2}{B_o}E_y - 2cv_y^i\right\} \qquad (2.3.10c)$$

where $c=w_k\Delta t/2$, and w_k is the gyrofrequency of the particle species k.

2.4 Particle Density Calculation

A kinetic treatment of the plasma-edge transition layer presupposes the discrete sampling of continuous particle and current density distributions along a spatial grid. The direct implication is that particles are no longer points in space, rather they have a finite size proportional to the grid spacing. The basic physics under investigation is not altered by a collection of finite-sized particles as opposed to that of point particles, because close encounters between plasma particles have been neglected by previously assuming that the collisional mean-free-path is much greater than the Debye length. The most common means of simulating the collective behaviour over a statistical sample of charged

particles is achieved by employing a particle-in-cell (PIC) method.[66]

Calculating the charge density of a discrete spatial grid requires a weighting scheme for each particle among the nearest grid points. The selection of a "proper" weighting scheme is crucial to the required computational time and number of particle histories to be followed as well as the plasma problem at hand. For instance, a zero-order weighting scheme is accomplished by counting the number of particles within $\pm \Delta x/2$ (one cell width) of the jth grid point.[66] While computationally fast, as the particle moves through the jth cell, the jumps up and down will produce a density and resultant electric field which are "noisy" both in space and in time. Higher-order weighting schemes tend to smooth out the density and electric-field statistical fluctuations at the cost of additional computational time.

The initial PIC method employed to track the particle motion (more appropiately referred to as a velocity-in-cell or "flux"-in-cell approach) is attune to the methodology implied by Chodura.[51] For ions whose flux is conserved across the transition layer, the density at the jth grid point for a given phase angle is defined as

$$n_j = n_{ko} \frac{v_{x'}|_{j=1}}{v_{x'}|_j} \qquad (2.4.1)$$

where n_{ko} is the ion species density at $x'=0$ and $v_{x'}|_j$ is the net velocity along the x'-axis. Particle motion translated from the guiding center of motion (x-axis) to the geometrical normal (x'-axis) results in the possibility of negative velocity x'-component values due to the helical gyromotion. The net particle velocity, thus is defined as

$$v_{x'}\Big|_j = \sum_{\omega=1}^{N} v_{x',\omega}\Big|_j \qquad (2.4.2)$$

where ω is the index which corresponds to the number of times the particle crossed the jth grid point in a time Δt. The directionally dependent velocities are weighted by an appropiate scheme. For a given phase angle, the helical behaviour of the ion velocity and density translated to the x'-axis is displayed in Figure 2.3. Averaging over all angular phase space should yield monotonic density and velocity profiles in the case of no electric field and in the presence of an electric field provided the correct edge-conditions are supplied. Flat profiles were indeed calculated when $\vec{E}=0$ everywhere; however, oscillating velocity profiles (and, hence density profiles) resulted when space-charge effects were allowed to evolve for oblique magnetic angles. Chodura observed a similar behaviour and attributed it to a neccessity for changing the upstream velocity conditions.[51] While such a conclusion may indeed
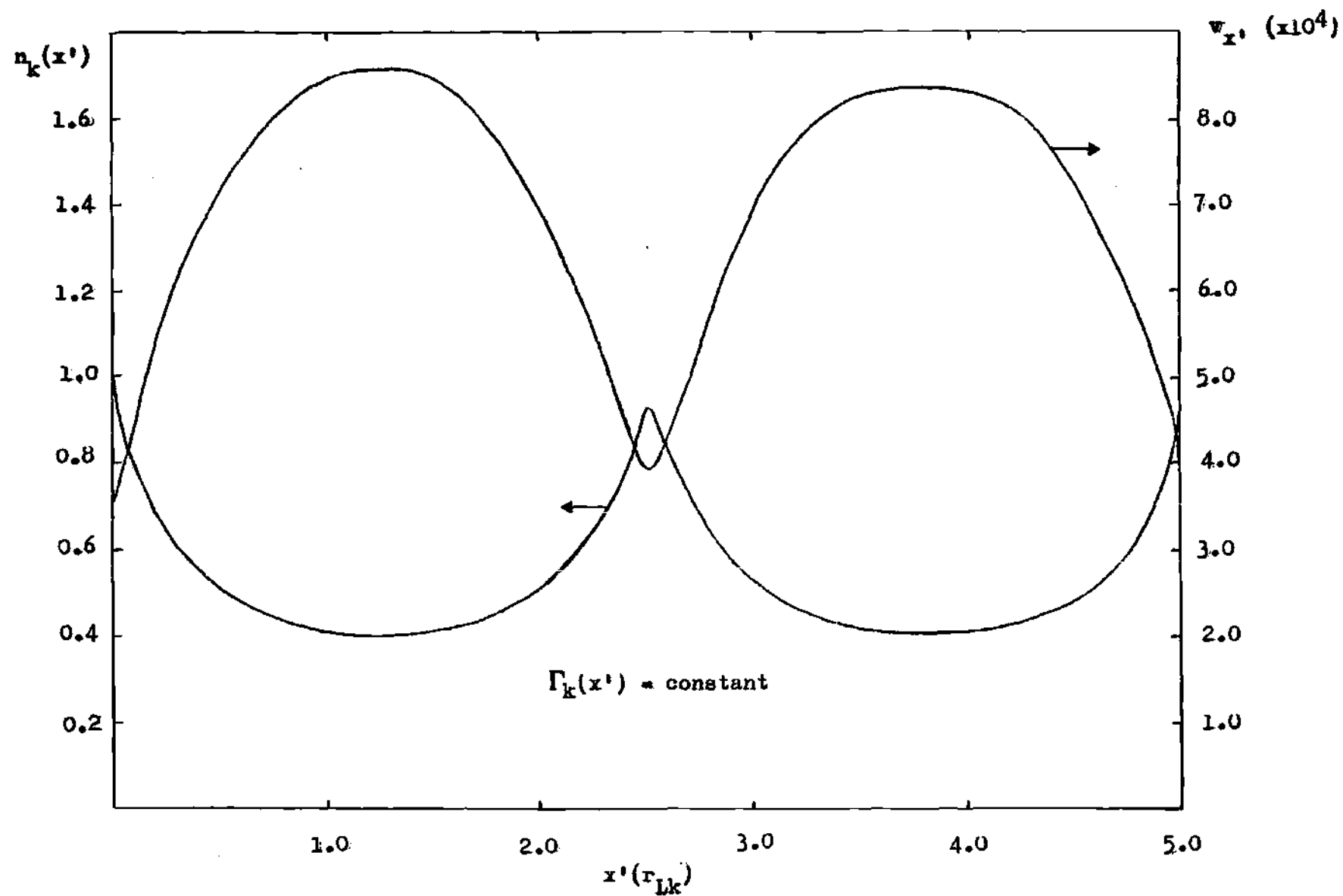
Figure 2.3 Translated Helical Phase Density and Velocity Along the x'-Axis Within the Sheath Region for $\psi = 45°$

be valid, it is the opinion of the author that the oscillatory behaviour is a result of the numerical technique as opposed to the modeled physics. Several variations of the "flux"-in-cell method did not yield numerically stable (monotonic) behaviours, thus the velocity-in-cell approach was discarded in favor of a true PIC methodology.

The method of choice in the current study is a modified cloud-in-cell (CIC) scheme which allows charged particles to be finite-sized rigid clouds that may pass freely through each other. No oscillations have been observerd with the CIC scheme. The CIC weighting [66] is of first order (Figure 2.4) placing that part of the cloud which is in the j-1 cell at x'_{j-1} and that part of the cloud in the jth cell at x'_j. The cells are all of width $\Delta x'$ about the nodal points, x'_j. Thus, for the total cloud charge of q_k, the part assigned to j-1 is

$$q_{j-1} = q_{j-1} + q_k (x'_j - x'_\ell)/\Delta x' \qquad (2.4.3)$$

and that assigned to j is

$$q_j = q_j + q_k (x'_\ell - x_{j-1})/\Delta x' \qquad (2.4.4)$$

where x'_ℓ is the center of the uniformily charged cloud. A higher-order modification to the CIC method can be
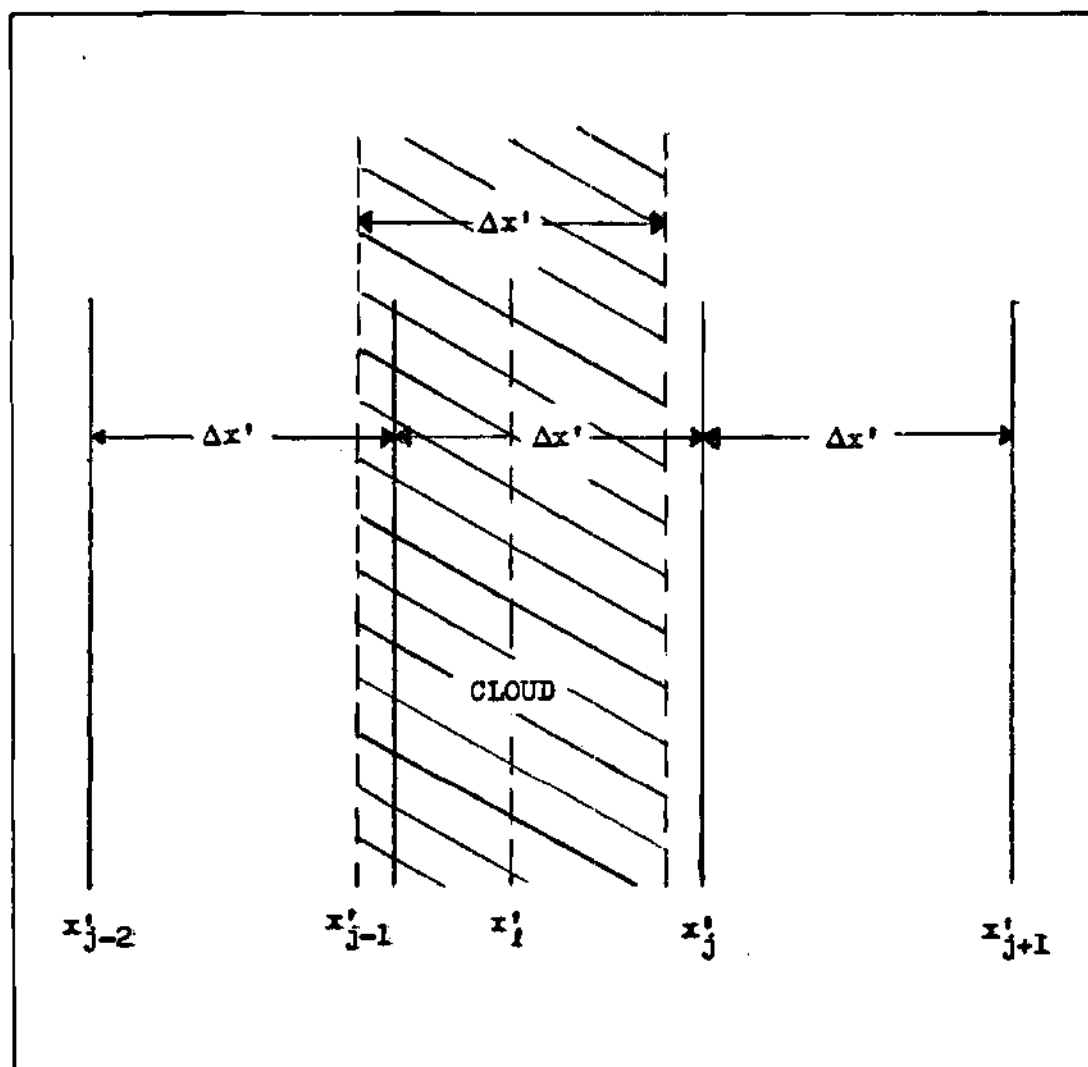
Figure 2.4 First-Order Cloud-in-Cell Weighting Scheme

accomplished by averaging the charge at j, q_j, over two consecutive time increments such that

$$q_j = \left(q_j^{i+1} + q_j^{i} \right)/2 \qquad (2.4.3)$$

The modified CIC scheme requires fewer particle histories per cell to be followed at the expense of a slower evolving density and electric field.

As a further means of smoothing the particle density noise, a least-squares spline fit is employed through all of the values, q_j. The "knots" are chosen to most accurately model the sheath profile behaviour (Figure 2.5). Grid spacing of the knots, Δ_m, was defined as

$$\Delta_m = \left(\Delta_1 \right)^{\alpha} ; \quad \alpha > 1 \qquad (2.4.6a)$$

where

$$\Delta_1 = \Delta x' = f \lambda_D ; \quad f \sim O(10^{-1}) \qquad (2.4.6b)$$
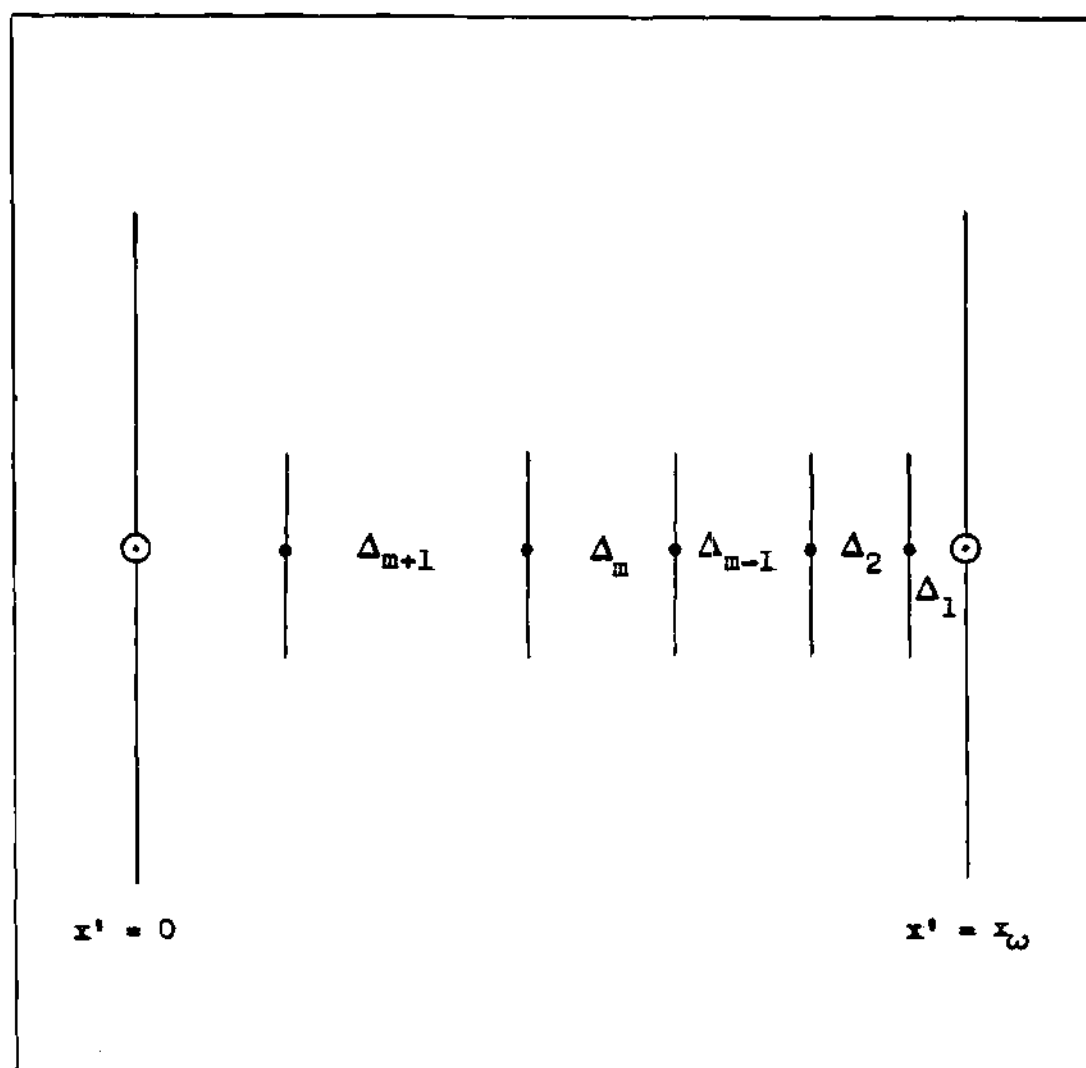
Figure 2.5   Grid Spacing of the Least-Squares Spline
Knots for the CIC Density Smoothing

2.5   Initial Conditions

The sheath solution is sought over a number of primary and secondary charged-particle fluxes (Figure 2.6). Neutral fluxes due to recycling and their subsequent secondary charged particle generation have been neglected because an accurate modeling of these processes would require the inclusion of collision and ionization events. The plasma outflux streaming to the wall, thus, consists of primary electrons, Γ_{pe}, and primary ions where

$$\Gamma_{pi} = \sum_k \bar{\bar{z}}_k \Gamma_k \qquad (2.5.1)$$

is the summation over fuel ion fluxes (D and T) as well as any partially ionized impurity fluxes. The species outflux, Γ_k, is defined in terms of the parallel flux along the magnetic axis, $\Gamma_{k\parallel}$, entering the control surface at $x' = -x_w \sin \psi$ (Figure 2.7) such that

$$\Gamma_k = \Gamma_{k\parallel} \sin \psi \qquad (2.5.2)$$

Influxes into the sheath from the wall are comprised of secondary electron emission, Γ_{se} (due to primary ion and secondary electron impact processes), secondary-ion emission, Γ_{si}, as a result of primary ion sputtering, and reflected
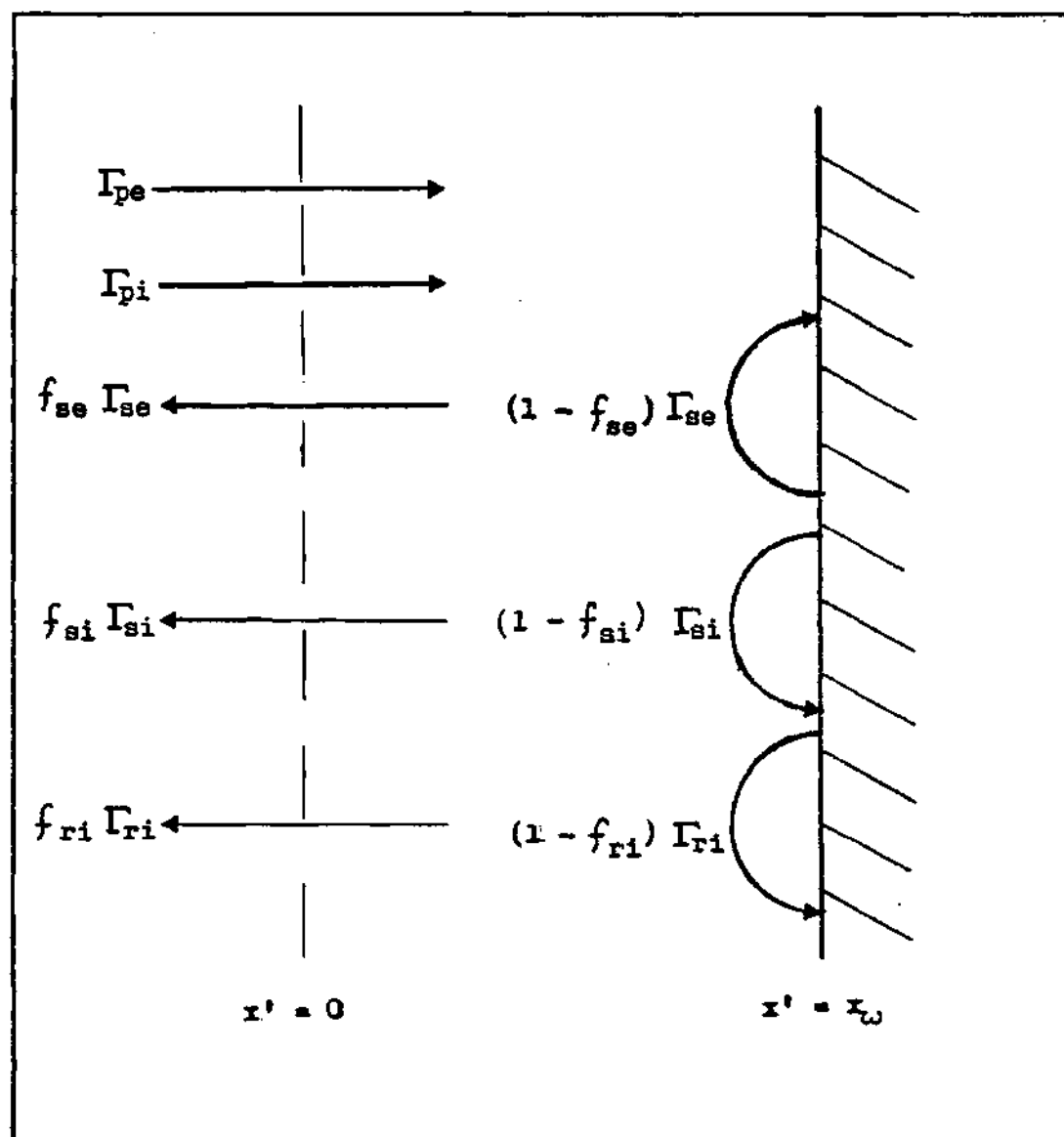
Figure 2.6   Primary/Secondary Charged Particle Fluxes
over Which the Sheath Solution is Found
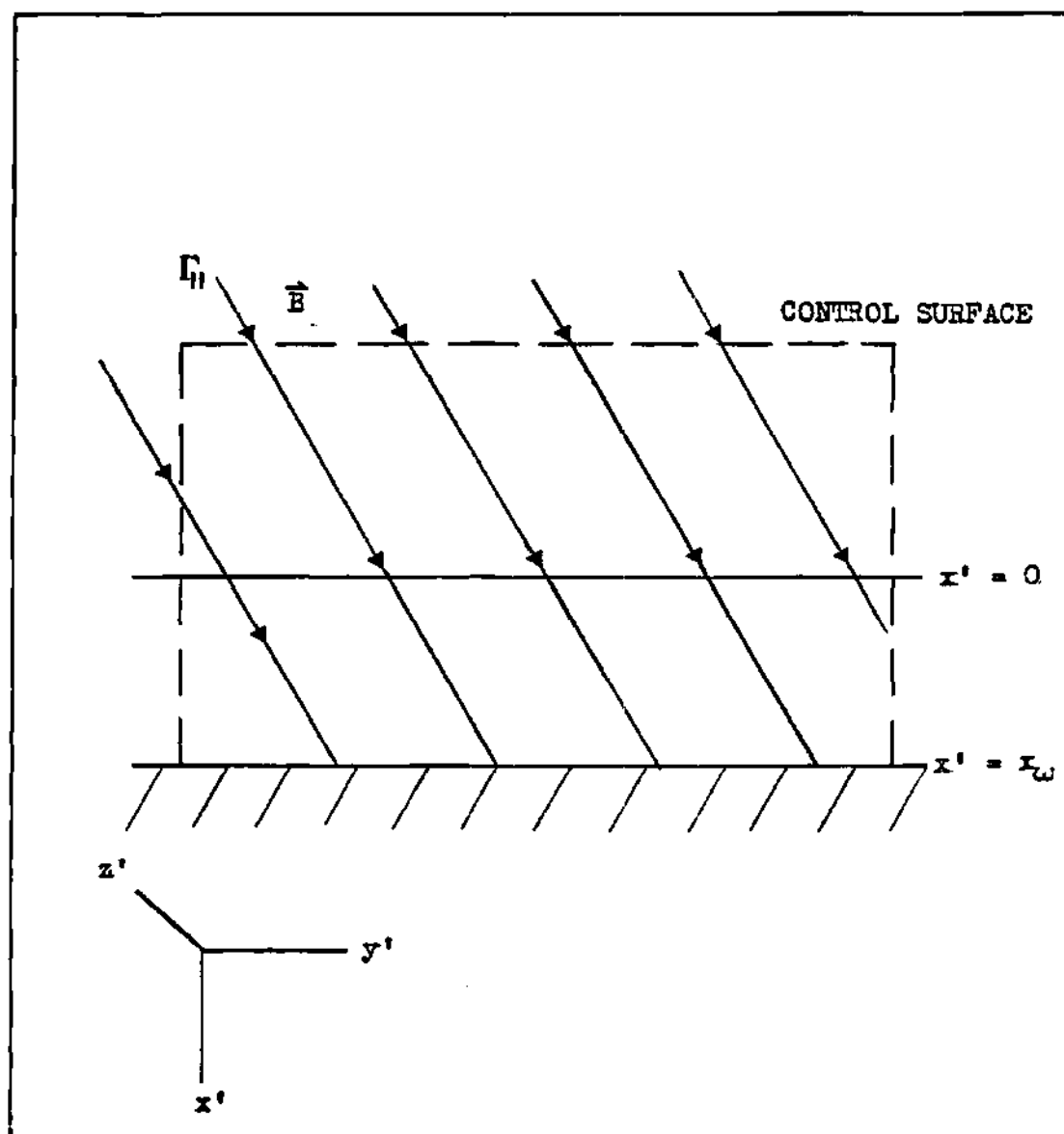
Figure 2.7   Control Surface Defining the Region of
              Sheath Solutions for the Appropiate B.C.'s

primary ions, T_{ri}. Also, the influxes are resolved in terms of the causal primary particle fluxes. The fractions f_{se}, f_{si}, and f_{ri} are survival probabilities of secondary electrons, secondary ions, and reflected ions, respectively, across the sheath emanating from the wall to $x' = 0$. Only the most energetic secondary and reflected ions are able to overcome the sheath potential such that $f_{si}, f_{ri} \longrightarrow 0$. Also, for an oblique magnetic field, the gyromotion will return the electron and ion influx, further reducing f_{si} and f_{ri} and resulting in $f_{se} < 1$.

Initially, at time $t = 0$, no influx exists and the primary outflux assumes the conditions of the presheath. Primary-ion velocity distributions are assumed half-Maxwellian parallel to the magnetic axis, x,

$$f_k(v_x) \propto \exp\left\{-m_k(v_x - v_s)^2 / 2T_k\right\} ; \quad v_x \geqslant 0 \qquad (2.5.3)$$

and Maxwellian in the plane perpendicular to the magnetic axis

$$f_k(v_y, v_z) \propto \exp\left\{-m_k(v_y^2 + v_z^2)/2T_k\right\} \qquad (2.5.4)$$

where v_s is the flow velocity due to the weak electric field over the presheath and plasma. The methodology for determining the velocity cooridinates v_x, v_y, v_z, and the

flow velocity, v_s, for each particle history that adequately describes the assumed Maxwellian distributions is outlined in Appendix A.

The primary electron distribution is assumed to be Maxwell-Boltzmann (fluid treatment) such that

$$n_{ep}(x') = n_{eo} \exp\left\{e\phi(x')/T_e\right\} \qquad (2.5.5)$$

Chodura treats the primary electron distribution kinetically in the same manner as the primary ion distribution.[51] Kinetic effects of the primary electrons on the potential profile should be relatively insignificant compared to those of the primary ions, since the ratio of the electron to ion gyroradii scales as $(m_e/m_i)^{1/2}$. Also, the kinetic time step necessary to track electrons is small compared to that of the ions (scaling as the electron to ion gyroradius ratio) so that the computional time required for space-charge equilibrium is much greater than for the kinetic treatment of primary ions alone. Neglecting kinetic primary electrons directly implies that the angular dependence of secondary electron emission due to electron impact can only be analyzed on an average basis. Chodura, as a result of the kinetic electron analysis, has been able to investigate the effects of secondary electron emission (on an exact basis) on the sheath potential as a function of magnetic angle.[67]

However, Chodura's kinetic analysis of primary electrons [68] indicates that the average angle of impact is relatively constant for magnetic angles $\psi \leq 70°$ and only shows a strong variation for magnetic angles $\psi > 80°$ (grazing incidence).

Quasineutrality at the sheath edge is written as

$$n_i \approx n_e \quad ; \quad n_i = \sum_k u_k^° \bar{\bar{Z}}_k n_{pk} (x'=0) \tag{2.5.6}$$

where n_{pk} is the kth primary-ion density and $u_k^°$ is a weighted fraction such that $\sum_k u_k^° \bar{Z}_k = 1.0$, at time, t=0.

After a number of time increments, Δt's, quasineutrality at $x'=0$ requires that

$$\sum_k u_k^t \bar{\bar{Z}}_k n_{pk} (x'=0) + n_{si} (x'=0) + \sum_k n_{rk} (x'=0)$$

$$= n_{pe} (x'=0) + n_{se} (x'=0) \tag{2.5.7}$$

and

$$n_{pe} (x') = \left\{ n_{eo} - n_{se} (x'=0) \right\} exp \left\{ e\phi(x') / T_e \right\} \tag{2.5.8}$$

where $u_k^t \lesssim u_k^°$ due to the wall-ion influx, n_{si} is the secondary-ion density (assuming only one sputtered ion species), n_{rk} is the kth reflected-ion density, and n_{se} is the secondary-electron density.

2.6 Electric Field Solution

The calculation of a convergent and self-consistent electric field over the sheath region, $0 \leq x' \leq x_w$, requires that the following conditions be satisfied.

$$\phi(x') = 0 \quad @ \; x' = 0$$

$$\text{(2.6.1)}$$

$$\lim_{t \to \infty} T_e = T_i \quad @ \; x' = x_w$$

$$\text{(2.6.2)}$$

The first condition is a relative value of the potential at the "presheath"-sheath boundary, $x' = 0$, to the wall potential value. A long range potential variation exists in the "presheath" region due to the weak electric-field $\sim O(10^3$ - 10^4 eV/m). The second condition requires that at equilibrium no net current of ions or electrons impinges upon the wall for an electrostatic field.

Initially, at time t=0, the relative disparity in the electron flux to that of the ion flux incident on the wall is proportional to the ratio of their velocities streaming into the sheath region.

$$\left(T_e / T_i\right)\Big|_{t=0} \propto \left(\frac{m_i}{m_e}\right)^{1/2}$$

(2.6.3)

The convergence scheme takes advantage of the charge-buildup at the wall due to the electron and ion flux disparity. During a time increment, Δt, the change in the wall space-charge is

$$\delta \rho = \frac{|e|}{\varepsilon_o} \left(T_e - T_i\right)\Big|_{x'=x_w} \Delta t$$

(2.6.4)

and the resultant wall electric-field is given by

$$E_w^{i+1} = E_w^i + \delta \rho \quad @ \; x' = x_w$$

(2.6.5)

Thus, the proper convergence scheme will result in $\delta \rho \rightarrow 0$ and $E_w^{i+1} = E^i$ as $t \rightarrow \infty$.

For each time increment of the electric-field development, an iteration of the equations

$$\phi(x') = \int_o^{x'} E(s) \, ds$$

(2.6.6a)

$$n_{pe}(x') = \left\{ n_{eo} - n_{se}(x'=0) \right\} \exp\left\{ e\phi(x') / T_e \right\} \qquad (2.6.6b)$$

$$\nabla \cdot E(x') = \frac{|e|}{\varepsilon_o} \left\{ n_i(x') - n_e(x') \right\} \qquad (2.6.6c)$$

is solved seeking an electric-field solution where $E(x'=x_w) = E_w^{i+1}$ and $\phi(x'=0)$. Also, the solution must be such that $0 \le E(x') \le E_w^{i+1}$ over the sheath region. The new electric-field profile is subsequently used to update the particle trajectories and currents over the next time increment.

2.7 Secondary Electron Emission

Secondary electron emission processes act to reduce the sheath potential such that [69]

$$\phi(x'=x_w) \propto \ln(1-\gamma) \qquad (2.7.1)$$

where γ is the ratio of the secondary emission to primary electron fluxes defined as

$$\gamma = \frac{(\sigma_e + \sigma_i + \sigma_o)}{(1 + \sigma_i + \sigma_o)} \qquad (2.7.2)$$

where σ_e is the electron-impact coefficent, σ_i is the ion-impact coefficient, and σ_o is the coefficient due to all other processes. To first-order electron and ion impact processes are the most important in determining γ, i.e. $\sigma_o \ll (\sigma_e + \sigma_i)$.

For monatomic (non-alloy) metal surfaces, empirical scaling laws exist whereby secondary electron emission can be modeled via electron and ion impact. At normal incidence, σ_e approximates [70]

$$\sigma_e = \left\{ a_1 \ln (a_2 \xi + 1) \right\} \left\{ 1 + a_3 \exp (-a_4 \xi) \right\} / (1 + \xi) \qquad (2.7.3)$$

where the constants a_i ($i=1,2,3,4$) have the values $1.533 \sigma_e^{mAX}$, 2.676, 0.2218, and 14.032, respectively. The factor σ_e^{mAX} corresponds to the maximum value of σ_e which occurs at the energy E_e^{mAX} or $\xi = 1$, where $\xi = E_e^P / E_e^{mAX}$ and E_e^P is the primary electron impact energy. For nonnormal incident angles, both σ_e and E_e^{mAX} are angularly dependent. The expression

$$E_e^{mAX}(\theta) = E_e^{mAX}(\theta = 0°)/\sqrt{\cos \theta}$$

(2.7.4)

appears to be quite adequate for $0 \leqslant \theta \leqslant 85°$ (Figures 2.8a,b).[71] The magnitude of σ_e, as a function of θ, scales exponentially [72]

$$\sigma_e(\theta) = \sigma_e(\theta = 0°)\exp\left\{a\overline{x}(1-\cos \theta)\right\}$$

(2.7.5)

where a is the absorption coefficient of electrons in the metal, and $\overline{x}$ is the mean depth of origin of secondary electrons in the metal.

The emission energy distribution, E_e^s, is independent of the primary electron energy in the range $E_e^p > 0(10^2$ eV)[72,73] and tends toward a Maxwellian with a most probable energy that is material dependent

$$E_e^s \propto \left\{\frac{U}{U_p}\right\}\exp\left\{\frac{-U}{U_p}\right\}$$

(2.7.6)

where U is the emission energy, and U_p is the most probable emission energy. For energies, $E_e^p \leqslant (20-30)$ eV, the emission spectra are peaked at E_e^p.[73] Furthermore, the energy distribution is independent of the primary angle of incidence and the crystal structure of the target.[72] The angular
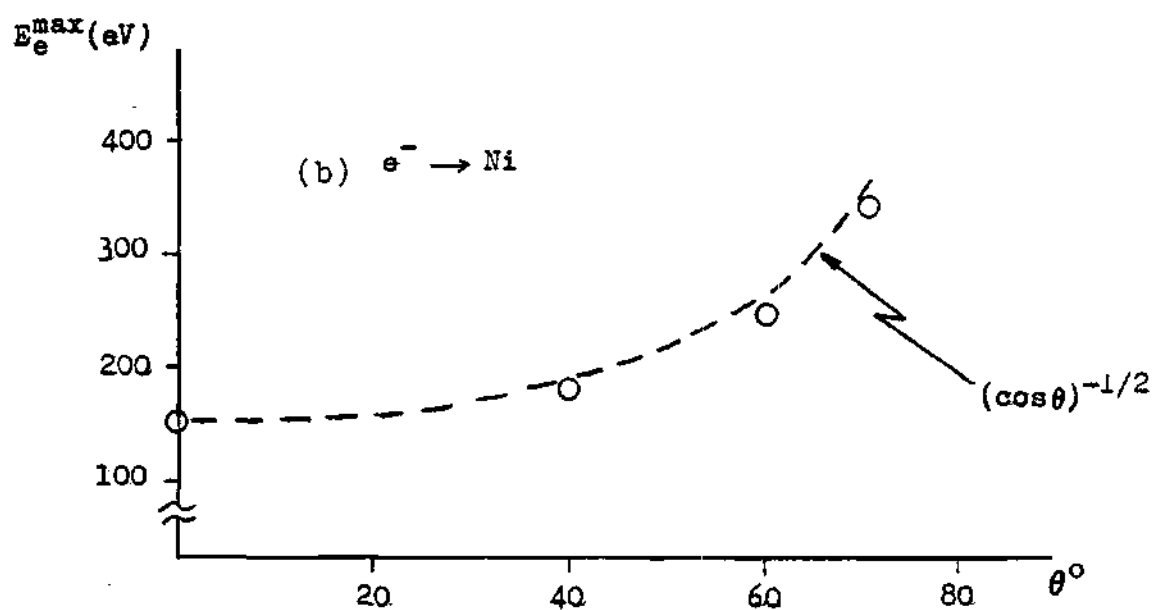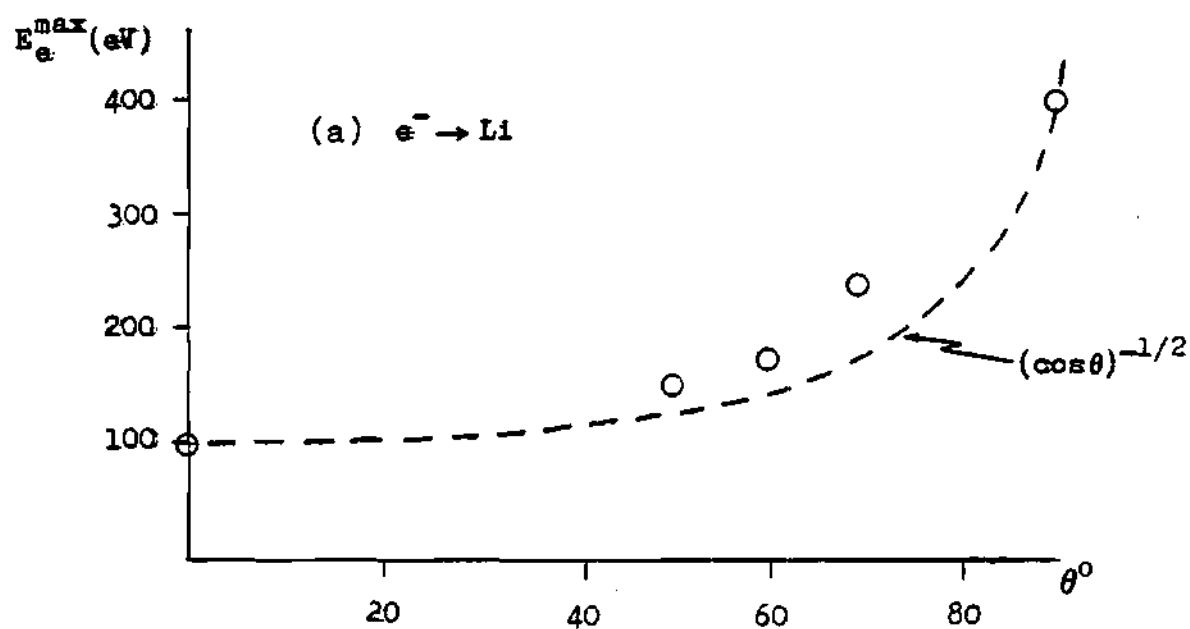
Figure 2.8   Angular Dependence of the Electron
             Impact Energy for Maximum Secondary
             Electron Emission (a) Lithium
             (b) Nickel Carbide

distribution of the secondary electrons, except rediffused primary electrons, roughly follows a cosine law.[72]

Ion-induced electron emission proceeds by two distinct processes, potential and kinetic electron emission. Potential electron emission (PEE) occurs when the potential energy released upon the neutralization of the projectile ion provides sufficient energy to release electrons from the wall material. Kinetic electron emission (KEE) occurs via the kinetic energy transfer of the projectile to the wall material electrons and is a threshold process at velocities greater than $(4-6) \times 10^4$ m/sec.[74] For singly-charged ions having velocities $\sim 0(10^5$ m/sec), KEE becomes more important than PEE.[74,75]

The dependence of potential electron emission, σ_i^P, for singly-charged ions can be prescribed as follows [74,76]:

$$\sigma_i = .032 \left(.78 E_i - 2\varphi\right) \; ; \; 2.6\varphi < E_i < 3\varphi \qquad (2.7.7a)$$

$$\sigma_i = 0.2 \left(.8 E_i - 2\varphi\right)/\varepsilon_F \; ; \; 3\varphi < E_i \leq 2\left(\varepsilon_F + \varphi\right) \qquad (2.7.7b)$$

$$\sigma_i = .5 - .16 \sqrt{\frac{\left(\varepsilon_F + \varphi\right)}{\left(E_i - \varepsilon_F\right)}} \; ; \; E_i > 2\left(\varepsilon_F + \varphi\right) \qquad (2.7.7c)$$

where E_i is the ground-state neutralization energy of the projectile ion, φ is the wall material work function, and ε_F is the Fermi energy of the wall material. For multiply-charged incident ions,

$$\left(\sigma_i^P\right)_\ell \propto \left(\frac{E_i^{2+}}{E_i^+}\right) \cdots \left(\frac{E_i^{\ell+}}{E_i^{\ell-1+}}\right)\left(\sigma_i^P\right)_1 \qquad (2.7.8)$$

where the emission coefficient is the cumulative product of the relative ratios of the ionization energy between levels 1 and 1-1.[77]

The kinetic electron emission coefficient scales as [78,79]

$$\sigma_i^k = \frac{P}{E_o} \int_0^\infty \exp\left(\frac{-x\cos\theta}{\lambda_c}\right)\left(\frac{dE}{dx}\right)_e dx \qquad (2.7.9)$$

where P is the probability of electron escape from the target surface barrier, E_o the electronic energy required to produce an electron above the vacuum level, λ_c the characteristic wavelength for electron diffusion inside the target material, θ the ion-incidence angle, and $(dE/dx)_e$ the total inelastic stopping power. It follows that for nonnormal ion incident angles, $\sigma_i^k(\theta) \sim (\cos\theta)^{-1}$. Kinetic emission yields are the same for singly and multiply-charged incident ions.[75]

The angular distribution for both potentially and

kinetically emitted electrons follows a cosine for polycrystalline materials.[80] The energy distribution for kinetically emitted electrons is similar to that due to electron impact, i.e. Maxwellian.[75] The potentially emitted electron energy distribution is "lognormal" in shape with a maximum at $(E_\lambda - 2\varphi)$ and a minimum at zero.[77]

2.8 Reflected Ions

Electron transfer processes via Auger neutralization, resonant charge-exchange, and quasi-resonant neutralization of backscattered projectile ions result in the possibility of neutral, positive, and negative charge states. The neutral fraction of reflected ions is defined as

$$\eta^\circ = 1 - \sum_\ell \eta^{\ell+} - \sum_m \eta^{m-} \qquad (2.8.1)$$

where η is the charge state fraction, ℓ the positive charge state, and m the negative charge state. For incident energies less than 10 keV, no multiple reflected ion states have been observed [81]; thus, $\ell = m = 1$ justifying that $Z = 1$ for the reflected ions in the sheath model. The charged fractions η^+ and η^- are not dependent on the incident energy or incident angle [81,82], rather they are functions of the exit energy and exit angle.[81-83] Thus, the reflected ions

can be defined in terms of the reflected neutral atom energy and angular distributions which are calculated by the TRIM model (to be discussed later).

The positive charge state tends to be a linear function of the exit energy for H, D, and He projectiles such that $\eta^+ = a\chi$, where a is a constant and χ is the exit energy. At "low" energies the following formula

$$\eta^+ = .00928 \ r_s \ \chi_n / m_k \qquad (2.8.2)$$

gives good agreement with experimental results [81,82], where r_s is the Wigner-Seitz radius of the target material and χ_n is the normal component of the exit energy. Restrictions are such that the projectile mass, m_k, must be H, D, T, or He ions/atoms and that the applicability at "low" energies is material dependent, e.g. $\chi_n < 1$ keV for Cs and $\chi_n < 8$ keV for Au.[81] The angular distribution of η^+ reflects that of η^o, the neutral atom fraction.[84]

For the negative charge state, no simple empirical expression exists to quantify $\eta^-(\chi)$ over a wide range of target metal types. Negative ions have been observed for only hydrogen isotope projectiles.[81] Qualitatively, the negative fraction, η^-, in its relative importance to the positive fraction, η^+, is a function of the target work function and the valence electron density.[81,83] Refractory

metals such as Ta, W, and Nb having high work functions yield ratios of

$$\eta^{-}(\chi)/\eta^{+}(\chi) \sim 0(.2)$$

$$(2.8.3a)$$

for all χ [83], while in the case of oxides and alkali metals, having low work functions, the yield ratios are [83,84]

$$\eta^{-}(\chi)/\eta^{+}(\chi) \sim 0(5)$$

$$(2.8.3b)$$

Materials having intermediate work function values show a cross-over ratio behaviour, e.g. $\eta^{-}/\eta^{+} > 1$ when $\chi < 5$ keV and $\eta^{-}/\eta^{+} < 1$ otherwise for H ,D $\rightarrow$ Au.[83] The angular distribution of η^{-} tends to peak more in the surface normal direction than η° or η^{+}.[84]

2.9 Secondary-Ion Emission

Ejected ions escaping from a clean metal surface due to sputtering mechanisms have a high probability of neutralization through the combined processes of auto-ionization, resonance charge-exchange, and Auger transitions. The probability of secondary-ion emission at a given exit energy can be written as [43]

$$R^+ = \sum_{A,B} \int_0^\infty P_A^{ion} \cdot P_B^{sur} \, dt \tag{2.9.1}$$

where P_A^{ion} is the production rate of ions by process A, and P_B^{sur} is the ion survival probability for neutralization process B. It follows that the relative secondary-ion yield, β^+, is the integral of R^+ over all ion exit energies.

$$\beta^+ = Y^+/Y_T = \int_0^\infty R^+(E) \, dE \tag{2.9.2}$$

The total sputtering yield is denoted by Y_T and the total secondary-ion yield by Y^+. For most elements, multiply-charged secondary-ions ($Y^{\ell+}$, $\ell > 1$) yields are significantly less than those of singly-charged ions, e.g. $Y^{2+}/Y^+ < 1\%$ for Ar+ energies less than 5 keV.[85] Thus, for secondary-ion emission, the choice of Z=1 in the sheath model is justified. Furthermore, the relative yield, β^+, is only on the order of 1% or less for all clean elemental surfaces, except the alkali metals which exhibit β^+ values of $\sim O(>10\%)$.[43,86]

Because the neutralization probability increases proportionally with the time spent by a secondary ion in the near-surface region, the secondary energy distribution, $N^+(E)$, relative to that of the sputtered neutrals is shifted

to higher energies.[43,87] Also, the high-energy tail falls off more slowly, E^n where $.5 < n < 1.5$, as opposed to n=2 for neutral behaviour.[88]

In the presence of the reactive gases (oxygen, nitrogen, and hydrogen) significant enhancement of the secondary-ion yield is observed.[86,88-90] Oxygen acts to prevent neutralization of low energy ions by electrons from the conduction band of the metal target [88] so that β^+ increases substantially, e.g., $\beta^+ > 10\%$ for Al, Cr, Fe, Ti, and Mo.[86] Hydride forming metals, e.g., Ti and V exhibit β^+ values of 41% and 6%, respectively for 1.5 keV incident deuterium.[90] Thus, these reactive gases, which are present in fusion reactors, may be capable of producing β^+ values sufficient to alter the potential profile.

2.10 Summarization of Sheath Model Development

A kinetic collisionless sheath model has been developed for an arbitrary magnetic angle in analogous fashion as first proposed by Chodura: charged particle trajectories are governed by Newton's equation of motion; the time-dependent space-charge is determined by a PIC methodology; and Poisson's equation is subsequently solved for each time iterate for the electric sheath profile, assuming the appropiate boundary conditions. However, the current sheath

model may be differentiated and considered as an independent development in that the particle following numerics, the PIC methodology, and the numerical convergence scheme employed by Chodura have been publically unavailable. Beyond the "simple" sheath modeling of Chodura and of the current effort, a generalization of the modeling has been performed to include primary impurity ions as well as secondary electrons, secondary-ions, and reflected ions. A brief summary of the research accomplished within the scope of the sheath modeling is as follows:

(1) A self-consistent sheath model for arbitrary magnetic angles has been developed, assuming a Boltzmann background of primary electrons. Newton's equation of motion has been solved by using a second-order accurate, numerically implicit scheme that insures the properties of time reversibility and energy conservation within a conservative field of force. The space-charge density is determined by a modified CIC method and is subsequently "smoothed" using a least-squares spine fit. In contrast to Chodura, no numerical oscillations (numerical instability) result from the current sheath potential formalism.

(2) The sheath development has been generalized to include an arbitrary number of primary-ion species of differing charges (positive or negative) and of differing masses.

(3) A framework has been developed to couple primary and

secondary charged particles during the temporal evolution of the sheath potential. However, due to the constancy of the plasma-edge boundary conditions (absence of collision and ionization events), a "true" coupling of the secondary particles and primary particles is not possible since the secondary particles will alter the primary-particle distributions, therefore altering the form and structure of the potential sheath.

(4) An overview of the relevant secondary-particle and reflected-ion characteristics has been presented in conjunction with expected conditions for fusion reactor operations. Models for secondary-electron emission (due to electron and ion impact), secondary-ion emission, and reflected-ion emission have been incorporated within the sheath model framework as a function of the material make-up of the wall surface. Chodura has parametrically modeled the effects of the secondary-electron coefficient upon the magnetic sheath; however, no actual material studies have yet been performed.

2.11 Sheath Model Verification

Verification of the basic physics underlying the proposed sheath model necessitates comparisons to previous sheath theory concepts and to those results found by Chodura

for a similar modeling. In general, the sheath profile obtained for a transition layer consisting only of primary charged-particle fluxes (in the absence of secondary emission) and a normal magnetic field ($\psi = \overset{o}{0}$) is simply expressed as

$$\frac{e\phi}{kT_e} = \ln\left(\frac{T_i}{T_e}\right)\bigg|_{x'=0}$$

(2.10.1)

As long as stable sheath conditions are fulfilled, Equation 2.10.1 is valid regardless of the flow velocity conditions accompanying the ions. Indeed, a parametric analysis of the current model (Figure 2.9) shows that for various flow velocity conditions (chosen in the range between the collisionless and collisional limits), the potential exhibits the expected theoretical behaviour.

Extending the previous potential expression to explicitly show the potential dependence upon the impurity fraction, the result (assuming Boltzmann electrons and $\psi = \overset{o}{0}$) is

$$\frac{e\phi}{kT_e} = \ln\left\{\frac{4}{\overline{V}_e}\left(u_D^o \overline{V}_D + u_T^o \overline{V}_T + \sum_{I=1}\left(u^o Z\right)_I \overline{V}_I\right)\right\}$$

(2.10.2)

where the subscripts D, T, and I refer to deuterium, tritium, and impurity ions, respectively. Varying the impurity species fraction quantity $(u^o Z)_I$ for a plasma in which
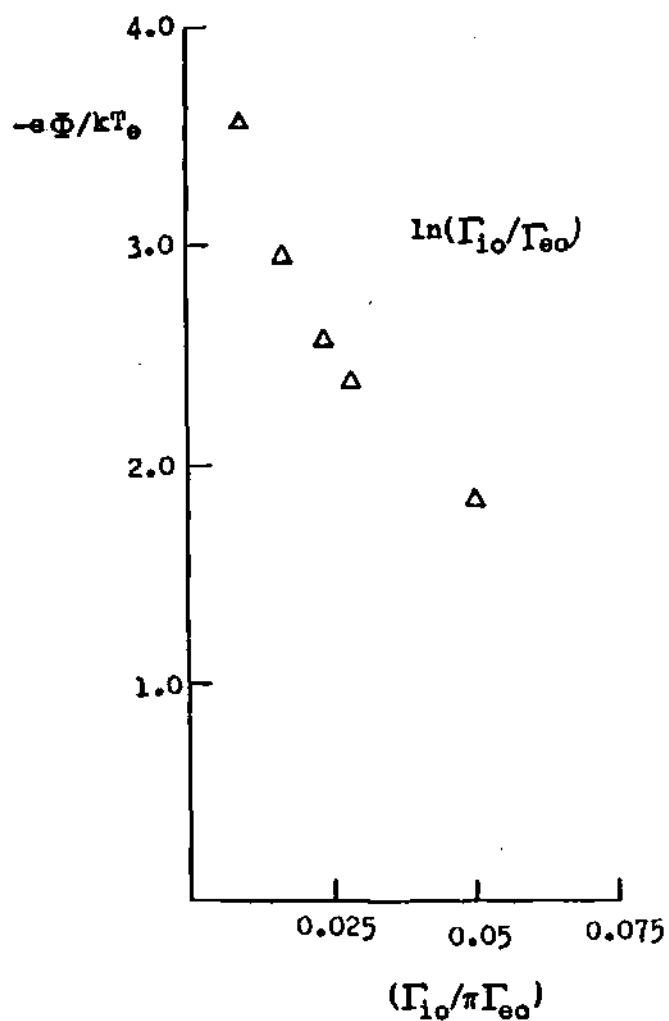
Figure 2.9   Sheath Potential Variation
Dependence on Presheath Ion
Flow Velocity
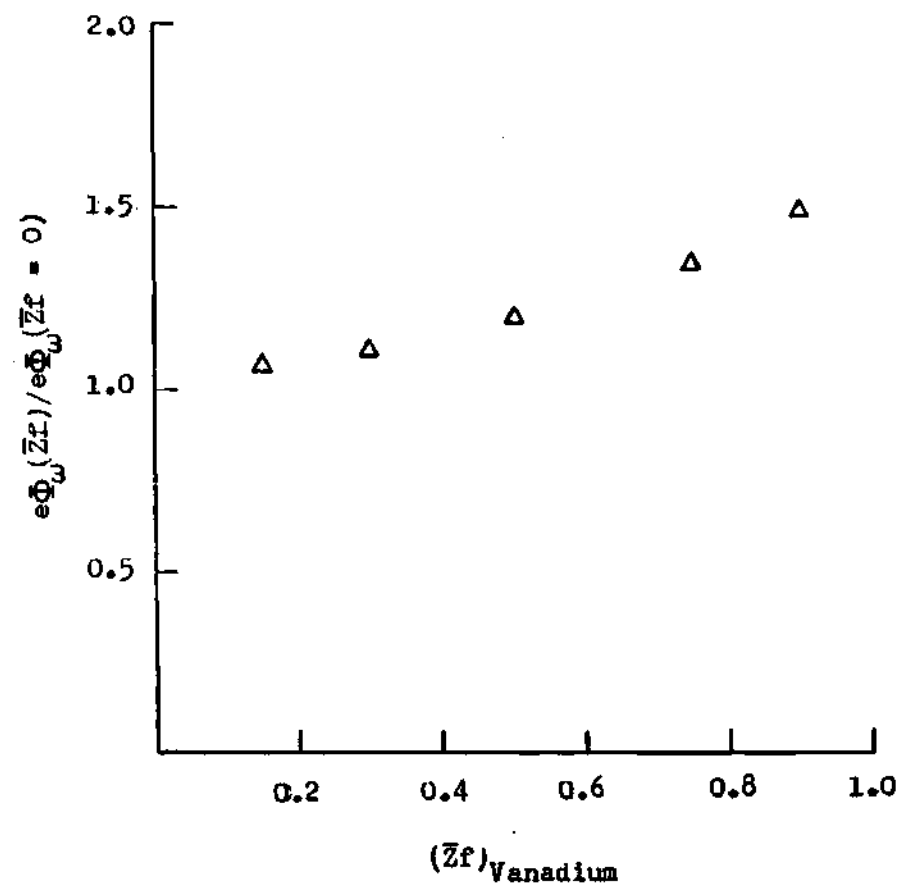
Figure 2.10   Sheath Potential Variation
Dependence on the Vanadium
(Z=3) Impurity Fraction

vanadium is the only impurity assumed present, the potential behaviour of the current model is displayed in Figure 2.10. Again, the model concurs with theory regardless of the impurity fraction condition, and the same functional behaviour was verified (but not shown) for helium, beryllium, and aluminum impurities.

For a nonneutral plasma (to reiterate), the scaling distance is proportional to the Debye length; hence, the spatial development of the sheath is inversely proportional to the square-root of the plasma-edge density. Such a characteristic is shown by Figure 2.11 for the three edge densities of 10^{16}, 10^{17}, and 10^{18} m^{-3}, assuming the normal magnetic field condition. Correspondingly, it has been observed (but not shown) that the potential magnitude does not statistically vary over the edge density range of 10^{16} to 10^{19} m^{-3} for constant temperature and angle conditions. As shown by Table 2.1, the sheath development can be approximated by the e-folding relationship

$$e\phi(x') = \exp\left(-x'_D\right) e\phi\left(x' = x_\omega\right)$$

(2.10.3)

where the dimensionless quantity x'_D (measured from the wall along the negative x'-direction) is proportional to the quantity, x'/λ_D, indicating the Debye length scaling of the sheath. The edge density condition of 10^{18} m^{-3} appears to
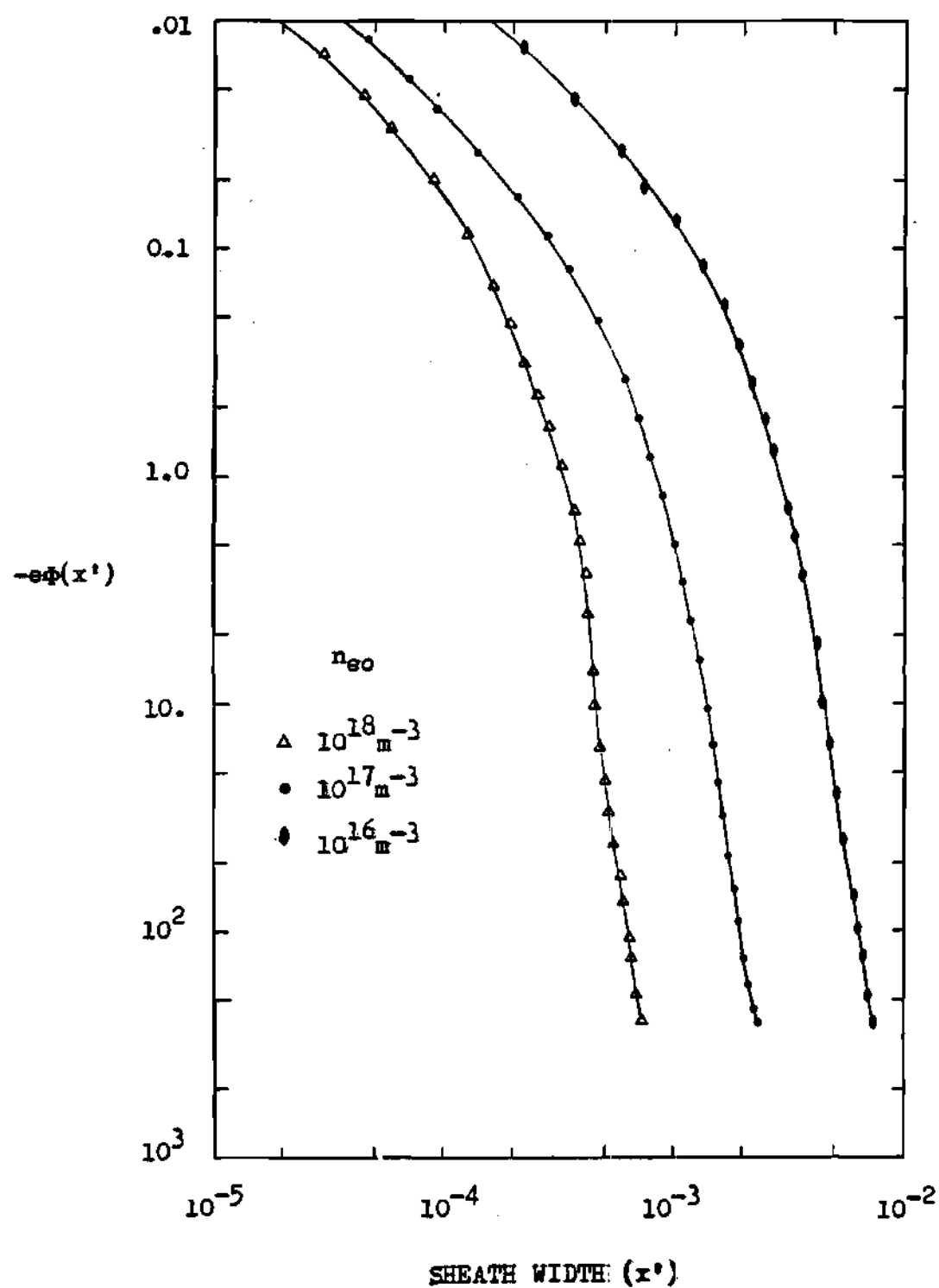
Figure 2.11   Spatial Development of the
              Sheath Potential for Different
              Plasma-Edge Densities

Table 2.1   Potential Sheath Spatial Dependence upon
the Debye Length as Measured from the Wall
$(x'=x_w)$ for Different Edge-Densities and
Normal Magnetic Angle ($\psi=0°$)

$$x'_D \text{ vs. } n_e (m^{-3})$$

x'/λ_D	10^{16}	10^{17}	10^{18}	10^{19}
1	1.6	1.5	1.5	1.5
2	2.7	2.7	2.7	2.6
3	3.7	3.8	3.7	3.5
4	4.5	4.9	4.3	4.45
5	5.5	5.8	5.0	5.3

inconsistently develop more rapidly than the other edge densities behaviours exhibited in Table 2.1; however, the data have a small reflective ion contribution (to be discussed later) unlike the other edge density data presented.

The Debye shielding relationship, as implicitly expressed by Equation 2.10.3, loses validity when ion gyroradii, r_{Lk}, effects become significant as indicated by Figures 2.12 a-c. Briefly, at low densities where $r_{Lk} < \lambda_D$ the ion over a gyroperiod experiences a relatively constant electric field regardless of the magnetic angle. As the density increases towards the limit where $r_{Lk} > \lambda_D$ variation in the electric field experienced by an ion in one gyroperiod (especially at oblique magnetic angles) is sufficient to dramatically alter the spatial development of the sheath potential profile. At oblique angles where $r_{Lk} > \lambda_D$ and $\psi \rightarrow 90°$, the sheath width increases, and the electric field experienced by an ion at a fixed distance from the wall (measured in Debye lengths) increases as well. In all cases, regardless of the gyroradius to Debye length ratio, the potential profile converges to the degenerative Debye shielding relationship (Equation 2.10.3) as $\psi \rightarrow 0°$, because the gyromotion is directed perpendicularly to the electric-field.

It has been observed that any variation in potential magnitude as a function of magnetic angle is nonexistent for
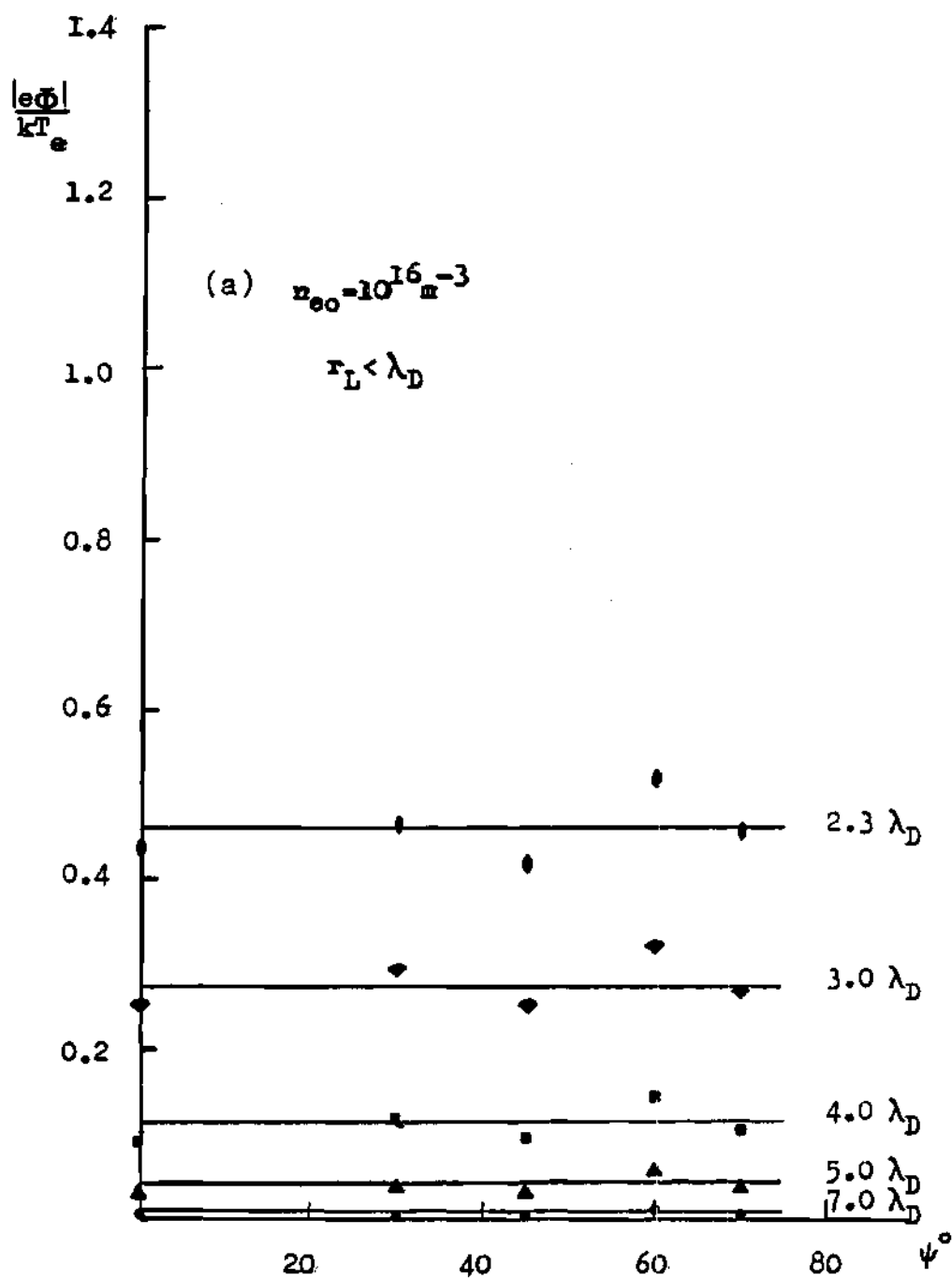
Figure 2.12   Potential Sheath Spatial Variation
Dependence upon the Magnetic Angle
for Different Edge-Densities
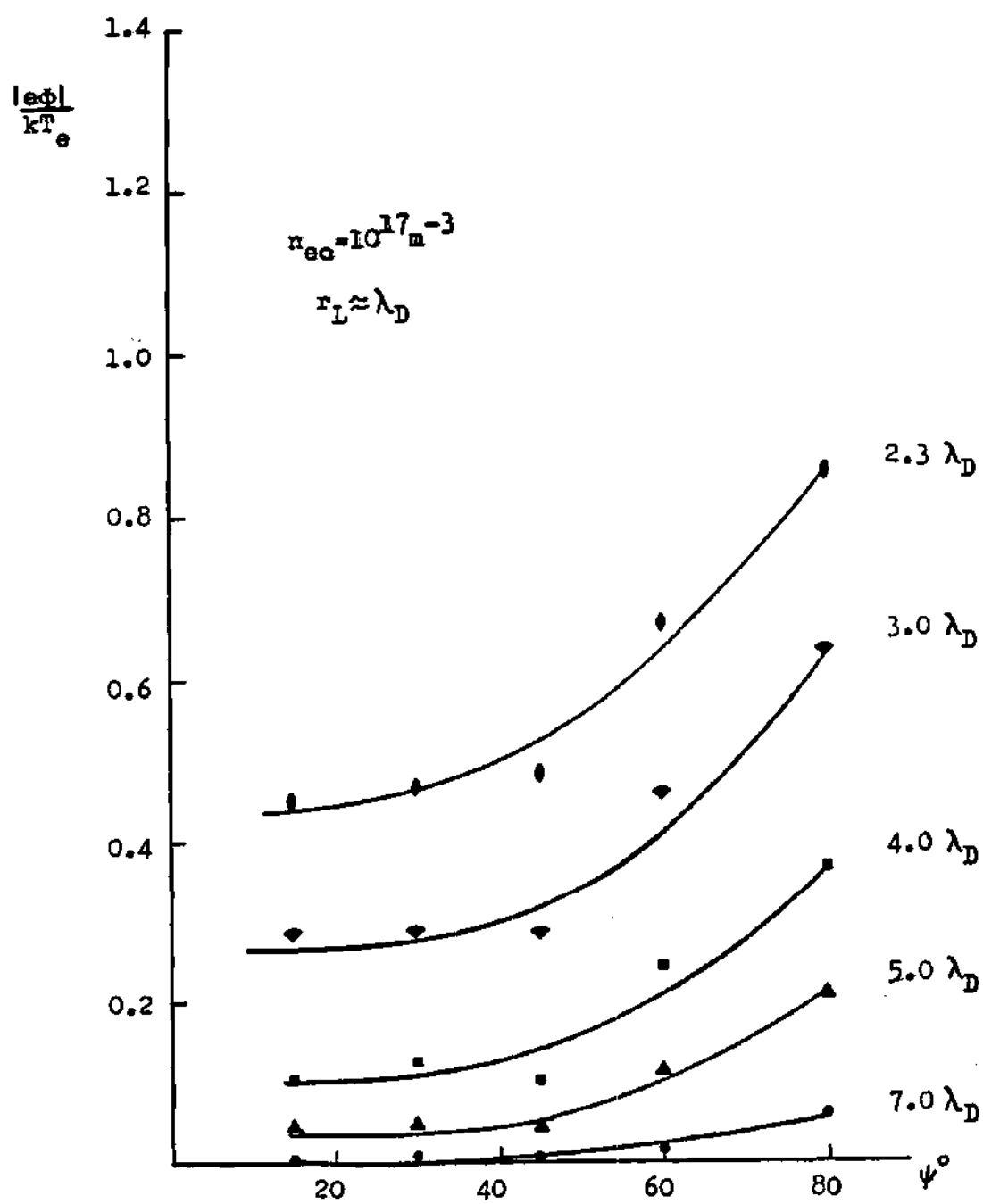
Figure 2.12b
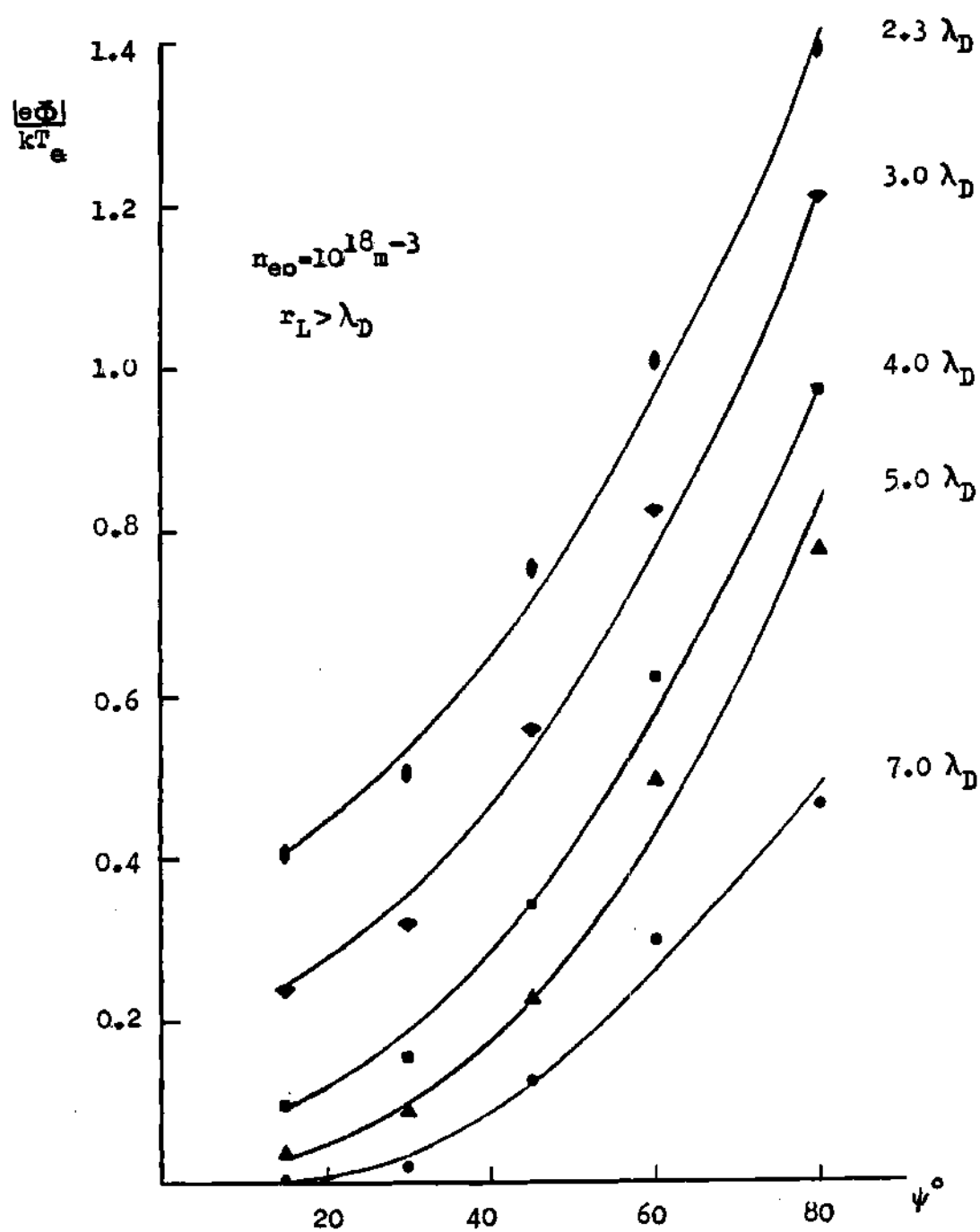
Figure 2.12c

constant edge density and constant flow velocity conditions (Figure 2.13) in agreement with Dabelge and Bein.[50] In contrast, Chodura's results [51] indicate the existence of a weak dependence of the potential magnitude upon the magnetic angle. The qualitative difference between the two models is directly related to a magnetic presheath criterion enforced by Chodura in order to insure sheath stability. The magnetic presheath criterion dictates that the flow velocity is angularly dependent [51]; hence, the primary charged-particle fluxes are angularly dependent, and according to basic sheath theory (Equation 2.10.1), the sheath potential magnitude must vary correspondingly. For the current model, no such angularly dependent flow velocity conditions are required to insure sheath stability. As previously stated, the CIC scheme chosen to track particle motion eliminated oscillatory (unstable) sheath behaviour as opposed to other flux-in-cell methods in which stricter flow velocity conditions would be required to diminish such unstable modes. While the oscillations observed by Chodura may be nothing more than a numerical defect, the possibility remains that there may indeed be an angularly dependent flow velocity which results when a magnetic presheath (fluid) analysis is performed and coupled to a kinetic sheath analysis.

As a consequence of the nonvariation of the sheath potential magnitude upon the magnetic angle, the average impact energy, $\langle W \rangle$, is relatively (statistically) constant
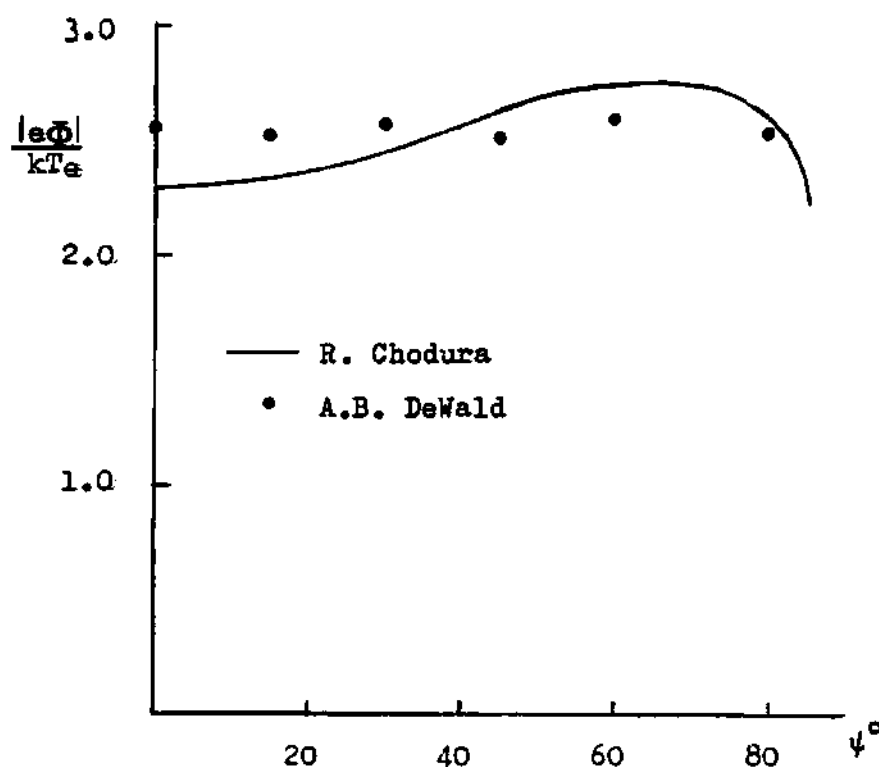
Figure 2.13   Potential Magnitude Variation
as a Function of Magnetic Angle
for Constant Edge-Density and
Flow Velocity Conditions
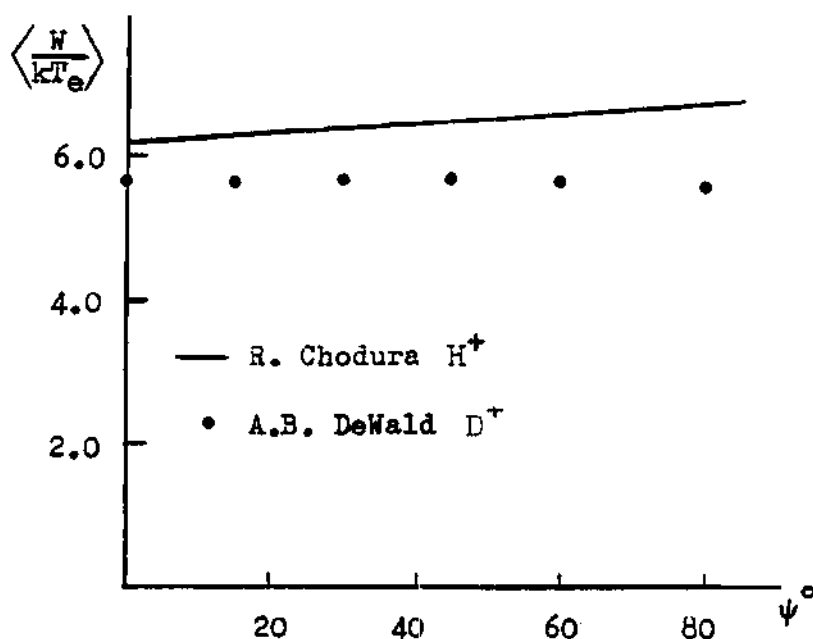
Figure 2.14   Average Hydrogen Impact Energy
as a Function of Magnetic Angle
for Constant Edge-Density and
Flow Velocity Conditions

over all magnetic angles (Figure 2.14). An angular
dependence is noted again by Chodura; however, the
correspondence between the average impact energy and
potential magnitude as a function of magnetic angle is
inconsistent. For an angular range $0° \leq \psi \leq 70°$, the potential
magnitude and the impact energy predicted by Chodura increase
monotonically; while for angles $\psi > 70°$, the potential
magnitude and impact energy gradients are of opposite signs
(a physical inconsistency).[51,68] Numerics may explain the
apparent discrepancy: for the current modeling, smaller cell
sizes (a reduction in $\Delta x'$) have been necessary in order to
properly weight particle impact quantities.

2.12 Wall Impact Angle

As a simple proof that the projectile impact angle as a
function of magnetic angle is calculated correctly, the
trivial case of cold ions in the absence of an electric field
will be initially investigated. For cold ions where the
velocity is directed solely along the magnetic axis, the
impact angle, θ, must be a linear function of the magnetic
angle. Indeed, such behaviour is exhibited in Figure 2.15;
furthermore, the linear dependence of θ on ψ has been
verified for several ion species regardless of mass or
charge.
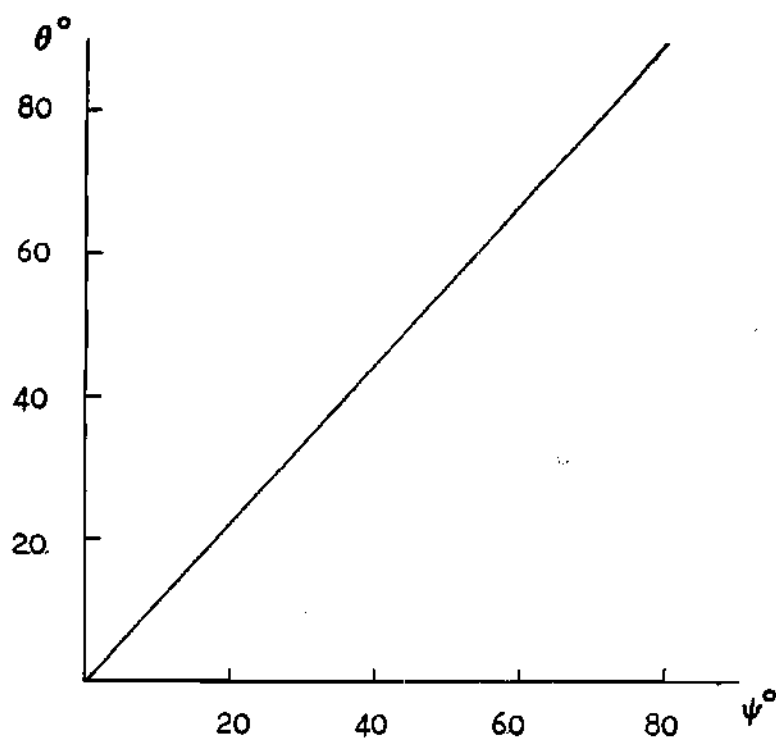
Figure 2.15 Cold-Ion Impact Angle Versus Magnetic Angle for No Electric Field
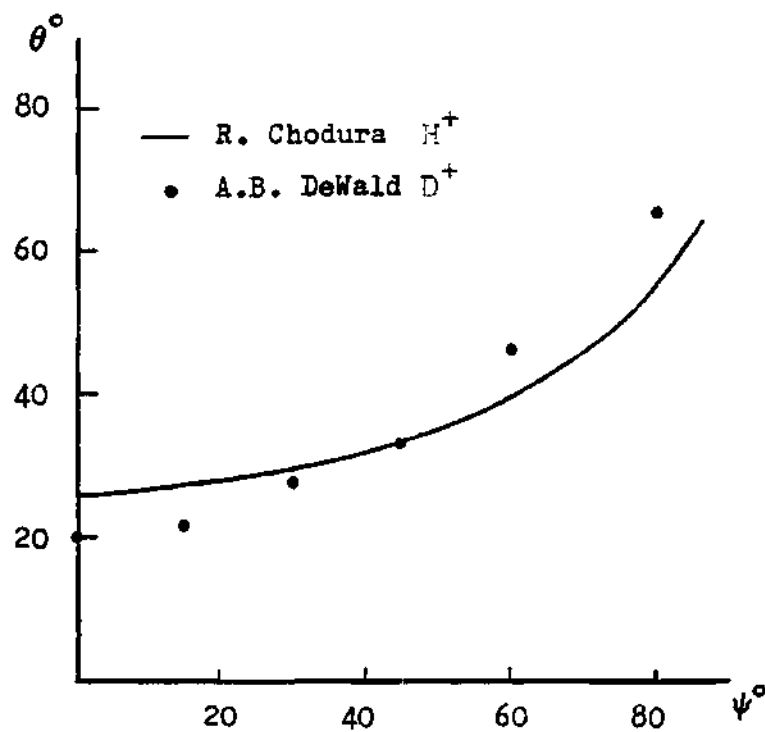
Figure 2.16 Hot-Ion Impact Angle Behaviour Versus Magnetic Angle in the Presence of a Sheath Potential

When imposing the condition of hot ions $(T_i = T_e)$ in the presence of an electric field, the perpendicular velocity components (along the magnetic axis) coupled to the driving force of an electric sheath alters the impact angle behaviour. The new Θ characteristics are shown in Figure 2.16 for deuterium and are compared to Chodura's results for hydrogen. Of significance is the qualitative prediction of the current model: hot ions in the presence of an electric field will impact at more oblique angles ($\Theta \rightarrow 90°$) as the magnetic angle becomes more oblique ($\psi \rightarrow 90°$), adding credence to similar results first obtained by Chodura.[68] In comparing the hot ion behaviour to that of cold ions, the hot ions, because of the perpendicular velocity components, exhibit a nonzero Θ behaviour for $\psi \rightarrow 0°$, while for $\psi \rightarrow 90°$, perpendicular velocity components act along the wall surface normal (x'-axis). The driving force of the electric sheath suppresses the obliqueness of the impact angle as a function of magnetic angle; however, in the limit where $\psi \rightarrow 90°$ both the ion and electron fluxes to the wall must vanish. Hence, the electric field is nonexistent, and if a potential does exist, it is positive due to the larger gyroradii associated with ions as compared to electrons. Thus, in the degenerative limit, $\psi \rightarrow 90°$, the impact angle $\Theta \rightarrow 90°$ as well.

Extending the current model calculations to investigate impurity species behaviour (not performed by Chodura), Figures 2.17 a-d show the results obtained for Al,V, Be, and
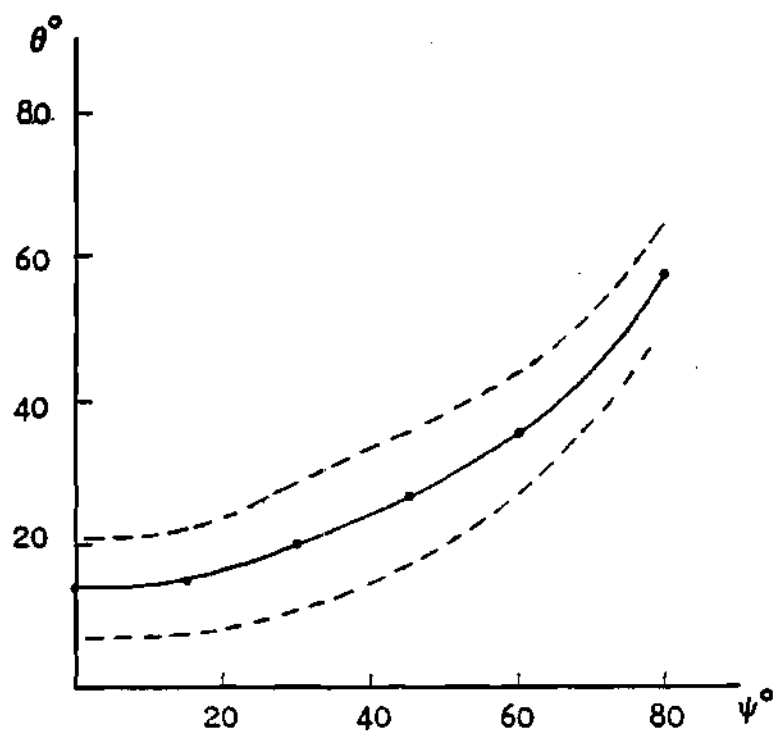
Figure 2.17   Al (Z=3) Impact Angle
    (a)   Dependence ± One
               Standard Deviation
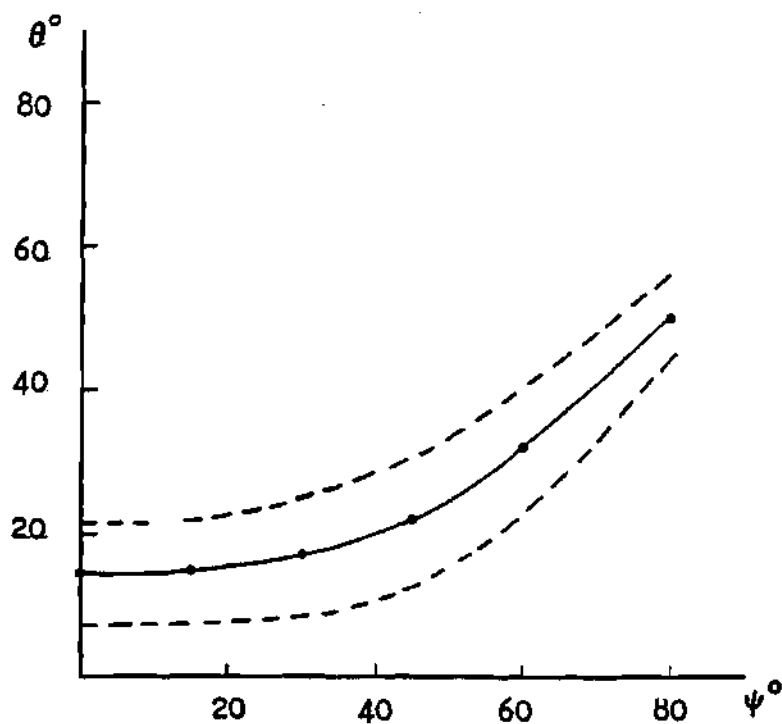
Figure 2.17   Impact Angle Dependence
    (b)   for V (Z=3) ± One Standard
               Deviation
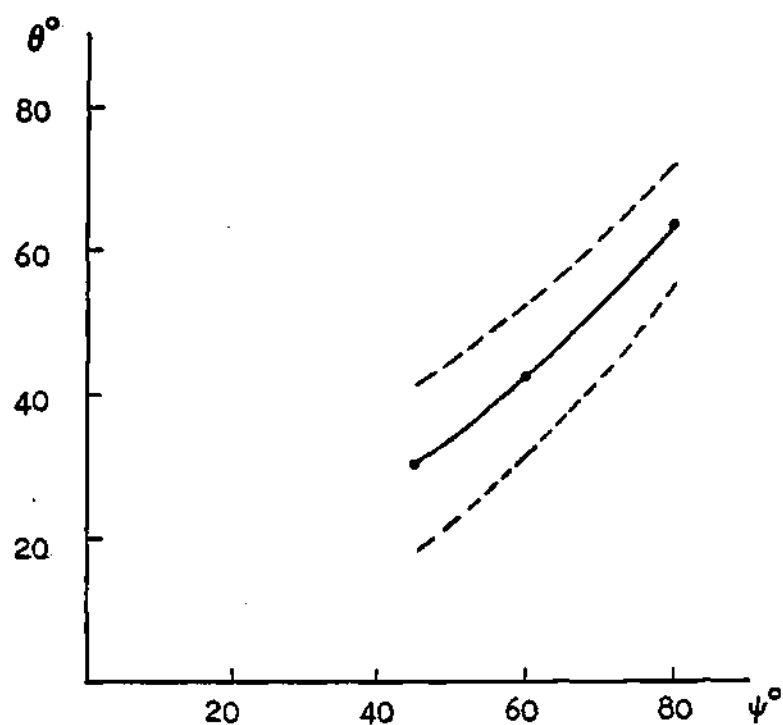
Figure 2.17   Impact Angle Dependence
     (c)   for 3e (Z=2) ± One Standard
               Deviation
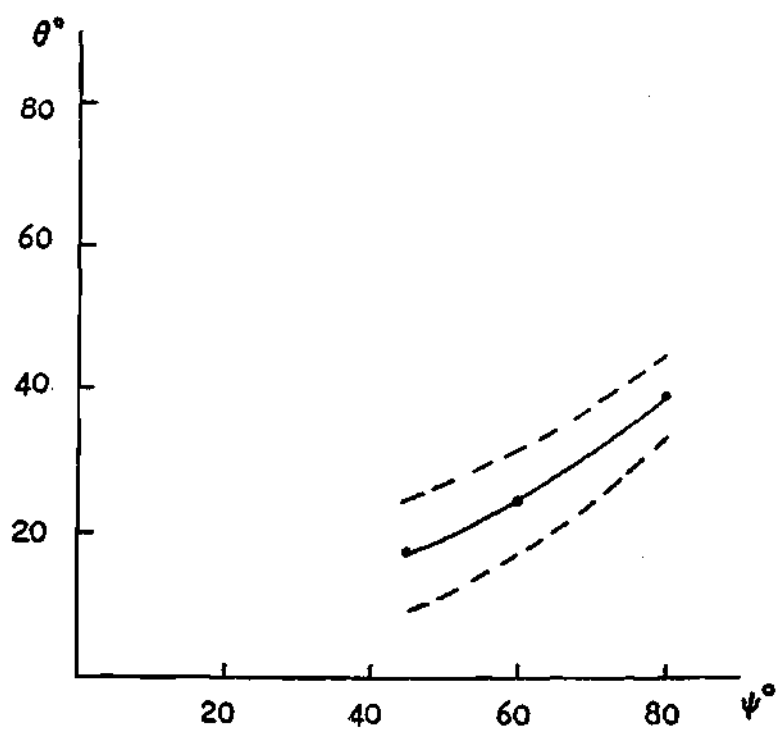
Figure 2.17   Impact Angle Dependence
     (d)   for W (Z=4) ± One Standard
               Deviation

W, assuming constant edge conditions. Similar qualitative results and trends have been obtained (but not shown) for He, Li, and Cu. The most significant result reveals that heavier ions will impact at a less oblique angle, Θ, for the identical magnetic angle in contrast to lighter ions; although, in the limit of $\psi \to 90°$, all ions tend towards $\Theta \to 90°$. With regard to the observed mass dependency of the impact angle, the ratio of the surface normal (x'-axis) acceleration component to that along the surface $y'z'$-plane dictates that heavy ions have a greater acceleration along the x'-axis than do light ions, resulting in less oblique Θ values for the same magnetic angle. Briefly, the acceleration components can be composed as

$$\vec{a}_{x'} = \frac{q}{m} \left\{ E_{x'} \left(1 - \frac{B_{y'}^2}{B^2} \right) - v_{z'} B_{y'} \right\} \hat{x}'$$

(2.11.1a)

$$\vec{a}_{y'} = \frac{q}{m} \left\{ B_{x'} \left(v_{z'} + \frac{E_{x'} B_{y'}}{B^2} \right) \right\} \hat{y}'$$

(2.11.1b)

$$\vec{a}_{z'} = \frac{q}{m} \left\{ v_{x'} B_{y'} - v_{y'} B_{x'} \right\} \hat{z}'$$

(2.11.1c)

The magnetic field is assumed to be of the form $\vec{B}=B(x',y')$, and the $\vec{E}\times\vec{B}$ drift velocity has been folded into the force equations as a Lorentz term. In the limit where $\psi \to 0°$ (hence, $B_{y'} \to 0$), the ratio of the acceleration along the surface normal (x'-axis) to that along the surface y'z' plane is proportional to the square-root of the mass as observed. In the limit where $\psi \to 90°$ (hence, $B_{x'} \to 0$), the mass dependence vanishes for the ratio of the acceleration components; thus, all ions species will tend toward the same limit as observed.

In an investigation of the edge-density effect (if any) on the average impact angle, $\langle \theta \rangle$, dependence upon the magnetic angle (Figures 2.18 a,b), and the physics underlying "why" charged-particles impact at oblique angles of incidence for oblique magnetic angles is elucidated. In the low density limit (constant edge-temperature), where the Debye length becomes much larger than the ion gyroradius ($\lambda_D > r_{Lk}$), the magnetic moment; i.e., the velocity components perpendicular to the magnetic axis, is an adiabatic invariant.[49] Over a single gyroperiod, the kinetic energy of the electric field is solely directed along the magnetic axis; hence, the pitch of the particle orbit with respect to. the surface normal increases for a corresponding increase in the pitch of the magnetic angle.

Conversely, when the density (constant edge-temperature) is increased such that $r_{Lk} > \lambda_D$, then the adiabatic invariance of the magnetic moment vanishes. Now, the gyromotion
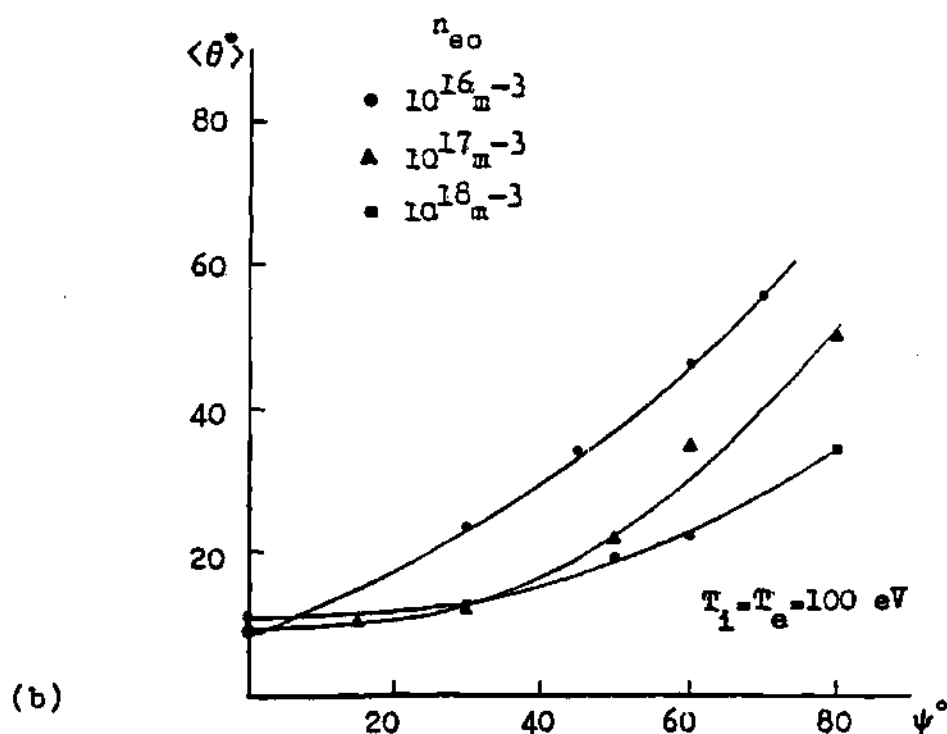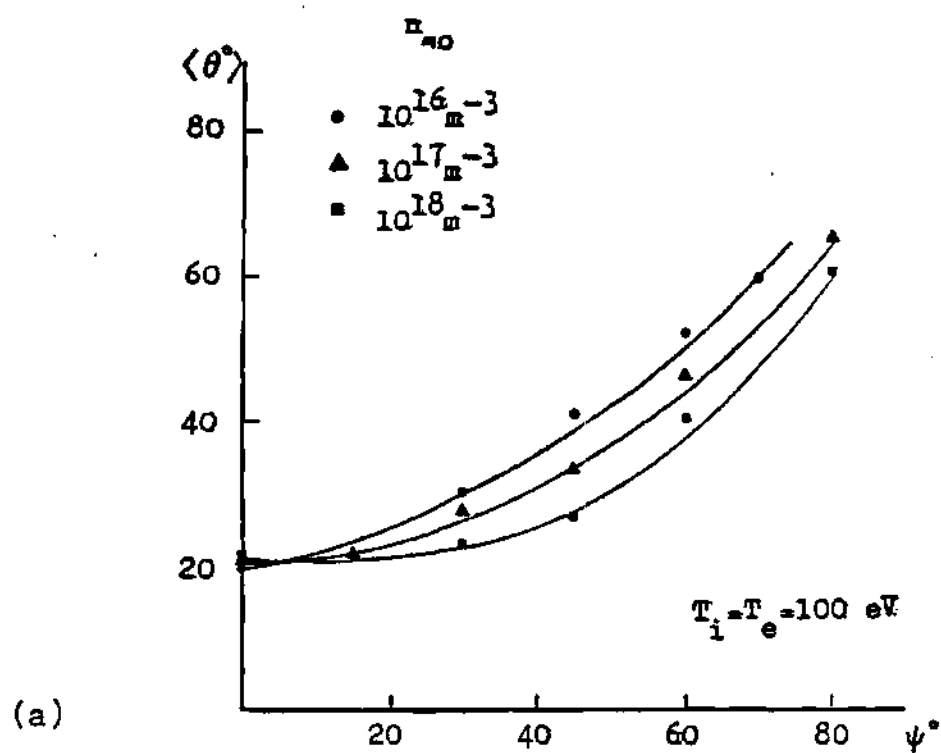
Figure 2.18 Average Impact Angle Dependence
Upon the Magnetic Angle as a
Function of Plasma-Edge Density
(a) Deuterium (b) Vanadium (Z=3)

responds to the electric field resulting in reduced impact angles, $\langle \theta \rangle$, as a function of increasing magnetic angle. Thus, the density effect upon the gyromotion in the presence of an electric driving force alters impact phenomena as well as sheath potential characteristics.

2.13 Secondary/Reflective Particle Effects

Reflective effects employing the positive charge-state formalism outlined in Section 2.8 appear to have little (if any) impact on the sheath potential magnitude. For the conditions studied, a consistent three to five percent increase in potential magnitude has been observed which may be attributed to reflected ions that result from the high energy "tail" of the primary particle distribution, and, thus, have the energy to overcome a retarding potential. However, the variance in the potential magnitude for reflected ions is within the convergence criterion of the current modeling; hence, the change in the potential magnitude (although consistent) may indeed be a statistical artifact. Small changes in the potential magnitude for reflected ions on the order of a 3% increase have been previously simulated by Brooks [91] (kinetic magnetic-field free model, $\psi = 0°$), lending credence to the current results.

As alluded to earlier, the more noticeable effect of

reflected ions is that of altering the sheath potential profile and, correspondingly, the ion and electron density profiles (Figure 2.19). The ion space-charge for the reflected ion case increases substantially at the wall due to the fact that most reflected ions are repelled back by the sheath potential. The reflected ion-space charge distribution directly impacts the potential profile in reducing the sheath width, a result subtantiated by previous investigations [50,91].

Secondary-electron emission due to ion impact for $Z_k=1$ results in a small decrease in the potential sheath magnitude on the order of +10 eV. The decrease is a direct result of the reduction of the net electron flux to the material surface. The potential reduction is proportional to the scaling law given by Equation 2.7.1 where $e\phi \propto kT_e \ln(1-\gamma)$ and γ is the electron emission coefficient. For most materials, the electron emission coefficient due to ion impact is less than $O(.1)$, hence, having a small effect on the potential magnitude. However, electron emission due to ion impact does significantly alter the sheath profile. For the magnetic angle $\psi=60°$ and the e-folding distance of $x'_D=5$, the sheath width without electron emission is equal to $5.5\lambda_D$ in contrast to the inclusion of electron emission where the sheath width is equal to $8.2\lambda_D$. Thus, secondary-electron emission has the opposite effect upon the sheath development in comparison to ion reflection. Secondary-electron emission due to heavy-ion
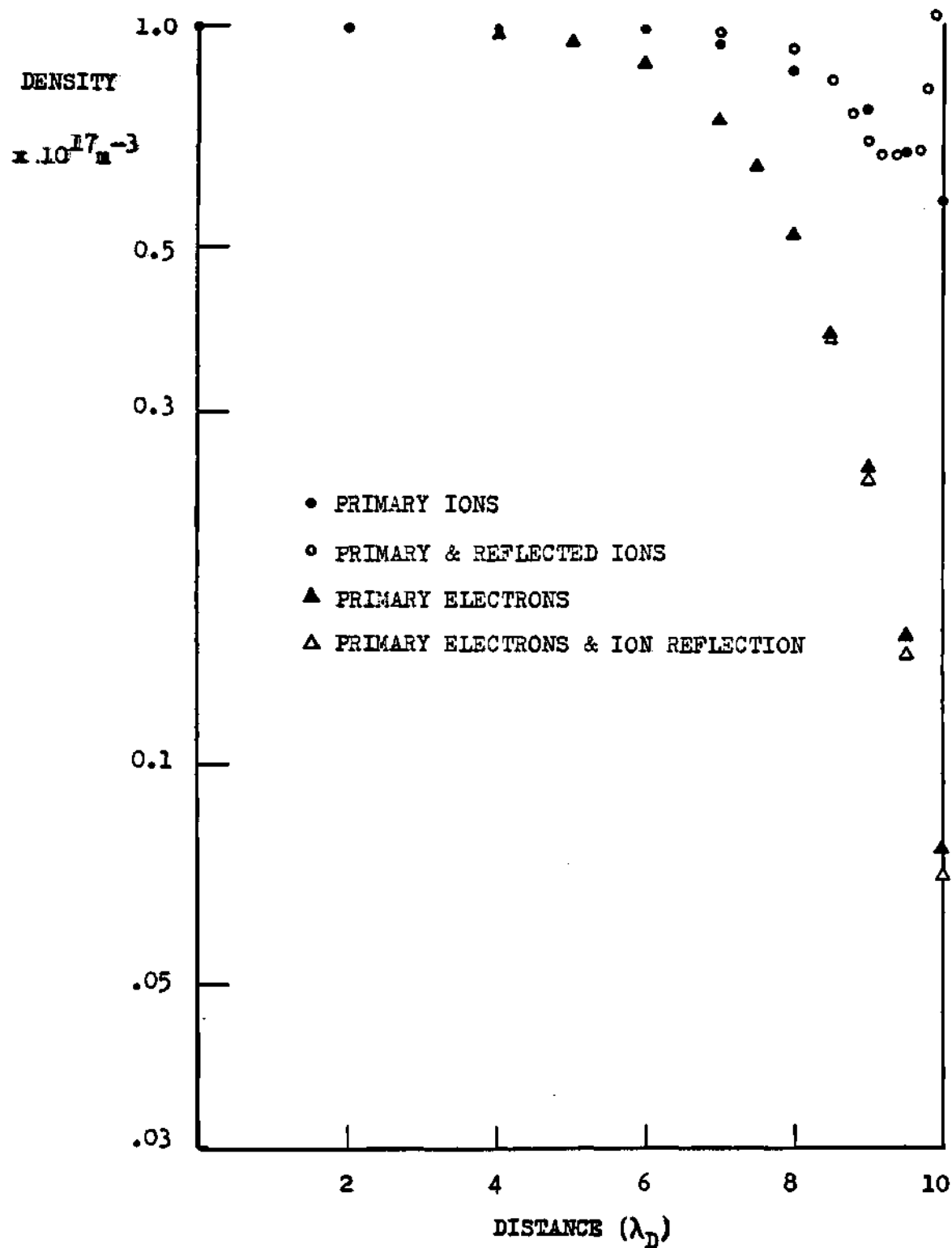
Figure 2.19   Electron and Ion Space-Charge Density
Profiles for Light-Ion Reflection and
$\psi=30^{\circ}$

impact $(Z_k=3\pm1)$ has not been modeled, because (1) the heavy-ion flux incident upon the material surface is much less than the incident deuterium flux and (2) the proportionality factor for electron emission due to ion impact for $Z_k=1$ in comparison to $Z_k>1$ is not well known for the wall materials of current interest.

A larger reduction in the potential magnitude should be affected by secondary-electron emission due to electron impact since the electron emission coefficient exceeds 0.5 for most materials. Attempts to model secondary-electron emission within the current framework, though, have failed due to exclusion of a kinetic electron treatment. Because of the fixed nature of the primary background of Boltzmann electrons in conjunction with a high secondary-electron emission coefficient, the space-charge near the wall $(x'=x_w)$ is unable to respond in a stable fashion. Also, because the secondary-electrons due to electron impact are emitted according to a Maxwellian with most probable energies of 2-5 eV, the kinetic ion time step, upon which the current modeling is based, is too large to track electrons in a continuous manner. Thus, the electron distribution appears to be discretized such that some cells within the CIC geometry are void of an electron population, resulting in an extremely noisy space-charge that leads to sheath instabilities.

The sheath evolution response to secondary-ion emission

has been hindered as well for high emission coefficients. Here, the fixed Boltzmann (electron) background is unable to respond rapidly enough to a high ion density in the vicinity of the material surface. Thus, high β^+ coefficients on the order of 90% (as would be expected for Li) cannot be modeled within the current framework; however, scoping calculations have been performed, assuming $\beta^+=10\%$. Secondary-ion emission has been observed to have no effect the potential magnitude for edge temperatures $\sim O(100$ eV). Because the sputtered energy distribution is peaked at low energies (< 10 eV), the probability of ejected ions overcoming a retarding potential is negligible, except at very low edge temperatures $\sim O(10$ eV) or, correspondingly, small potential magnitudes. For the condition $T_e=T_i=100$ eV and $\psi=0°$, the secondary-ion probability of escape is less than 5×10^{-4}, and for more oblique magnetic angles, the probability decreases due to gyromotion reimpact. While secondary-ions do not influence the potential magnitude since no change is made in the net ion flux to the material surface, potential profile (space-charge) changes are incurred. In particular, the ion space-charge exhibits a local maximum immediately in front of the wall surface similar to that observed for ion-reflection.

CHAPTER III

Sputtering Mechanics

3.1 Introduction

The sputtering mechanics or more aptly the slowing down and scattering of energetic projectiles and their resultant cascade events is computationally simulated using an extension of the 1-D Monte-Carlo TRIM (TRansport of Ions in Matter) formalism.[58,92,93] Through an independent effort, the original TRIM framework as applied to monatomic target materials has been extended to heteorgeneous multi-layer compound/alloy systems in order to model realistic first-wall fusion materials. In addition, modifications to the geometry, binding energy model, electronic energy loss, interatomic potential, and the reflected-ion treatment have been made to improve the underlying (athermal) physics of solid targets under ion bombardment.

Within the TRIM formalism, each projectile history begins with initial energy, angle, and position conditions and subsequently is allowed to undergo a series of scattering events with target atoms of a material of an amorphous nature. Scattering and the associated energy losses (elasitic and inelastic) occur through the local phenomena of

binary nuclear collisions. Target atoms recoil with an energy equal to the binary collision energy tranfer minus the local heat of vacancy formation. Atom trajectories (projectile or target) are followed until their energies have dropped below the local damage energy. Projectile or target atoms attempting to leave the material surface must overcome the attractive planar potential.

Information that is readily obtained through the TRIM formalism, presented in the text, includes: (1) the sputtering energy, angle, depth of origin (angstroms), layer of origin, and cascade membership, (2) the projectile depostion and damage profiles, pathlength, and the backscattering energy and angle dependence, (3) the causal sputtering event energy, impact parameter, collsion apsis, and electronic excitation energy, and (4) the implantation and cascade mixing spatial and energy profiles across a given marker plane.

3.2 Geometrical Considerations

For single or multi-component target materials, the atom sites are assumed to lack any of the directional properties associated with a given crystal lattice orientation. The target atoms are randomly distributed according to the atomic number density, N, and, thus, no correlation exists between

the postions of successive atoms. Only one target atom is assumed to occupy the volume element of length $N^{-1/3}$ and base area $N^{-2/3}$.

Even though the target is characterized as a structureless medium, it is necessary to define the target in terms of a surface layer (of atomic thickness) with an underlying bulk layer of arbitrary thickness. Within the bulk layer, a subset of layers may be defined in order to accurately model alloy component concentration profiles or regions of differing constituents (Figure 3.1a). Delineation of the surface layer from the bulk layer as well as defining a subset of bulk layer allows specification of unique layer properties such as bond energies, binding energies, and component densities. The properties of each layer (unless otherwise specified) reflect the concentration weighted average of pure component properties.

The scattering mean-free-path (MFP) is defined as the local atomic separation $L_u = N_u^{-1/3}$ where u specifies the atomic layer (Figure 3.1b). Scattering crossover from one layer to an adjacent layer (assuming the layers are one MFP thick, a condition which can be relaxed) requires that the atom in motion travel one MFP such that

$$\text{MFP} = f_u + f_{u \pm 1} \qquad (3.2.1)$$
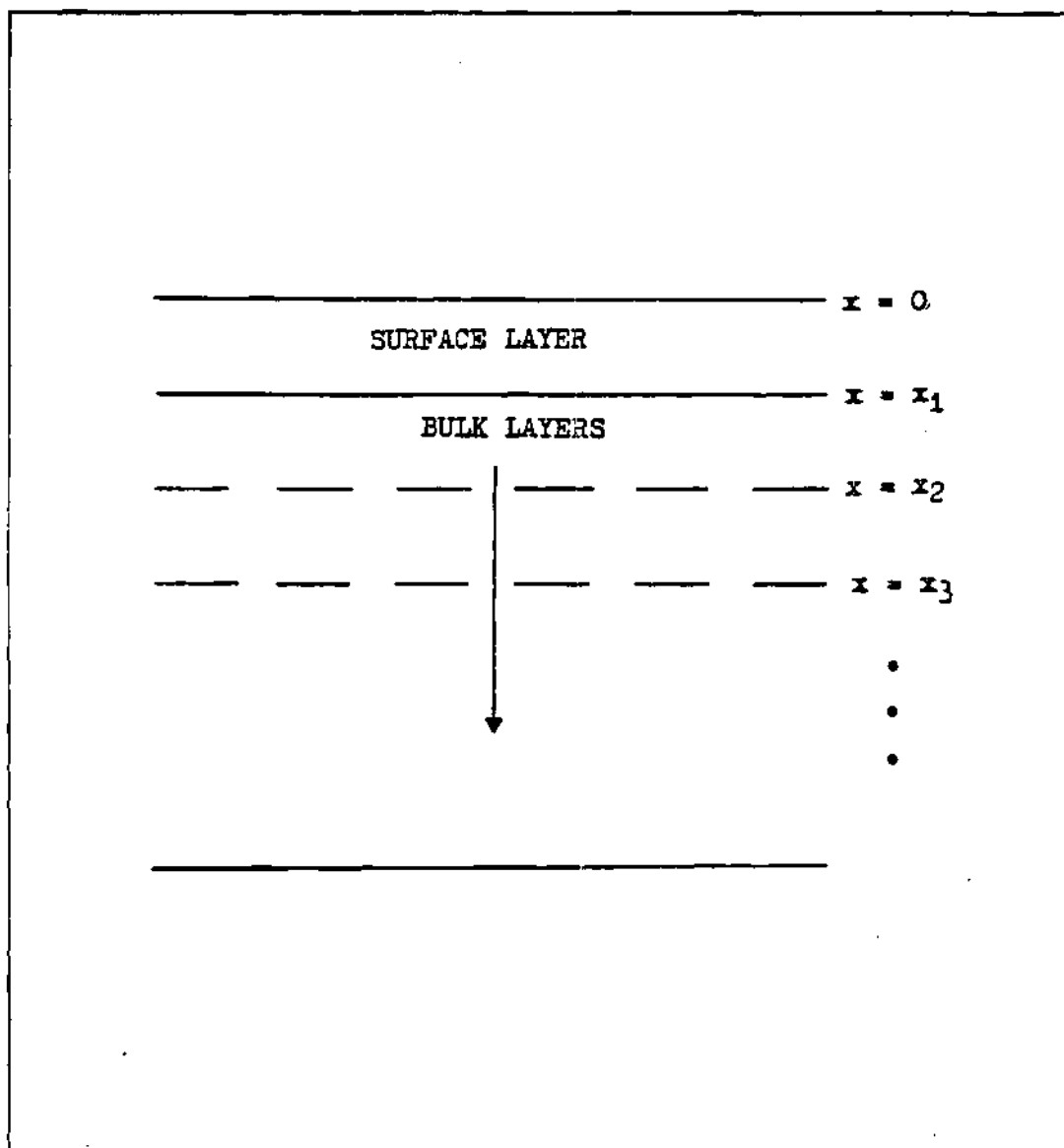
Figure 3.1a   General Multilayer Structure of the
Target Material
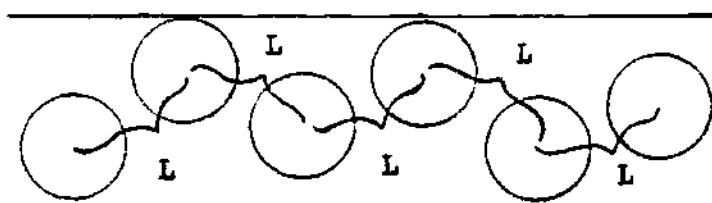
Figure 3.1b   Local Atomic Separation Within
a Given Atomic Layer Designated
as the Mean-Free-Path Distance
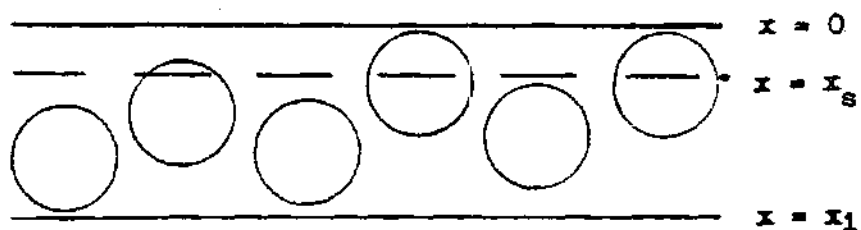
Figure 3.1c   Surface Layer Geometry

Here f_u is the fraction of a MFP traveled within layer u before intersecting an adjacent layer, u±1, and is further defined as

$$f_u = \left\{ \frac{x_t}{L_u} \right\} \qquad (3.2.2)$$

where x_t is the distance traveled by the atom in motion.

A final note concerns a more detailed description of the surface layer. Unlike the bulk layers, the surface layer bounds a vacuum so that the definition of vacancies and interstitials becomes obscure for an amorphous "structure" close to x=0, the vacuum/surface interface. Thus, an effective surface skin thickness, x_s, will be assumed defect free (Figure 3.1c). In actuality, a real surface is characterized by various steps and kinks; however, for the current investigation, a flat surface of surface roughness of x_s will be assumed adequate.

3.3 Scattering Mechanics

If ion/atom scattering is in the conditional realm where magnetic effects and noncentral forces can be neglected, relativistic and many-body events are of little consequence, and ion/atom interaction is governed by a conservative central repulsive force, then scattering can be approximated

as a series of binary collision events. Where the elasticity and the conservation of momentum of ion/atom collisions is assumed, scattering kinematics is determinant through the laws of classical mechanics.[94,95] A "black box" treatment is valid in the vicinity of the deflection since the details of the scattering process are irrelevant even if the phenomena are essentially quantum in nature.[94]

Inelastic processes (excitation, ionization, and charge-exchange) result in an uncertainty of the kinetic energy and of the interatomic potential of the colliding atoms that is missing from the classical mechanics (elastic) picture. For low collision velocities, the probability of inelastic processes is small, while for velocities $\sim O(10^7$ cm/sec), the inelastic and elastic cross-sections are comparable.[95] Regardless of the collisional velocity regime, the kinetic energy and the interatomic potential uncertainties associated with inelastic processes affect the scattering kinematics by less than a few percent.[95] Thus, the separability of the nuclear energy loss and the electronic energy losses can be assumed for binary scattering events.

The trajectories of the binary collision partners (depicted in Figure 3.2) are determined classically by evaluating the center of mass (COM) scattering angle [57]
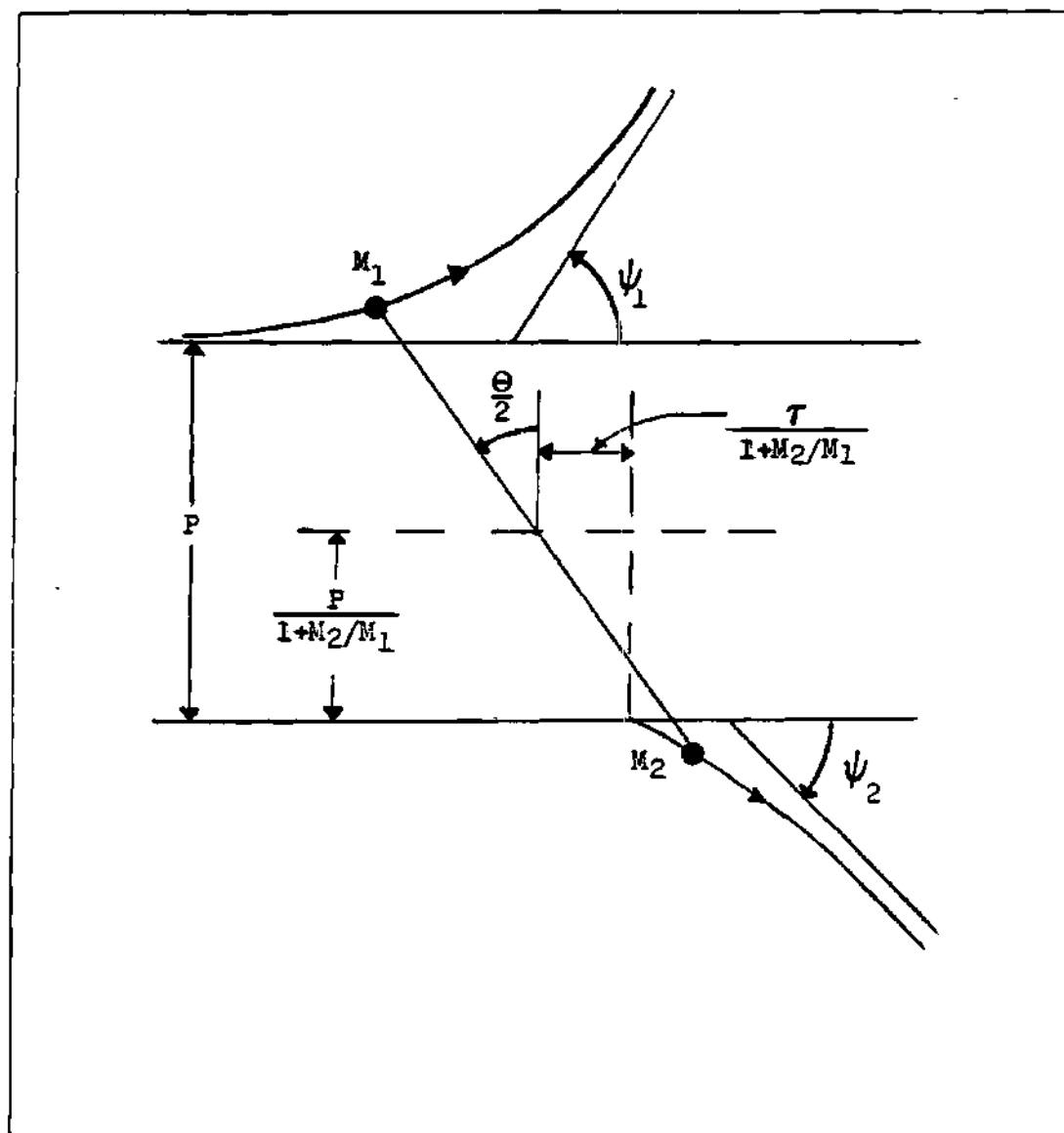
Figure 3.2   Trajectories of a Classical Binary Collision
for a Conservative Central Repulsive Force

$$\Theta = \pi - 2p \int_{r_o}^{\infty} \left[r^2 g(r) \right]^{-1} dr \qquad (3.3.1)$$

and the time integral

$$\tau = \left(r_o^2 - p^2 \right)^{1/2} - \int_{r_o}^{\infty} \left\{ \left[g(r) \right]^{-1} - \left(1 - \frac{p^2}{r^2} \right)^{-1/2} \right\} dr \qquad (3.3.2)$$

where

$$g(r) = \left[1 - \left(\frac{p}{r} \right)^2 - \frac{V(r)}{E_c} \right]^{1/2} \qquad (3.3.3)$$

Here p is the impact parameter, r_o is the distance of closest approach (collision apsis defined as $g(r)=0$), $V(r)$ is the interatomic potential between the scattering atoms, and E_c is the COM kinetic energy defined as $E_o/(1+M_1/M_2)$. E_o is the lab system kinetic energy and M_1 and M_2 are the masses of the incoming and target atoms, respectively.

Determination of the impact parameter is based on the assumptions that one target atom occupies the volume element of length $N^{-1/3}$ with base area $N^{-2/3}$ and that no successive lateral correlation exists among target atoms. Thus, the impact parameter follows the Monte Carlo presription [58]

$$P = \left[R_n \Big/ \left(\pi N^{2/3} \right) \right]^{1/2}$$

(3.3.4)

where R_n is a random number uniformily distributed over the interval [0,1]. Furthermore, it is necessary to recognize the surface effect where particles within a distance of $x = \frac{1}{\sqrt{\pi}} N_i^{-1/3}$ of the surface preferentially have collisions with atoms in the transverse surface plane. The surface impact parameter is distributed over [96]

$$P = \left[\left(R_\ell^2 + R_m^2 \right) \Big/ \left(\pi N^{2/3} \right) \right]^{1/2}$$

(3.3.5)

where R_ℓ and R_m are uniform random numbers in the interval [0,1].

The time integral which is a measure of electronic straggling becomes important for energies less than 1 keV since the target atom actually begins to move before the deflection of the incoming atom.[57] Thus, the free flight path of an ion/atom is less than $N^{-1/3}$, since the deflection point of its trajectory lies in front of the target atoms's center.[58] Using the hard-core approximation to the time integral where $\tau = p\tan(\Theta/2)$ [57], the free flight prescription is

$$L = N^{-1/3} - p \tan(\Theta/2)$$ (3.3.6)

with the added constraint that L > 0 for all Θ values. The incoming particle would otherwise interact with other neighboring target atoms, if L were less than zero. The resultant lab scattering angles, ψ_1 and ψ_2, are defined as [57]

$$\psi_1 = \arctan\left\{ \sin\Theta \big/ \left(f^{-1} \frac{M_1}{M_2} + \cos\Theta \right) \right\}$$ (3.3.7a)

$$\psi_2 = \arctan\left\{ \sin\Theta \big/ \left(f^{-1} - \cos\Theta \right) \right\}$$ (3.3.7b)

The factor f is a measure of the relative importance of the inelastic energy loss to that of the kinetic energy available in the collision and is defined as [57]

$$f = \left(1 - Q/E_c \right)^{1/2}$$ (3.3.8)

such that Q is equated to the excitation energy loss. Thus, while the inelasticity is assumed separable in the determination of the COM scattering angle, Θ, it is

subsequently resolved into the lab system scattering angles yielding a quasi-elastic treatment for binary collisions. Note that for $Q/E_c \lesssim 0(.1)$, the electronic energy loss factor, f, has a minor influence on the lab angle kinematics.

The azimuthal scattering angle is simply selected as

$$\phi = 2\pi R_\phi \qquad (3.3.9)$$

where R_ϕ is a uniformily distributed random number in the interval $[0,1]$.

In the standard TRIM formalism, the electronic energy loss factor is neglected, and the COM scattering angle integral is approximated from the scattering triangle [58] (a semi-analytical, semi-empirical expression for computational expediency) such that (Figure 3.3)

$$\cos\left(\Theta/2\right) = \frac{\rho + \rho + r_0}{\rho + r_0} \quad ; \quad \begin{cases} \rho = \rho_1 + \rho_2 \\ \delta = \delta_1 + \delta_2 \end{cases} \qquad (3.3.10)$$

The quantities, ρ_1 and ρ_2, are the radii of curvature of the trajectories evaluated at closest approach (determined from a centrifugal force argument [58]), and δ_1 and δ_2 are correction terms associated with interatomic potential screening. Within the original TRIM framework, an empirical
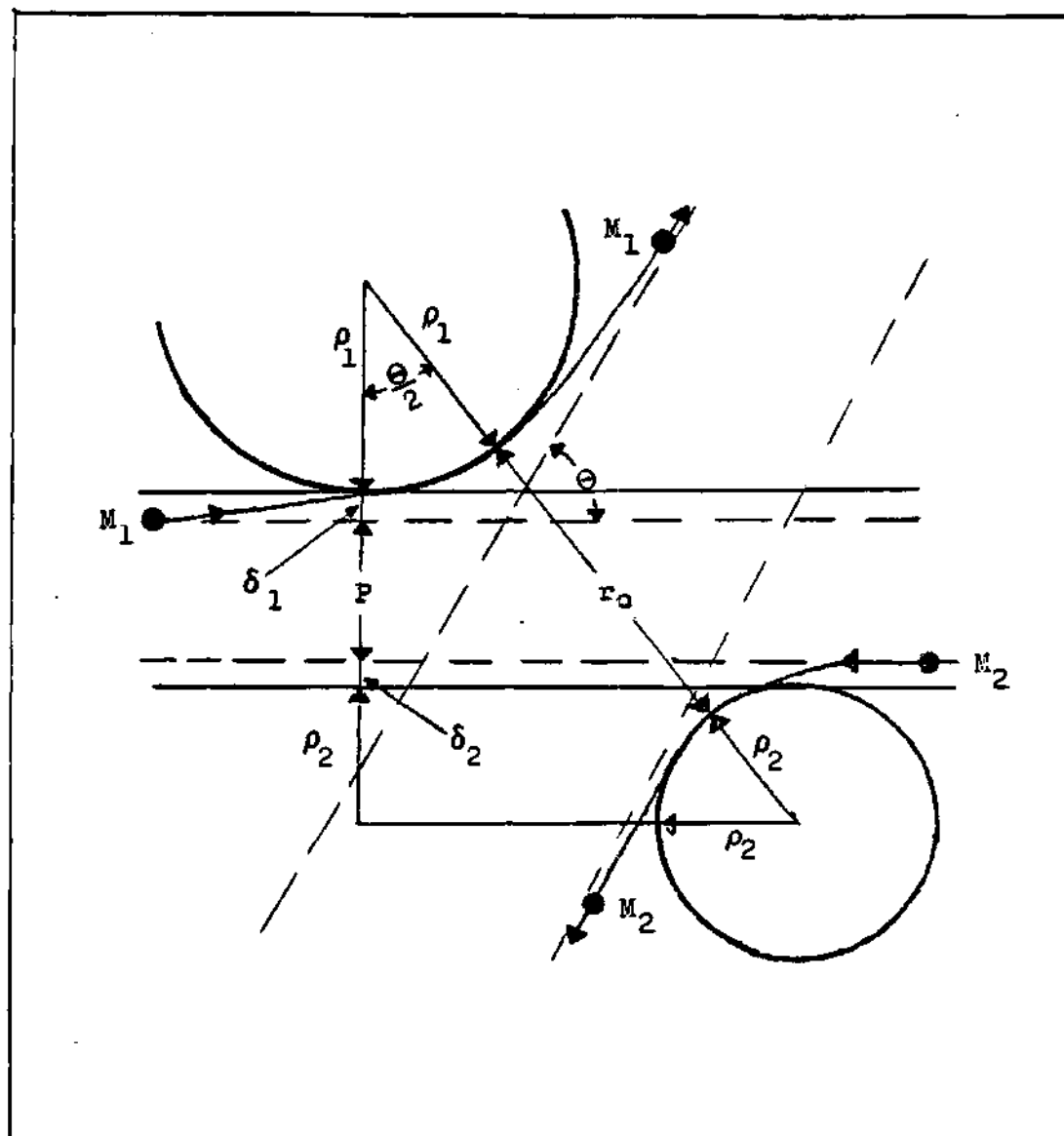
Figure 3.3   Center of Mass Triangle

fit has been applied to the factor δ and when compared to the exact determination of the COM scattering angle integral has an associated error of less than 1% over six decades of energy.[58]

3.4   Interatomic Potential

The sum of the Coulomb interaction energy and the change in the electron energy connected with the mutual approach (COM) of two nuclei is defined as the interatomic (interaction) potential.[97] When the scattering apsis, r_0 , is small ($r_0 \rightarrow 0$), ion/atom scattering is governed by the Coulomb force (Rutherford scattering); while at larger distances of separation, the Coulomb force is screened and scattering is influenced by the associated electron field of the colliding ions/atoms.[98] In velocity terms, Rutherford scattering is predominant at high ion/atom velocities and is characterized by multiple small angle events, whereas at collision velocities much less than the orbital velocity, screening is predominant and nuclear stopping becomes important.[98] The orbital electron velocity is defined as

$$v \ll v_1 = Z_1^{2/3} v_0 \qquad (3.4.1)$$

where v_0 is equal to $e^2/\hbar$ and Z_1 is the charge number of the

incoming ion/atom. Electronic and nuclear stopping are of the same order of magnitude when $v \leq O(.1 v_1)$ [98] which corresponds, for example, to a 250 eV proton or a 1 MeV copper atom. Thus, deviations from Rutherford scattering must be considered in the slowing down of light projectiles (D, T, He) as well as collision cascade events for fusion reactor wall conditions. The interatomic potential must then be of the type

$$V(r) = \frac{Z_1 Z_2 e^2}{r} u(r) \qquad (3.4.2)$$

where $u(r)$ is the screening function which satisfies the conditions that $u(r) \rightarrow 1$ as $r \rightarrow 0$ and $u(r) \rightarrow 0$ as $r \rightarrow \infty$.[97-99] Universality of the screening function parameterized in the terms of the screening length is commonly sought after to "ease" scattering calculations such that

$$V(x) = \frac{Z_1 Z_2 e^2}{x a_s} \phi(x) \qquad (3.4.3)$$

where $x = r/a_s$ and a_s is the Firsov screening length prescribed as [97]

$$a_s = \left(\frac{9\pi^2}{128} \right)^{1/3} a_0 \left(Z_1^{1/2} + Z_2^{1/2} \right)^{-2/3} \qquad (3.4.4)$$

and a_0 is the Bohr radius ($a_0 = .5291$ Å).

Scattering calculations employing the Thomas-Fermi statistical modeling of the colliding nuclei potential [97,100] prove to be too weakly screened.[101] Thomas-Fermi statistics ignore the external shell contribution of the electron interaction energy; therefore for low energy collisions where the apsis is greater than 1 $\overset{\circ}{A}$ (correspondingly, $x_0 \sim 5$ to 15 depending on a_s), the Thomas-Fermi potential lacks validity.[97,100] Errors of 100% in stopping power and range calculations compared to experimental values result when assuming a Thomas-Fermi interaction potential at low scattering energies.[101]

On the other hand, the Bohr screening potential [102] where

$$u(r) = \exp\left(-r/\beta\right) \; ; \; \beta = a_0\left(Z_1^{2/3} + Z_2^{2/3}\right)^{-1/2}$$

(3.4.5)

is too heavily screened and is only applicable to short-ranged interactions where $r < .1 \overset{\circ}{A}$.[101] Over a considerable interval of internuclear separation, r, the screening potential is of the general Born-Mayer form [103]

$$u(r) = A \exp\left(-br\right) \; ; \; 1.5\, a_0 < r < 3.5\, a_0$$

(3.4.6)

where parameters A and b are constants for a given pair of atoms. While potential fits to within a 6% deviation of the

actual potential are obtained when employing the Born-Mayer form over the allowed range of separation distances [103], TRIM calculations show that 25% of the collisions associated with the slowing down of the projectile and > 50% of the collision cascade events fall outside the interval $[1.5a_o, 3.5a_o]$. Furthermore, the Born-Mayer potential clearly does not satisfy the condition that $u(r) \rightarrow 1$ as $r \rightarrow 0$ unless $A = 1$ which is never the case.

Of more common use, recently, is the Moliere type potential [101]

$$\phi(x) = \sum_{i=1}^{3} C_i \exp(-b_i x) \quad ; \quad \sum_{i=1}^{3} C_i = 1 \qquad (3.4.7)$$

where the constants C_i and b_i are atom pair-wise dependent. A least squares fit to a quantum mechanically corrected free-electron approximation of the interatomic potential for selected ion/atom pairs has yielded constants C_i and b_i for Moliere type potentials that agree within 10% of the actual potential.[101] However, very few of these ion/atom pair constants have actually been determined, thus necessitating another approach. Such an attempt is to make use of the standard (universal) Moliere potential where

$$\phi(x) = .35 y + .55 y + .1 y^{20} \qquad (3.4.8)$$

and $y=\exp(-.3r/(\langle CA \rangle a_s))$ such that $\langle CA \rangle$ is defined as the average correction factor of the screening length which best approximates the scattering potential. Inherent within the approximation of the COM scattering angle integral of the TRIM code is the incorporation of the universal Moliere potential with correction factor, $\langle CA \rangle$.[104] The only means for determining $\langle CA \rangle$ using this approach is to adjust the $\langle CA \rangle$ value iteratively until convergence of experimental and calculated quantities (e.g., range, sputtering, reflection, etc.) is attained. However, such a technique is quite laborious, time-consuming, and assumes that an experimental benchmark is available. Furthermore, the approach is physically meaningless since the correction factor now compensates for omitted phenomena such as thermal vibration effects, inelastic loss energy, and inaccuracies in the potential satisfying only a restricted set of scattering conditions.

Recently, a universal potential, developed by Biersack and Ziegler [99], has been empirically derived solely as a function of Z_1, Z_2, and r (no unique pair-wise species parameters need be known) to within (5-20)% accuracy of the actual potential (ab initio calculations) over all collision separation distances. The potential fit is based on the application of free electron statistics with the addition of correlation and exchange energy terms. For homonuclear collision events, the Biersack-Ziegler screening function is

defined as the sum of two universal expressions [99]

$$V(x) = \frac{Z^2 e^2}{x\, a_s} \left\{ \phi_1(x) - Z^{-2/3} \phi_2(x) \right\} \qquad (3.4.9a)$$

where

$$\phi_1(x) = .09\, y + .61\, y^3 + .3\, y^{10.525}; \quad y = e^{-.19 x} \qquad (3.4.9b)$$

and

$$\phi_2(x) = .07\, \exp\left[-\left(\frac{1}{7R}\right)^2 - \frac{R}{4} - \left(\frac{R}{7}\right)^2 \right]; \quad R = .295\, x \qquad (3.4.9c)$$

The first term, $\phi_1(x)$, being of the general Moliere form is the sum of two effects: the Coulomb interaction and the kinetic energy increase of electrons due to the increased electronic density in the overlap region of the two atoms. The second potential term, $\phi_2(x)$, incorporates exchange and correlation energies reflecting the local repulsion of equal spins and equal charges of electrons. Exchange and correlation effects act to lower the local electron density (thus, lowering the interaction energy) and contribute about 50% to the total interaction at large interaction distances.[99] Interatomic potentials for heteronuclear atom pairs are calculated using the "combining (or geometrical

mean) rule" of the constituent homonuclear potentials [99,103] so that

$$\phi_{12} = \left\{ \phi_{11}\left(\frac{r}{a_{s1}}\right) \cdot \phi_{22}\left(\frac{r}{a_{s2}}\right) \right\}^{1/2} \qquad (3.4.10)$$

where a_{s1} and a_{s2} are the single atom screening lengths.

In order to retain the TRIM formalism (empirical approximation to the scattering angle integral), a correction factor, CA, as a function of the apsis distance, r, has been determined for a given atom pair that would best fit the Biersack-Ziegler potential to the universal Moliere potential. Such an approach is the same as adjusting the Firsov screening length where $a_s = a_s CA(r)$. The behaviour of CA(r) for $Ar^+ \to Cu$ is displayed in Figure 3.4. Rather than forcing the TRIM code to iterate on r_o and $CA(r_o)$ simultaneously which is computationally time-consuming, a modified TRIM version (known as DCATV) is used to quantify the distance of the closest approach frequency for a given $\langle CA \rangle$ (Figure 3.5). Using the DCATV output in conjunction with the Biersack-Ziegler/Moliere CA(r) fit, the average correction factor is iterated until $\langle CA \rangle$ according to DCATV scattering calculations is convergent with the corresponding Biersack-Ziegler value, $\langle CA(r_o) \rangle$. The use of the $\langle CA \rangle$ procedure as opposed to incorporating CA(r) directly in the TRIM apsis determination is founded on a number of experimental and theoretical results.

CA

1.30

1.20

0.70

2   4   6   8   10   12   14   16   18

REDUCED COLLISION APSIS
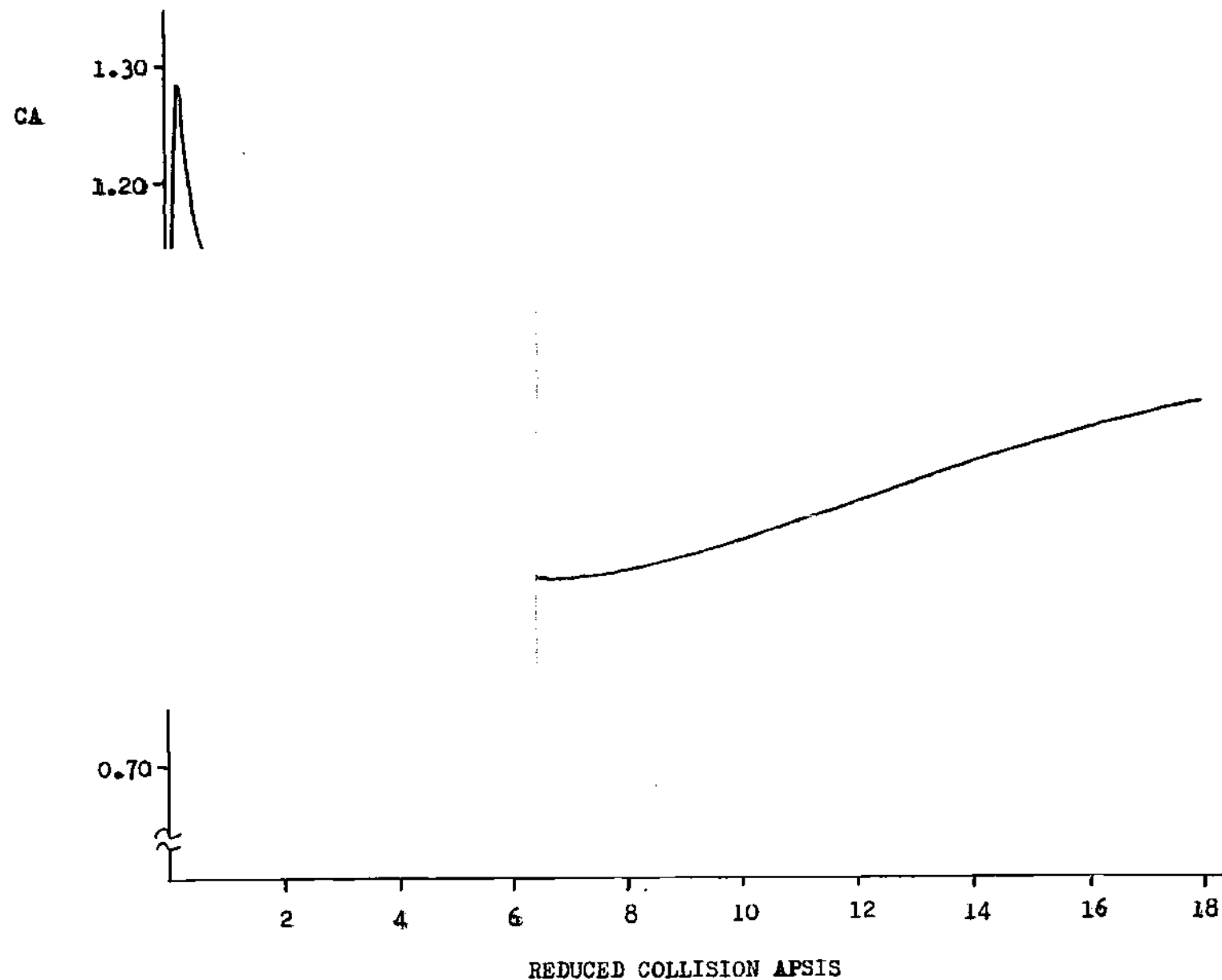
Figure 3.4   Universal Moliere Correction Factor to the Biersack-Ziegler
Potential as a Function of Reduced Collision Apsis
for Ar+ on Copper
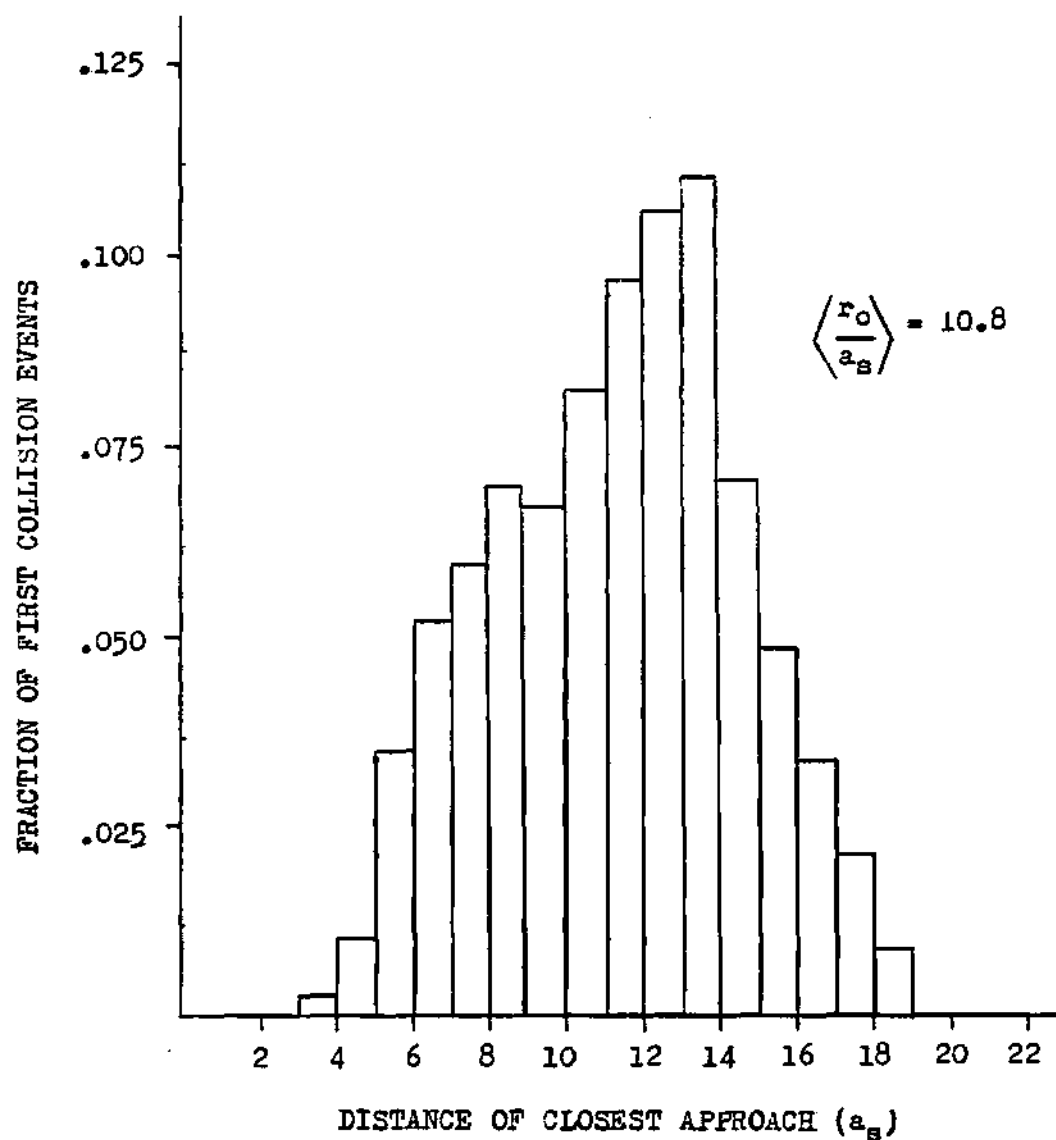
Figure 3.5 Fraction of First Collision Dependence
upon the Reduced Distance of Closest
Approach for 3 keV Ar+ off Copper at
Normal Incidence (TRIM calculation)

Comparisons of ab initio potential calculations to that of the Moliere potential for 4 keV $Ar^+ \rightarrow Mg$ are indicative of an average correction factor of .85 [105], while the DCATV approach converges to $\langle CA \rangle = .87$. For the same calculation, it appears that a corrected Moliere potential is closer to the actual potential than the Biersack-Ziegler function over a large distance. Experimental focusing energy data for $Ar^+ \rightarrow Cu$ indicate a screening length of .092±.007 Å [106] which corresponds to $\langle CA \rangle = .89 ± .07$ and is in agreement with the DCATV result of $\langle CA \rangle = .91$. Computer simulations in conjunction with experimental data for uranium self-sputtering are in best agreement when a screening length 1.15 times the predicted Firsov value is chosen [107]. Once again the DCATV approach yields a similar value of $\langle CA \rangle = 1.12$.

3.5 Inelastic Energy Loss

For projectiles of low energy $\sim O(<10^3)$ and/or of oblique angles of target incidence, backscattering is brought about by "cascade" sequences that are no longer than a few collision partners. Likewise, for low energy sputtering (regardless of the projectile mass), it can be shown that cascade chain-lengths are relatively short. In Figure 3.6, TRIM calculations for 3 keV $Ar^+ \rightarrow Ti$ at normal incidence indicate that roughly 80% of all cascades resulting in a

sputtering event are less than six target atoms in length. For light projectiles such as deuterium, over 50% of all sputtered atoms are PKAs.[62] It is thus clear that the scattering kinematics (elastic and inelastic) associated with reflection and sputtering must be characterized by "local" collision physics as opposed to "nonlocal" continuum models. Range, stopping power, and cascade mixing calculations better lend themselves to a continuum inelastic energy since slowing down collision sequences commonly exceed 50 partners, determined from TRIM calculations.

The most common approximations to the local inelastic energy loss, T_e, are the Oen-Robinson [108], "semilocal" [96,107,109], and Firsov [110] models. The Oen-Robinson model is cast as

$$T_e\left(\rho,E\right) = \frac{\cdot 045}{\pi\, a_s^2}\, k\, E^{1/2} \exp\left(-.3r/a_s\right)$$

(3.5.1)

where the constant k is a stopping parameter which matches the high energy predictions of nonlocal LSS theory.[111,112] The continuum approach (LSS theory) at high energy due to the full development of cascades is given as

$$T_e\left(\rho,E\right) = T_e(E) = k\, E^{1/2}$$

(3.5.2)

In the semi-local approach, an attempt is made to "bridge the

gap" between the local and nonlocal models by equating inelastic energy losses to the equipartioning of the Oen-Robinson and the LSS formulations.[109] As for the Firsov model (to be discussed in detail later), Thomas-Fermi statistics coupled with a classical mechanics approach are used to derive the inelastic energy loss on a local basis.[110] However, as initially proposed, the Firsov model is restricted to small angle scattering events, a limited range of interatomic separation (.2-1 $\overset{\circ}{A}$), and charge ratios, (Z_1/Z_2), not differing by a factor of four. Subsequent modifications by Kishinevskii [113] and Robinson [57] improved the Firsov model's applicability, but it has been the recent extension by Karpusov [115] that has removed all of the imposed model restrictions.

Comparison of computer simulations with experimental data indicate that nonlocal approximations overestimate inelastic losses, whereas the local Oen-Robinson model consistently underestimates these same losses.[58,107,114] Thus, the need for a mid-range (semi-local) model or a "first-principles" (such as the Karpusov) model must be incorporated into the TRIM framework to more accurately model local electronic energy losses. The Karpusov (extended Firsov) approach is taken to be the model of choice in view of its consistency with the individual local collision event as opposed to the empirical semi-local assumption which implies an averaging or continuum treatment of the inelastic

energy losses.

In the Firsov model [110], the average energy of excitation of the colliding atoms is based on the assumption that the nuclei move in a straight line and uniformly in the sense of classical mechanics. Thus, the probability of excitation is functionally dependent upon the collision impact parameter and the relative velocity of motion. Excitation dependence on orbital moments, spins, quantized energy levels, and curve crossings is ignored. Rather, the electronic shell penetration of the two atoms during the collision is assumed to result in quasimolecule formation. The model is applicable when a "sufficiently" large number of electrons of the colliding atoms, corresponding to a high quantum state, is present. More specifically, the distance between adjacent excited energy levels of the quasimolecule must be small relative to the mean energy of excitation.

Briefly as an outline of the excitation events, the electrons of the incoming colliding atom lose their excess energy associated with their translational momentum, while the electrons of the target atom aquire an additional energy as they enter into the potential range of the incoming atom.[110,111] Thus, kinetic energy of the incoming atom is inelastically transferred to the electrons of both colliding atoms. Excitation energy not lost in the ionization of atoms is emitted or contained in a metastable state. The total force (or momentum transfer) acting on each atom is given by

[110]

$$F = \pm m_e \dot{R} \int_S \Gamma_e \, dS \qquad (3.5.3)$$

where m_e is the electron mass, $\dot{R}$ is the relative nuclei velocity, S is the surface dividing the potential regions of action of the nuclei, and Γ_e is the electron flux density through the elemental area dS. The electron velocity distribution is assumed spherically symmetric, implying that Γ_e can be approximated as $n\upsilon/4$. The electron excitation energy is obtained by integrating the force over the radius vector connecting the centers of the colliding atoms.[110,113] By employing the Karpusov modification to the Firsov model [115], the mean excitation energy can be written as

$$\mathfrak{F}(p, E_c) = g \int \left\{ \sum_{k=1}^{2} Z_k f(r_k) \right\} \dot{R} \, dR \qquad (3.5.4)$$

Here, p is the collision impact parameter, E_c is the COM kinetic energy of the nuclei, g is a constant, and $f(r_k)$ is defined as

$$f(r_k) = \int_{r_k}^{\infty} \frac{\phi^2(x)}{x} \, dx \quad ; \quad r_k = \alpha_k Z_k^{1/3} r/a_0 \qquad (3.5.5)$$

The constant $\propto_k$ is the fraction of the line segment, R, that lies on the kth side of the potential surface S.[113] Rewriting the inelastic energy loss. in simpler notation yields

$$\mathcal{F}\left(p,E_c\right)= 2\,q\,\mathcal{V}_c\left(Z_1^2\,Y_{e1} + Z_2^2\,Y_{e2}\right) \; ; \; Z_1 \gtrless Z_2 \qquad (3.5.6)$$

such that $\mathcal{V}_c$ is defined as the relative COM atom velocity and Y_{ek} is the inelastic energy loss per unit velocity (defined in Appendix B). The Karpusov formulation has no inherent limitations on the scattering angle, impact parameter, nuclei charge ratio, or the interatomic potential behaviour.

In the comparison of the Karpusov model to the semi-local and Oen-Robinson models, the characteristics of the causal knockon atom (CKA) can provide some beneficial insight. A CKA is defined to be the energetic collision atom which directly results in a sputtered ejection event. Causal atoms are inclusive of projectiles, cascade atoms causing the ejection of surface atoms, and energetic surface or subsurface atoms which after having a last collision with a surface atom sputter themselves. Thus, while 6.75% of the sputtered atoms for 3 keV $Ar^+\rightarrow Ti$ are PKAs (i.e. target atoms directly set in motion by the argon projectile, Figure 3.6), only .5% of all CKAs are argon (i.e. most sputtered PKAs have a target atom collision before ejection). Of course,
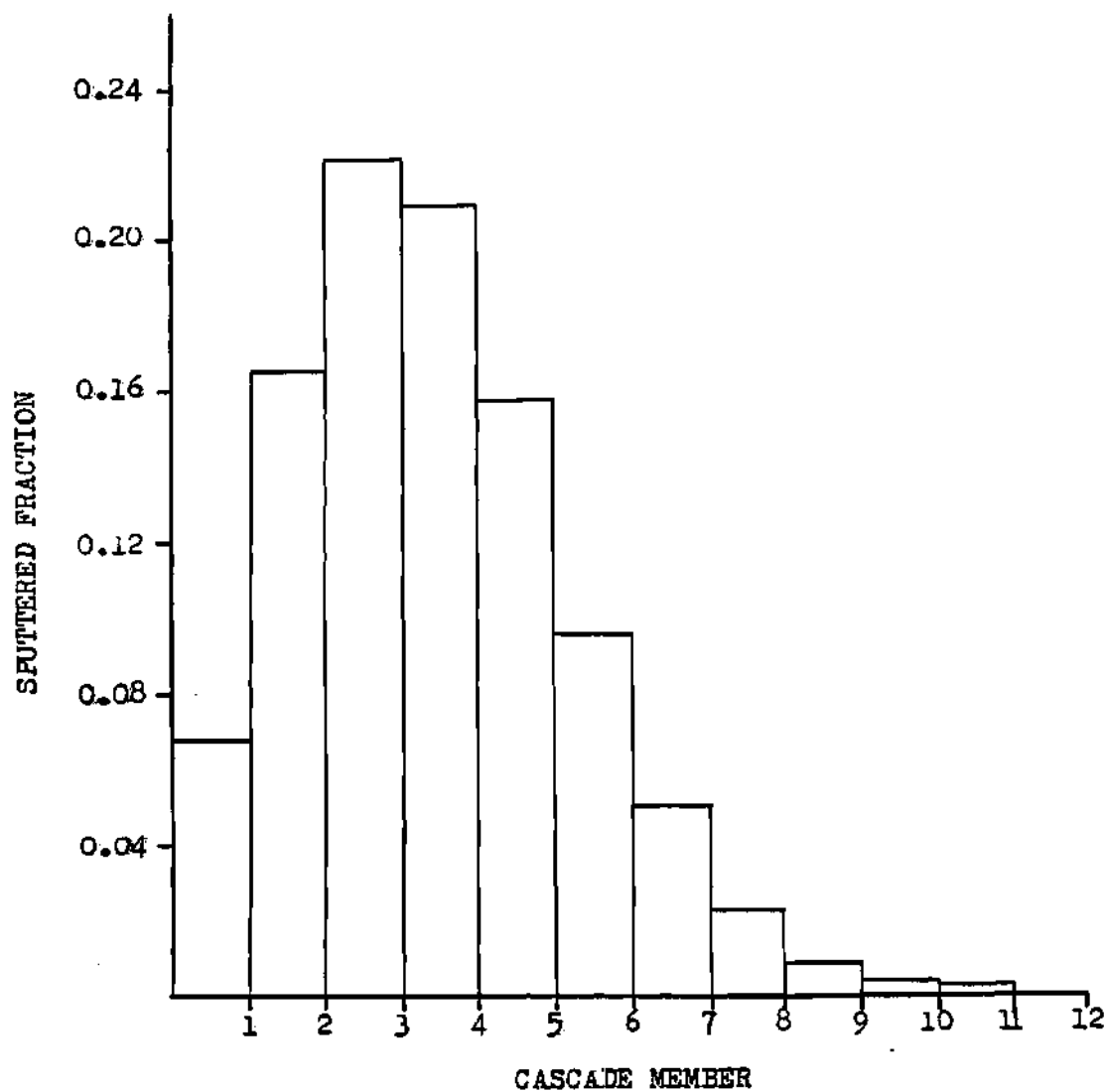
Figure 3.6   Sputtered Fraction as a Function
of Cascade Membership for 3 keV Ar+
on Titanium at Normal Incidence
(TRIM calculation)

for oblique angles of projectile incidence the percentage of PKAs that are CKAs increases due to the higher likelihood of direct ejection.

In a calculation using TRIM for 3 keV $Ar^+{\rightarrow}Ti$ at normal incidence where approximately 100,000 sputtering events were tabulated, an extensive study of CKA kinetic energy and reduced impact parameter versus sputtered fraction has been made to "bracket" the inelastic energy loss dependences of importance (Figures 3.7 and 3.8). It is clear that most CKAs are of low energy such that 50% have kinetic energies below 25 eV, 88% have kinetic energies less than 100 eV, and no CKAs have energies greater than 1 keV (which is much more representative of "first" collisions of the projectile). The CKA reduced impact parameter, b, dependence shows a range of $2 < b < 16$ to be of primary importance while "first" collision Ar-Ti events (not shown) indicate a range of importance as $5 < b < 18$. Using these observed behaviours for Ti-Ti collisions, the Karpusov model is shown in comparison to other local excitation models for the collision energy limits of 10 eV and 1 keV (Figure 3.9). Over the applicable range of impact parameter, deviations of a factor of 3 exist between the Karpusov model and the semi-local model and there exists as much as an order of magnitude difference between the Karpusov approach and the Oen-Robinson formulation. However, it was found that for the reduced energy range of $\varepsilon = 10^{-3 \pm .5}$ the semi-local model and the Karpusov model agree to
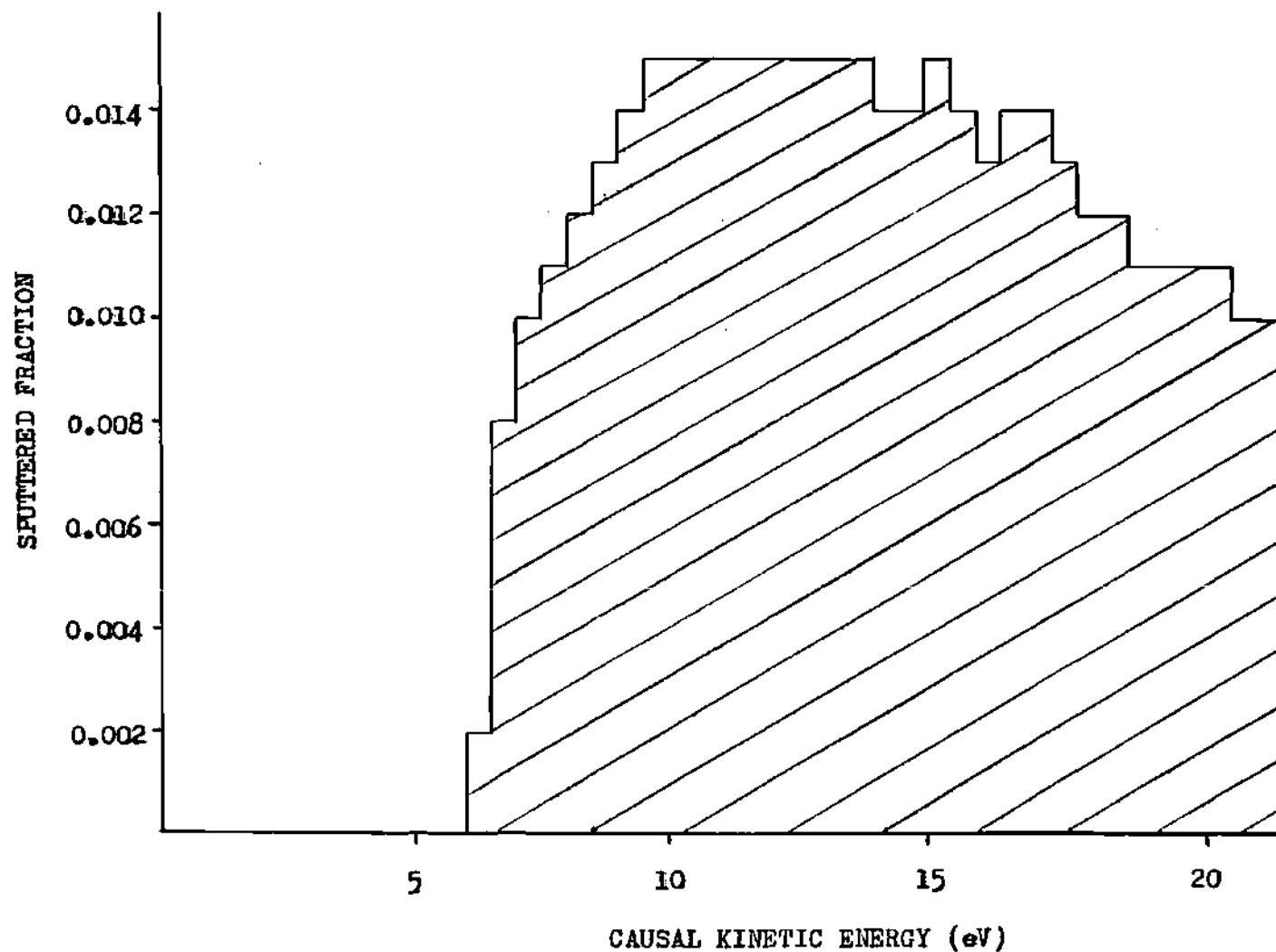
Figure 3.7   Sputtered Fraction Dependence upon the Causal Kinetic
Energy for Titanium Causal Sputtering Events Set in
Motion by 3 keV Ar+ off Titanium at Normal Incidence
(TRIM calculation)

CAUSAL REDUCED IMPACT PARAMETER EVENT (b)
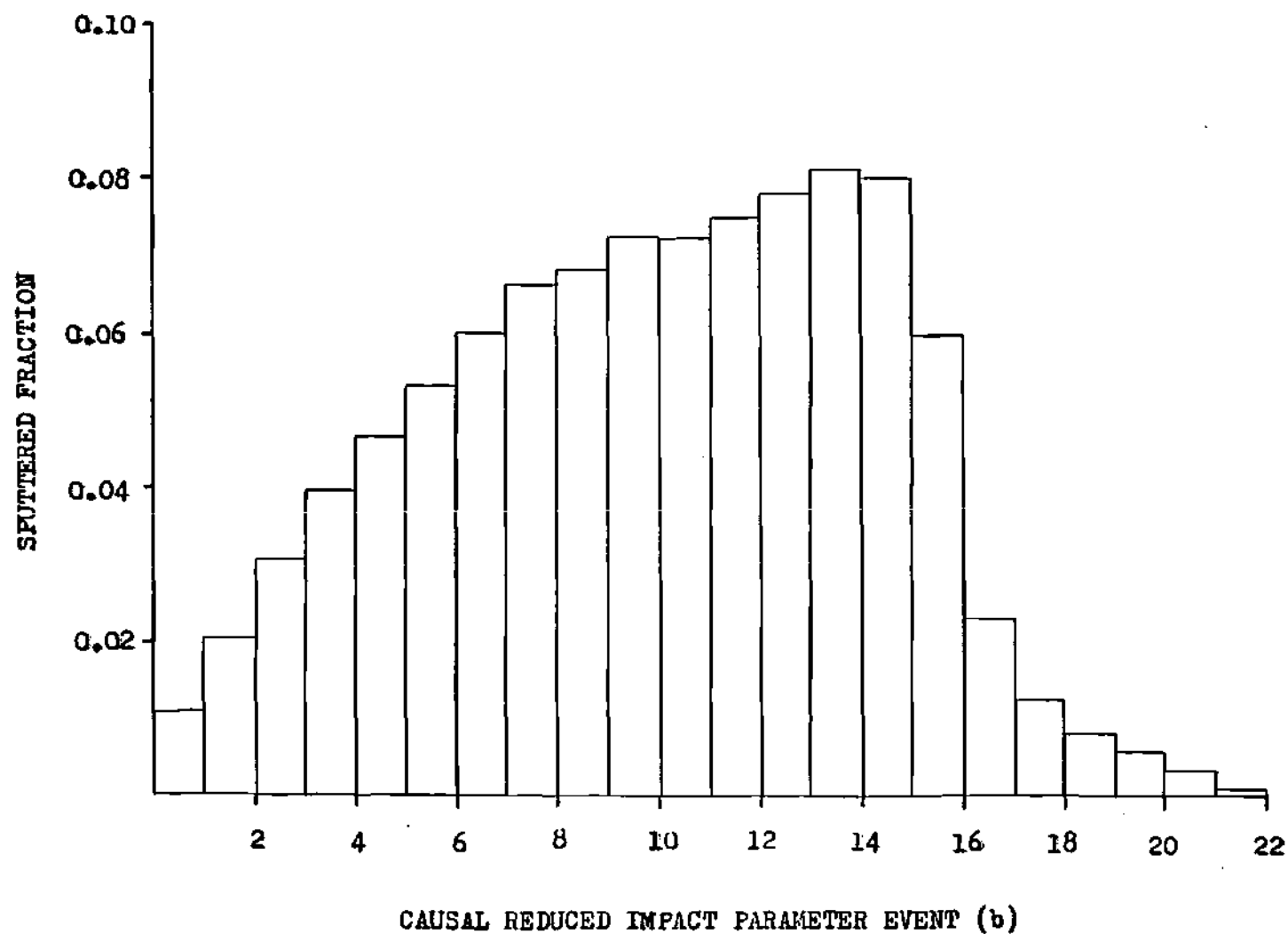
Figure 3.8   Sputtered Fraction Dependence upon the Causal Reduced
Impact Parameter for 3 keV Ar+ off of Titanium at
Normal Incidence (TRIM calculation)
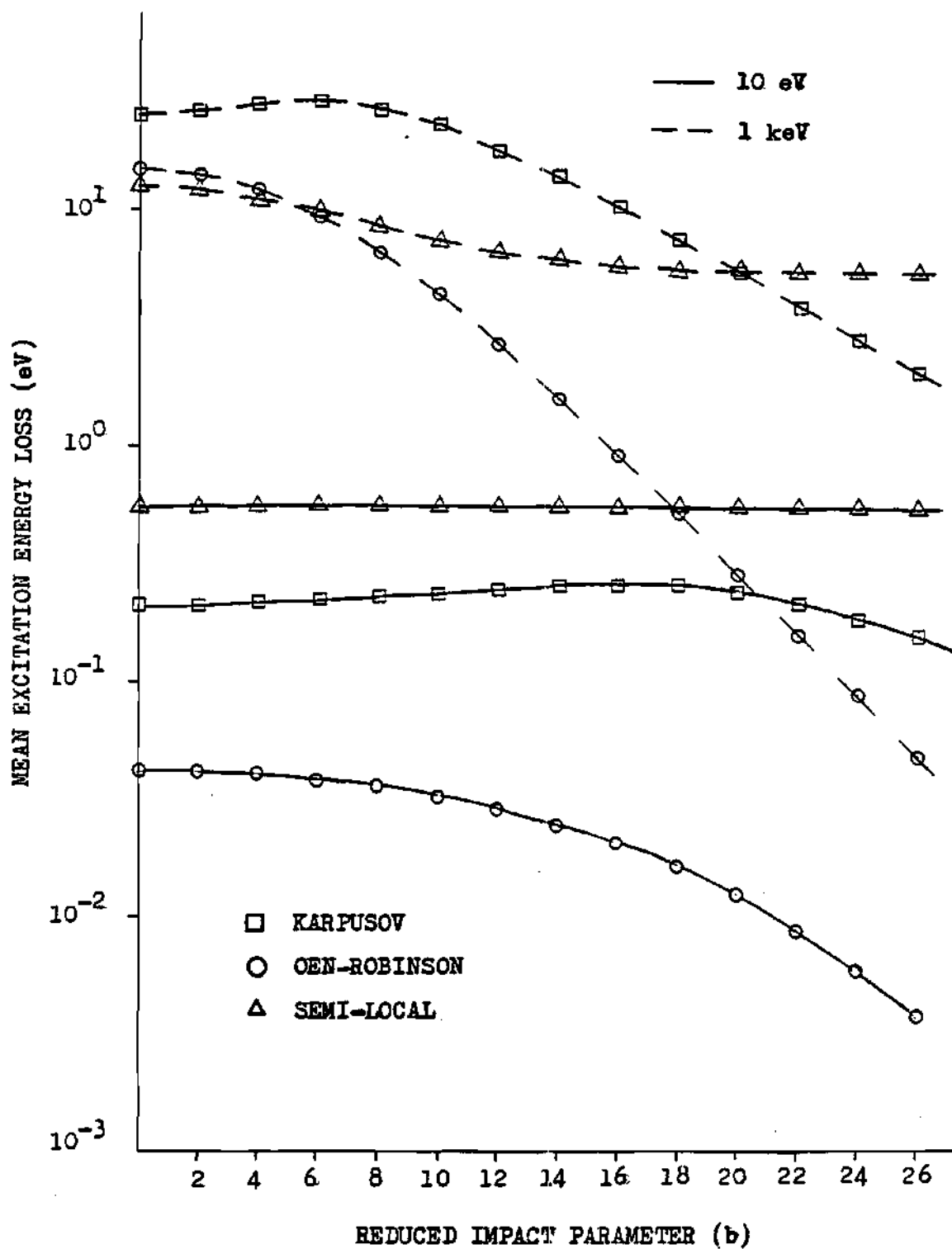
Figure 3.9   Comparison of Local Excitation Models
as a Function of Reduced Collision Impact
Parameter for 10 eV and 1 keV

within 25% over the range of 0<b<20. It is at the collision "extremes" that an overestimation of the electronic energy loss occurs for low energy events (indicative of the cascade) while an underestimation occurs at the higher energies. Note that for both the Karpusov and the semi-local models, the integral over impact paramter in the range 0<b<32 would result in approximately equal total stopping powers at $\varepsilon > 10^{-2.5}$ (1000 ev Ti-Ti collisions). These results were qualitatively substantiated for projectile-target systems of 3 keV Ar→TiO, 3 keV Ar→U, and 10 keV Ar→Fe where in excess of 50 to 100 thousand sputtered events were tracked via TRIM.

It was found computationally expedient to employ an empirical approximation to the Karpusov model for scoping studies. The model developed has an associated 25% deviation with that of the exact Karpusov model over the ranges $10^{-5} < \varepsilon < 10^{-2}$ and 1<b<18 with the added limitation that the charge ratio Z_1/Z_2 not exceed 6, otherwise the empirical formulation is no better than the other commonly used models.

3.6 Cascade Atom Energy Requirements

The collision cascade development requires that the kinetic energy transferred to a "new" target atom, T, (due to the slowing down projectile, PKA, or other cascade member atoms) exceed a threshold energy, E_T. Furthermore, for a

target atom to be set in and remain in motion requires that it overcome a local binding energy, E_b. Both of these quantities are dependent on the origin of the target atom.

In the absence of relaxations, the average bond energy of a surface atom in a structureless medium is equal to the cohesive energy, U_o. Because on the average an atom lying within the crystal surface has half the number of neighbors of an interior atom, the bulk bonding energy is simply twice that of the surface bond energy, $2U_o$.[116]

The local binding energy is defined as a radiation damage energy, specifically, the Frenkel pair formation energy

$$E_b = H_v^f + H_i^f$$

(3.6.1)

where H_v^f and H_i^f are the vacancy and interstitial formation energies, respectively. An atom energetically ejected from its lattice site immediately causes a vacancy; however, the new cascade member may be available for further collision sequences. Also, once the cascade atoms slow down below the threshold energy, E_T, trapping of the atom in an interstitial site or substitutional atom replacement become possible. Thus, an energy debit of the cascade atom at the end of its scattering flight is made for interstitial formation or phonon damping (if its kinetic energy is below H_i^f).

A synopsis, then, of the cascade development energy requirements follows.

(1) An atom is added to the cascade if the transferred

kinetic energy, T, is greater than the local bond energy.

(2) The cascade atoms's kinetic energy of motion is equal to $T-H_v^f$ where it must overcome the local binding energy.

(3) The cascade atom is no longer followed once its

kinetic energy drops below the interstitial formation

energy. As previously assumed in the surface geometry considerations, when $x < x_s$, defect formation is obscure. Hence, in this region an atom set in motion has the energy T (no vacancy formation energy).

3.7 Displacements

By definition, the displacement energy, E_d, is the threshold energy that an irradiated particle must transfer to a lattice atom to produce a stable defect in the lattice.[117,118] The displacement energy is not to be confused with the necessary energy transfer, E_T, required for a target atom to participate in the collision cascade. Most atoms which affect cascade development receive energies much less than the displacement energy threshold.[119] Thus,

bond-breaking is not the determining factor in defect production, rather the critical criterion is the interstitial-vacancy (Frenkel defect pair) separation distance.[117,120] Experimentally, the threshold energy has been observed to decrease with increasing interatomic distance.[117] Along the close-packed lattice directions, the threshold energy can be approximated as [117]

$$E_d = \frac{A}{2} e^{-r_{nn}/2R}$$

(3.7.1)

where r_{nn} is the interatomic distance, and A and R are interatomic potential parameters of the Born-Mayer type. Because the above model does not pertain to polycrystalline solids and because of the insufficient knowledge of parameters of A and R for metals [117], another means of determining E_d is necessary if experimental data are lacking.

A correlation between the sublimation energy and the displacement energy first proposed by Seitz [121] is chosen as the means for estimating E_d where

$$E_d = k_c E_s$$

(3.7.2)

and k_c is a lattice type constant. Through the use of relatively recent experimental values for E_d [122,123] plotted against the respective atomic sublimation energies,

the constant, K_c, is determined via linear regression from the data displayed in Figure 3.10.

Knowledge of the displacement energy permits the calculation of the damage generated in a solid by primary-knockon-atoms (PKA's). The number of defect pairs created in a cascade (number of displacements), N_d, is given accurately by the modified Kinchin-Pease (MKP) model [118]

$$
N_d = \begin{cases}
0 & ; \ 0 < \hat{E} < E_d \\
1 & ; \ E_d < \hat{E} < 2E_d/K \\
K\hat{E}/2E_d & ; \ \hat{E} > 2E_d/K
\end{cases}
\qquad (3.7.3)
$$

where K is the displacement efficiency, and $\hat{E}$ is the damage energy of the PKA available for atomic displacement. Computer simulations [57] indicate that the displacement efficiency is independent of target material and temperature. A value of $K = .86$ has been determined for Cu, Fe, and Au [57] and will be assumed applicable for all metals studied. The damage energy is further defined as $\hat{E} = E_o - Q$. E_o is the initial PKA energy, and Q is the total inelastic energy loss of the resultant cascade.

A potentially serious limitation of the MKP model concerns the PKA damage efficiency as a function of recoil energy, E_o. Computer simulations predict the damage efficiency is independent of PKA energy for energies up to
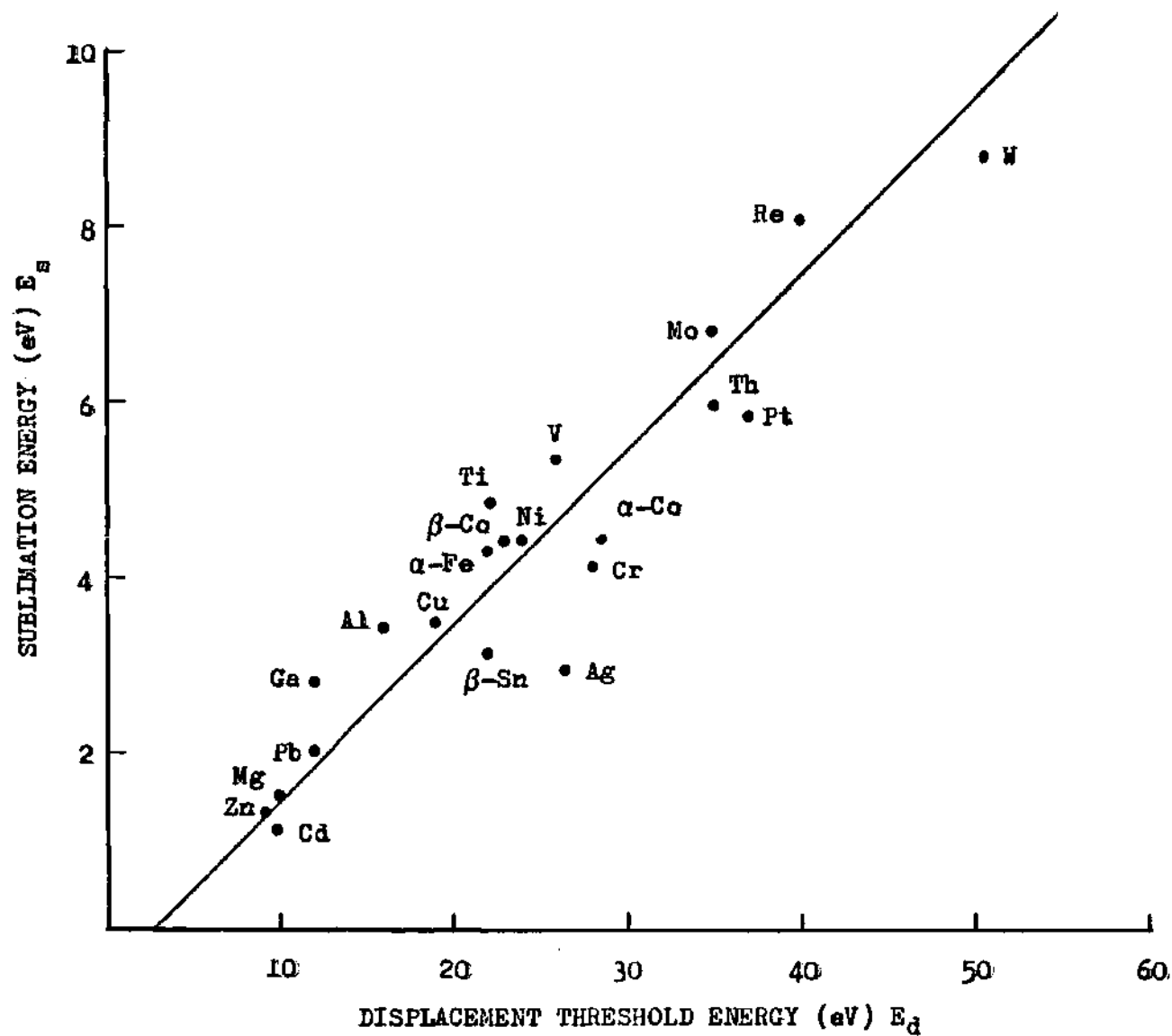
Figure 3.10   Atomic Threshold Displacement Energy as a Function
of Atomic Sublimation Energy

100 keV [57]; however, experimental data for Al, Cu, and Ag indicate that the damage efficiency is a function of PKA energy.[124] By defining the relative damage efficiency, $\mathcal{F}$, as the ratio of the experimental to the MKP prediction such that

$$\mathcal{F} = N_d^{exp}/N_d^{mkp}$$

(3.7.4)

various damage efficiences for ion and neutron bombardment of Al may be determined and are displayed in Figure 3.11. In general for a given projectile, the experimental defect production agrees closely with the MKP model for low energy recoils $\sim O(1 \text{ keV})$; however, $\mathcal{F}$ decreases to an asymptotic value of .35-.50 in the energy range of 2-10 keV, whereas above these energies, the displacement production is independent of the recoil energy for energies up to several hundred keV.[124] For the plasma-wall interaction ion energies under study $\sim O(<1 \text{ keV})$, the MKP model should be adequate in predicting defect production.

The displacement rate profile, K_o, necessary for the target alloy kinetics calculation is expressed as

$$K_o = \phi A N_d(x)$$

(3.7.5)

Here, ϕ is the incident projectile flux and A is the atomic
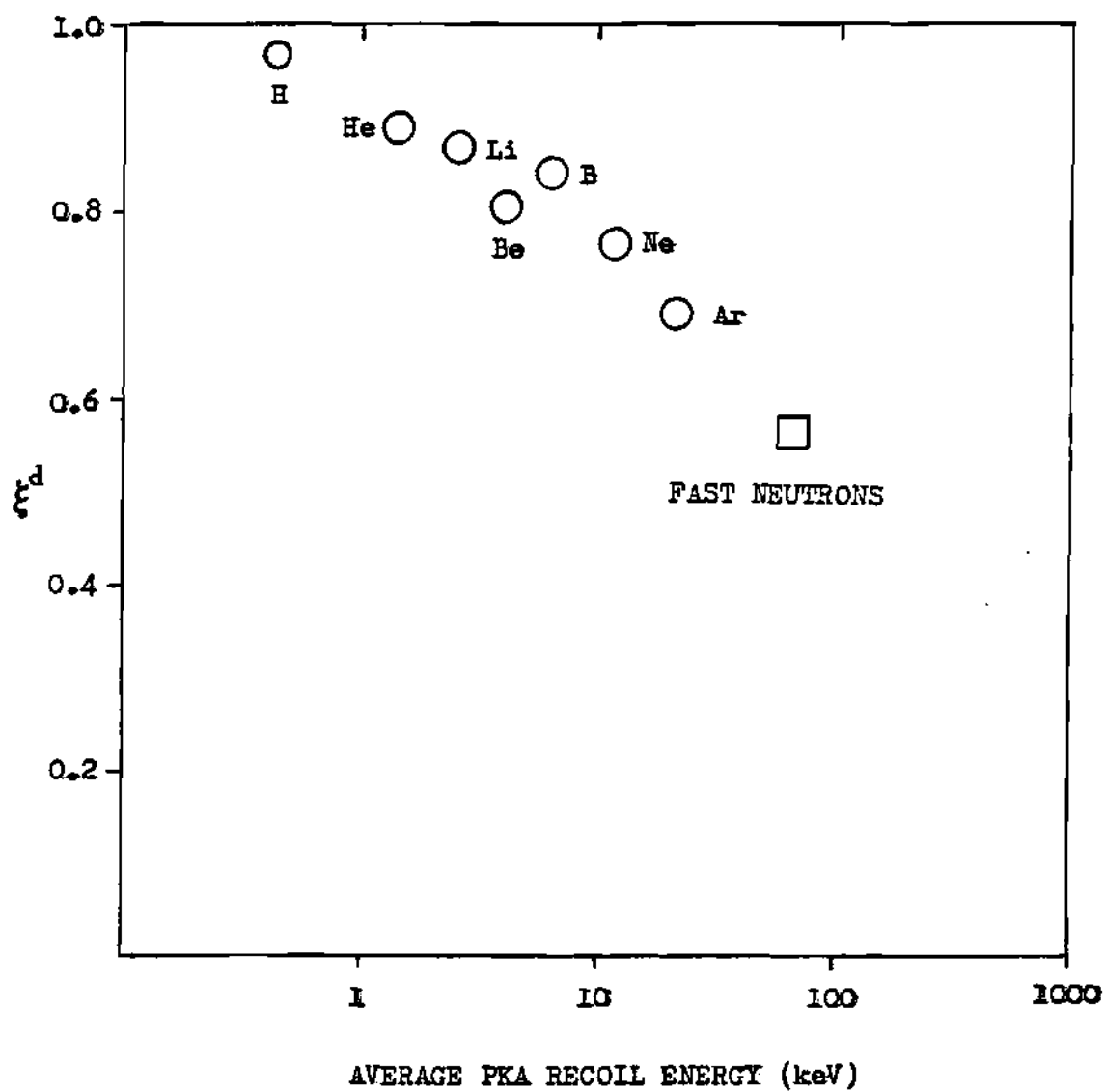
Figure 3.11   Relative Damage Efficiency Dependence upon the Average PKA Damage Energy for Several Projectile Species

cross-sectional area. The defect production profile $N_d(x)$ actually corresponds to PKA(x) where it is assumed that all defects occur locally about the causal PKA.

3.8 Surface Binding Energy

The magnitude, energy, and angle of sputtered atom ejection from a crystalline surface are directly influenced by the surface atom energy barrier, ΔU, that must be surmounted by all atoms attempting to escape. In general, a distribution of surface binding energies exists which is dependent upon the crystal surface structure and on the damage state of the surface.[52,125] It is common practice to equate the surface binding energy to the heat of sublimation, E_s, which is defined as the sum of the cohesive energy plus the heat of vaporization. The two most common means for describing the surface binding energy conditions are the isotropic and planar potential models.

In the isotropic model, a spherically symmetric potential barrier is assumed such that a particle escapes the target surface if its kinetic energy exceeds ΔU regardless of its ejection angle, ϑ .[52,125-127]

$$\Delta U(\vartheta) = \Delta U$$

(3.8.1)

For the planar model [52,125-127]

$$\Delta U(\vartheta) = \Delta U \sec^2 \vartheta \qquad (3.8.2)$$

where only the perpendicular velocity component of an escaping particle is available to overcome the planar potential barrier. In both models, escaping atoms have an energy of $E_o - \Delta U$; however, the energy is debited only along the surface normal component in the planar potential model as opposed to a total energy debit in the istropic model. Thus, sputtered atoms experience a directional change (refraction) in overcoming a planar potential (Figure 3.12). When the normal component of the escaping atom is less than the planar potential, total internal reflection occurs.[125] The atom may undergo subsequent scattering events allowing it to meet the necessary conditions for ejection.

Preference of one model over the other is based primarily on the observed experimental sputtered energy distribution. Computer simulations employing the isotropic model [126] show that the resultant sputtered atom energy spectrum is proportional to a monotonic function of E^{-2}, whereas the planar model exhibits a maximum in the yield spectrum (Figure 3.13). Experimental evidence approximates the E^{-2} functional behaviour in the high sputtered energy tail range of $10-10^3$ eV [125,126,128]; however, it, too, is
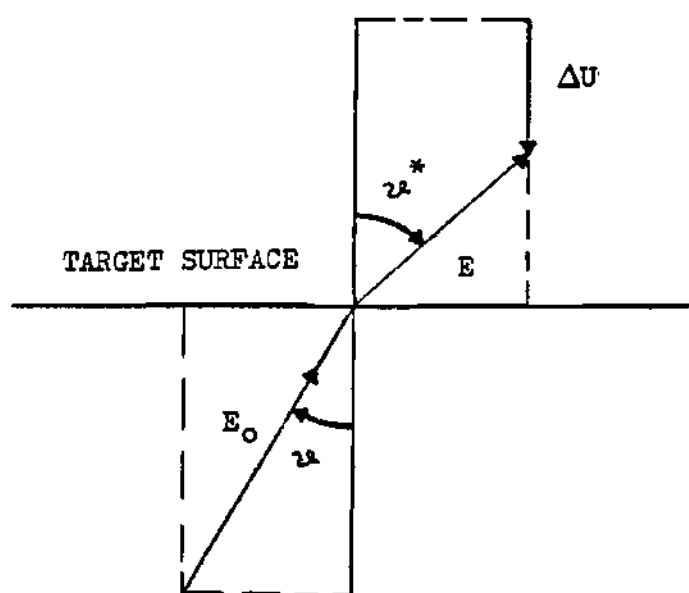
Figure 3.12 Refraction of Atoms Overcoming
a Planar Potential
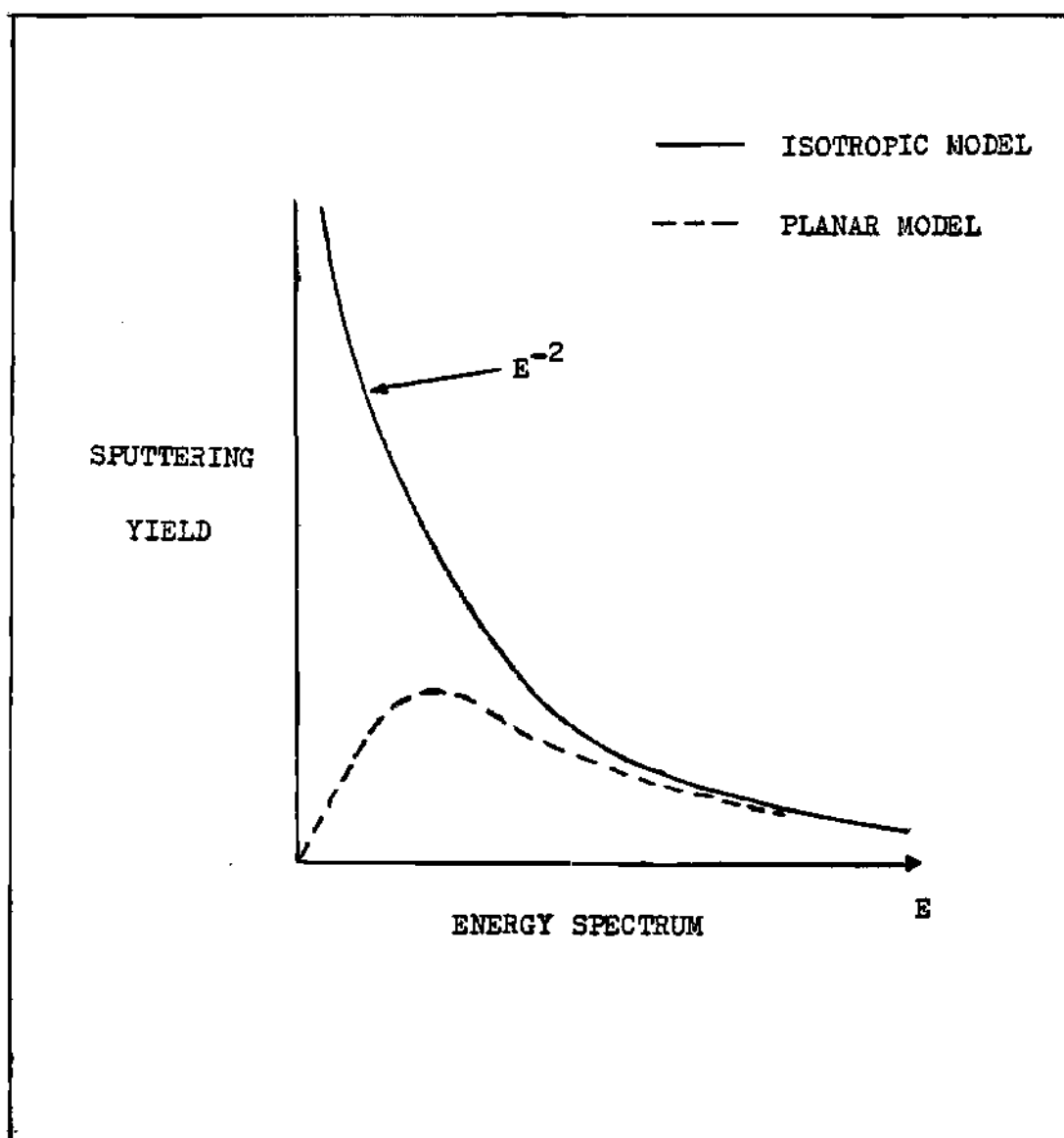
Figure 3.13 Sputtered Energy Distributions for
Isotropic and Planar Surface Potentials

characterized by a maximum in the yield spectrum at low energies. Therefore, the planar potential model has the widest acceptance in describing the surface binding energy effects.

Not only are sputtered atoms influenced by the presence of a surface energy barrier, but incoming and backscattered projectiles are affected as well.[107,129,130] The projectile-target potential barrier (trapping energy), U_t, acts to accelerate and to deflect towards the surface normal an incident projectile while for a backscattered projectile a similar deceleration and refraction as that undergone by sputtered atoms is experienced. Projectile/target combinations where the trapping energy is significant ($\sim O(<.5$ eV)) include those susceptible to hydride or oxide formation (e.g., $D\rightarrow Ti$ and $O\rightarrow W$) and self-sputtering events. The inclusion of a projectile surface binding energy acts to increase the trapping efficiency of the target. With respect to sputtering, an increase in the trapping efficiency for self-projectiles (especially at low impact energies) may result in a decrease in the overall self-sputtering efficiency due to a reduction in the backscattering probability; however, an increase may result from further scattering events within the target due to the trapped projectile.

3.9 Summarization of Sputtering Mechanics Development

An overview of athermal scattering phenomena related to the sputter ejection of surface atoms from (assumed) amorphous materials has been presented within the Monte Carlo TRIM framework. In contrast to previous TRIM model developments (as well as MARLOWE applications), development of a TRIM formalism without adjustable "fudge" factors to guarantee experimental agreement has been sought. Also, the modified TRIM formalism has been generalized to model heterogeneous materials for sputtering, damage, implantation, and reflection studies.

The revisions, extensions, and new modeling incorporated within the TRIM formalism are briefly summarized as follows:

(1) On an average basis, the Moliere interatomic potential within the TRIM mechanics has been matched to the more exact Biersack-Ziegler (B-Z) interatomic potential.   A technique has been developed to calculate the average correction factor, $\langle CA \rangle$, of the screening length necessary to equate the Moliere potential to the B-Z potential in agreement with various scattering experiments.

(2) An inelastic energy model based on local collision physics has been substituted for the semi-local and the continuum (nonlocal) models commonly employed by previously proposed TRIM and MARLOWE model prescriptions. Low-energy sputtering and reflection necessitates a local inelastic

energy loss model due to short scattering sequences. The Karpusov model either prescribed exactly or as an (empirical) asymptotic approximation has been incorporated within the TRIM formalism to describe electronic excitation (scattering) losses.

(3) An alternative local binding energy scheme necessary for a target atom to participate in the collision cascade is included in the TRIM formalism. Previous scattering calculations have assumed a zero binding energy, an arbitrary binding energy to match experiment, and a binding energy equal to the local displacement energy. The current formalism is analogous to the displacement energy concept, except a differentiation has been made "as to when" energy is debited from a displacement event.

(4) The trapping energy mechanics necessary for the reflection of hydrogen or oxygen from elements susceptible to hydride or oxide formation or for self-sputtering have been incorporated into the TRIM framework in terms of a surface energy barrier.

(5) The surface geometry prescription assumes a "skin" thickness in which the defining of a defect is obscure. Also, the geometrical prescription in terms of a multi-layer concept allows the study of cascade mixing and recoil mixing for heterogeneous systems.

(6) Finally, the generalization of the TRIM formalism for an arbitrary multi-component and multi-layer

heterogeneous material provides the means for investigating various projectile/target phenomena of the proposed thin-film alloy systems.

3.10 Verification of the Sputtering Mechanics

Confirmation that the general quantitative and qualitative sputtering behaviour of the modified TRIM model is accomplished through the comparison to theory and experiment for a number of projectile/target combinations. Fair to good experimental agreement of the current TRIM model had been previously obtained (and published) for the projectile, target systems of (He/Al, Ar/Al, and He/Al-Li [131]), (Ar/Ti and Ar/TiO [132]), and (D/Mo).[42] For the current alloy solvents of Cu, V, and W, the sputtering yield (assuming the single ejection mode of neutral atoms) as a function of incidence for selected projectiles is displayed in Figures 3.14 a-g. In general, light-ion sputtering as predicted by TRIM is within experimental error (commonly ±30%), while for heavy-ion sputtering, experimental agreement is obtained if the projectile energy exceeds 200 eV. The discrepancy between TRIM and experiment for low-energy, heavy-ion sputtering is partially due to the approximation (empiricism) of the Karpusov electronic energy loss terms. For small values of reduced energy (representative of low
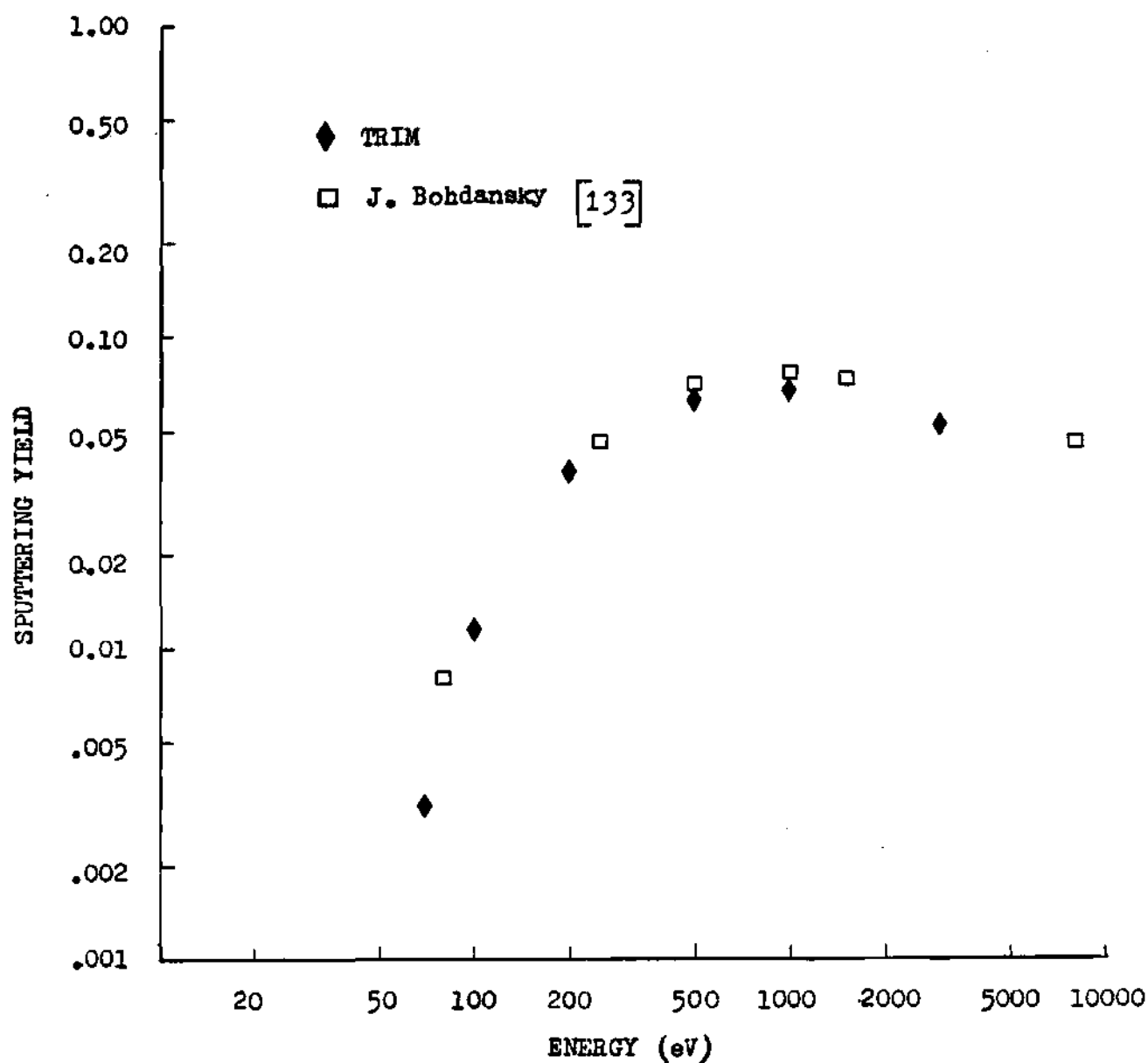
Figure 3.14a Sputtering Yield Energy Dependence
for D+ on Cu at Normal Incidence
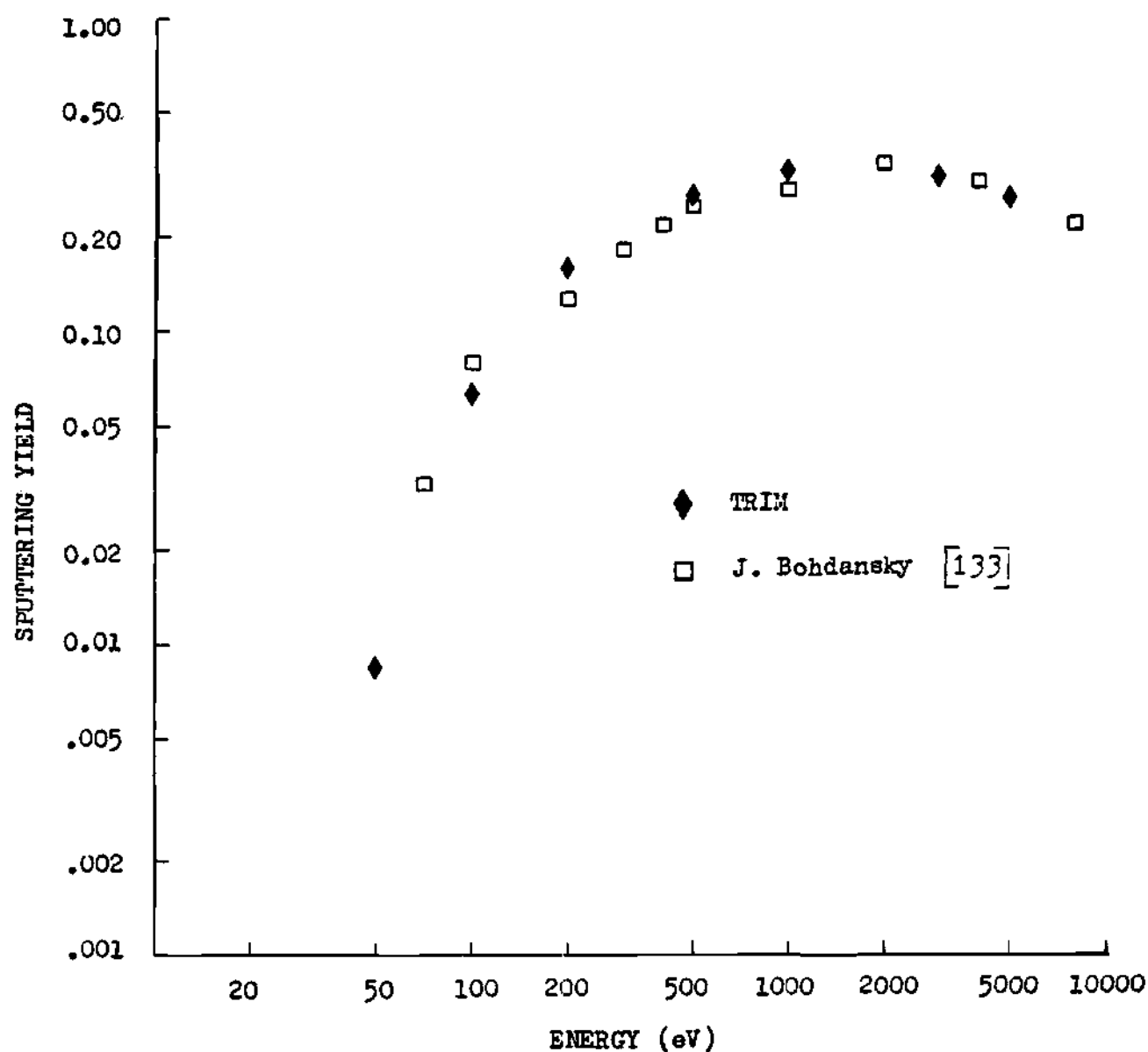
Figure 3.14b Sputtering Yield Energy Dependence
for He+ on Cu at Normal Incidence
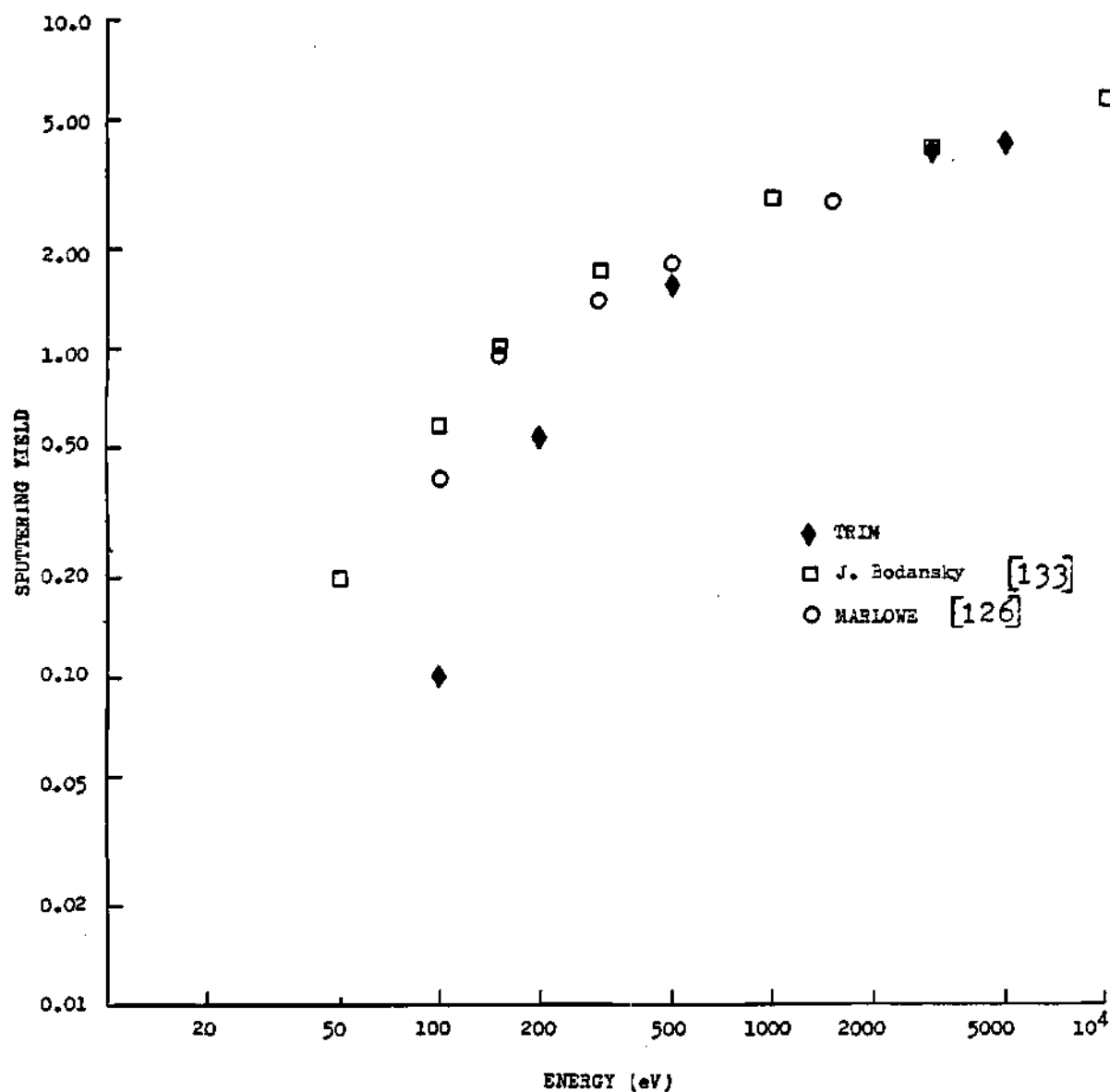
Figure 3.14c   Sputtering Yield Energy Dependence for
                Ar+ on Copper at Normal Incidence
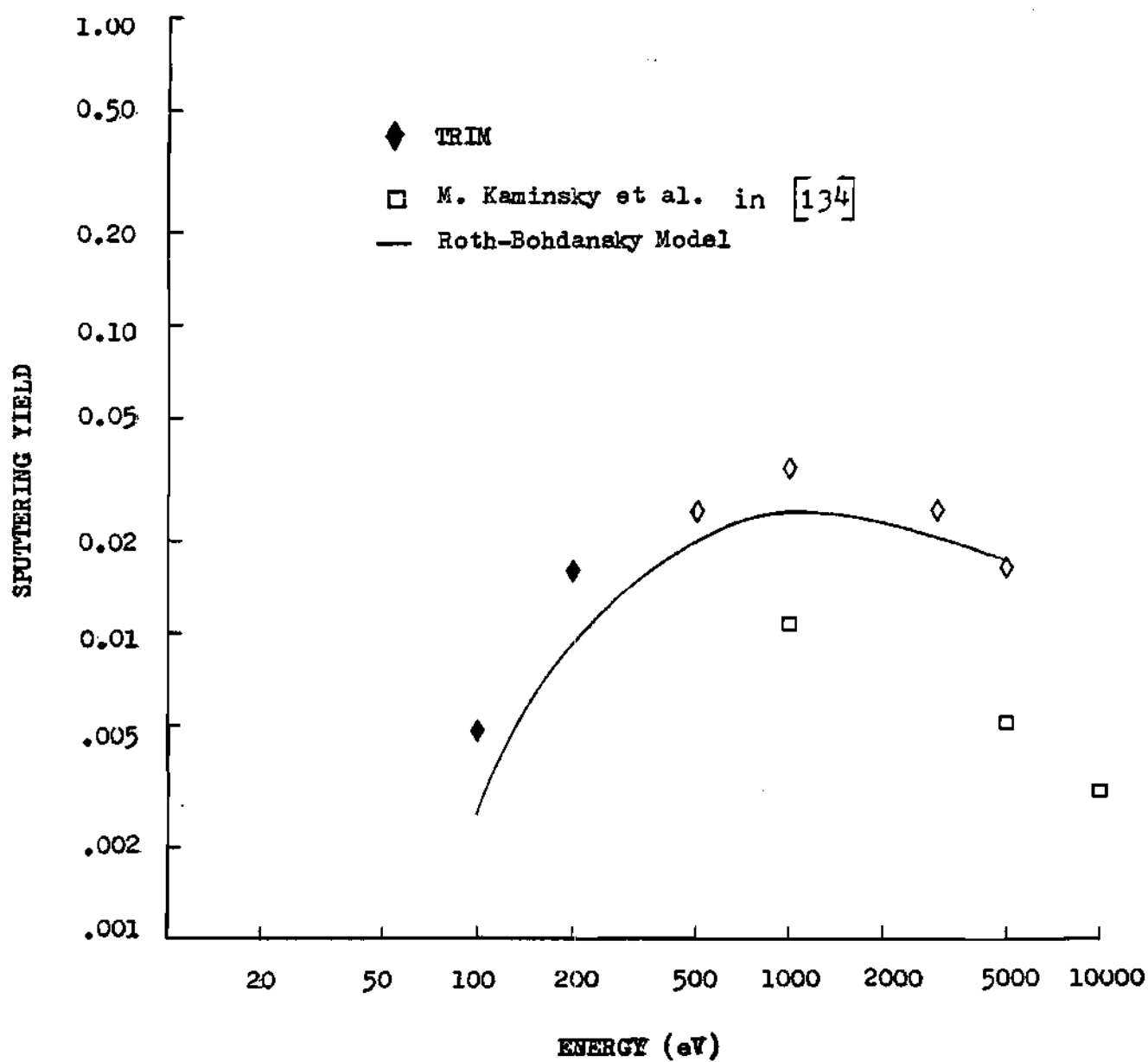
Figure 3.14d   Sputtering Yield Energy Dependence
for D+ on V at Normal Incidence
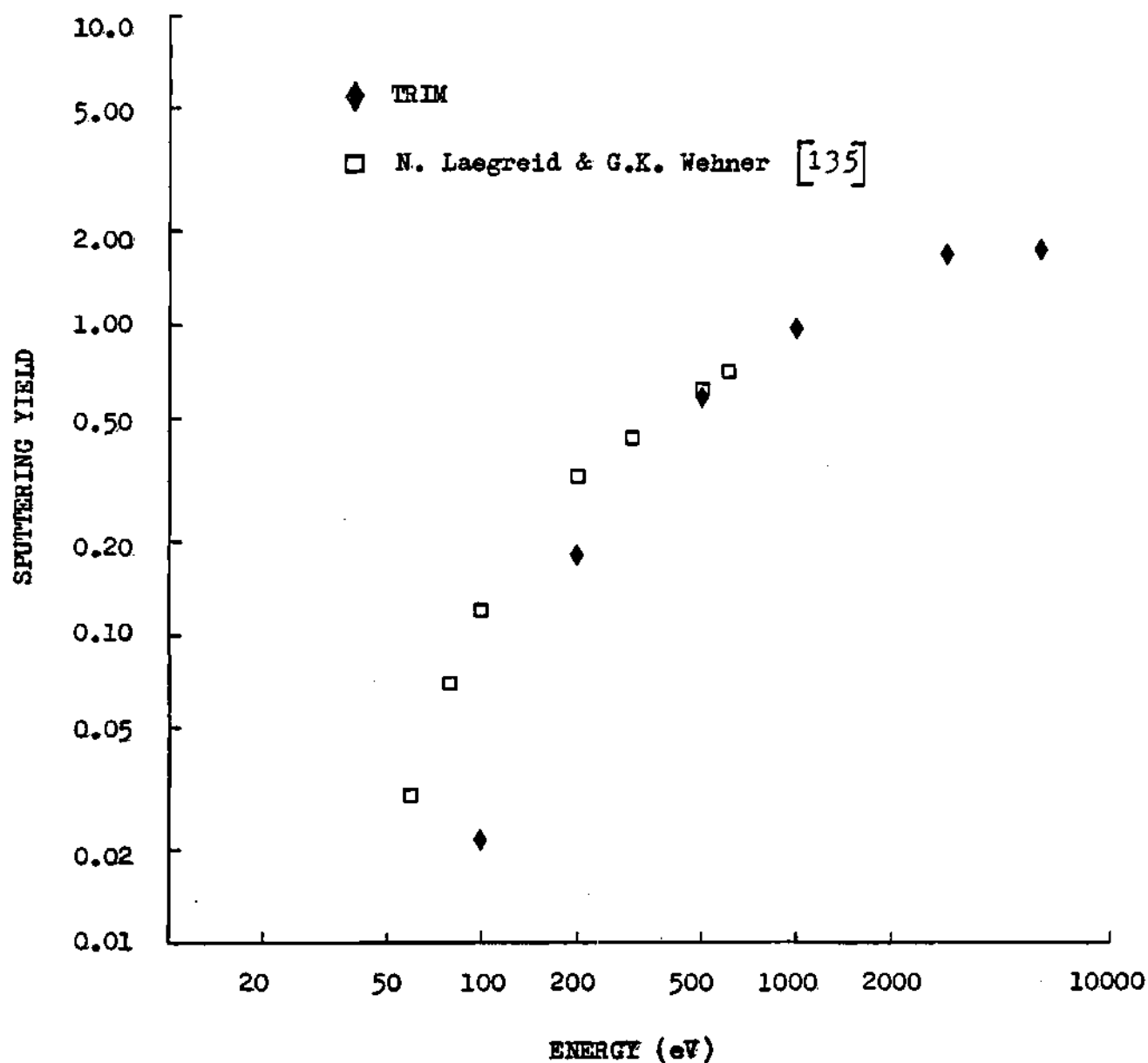
Figure 3.14e   Sputtering Yield Energy Dependence
for Ar+ on V at Normal Incidence
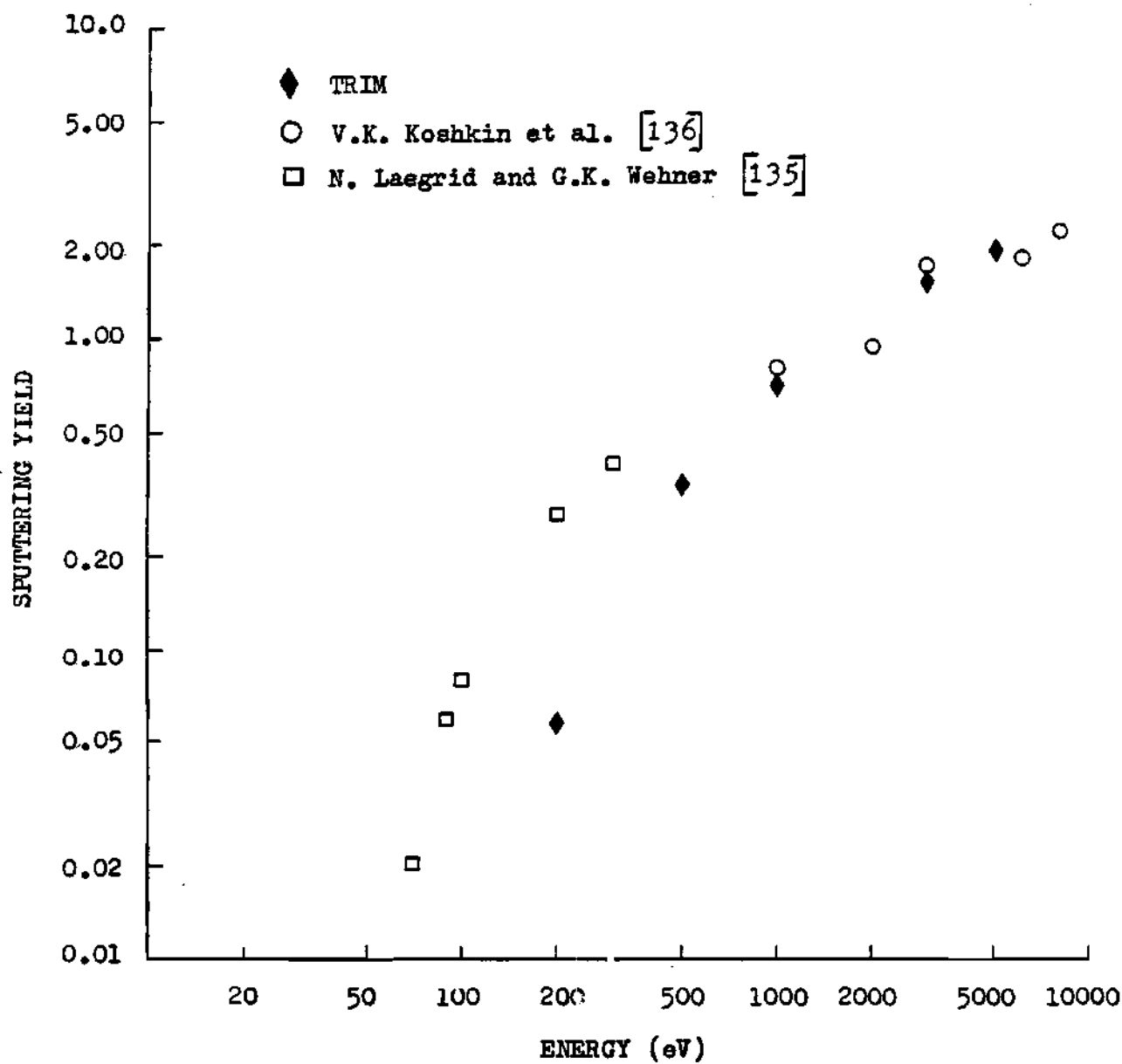
Figure 3.14f   Sputtering Yield Energy Dependence
for Ar+ on W at Normal Incidence
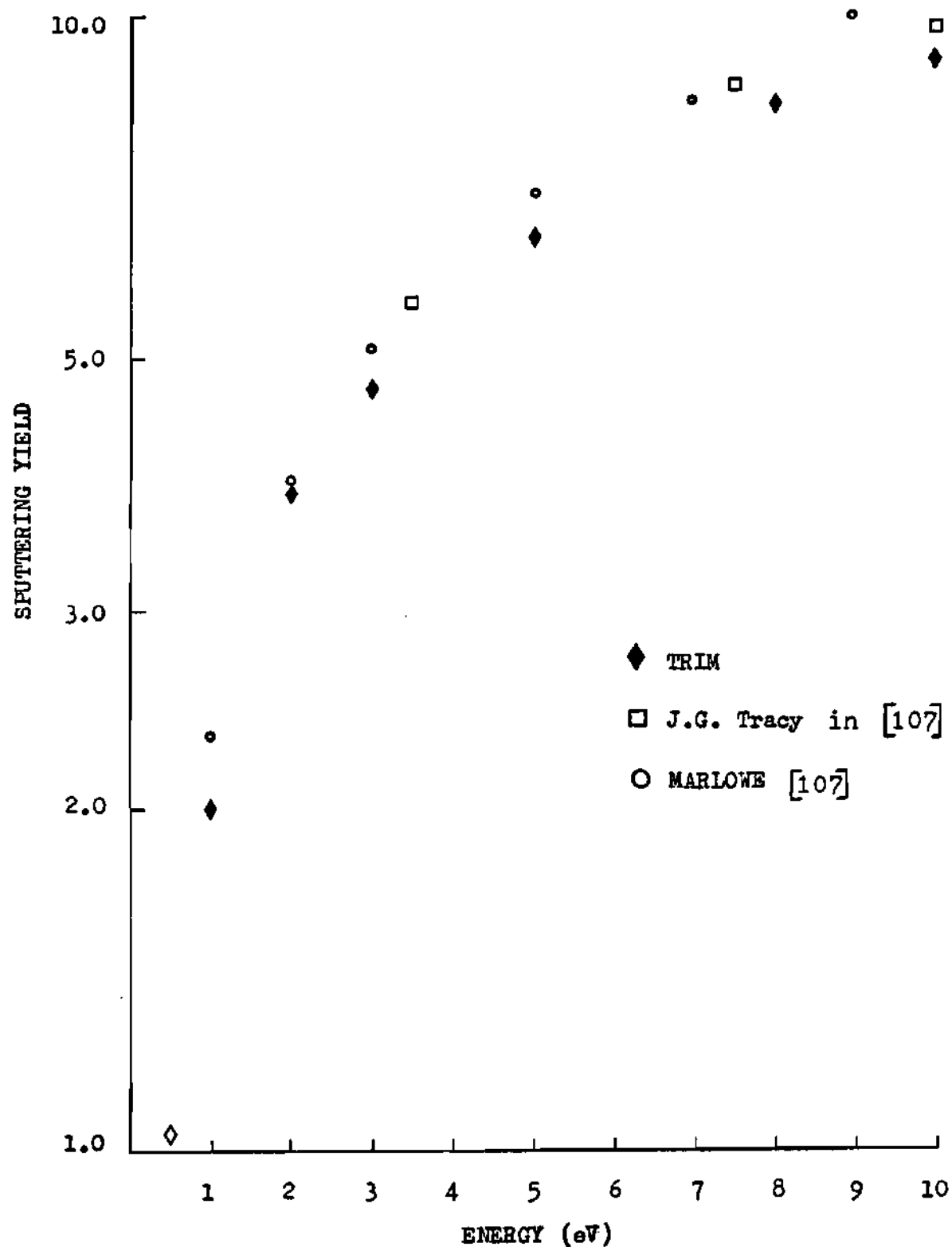
Figure 3.14g   Sputtering Yield Energy Dependence
for U+ on α-U at Normal Incidence

energy scattering between atoms of small mass disparity), the asymptotic formalism developed to model the Karpusov excitation losses has an order of magnitude inaccuracy. Also, coupled to the Karpusov approximation is the averaging of the CA factor as applied to the Biersack-Ziegler potential that may introduce a secondary (smaller) error. These errors act to reduce the energy deposition of the projectile in the near-surface region of the target; hence, a resultant reduction in the sputtering yields is calculated. While the quantitive yields are in error, the basic physics underlying the sputtering mechanics (e.g., sputtering yield as a function of angle and the sputtered energy and angular distributions) will be shown to be correct for heavy-ion sputtering. Finally, the discrepancy between TRIM and experiment for heavy-ion sputtering does not detract from applying TRIM to the thin-film systems of Cu-Li, V-Al, and W-Be. Rather than determining the benefit of "protective" overlayers on the basis of absolute sputtering yields, an erosion (sputtering) reduction factor as a function of incident energy is just as useful. It has been found that regardless of the TRIM model prescriptions for the various scattering phenomena the relative reduction of the sputtering yield due to a thin-film remains unaffected. Determination of the energy at which self-sputtering exceeds unity is probably accurate since such an energy is on the order of 1000 eV.

Any comparison of the sputtering yield results obtained from the current proposed TRIM formalism to that of previous TRIM and MARLOWE models must recall that the current TRIM framework is void of "adjustable" physics parameters to "fit" experiment unlike its predecessors. The adjustment of interatomic potential, electronic energy loss, and binding energy prescriptions in order to obtain experimental agreement does not lend itself to predicting sputtering yields for materials in which the experimental yields are unknown or to predicting other physical phenomena (e.g., implantation profile, dpa profile, or sputtered layer of origin) in which adjustable prescriptions may radically alter the underlying scattering physics.

Previous light-ion sputtering calculations performed by Haggmark and Biersack [104] and reflection calculations performed by Eckstein and Verbeek [137] have shown agreement with experiment if the Moliere potential correction factor or the sublimation energy of the material were properly adjusted. The value of $\langle CA \rangle$ required to obtain experimental agreement ($\langle CA \rangle$=.7 for transition metals) is nonjustified according to the DCATV fit to the B-Z potential which predicts of a $\langle CA \rangle$ value in the range of 0.80 to 0.95. Also, the arbitrary adjustment of the material sublimation energy is without physical basis. In another TRIM study performed by Haggmark and Wilson [92] for light-ion sputtering, good experimental agreement was obtained for physical

prescriptions of the interatomic potential and the sublimation energy; however, an unrealistic binding energy model was proposed to properly "fit" experiment. The binding energy prescription assumed that $E_b = H_v^f + H_i^f + E_s$ within the bulk with the interstitial formation energy as an adjustable parameter. Physically, a bulk atom does not lose the sublimation energy unless it actually undergoes a sputtering event; hence, the proposed model is inapplicable to bulk atoms. Furthermore, Haggmark and Wilson found it necessary to adjust the interstitial formation energy to values approaching 20 eV for bcc elements, far exceeding the actual physical values that more closely approximate the sublimation energy, being on the order of 6 to 10 eV.

In heavy-ion sputtering calculations performed by Robinson for Ar/Cu [126] and U/α-U [107] (Figures 3.14 c and g, respectively), MARLOWE calculations compare very favorably to the experimental data. However, in both cases Robinson makes use of a semi-local electronic energy loss model in conjunction with altering other physical parameters. For the Ar/Cu MARLOWE yield, a value of $\langle CA \rangle = .77$ was necessary in contrast to the DCATV prescription of 0.95. The U/α-U sputtering yields were based upon the assumption of an arbitrarily chosen value for the binding energy of an atom joining the collision cascade. Without the above assumptions, the MARLOWE calculations deviate from experiment by as much as 100%.

For normal incidence projectiles, a collision cascade or an energetic recoil are necessary to cause sputtering; whereas, for projectiles impacting at an oblique angle of incidence the probability of direct ejection as a result of impact increases. Thus, in general, as empirically predicted by the D.L. Smith model, the sputtering yield should increase monotonically for increasing angle of incidence. Shown in Figures 3.15 a,b are the sputtering yield dependences as a function of angle for Ar/W and Ar/Cu at 1 keV in comparison to experiment. Angularly dependent sputtering yields (as calculated by TRIM) are in excellent agreement with experiment. However, as indicated by experiment and TRIM, the sputtering yield does not increase monotonically as a function of increasing projectile incidence angle. Because the reflection probability of the projectile approaches unity for high angles of incidence $\theta \rightarrow 90°$, the energy transfer from the projectile to the target decreases for increasing incidence angles. Thus, the maximum sputtering dependence as a function of angle is determined by the competing processes of an increased direct ejection probability and a decreased energy transfer probability.

The sputtering dependence on incidence angle must further be defined in terms of impact energy which is proportional to the energy deposition within the target. Shown in Figure 3.16a is the ratio of the sputtering yield at $60°$ to that at normal incidence for deuterium on copper as a
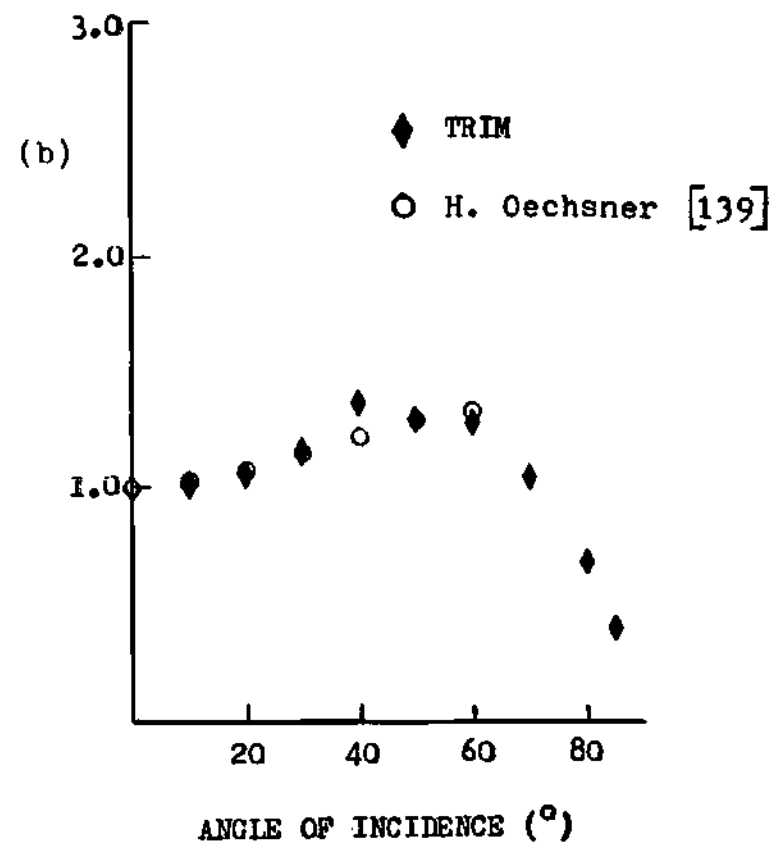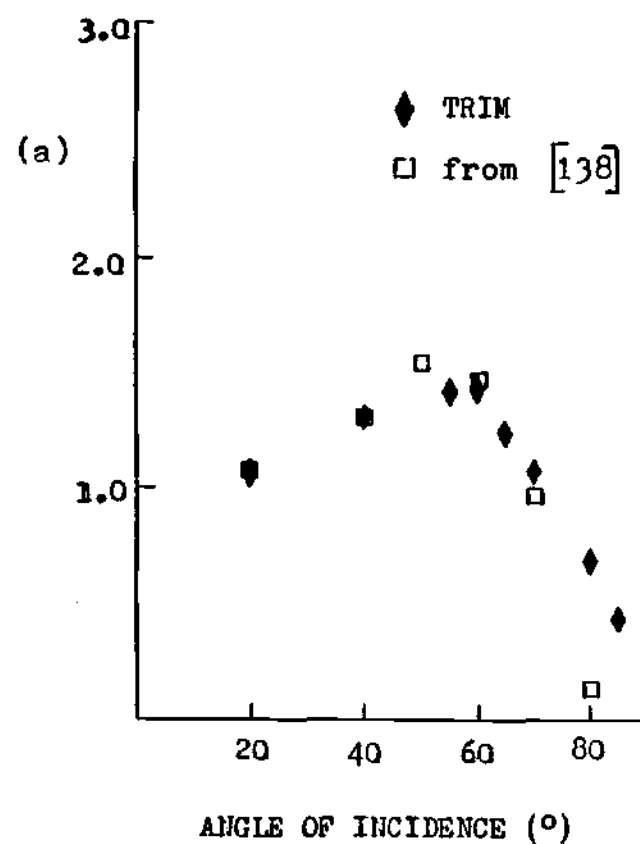
Figure 3.15   Angular Dependence of the Sputtering Yield at 1 keV
Incidence Energy for (a) Ar+ on Cu (b) Ar+ on W

function of impact energy. At low energies, the angular sputtering yield is less than the normal sputtering yield; however, at energies greater than 100 eV, the angular dependent yield becomes greater than normal incidence yield. At low energies, increased reflection (Figure 3.16b) or conversely reduced projectile deposition reduces the probability of sputtering for a given angle. At higher energies, energy deposition within the target surface increases; hence, the sputtering yield increases and, correspondingly, the projectile reflection decreases.

When the projectile mass approximates the target mass, reflection at normal incidence tends to be negligible or conversely the "sticking" coefficient of the projectile approaches unity. Experimentally, the sticking coefficient for normal incidence has been found equal to .95-.97 ±.05 for heavy-ion impact regardless of the impact energy.[140] Until very recently, most fusion design studies have accepted the premise of unity sticking coefficients even for nonnormal incident angles. However, as M.T. Robinson has shown through MARLOWE simulations for 100 eV $U \rightarrow \alpha$-U (laser isotope separation) [107], the self-reflection yield approached a maximum of 45% for an incident angle of 80 degrees. The significance of this result is that the determination alone of a self-sputtering energy exceeding unity may be an insufficient erosion limitation employed in fusion material studies. Thus, the "positive feedback" recycling of wall
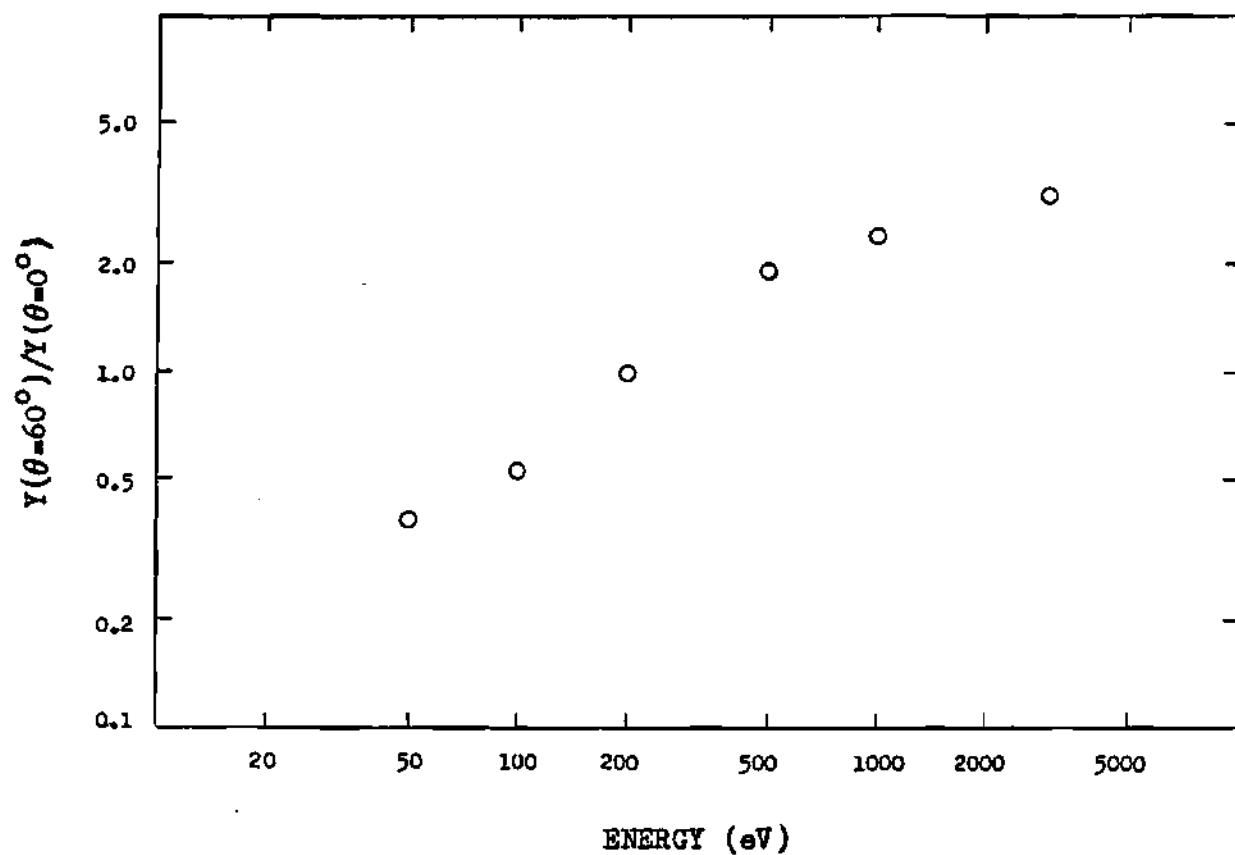
Figure 3.16a Sputtering Yield Ratio as a Function of Energy for D+ on Cu at 60 Degrees in Comparison to Normal Incidence
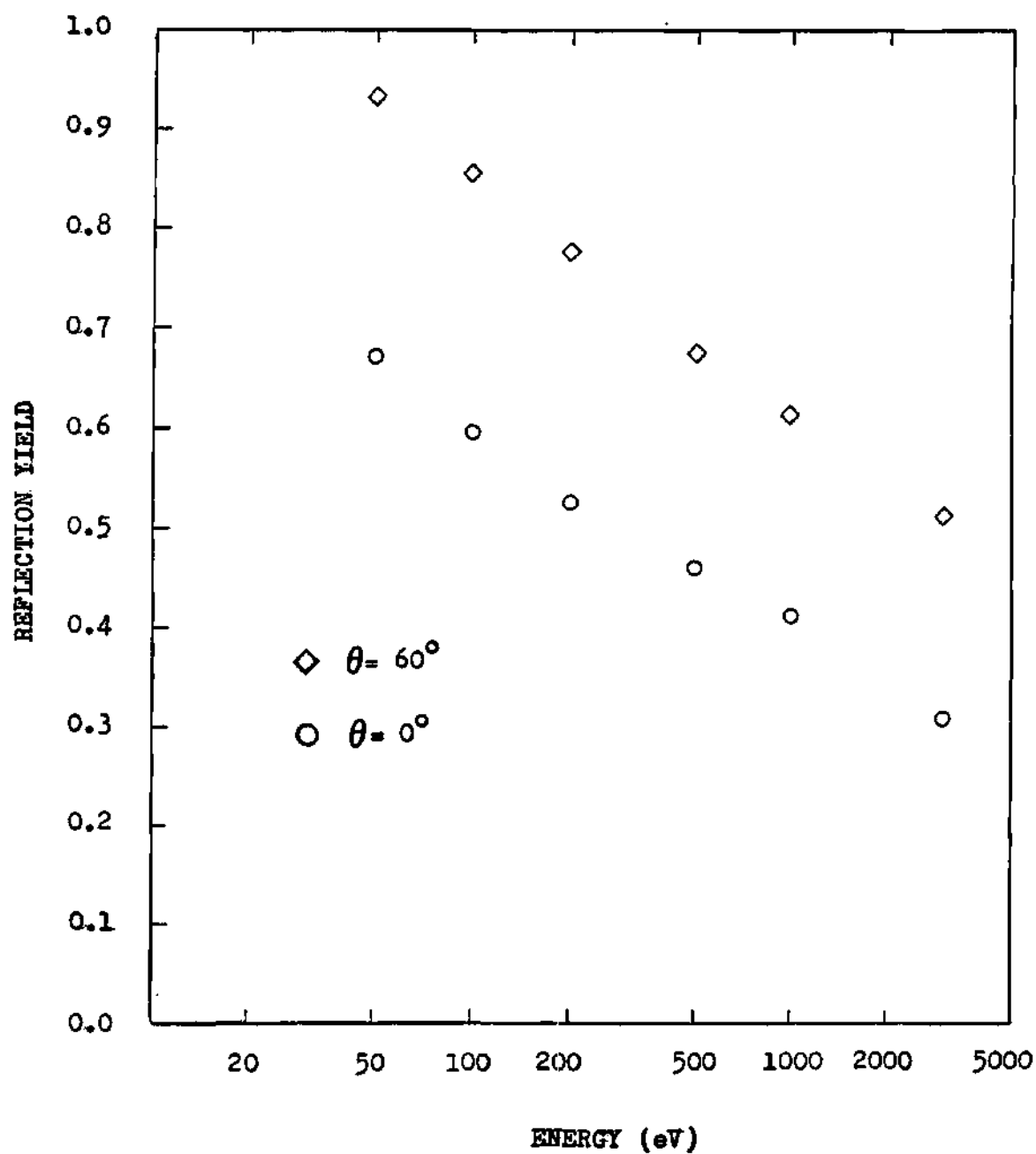
Figure 3.16b   Deuterium Reflection Probability
from Copper as a Function of Energy
for Normal and 60 Degrees Incidence

impurity ions/atoms, which could result in runaway erosion if for every incident ion more than one target atom returns to the plasma, must include self-reflection. For the alloy solvents Cu, V, and W, the self-reflection yield (TRIM) for an incident angle of 60 degrees as a function of impact energy can be significant (Figure 3.17). Over a range of intermediate impact energies (200-500 eV), the self-reflection yield ranges from 50 to 65 percent. At low energies, the self-reflection yield is suppressed by the attractive planar potential of the target, preventing the escape of "like" atoms. At high energies, the self-reflection yield decreases due to a higher probability of self-deposition within the target.

A histogram of the sputtered energy distribution in the presence of a planar potential should behave according to the theoretical Thompson-Sigmund dependence (Figure 3.13). For copper with the surface binding energy equal to 3.5 eV, the sputtered energy distribution for normally incident projectiles according to Thompson-Sigmund theory is given by Figure 3.18a. The self-sputtering energy distributions for 100 eV and 1000 eV calculated by TRIM are shown in Figures 3.18 b,c. The 100 eV sputtered energy distribution is dramatically skewed towards low sputtered energies in comparison to theory and the 1000 eV sputtered energy distribution. Similar shifts in the sputtered energy spectrum as a function of projectile energy have been
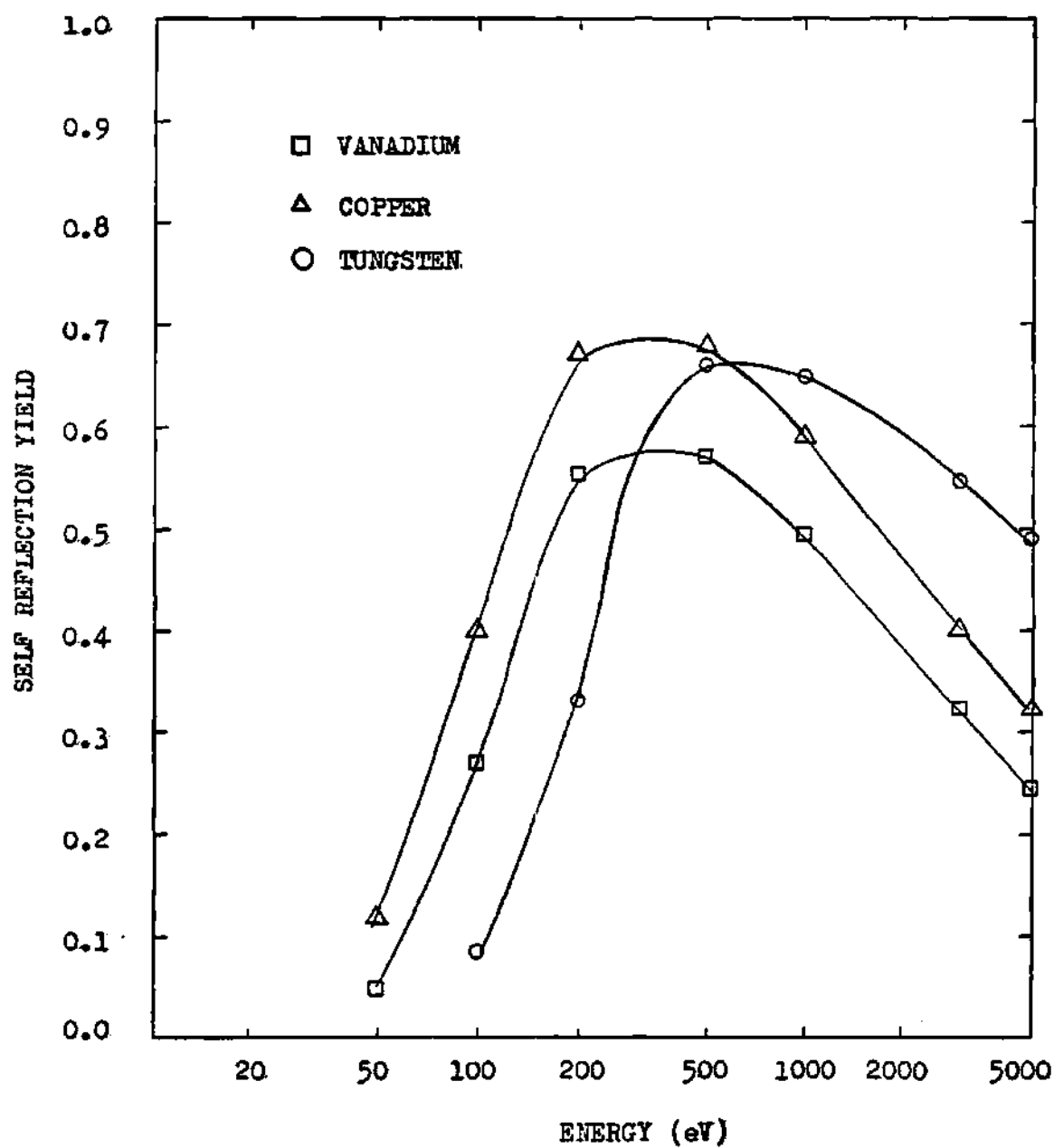
Figure 3.17   Self-Reflection Yield as a Function
of Energy for 60 Degrees Impact Angle
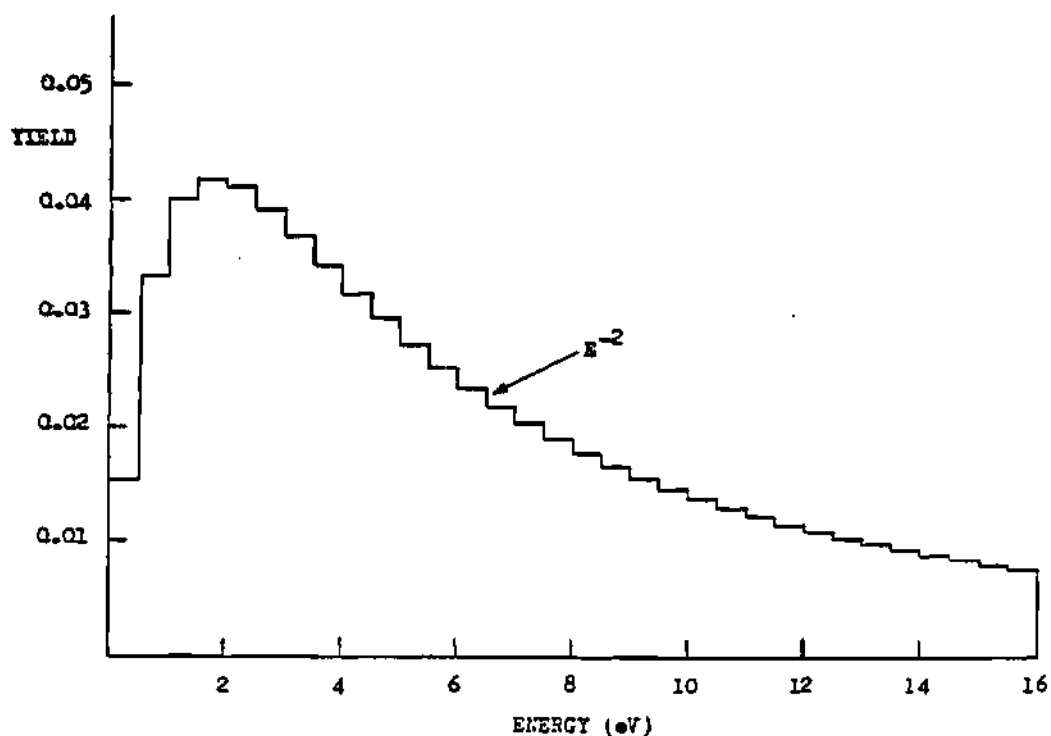
Figure 3.18a   Histogram of the Sigmund-Thompson
                Sputtered Energy Distribution for
                Copper (E_s=3.53 eV)
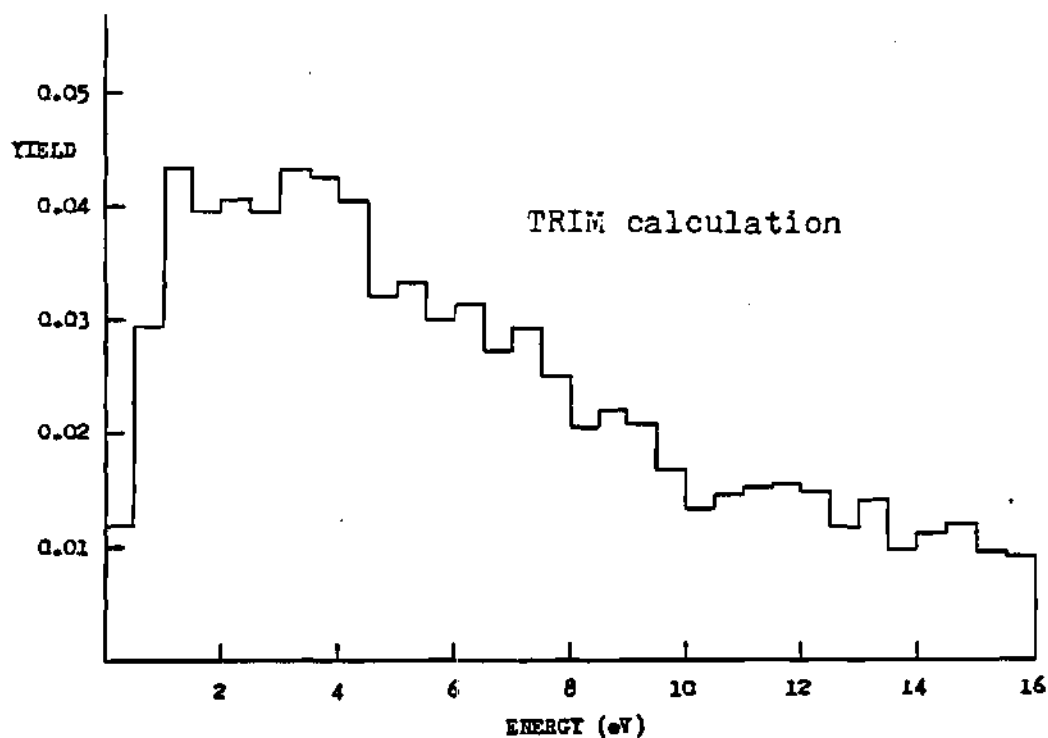
Figure 3.18b   Copper Self-Sputtered Energy
                Distribution for 1000 eV Cu+
                Normal Incidence
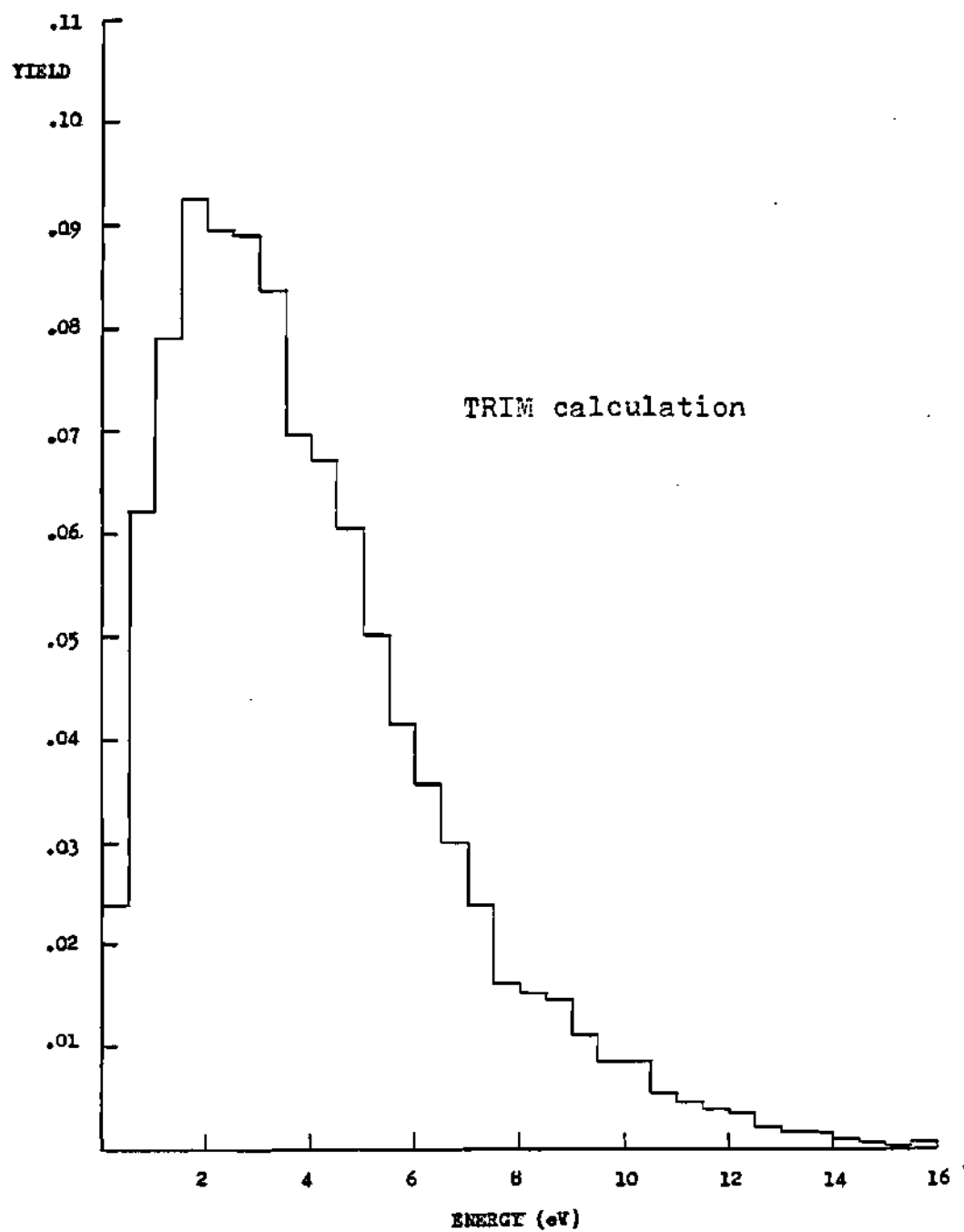
Figure 3.18c   Copper Self-Sputtered Energy
Distribution for 100 eV Cu+
at Normal Incidence

observed experimentally for light-ion sputtering as well.[141] Also, M.T. Robinson observed a similar behaviour in the MARLOWE simulation of U→α-U self-sputtering [107], where at 5 KeV 36% of the sputtered energy exceeded 20 eV and at 500 eV only 20% of the sputtered energy exceeded 20 eV. Inherently, within the derivation of the Thompson-Sigmund sputtered energy dependence is the assumption that the scattering energy greatly exceeds the atom binding energy. The resulting sputtered energy distribution (for high energy scattering) is approximated in the asymptotic limit where the scattering energy approaches infinity. However, for a finite projectile energy, a finite cut-off energy exists within the sputtered energy distribution. Hence, for low energy sputtering the sputtered energy distribution must be skewed towards low energy.

The most probable energy of sputtering as predicted by Thompson-Sigmund sputtering is $\Delta U/2$. Copper self-sputtering for both 100 eV and 1000 eV shows a maximum energy probability in the 2 to 3 eV range which exceeds the theoretical prediction of 1.75 eV. According to experiment (sputtering of silver) [142] and according to MARLOWE simulations [107], the most probable energy of sputtering better approximates $2\Delta U/3$ in agreement with the current TRIM calculations.

Because of the surface planar potential, the angular distribution of sputtered atoms conforms to a cosine for

projectiles at normal incidence. Experimentally, the cosine sputtered distribution has been observed for energetic heavy-ions (e.g., Ar/Au, Hg/Fe, and Hg/Mo) [143,144] and for energetic light ions (e.g., H,D,He on Ni,Cu,Au,Mo,W targets) [145]. TRIM calculations for copper self-sputtering (Figures 3.19 a,b) indicate agreement with the cosine behaviour at 1000 eV incidence energy; however, at low energy, the distribution is definitely "undercosine" and peaked along an ejection angle of 45 degrees rather than along the surface normal. MARLOWE calculations for Ar on Cu are indicative of a similar behaviour for low energy sputtering.[126] It is thought that the deficiency of ejected atoms along the surface normal is due to the incompleteness of the turning back of the incident particle momentum along the surface normal [126]; i.e., the lack of collisional isotropy. Undercosine sputtered distributions have been observed experimentally for Hg/Ni, Hg/Mo, Hg/Ge, and Hg/Fe [143] at low energy (< 250 eV), confirming the low-energy TRIM simulations.

For a binary alloy in which the surface is predominately enriched with one component and the subsurface layer is primarily composed of the other component, theory predicts a cosine behaviour for atoms sputtered from the surface layer, while those sputtered from the "underlayer" will exhibit a sharper angular distribution.[146] Experimentally, the sputtered atoms originating from the alloy subsurface have
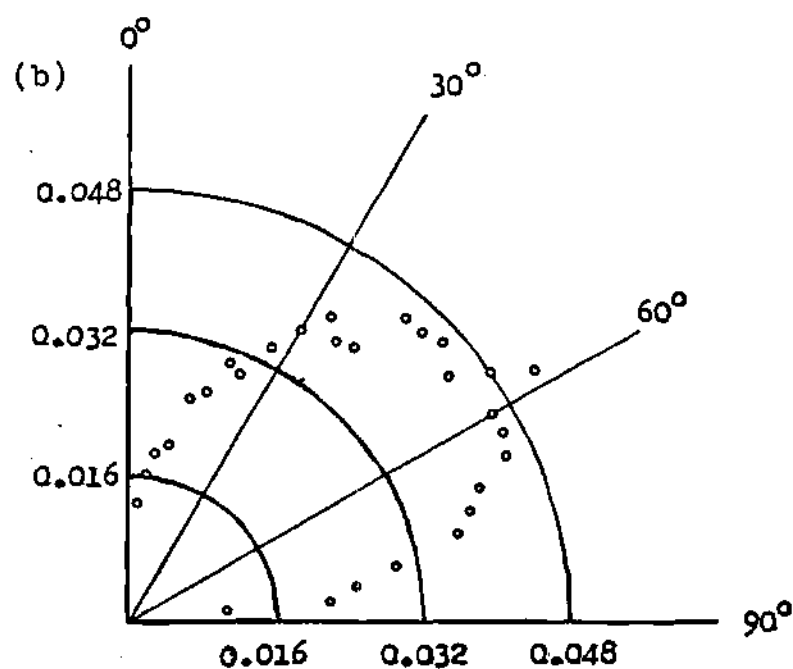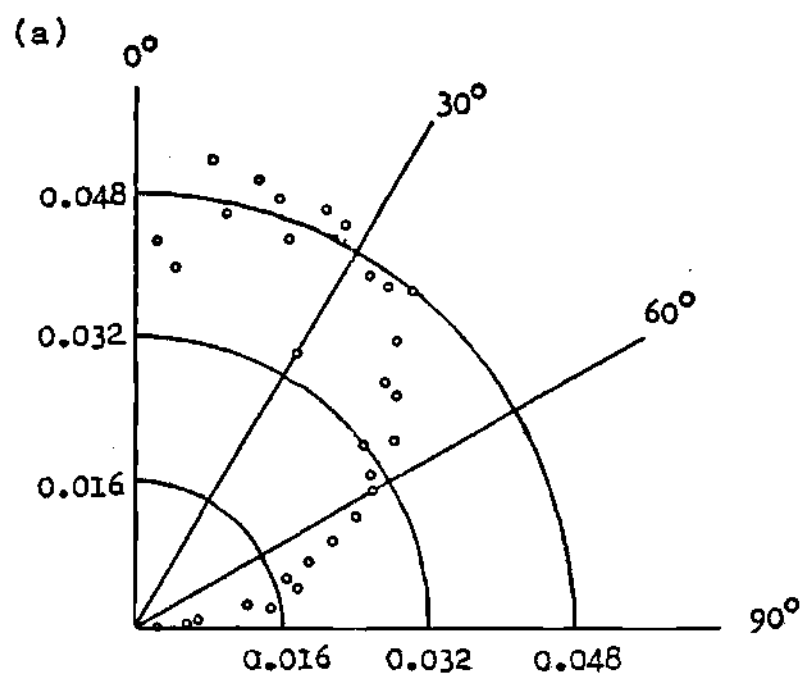
Figure 3.19   Copper Self-Sputtered Angular
Distributions for Normal
Incidence Cu+ at (a) 100 eV
and (b) 1000 eV

been observed to exit according to a $\cos^m\theta$ distribution where m>1.[147,148] Furthermore, the value of m increases with increasing projectile energy.[147]

TRIM simulations for an overlayer of lithium on pure copper are in agreement with theory and experiment (Figures 3.20 a,b). The angular distribution exhibited by the 60 degree copper incidence assumes that the incident copper is azimuthally isotropic.
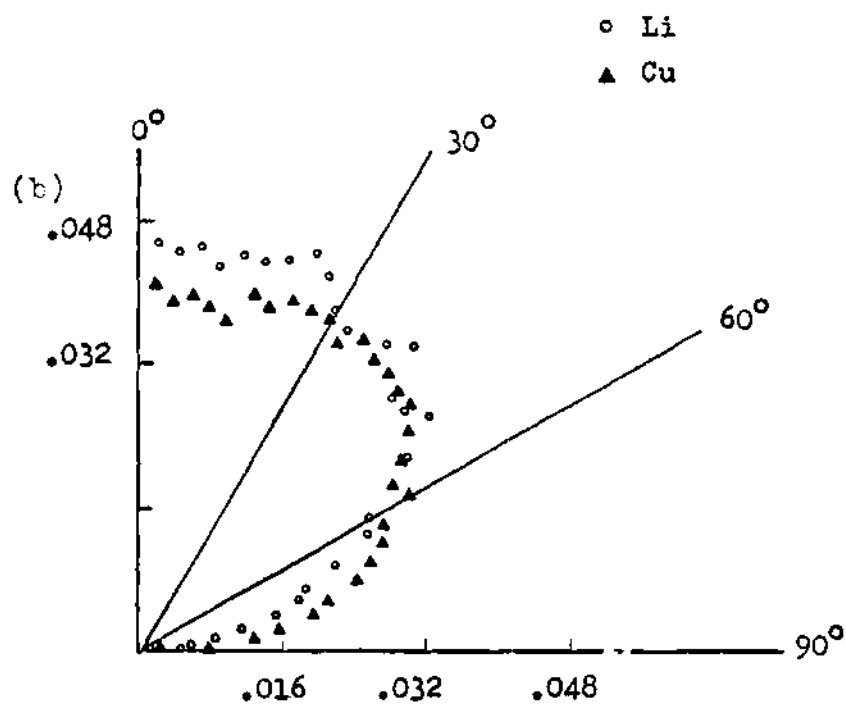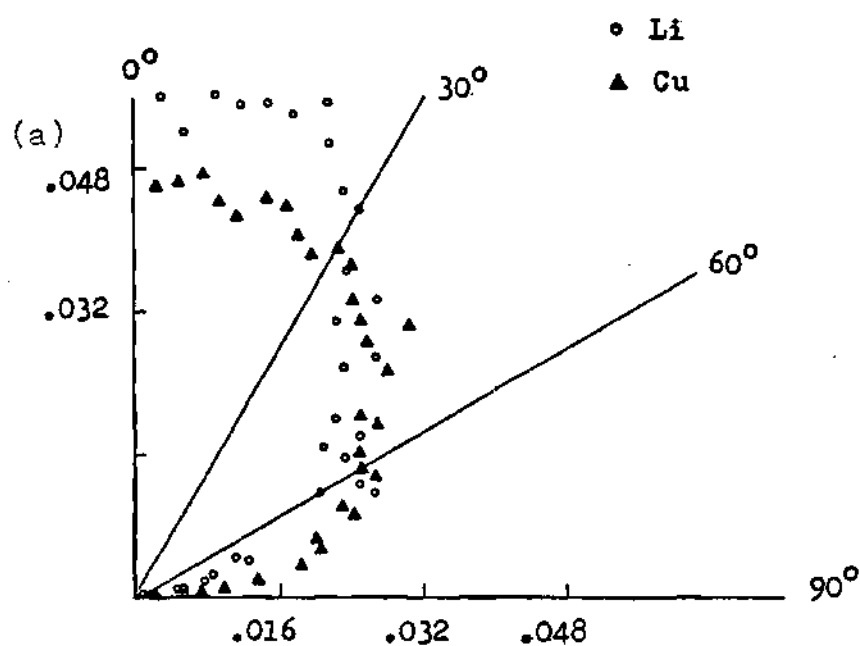
Figure 3.20 Copper and Lithium Sputtered
Angular Distributions from a
Li Monolayer on Elemental Cu
for 1000 eV Cu+ at (a) Normal
Incidence (b) 60 Degrees

CHAPTER IV

Surface Kinetics Model

4.1 Introduction

Nonequilibrium radiation-induced redistribution of alloying elements in the limiter/divertor near-surface region alters the sputtered species with time. Therefore, it is necessary to know if the proposed thin-film systems (as a means of fusion plasma impurity and wall erosion control) are truly self-sustaining and to what degree. A kinetic model which couples the point defect and alloying component fluxes resulting from radiation/thermal transport mechanisms and includes sputtering due to energetic ion-bombardment becomes important.

The Johnson-Lam (JL) kinetic model for fcc binary alloys [149-151] (subsequently extended to fcc ternary alloys [152]) provides the physical and numerical framework for investigating the Li thin-film/Cu-Li alloy system. The JL model tracks the space-time evolution of the alloy constituents under such effects as Gibbsian adsorption, preferential sputtering, displacement mixing, radiation-enhanced diffusion, and radiation-induced segregation. Inherent in the model is the assumption that

the transport of atoms and defects occurs via lattice migration mechanisms as opposed to grain boundary mechanisms. Anomalously, low diffusion activation energies are indicative of grain boundary transport [153]; however, ion-bombardment studies by A.R. Krauss [154] on the Cu-Li alloy system are indicative of lattice diffusion activation energies.

The time and temperature kinetics of the JL model has been previously validated in that good qualitative agreement between theory and experiment has been obtained for a number of irradiated alloys. Qualitative agreement of theory to experiment has been obtained for the nickel-based binary alloys of Ni-Al [155], Ni-Si [155,156], and Ni-Cu [157]. Also, the ternary alloys of Fe-Cr-Ni and Ni-Al-Si theoretically evolve according to experimental findings.[152] The quantitative mismatch between the JL model predictions and experiment is on the order of 20 to 50 percent for most calculations. Parametric adjustments of defect migration energies and/or of defect entropies have been necessary to match theory to experiment; although, such matches have not always been possible. While the JL model has been applied extensively to "undersized" and "oversized" solutes, it has been restricted to solvent/solute or solute/solvent mass disparities between 0.5 and 2.0. No theory/experiment comparisons have been made for a mass disparity that is reprsentative of the Cu-Li alloy under current research where a solvent/solute mass disparity ratio of seven exists. The

effects of such a large mass disparity upon the physics within the JL modeling remain unknown. However, mass disparity will tend to introduce nonlinear effects into athermal irradiation phenomena which are coupled to the alloy kinetics as opposed to "nondisparitive" mass systems where athermal phenomena of the alloy constituents are a linear function of the compositional profile.

In the following text, the formalism is developed for the expression of atom and defect fluxes in terms of concentration gradients, which necessitates the definition of partial diffusion coefficients. An overview is then presented of the relevant defect mechanisms associated with atom diffusion along with the kinetic phenomena of recombination, segregation, and sink annealing. Within the overview, conclusions are drawn on the importance of defect-types applicable to the pure Cu metal as well as to Cu alloys. Alternative models for recombination, segregation, and preferential sputtering, which are believed to be physically more accurate than the JL prescription, are presented and incorporated in the numerical kinetic scheme. Finally, the kinetic equations of a B-A (solvent-solute) binary alloy as applied to the time dependence of the Cu-Li system are prescribed.

4.2 Partial Diffusion Coefficients

The partial diffusion coefficients of atoms k via defects j and of defects j via atoms k are defined on the basis that each atom or defect in a crystal partakes in a random walk. For cubic (isotropic) crystals, the diffusivity coefficient of the conjugate atom-defect pair kj is [152,158]

$$d_{kj} = \frac{1}{6} \lambda_k^2 Z_k \nu_{kj} \tag{4.2.1}$$

Here λ is the atomic jump distance, Z is the number of first nearest-neighbor sites allowable for a given atom-defect interchange, and ν_{kj} is the atom-defect jump (exchange) frequency. The exchange frequency is further defined as [158]

$$\nu = \nu_0 \exp\left(-G^m/kT\right) \tag{4.2.2}$$

where ν_0 is the frequency of vibration of an atom in a normal lattice position in the jump direction and G^m is the free energy necessary for an atom-defect migration. Briefly, G^m is the energy necessary for an atom and a defect at an adjoining lattice site to overcome the energy barrier, permitting the atom and the defect to interchange positions. (Figure 4.1)
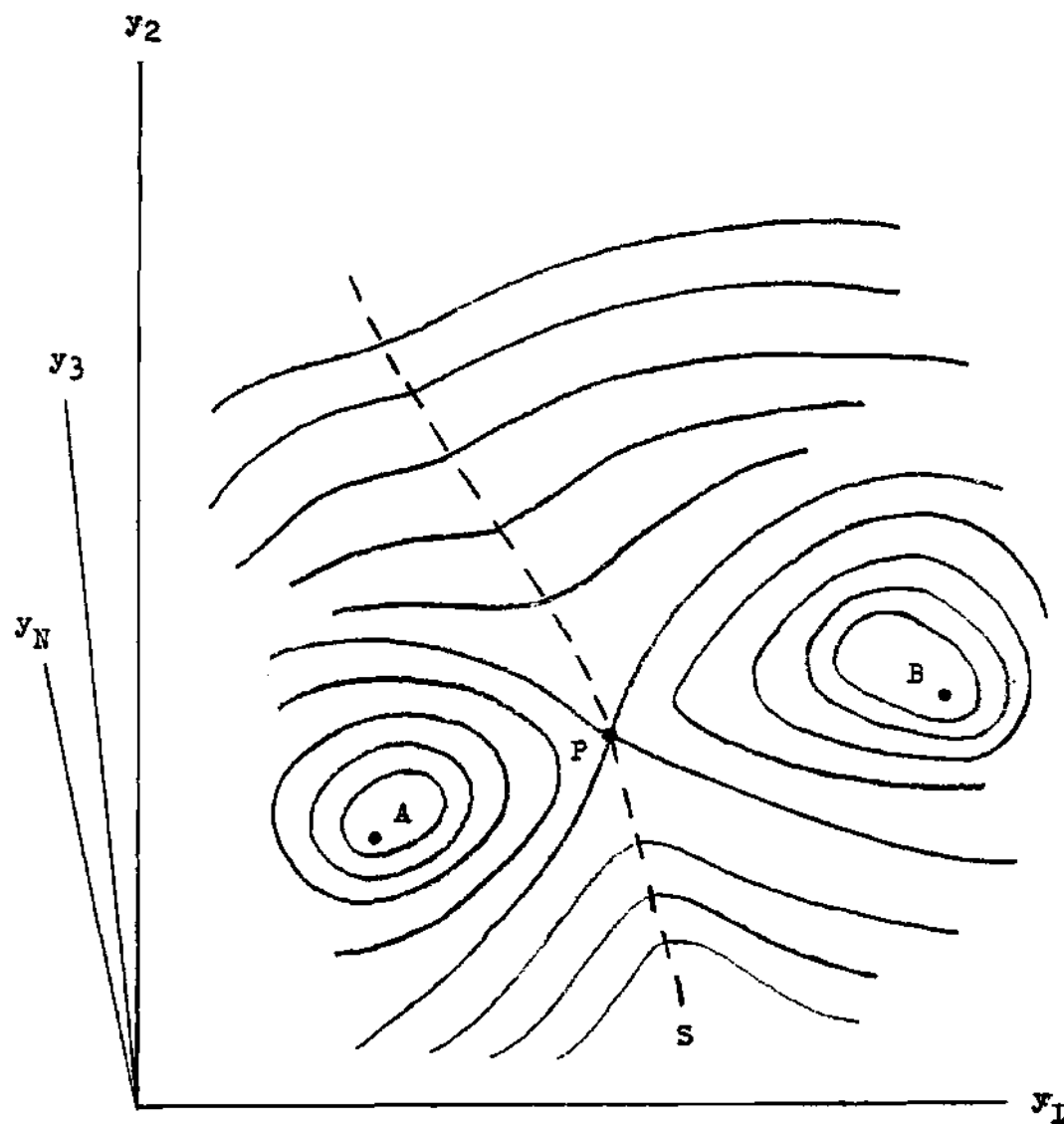
Figure 4.1   Defect Lattice Configuration Space for
N Atoms with 3N Degrees of Freedom.
The Hypersurfaces (solid lines) Correspond
to Constant Potential Energy. The Dotted
Line, S, is the Saddle Surface with a
Minimum at P, the Saddle Point for
Transitions from A to B. Redrawn [158]

Atoms diffusing by means of atom-defect exchanges, in actuality, will undergo correlated (non-random) diffusion. After an atom-defect exchange, the defect remains in the immediate vicinity of the diffusing atom, allowing the possibility of a reverse jump. These reverse exchanges will occur with a greater-than-random probability.[159,160] Modification of the diffusivity coefficient yields

$$d_{kj} = \frac{1}{6} \lambda_k^2 Z_k \nu_{kj} f_j \qquad (4.2.3)$$

where f_j is the correlation factor such that the fraction $(1-f_j)$ represents nonrandom atom-defect (kj) exchanges.

The partial diffusion coefficients are determined by the relations

$$D_k^j = d_{kj} X_j \quad \text{and} \quad D_j^k = d_{kj} X_k \qquad (4.2.4)$$

where $X_\ell = \Omega c_\ell$ $(\ell=j,k)$ is the atomic fraction of defects or atoms, Ω is the atomic (metal or alloy) volume, and c_ℓ is the concentration of defects or atoms. Initially, at time $t=0$, when the alloy assumes the conditions of thermal equilibrium (before the onset of irradiation), the single defect concentration j may be written in the form

$$X_j = \exp\left(-H^f/kT\right)\exp\left(S_j^f/k\right) \qquad (4.2.5)$$

where H_j^f and S_j^f are the defect formation energy and entropy, respectively. The total diffusion coefficients for atom and defect species are simply expressed as

$$D_j = \sum_k D_j^k \qquad (4.2.6a)$$

$$D_k = \sum_j D_k^j \qquad (4.2.6b)$$

4.3 Kinetic Equations

The net flux density of atoms or defects projected across a 1-D marker plane in the absence of sources or sinks is defined by Fick's first law

$$J = -D\nabla c \qquad (4.3.1)$$

Due to conservation of matter, the concentration time

dependence must equal the negative divergence of the flux such that

$$\frac{\partial c}{\partial t} = -\nabla J$$

(4.3.2)

where substitution of Fick's first law into Equation 4.3.2 yields Fick's second law. In the presence of a uniformily distributed sink concentration (dislocations) and as a consequence of irradiation, the (binary alloy) local atom and defect rate equations are

$$\frac{\partial c_A}{\partial t} = -\nabla J_A + P$$

(4.3.3a)

$$\frac{\partial c_i}{\partial t} = -\nabla J_i + K_o - R - L_i$$

(4.3.3b)

$$\frac{\partial c_v}{\partial t} = -\nabla J_v + K_o - R - L_v$$

(4.3.3c)

where atom and deflect fluxes are derived and defined in Appendix C. The recombination, R, and sink, $L_{j=i,v}$, terms are later defined, respectively, in Sections 4.9 and 4.12. The local self-deposition and dpa production rates, P and K_o, respectively, are defined and quantified as a result of TRIM

calculations. In general, the self-deposition rate of each alloy component is defined as

$$P_k = \phi\left(1 - RN_k\right)I_k \qquad (4.3.4)$$

where ϕ is the incident (eroding) particle flux, RN_k is the reflection coefficient of species k from the alloy, and I_k is the deposition depth profile of species k in the alloy. Furthermore, the self-deposition rate profile for a binary alloy is detailed as follows:

(1) P=0, if the projectile is neither component A or B

(2) $P=P_A$, if the projectile species is atom A

(3) $P=-P_B$, if the projectile species is atom B

(4) $P=P_A-P_B$, if a mixed (A,B) incident particle flux is present.

4.4 Vacancies

Under thermal equilibrium conditions, the experimental techniques of differential dilatometry [161,162], quenching [158], and positron annihilation [162-165] have shown that vacancies are the predominant crystal defect in metals as well as in many hcp and bcc metals. Thus, vacancies must be the dominant mechanism for thermally activated diffusion in

pure metals. As a result, the activation energy of self-diffusion, Q_{SD}, can be expressed as

$$Q_{SD} \approx \sum_m \left(\frac{c_{mv}}{c_v} \right) Q_{mv} \qquad (4.4.1)$$

where c_{mv} is the concentration of the mth vacancy type (monovacancy, divacancy, etc.), c_v is the total vacancy concentration, and Q_{mv} is the activation energy of the mth vacancy type. With the exception of "high" temperatures (those approaching the metal melting point), the self-diffusion coefficient, D, may be approximated by the monovacancy mechanism [158,162] yielding a single Arrhenius relation

$$D = D_o \exp \left(-Q_{1v}/kT \right) \qquad (4.4.2)$$

where $Q_{1v} \approx Q_{SD}$ and $c_{1v} \approx c_v$. Evidence of the Arrhenius behaviour is graphically displayed for tracer self-diffusion data in copper (Figure 4.2).[158] The curvature exhibited in the Arrhenius plot normally is interpreted as that attributed to a second diffusion mechanism, namely divacancies.[158,161] However, such deductions neglect any temperature dependences associated with the monovacancy formation energy and entropy. The inclusion of these dependences may explain the curvature of the Arrhenius plots in most metals.[166]
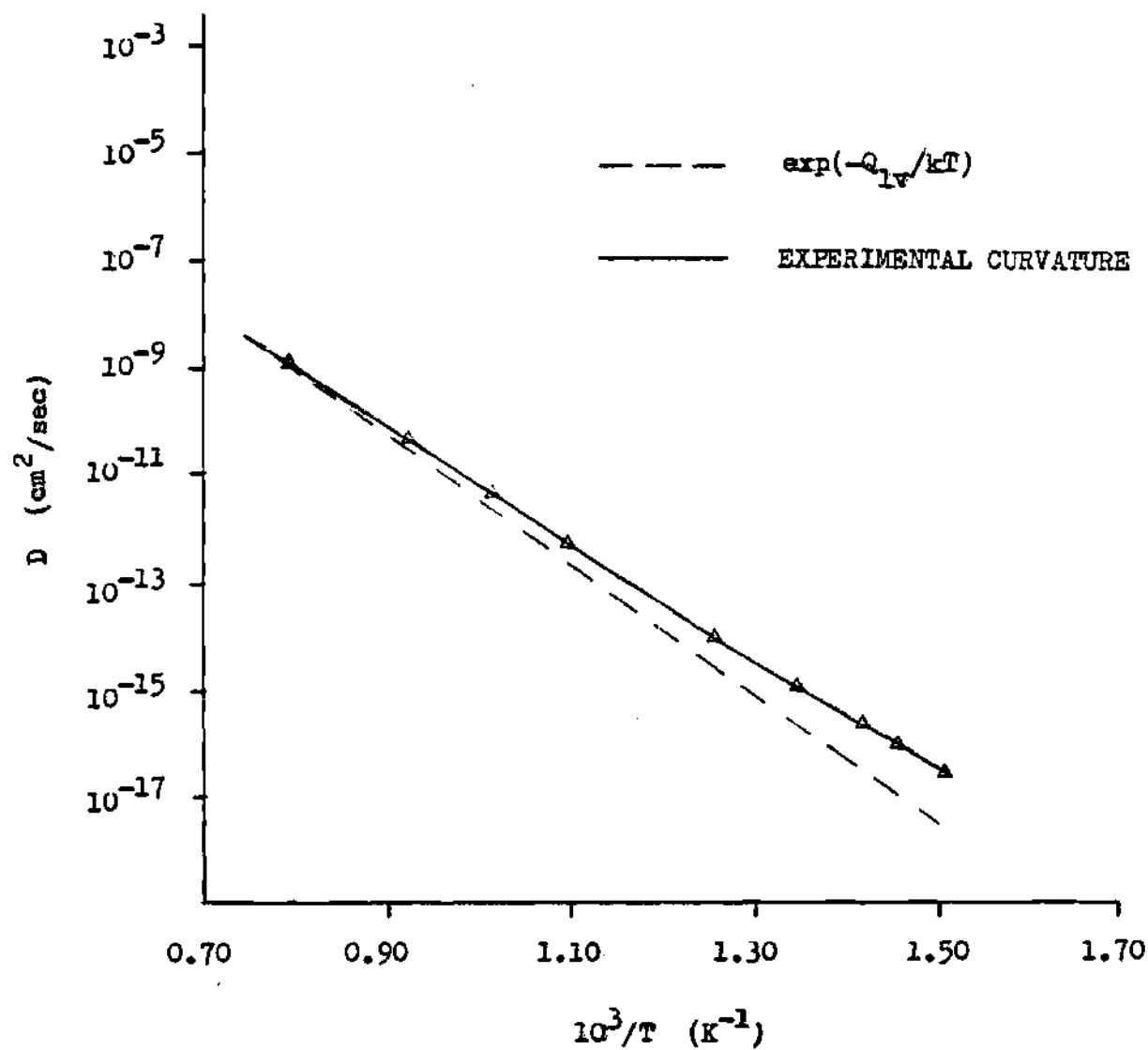
Figure 4.2   Arrhenius Behaviour of Copper
Self-Diffusion

Several universal empirical relationships have been proposed as a means of determining the monovacancy activation energy, Q_{1v}, and its components:

$$Q_{1v} = H_v^f + H_v^m$$
<div align="right">(4.4.3)</div>

where H_v^f and H_m^f are formation and migration energies, respectively. An analysis of fcc metal (experimental) activation and formation energies concludes that [167]

$$H_v^f / Q_v = .55 \pm .03$$
<div align="right">(4.4.4)</div>

if the vacancy formation entropy is equal to 1.5k (the validity of this assumption will be discussed in the following section). From positron annihilation experiments, a linear fit of the vacancy formation energy yields [168]

$$H_v^f = .0012 T_t + .0051$$
<div align="right">(4.4.5)</div>

where T_t is the threshold temperature of observable positron trapping. In bcc, fcc, and hcp metals dominated by vacancy diffusion, the proportionality [169]

$$Q_v \propto E_s / \Omega \qquad \qquad (4.4.6)$$

(where E_s is the sublimation energy and Ω is the atomic volume) is in excellent agreement with experiment. Correlations of vacancies with the fusion (melting) of metals yield definite linear behaviours [170]

$$H_v^f = k_F \, \Delta F \qquad \qquad (4.4.7a)$$

$$H_v^f = k_T T_F \qquad \qquad (4.4.7b)$$

where k_F and k_T are empirical constants of the crystal lattice, ΔF is the heat of fusion, and T_F is the temperature of fusion. Other relationships for determining H_v^f as a function of the Debye temperature [171] and of the cohesive binding energy [172], also, demonstrate equally good experimental compatibility. However, whether the choice of monovacancy energy values is made empirically or directly from experimental data, deviations of $\pm(.05-.10$ eV) remain.

4.5 Vacancy Formation Entropy

The structure of a monovacancy consists of a missing atom on a lattice position with the nearest neighbors relaxing towards the vacant site and the second nearest-neighbors moving away from the vacancy. Relaxation reduces the nearest-neighbor vibrational frequencies relative to the undisturbed lattice, resulting in a positive entropy effect of the form [158,173]

$$\Delta S_v^f = k \sum_i \ln \left(\nu_i / \nu_i' \right)$$

(4.5.1)

where ν_i and ν_i' are the original and final lattice frequencies of the ith atom. Electronic contributions to the entropy are negligible $\sim O(.05k)$.[174] For close-packed atom configurations (as in fcc), the entropy of relaxation is less than that of configurations having a greater free volume (as in bcc).[175] It has been found (theoretically) that the vacancy relaxation is related to the high-temperature thermal expansion coefficient and compressibility of metals (experimental observables).[175] The vacancy formation entropy is shown to be a monotonic function of the vacancy relaxation and approximates a linear empirical relationship within ±2% for all metals of a given lattice type such that [175]

$$\Delta S_v^f = \left\{ q_a + q_b \left(\frac{K}{\alpha V_m}\right)\right\} k \qquad (4.5.2)$$

where K is the metal compressibility, α is the thermal expansion coefficient, V_m is the molar volume, and the constants q_a and q_b are lattice structure dependent. Vacancy formation entropies predicted by equation 4.5.2 are 1.8-2.0k for most fcc metals (ΔS_v^f=1.89k for Cu) and 2.2-2.6k for bcc metals. Other theoretical approximations to S_v^f in Cu have yielded entropy values of 1.47k [173], 2.08k [174], and 1.67k.[176] Experimentally, the vacancy formation entropies are not well known [174,175] since they are inferred from the monovacancy concentration at thermal equilibrium, equation 4.2.1. If the experimental error of the measurable quantity ΔH_v^f is ±.1 eV, then the resultant entropy deviation is ±.7K.

In a self-consistent model analysis [177] of experimental data for fcc and bcc metals, alkali-halides, and rare gas solids, the entropy per vacancy is treated as a temperature dependent quantity (due to anharmonic effects). Entropy values of 1.5k and 1.7k have been found for Cu and Ag, respectively. Furthermore, the temperature dependent entropy has been found to coincide with the nonlinearity (curvature) of Arrhenius plots observed for metals, thus explaining vacancy formation by one mechanism, specifically, via monovacancies.[177] Hence, the additional divacancy and

trivacancy mechanisms commonly used to explain the Arrhenius slope behaviour are ignorable when the proper analysis of vacancy formation energy and entropy is performed.

4.6   Vacancy-Solute Interactions

Substitutional solute atom diffusivites can be enhanced when a vacancy moves into an adjacent neighboring lattice site.   If the binding energy of the vacancy-solute complex is positive,   migration of the solute is enhanced.[178,179] For dilute   alloys, $X_A \leqslant (10^{-2})$,   the   thermal   equilibrium concentration   of   vacancy-solute   pairs, X_{VA},   is   given by [178,179]

$$X_{VA} = Z X_A \exp \left\{ -(G_v^f - B_{VA})/kT \right\}$$ (4.6.1)

where Z is the coordination number and B_{VA} the vacancy-solute binding energy.   The fraction of free vacancies which are not nearest-neighbor sites of the solute atoms is [178,179]

$$X_v = \left(1 - Z X_A \right) \exp \left(-G_v^f/kT \right)$$ (4.6.2)

Thus, the total equilibrium vacancy concentration is

$$X_v^{\ddagger} = \left\{ 1 - Z X_A \left[1 - exp\left(B_{VA}/kT\right)\right]\right\} exp\left(-G_v^f/kT\right) \qquad (4.6.3)$$

where if $B_{VA} \rightarrow 0$, then $X_v^{\ddagger} \rightarrow X_v$ (no vacancy-solute complexes).

Experimentally, a range of binding energies where $.02\pm.02 \leqslant B_{VA} \leqslant .27\pm.10$ eV (dependent upon the specific solute-solvent alloy system) [178] have been determined for vacancy-solute pairs if an attractive interaction exists. If a repulsive interaction between a vacancy and a solute atom occurs, then no measurable value of B_{VA} is found [178], and vacancy-solute complexes are not formed.

Several theoretical and empirical relations have been proposed to quantitatively calculate B_{VA} values.[178] The simplest model suggested is the proportionality of the vacancy-solute binding energy to the heat of solution [178,180]

$$B_{VA} = a_B \, \Delta H_m^A \qquad (4.6.4)$$

where proposed values of a_B are 1/9 or 1/12, both of which provide relatively equal agreement with experiment. Typically, the relationship between equation 4.6.4 and experiment has an associated deviation of $\pm40\%$ which is within the experimental error in most instances. For the

Cu-Li alloy system under study, the heat of solution is negative; hence, vacancy-solute complexes are not formed.

4.7 Interstitials

The self-interstitial concentration, X_i, as a consequence of thermodynamic disorder is expressed as

$$X_i = \exp\left(-H_i^f/kT\right)\exp\left(S_i^f/k\right) \qquad (4.7.1)$$

where H_i^f and S_i^f are the interstitial formation energy and entropy, respectively. Interstitial diffusion, necessarily, is defined in terms of the most probable (stable) geometrical configuration as opposed to the isotropy of monovacancy diffusion. Numerous theoretical calculations and experimental results indicate that the 100-dumbbell in fcc metals and the 110-dumbbell in bcc metals (Figure 4.3 a,b) are the most probable (i.e., have the lowest formation energy and highest stability).[181-183] All other configurations require an additional interstitial formation energy of $\Delta H_i^f \sim (.1-.4)$ eV.[181] Typical values of H_i^f in fcc metals are in the range of 3-4 eV.[181] A theoretical determination of the formation entropy in copper yields the result $S_i^f = .8k$, which also should be applicable to most other fcc metals.[173]
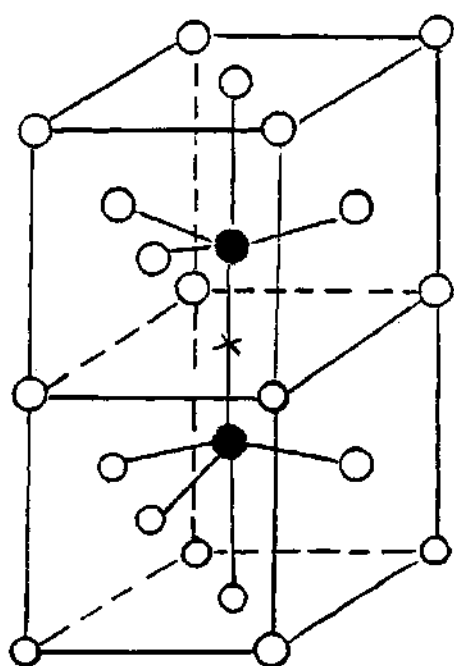
(a) 100-dumbbell in fcc-lattice   (b) 110-dumbbell in bcc-lattice
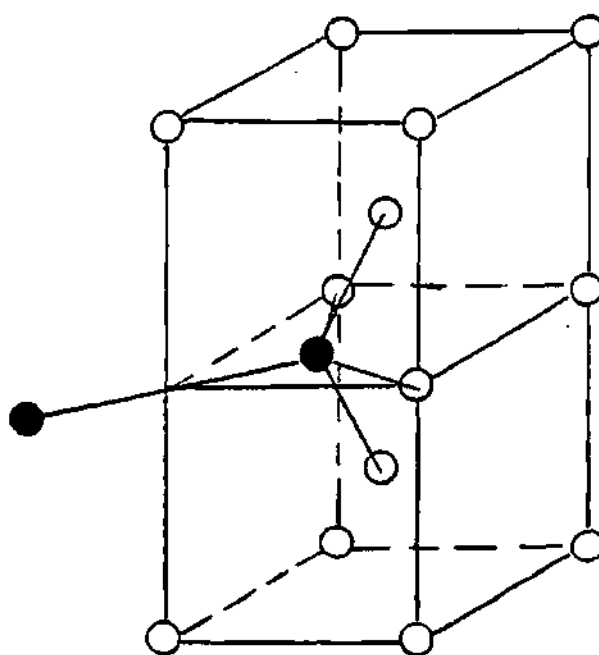
Figure 4.3   Most Probable Interstitial Dumbbell
Configuration for fcc and bcc Metals

The jump frequency of interstitials, $\mathcal{V}_i$, is given by

$$\mathcal{V}_i = \mathcal{V}_i^o \exp\left(-H_i^m/kT\right)\exp\left(S_i^m/k\right)$$

(4.7.2)

where $\mathcal{V}_i^o$ is the attempt frequency and H_i^m and S_i^m are the interstitial migration (activation) energy and entropy, respectively. Due to the strong relaxation associated with interstitials, large rearrangements in the center of the dumbbell require little energy.[181] Thus, the energy contours as a function of interstitial position (in reference to energy hypersurfaces shown in Figure 4.1) are relatively flat resulting in small migration energies on the order of .1 eV.[181,182] Electron-irradiated pure copper indicates a value of $H_i^m = .12 \pm .005$ eV.[184]

The elementary jumps having the lowest energy of migration for the fcc 100-dumbbell and the bcc 110-dumbbell are shown in Figure 4.4 a,b. Interstitial migration in fcc metals occurs via orthogonal jumps into nearest-neighbor positions on the (100) planes common to the dumbbell axis. Thus, the interstitial can jump to any one of 8 positions as it cannot jump in the four directions perpendicular to the dumbbell axis. Computer simulations show that all other configurational changes require an appreciably higher energy: a simple rotation of the 100-dumbbell by 90° about its center needs three to four times the energy of the reorientating orthogonal jump.[181]

(a) 100 jump   (b) 110 jump
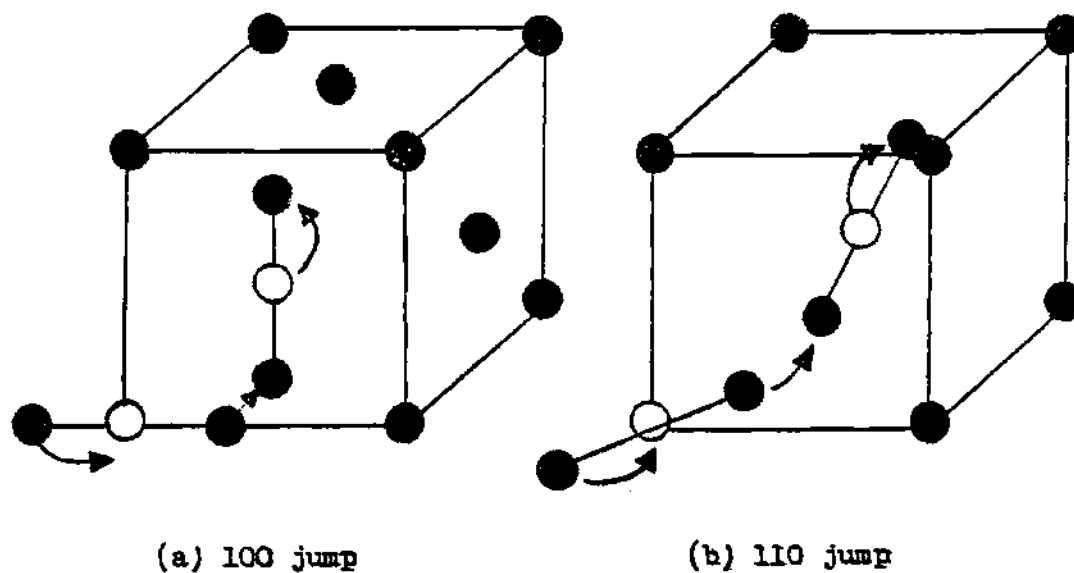
Figure 4.4 Elementary Dumbbell Jumps Requiring
the Lowest Migration Energy for fcc
and bcc Metals

Kinetic analysis of Cu, Al, and Pt diffusion experiments infers migration entropies of $S_i^m/k=1\pm2$ if the attempt frequency is equated to the resonant (vibrational) frequency of the dumbbells.[182] Experimental uncertainties prevent a more accurate determination of S_i^m.

The introduction of solute atoms (alloys) in copper has been shown experimentally not to alter the "identity" of the self-interstitial of the solvent.[185,186] Interstitials trapped (interstitial-solute complexes to be discussed in the following section) at the solutes Ag, Au, Be, Pd, and Sb are found to behave the same as the free interstitials in the pure copper solvent. Hence, the interstitial configurational behaviour of the pure solvent will be considered applicable to Cu-Li alloys.

4.8 Interstitial-Solute Complexes

Attractive interaction of solvent self-interstitials and solute atoms can lead to the formation of interstitial-solute complexes. Solute diffusion in copper via the complex (mixed dumbbell) mechanism has been observed experimentally as "orders" of magnitude greater than thermal diffusion alone in the temperature range 300-700K.[187] As has been shown both theoretically [181] and experimentally [188,189], the coupling of the solute and the solvent self-interstitial is a

function of the relative volume misfit and the solute capture radius, r_c^A. In copper and aluminum alloys, strongly undersized solutes provide deep traps for interstitials, while oversized solutes furnish several shallow traps (if any).[181,187-189] Small ($\pm$) misfits result in weak or no complexes.[187-189] For dilute copper alloys, experimental data show a definite correlation between the solute capture radius and the relative volume dilatation, ΔV, which is depicted in Figure 4.5.[188] The volume dilatation due to the substitutional solute is expressed as

$$\Delta V = \left(\tfrac{3}{a}\right)\left(\tfrac{da}{dc_A}\right)$$

(4.8.1)

where a is the lattice parameter. Thus, for copper alloys, knowledge of ΔV· should be sufficient to determine the importance of mixed dumbbell formation. For example, a Cu-Ni alloy yields a small negative misfit where $\Delta V < 10\%$; hence, little (if any) trapping is predicted in accord with experimental observation.[187]

Where there exists a solute-interstitial attraction (binding energy), the atomic fractions of the solute-and solvent-interstitials indicating the preference of A-interstitial complex rather than B-interstitial complex formation can be represented by [190]
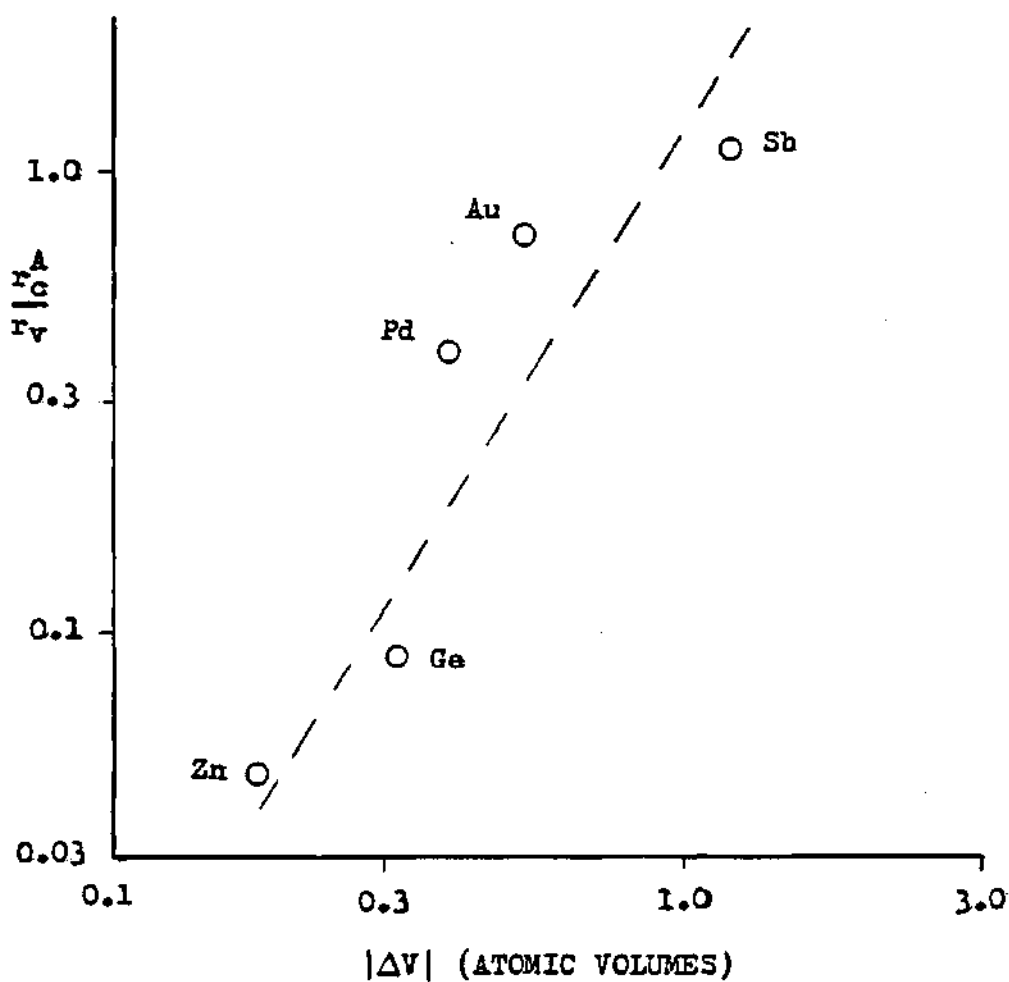
Figure 4.5 Experimental Correlation of the Solute
Capture Radius (Units of Vacancy Capture
Radius) in Copper Alloys as a Function
of Solute Volume Dilatation

$$X_A^i = X_i \left\{ X_A \exp\left(H_{Ai}^b / kT \right) \right\} / X \qquad (4.8.2)$$

$$X_B^i = X_i X_B / X \qquad (4.8.3)$$

Here $X = X_A \exp(H_{Ai}^b / kT) + X_B$, and H_{Ai}^b is the energy gained by converting a B-interstitial into an A-interstitial.

Of further importance is the experimental observation that the solute capture radius, r_c^A, decreases rapidly with increasing temperature, T, and for many solutes, r_c^A varies as T^{-2}, below the temperature of complex decomposition.[188] Thus, depending on the alloy solute, interstitial-solute complexes may exist for fusion-wall operating temperatures. Indeed, the solutes Ag, Ge, Mg, Ti, and Zn in Al and Au, Ge, Ni, Pd, Sb, and Zn in Cu lose their trapping properties above 125 K.[181,189] However, beryllium mixed dumbbells are stable in copper to temperatures ~700 K.[187]

4.9   Recombination of Interstitials and Vacancies

The loss of radiation-induced interstitials and vacancies by spontaneous recombination is given by the rate equation

$$R = \frac{dX_i}{dt} = \frac{dX_v}{dt} = -Z_{iv}(\nu_i + \nu_v)X_iX_v \qquad (4.9.1)$$

where Z_{iv} is the recombination cross-section. Equivalency of the interstitial and vacancy recombination rates assumes that defect clusters produced in collision cascades must either decompose thermally or annihilate by an opposite type of defect. Because the vacancy/interstitial interaction energy at long ranges beyond the nearest neighbor distance is small, recombination is considered to be a "nearest-neighbor" phenomenon. [191]

The value of Z_{iv} prescribed by the JL model corresponds to counting the orthogonal jumps made by the 100-dumbbell interstitial within a third nearest-neighbor site distance; i.e., $Z_{iv} = 30$ for fcc metals. [149,192] Such an approach counts jumps made into new sites as well as those covered in previous jumps. Monte Carlo atomistic simulations have shown substantially smaller values of Z_{iv} for small concentrations ($<10^{-3}$) of the relatively immobile defect. [193,194] In actuality, Z_{iv} should represent the number of new sites covered per jump by the migrating defect, not sites previously visited. In the atomistic approach, if one of the two defects is immobile, fcc Z_{iv} values of 4.3 [194] and 5.3 [193] are obtained for third and fourth nearest-neighbor recombination distances as the immobile

defect concentration asymptotically approaches zero. Increasing the immobile defect concentration, $>O(10^{-2})$, results in increased values of Z_{iv}.[193,195]

In the continuum approach, one of the two defects is treated as a permanent fixed sink surrounded by a diffusion profile formed by the mobile defect flow to the sink. For fcc metals where fourth nearest-neighbor spontaneous recombination is possible, $Z_{iv}=5.21$ in the limit of low sink concentrations.[193] Thus, the continuum model approach agrees with the atomistic approach when one defect is immobile relative to the other. The concentration dependent continuum model best approximating the atomistic simulations is given by the mean field approximation (MFA) of Brailsford [195]

$$Z_{iv} = Z_{iv}^{\circ}\left(1 + f_{\alpha}\sqrt{Z_{iv}^{\circ}\, X_s}\right) \qquad (4.9.2)$$

where Z_{iv}° is the limit of low sink concentrations, X_s is the sink concentration, and f_{α} is a lattice structure constant ($f_{\alpha}=4.31$ for fcc metals).

Further, it has been found that regardless of which defect is immobile ($\nu_i >> \nu_v$ and $\nu_i << \nu_v$) or whether both are equally mobile ($\nu_i \approx \nu_v$), Z_{iv} varies by less than four percent for low defect concentrations.[193] For the fusion wall conditions of the Cu-Li alloy under investigation, defect

concentrations are such that the use of the MFA continuum model is justified in determining the recombination cross-section.

4.10 Surface Segregation

Surface segregation (or adsorption) is the redistribution of the alloy species near a two-dimensional discontinuity in a bulk condensed-phase system such as a metal-vacuum surface boundary or a grain boundary.[196] The first treatment of this phenomenon for a binary solution is given by the Gibbs adsorption isotherm

$$\Gamma_A^s = - d\gamma / d\mu_A \qquad (4.10.1)$$

where Γ_A^s is the solute excess at the surface, γ is the surface tension, and μ_A is the solute chemical potential. For a dilute binary solution, it can be shown that the surface will be enriched with the solute that lowers surface tension and will be depleted with the solute that raises surface tension.[196] Because the surface tension as a function of chemical potential for solid solutions is not well known, an approximation for solute segregation is necessary:

$$\frac{X_A^s}{X_B^s} = \frac{X_A^s}{X_B^b} \exp\left(-\Delta F_s / kT\right)$$

(4.10.2)

where the superscripts s and b refer to the surface and bulk atomic concentrations, respectively, and ΔF_s is the free energy of solute segregation.[196-199] The free energy is the driving force of segregation and is equal to the exchange energy of a solute atom in the bulk with that of a solvent atom in the surface. Minimization of the surface free energy will result in the surface enrichment of the atom species having the lowest bond energy and the largest surface area.[196,197] The free energy of segregation is expressed in terms of a negative Gibbs free energy as

$$\Delta F_s = -\Delta H_s + T\Delta S_s$$

(4.10.3)

the sum of the heat of segregation, ΔH_s, and the entropy of segregation, ΔS_s, which acts to lower the molar concentration of the segregant in the surface layer. The heat of segregation is comprised of three major contributions [196,197,199]: the relative difference between the solvent and solute surface free energies (surface tensions), the heat of mixing (regular solution), and the strain energy associated with the strain field about a solute atom due to

size differences in the solute/solvent atom radii (if any). The entropy of segregation is brought about from the temperature dependences of the surface energies and strain energies and the excess entropy of mixing.

Miedema's surface segregation model has been selected as the method of choice because of its success in predicting experimental results and its ease in application (knowledge of the lattice structure is unnecessary). Briefly, the model prescription is as follows [197]:

$$\Delta H_S = f_b \left(g \left\{ \gamma_A^{S,o} - \gamma_B^{S,o} \right\} V_A^{2/3} - f_r \Delta H_m^A \right) - .42 \, \overline{KV_m} \, \delta^2 \quad (4.10.4)$$

where f_b is the fraction of near-neighbor bonds broken for a surface atom representing the average crystal surface, g is a (units) conversion constant, $\gamma_A^{S,o}$ and $\gamma_B^{S,o}$ are the surface free energies of components A and B at zero Kelvin, $V_A^{2/3}$ is the molar surface area of the solute metal, and ΔH_m^A is the partial molar heat of solution of metal A in metal B. The constant f_r is the relaxation coefficient of the electron density distribution in the surface layer that reflects the surface area reduction of surface layer atoms in contact with the vacuum. The size mismatch energy term $(\overline{KV_m} \delta^2)$ which is comprised of the average product of the bulk modulus, K, and molar volume, V_m, and an atomic radii difference term, δ. The entropy term is comprised solely of the surface free energy temperature dependence

$$\Delta S_s = .8k \left(1 - \{V_A/V_B\}^{2/3}\right)$$

(4.10.5)

where it has been assumed that the excess entropies of alloying can be neglected for dilute alloys.[197]

The kinetic formulation of the segregant atoms is accomplished through the coupling of the layer to layer solute fluxes. Assuming no concentration gradients within the alloy at time, t=0, the free energy of the alloy as a function of atomic layer depth is depicted in Figure 4.6. Solute fluxes, $j_{u,u\pm1}$, are prescribed by [198]

$$j_{12} = X_A^1 \, w_{12} \nu_1 \exp\left\{-(\Delta G_D - \Delta F_s)/kT\right\}/\chi^2$$

(4.10.6a)

$$j_{21} = X_A^2 \, w_{21} \nu_2 \exp\left\{-\Delta G_D/kT\right\}/\chi^2$$

(4.10.6b)

$$j_{23} = X_A^2 \, w_{23} \nu_2 \exp\left\{-\Delta G_D/kT\right\}/\chi^2$$

(4.10.6c)

$$j_{32} = X_A^3 \, w_{32} \nu_3 \exp\left\{-\Delta G_D/kT\right\}/\chi^2$$

(4.10.6d)
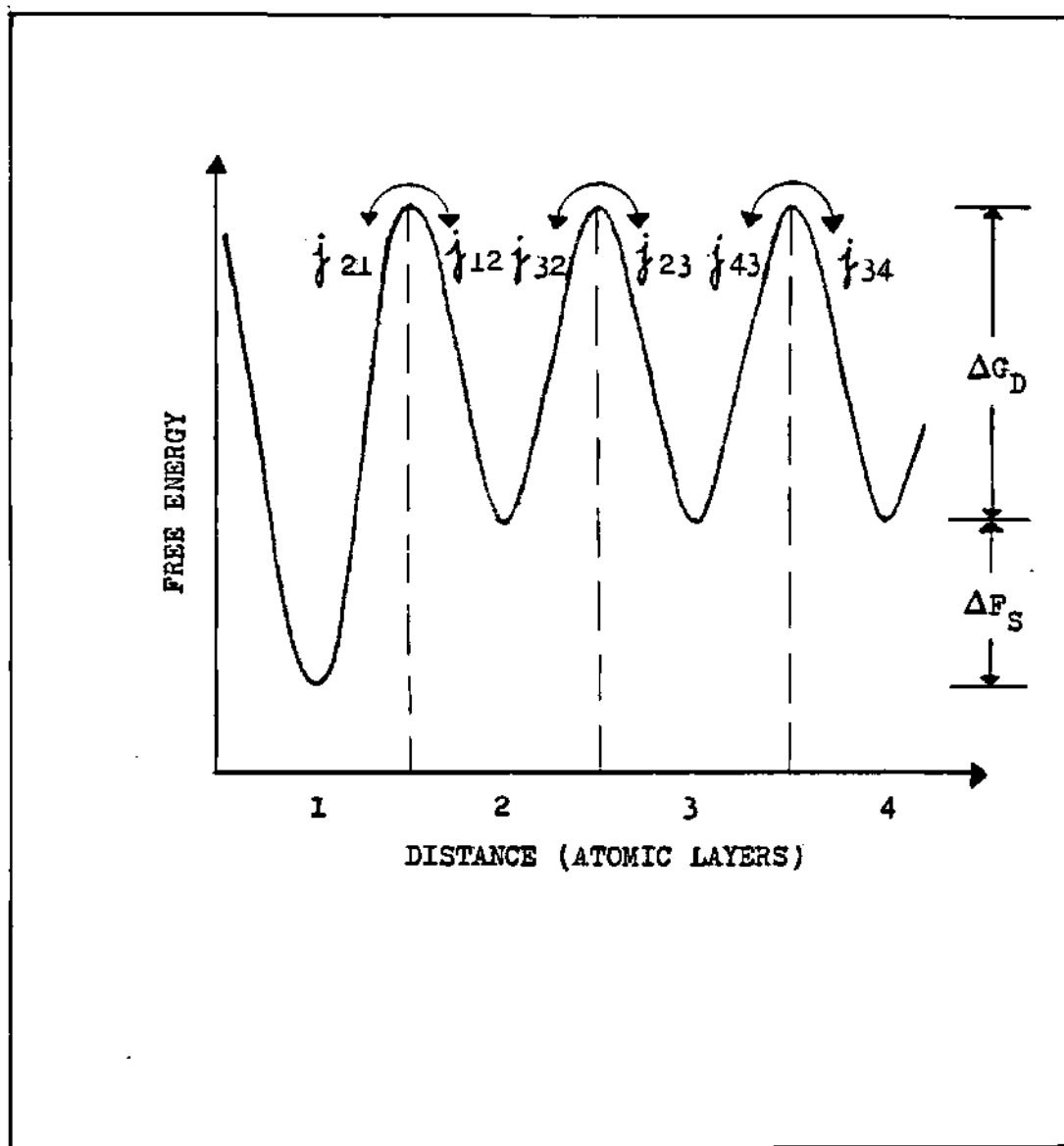
Figure 4.6   Segregant Atom Free Energy Dependence upon
             Surface Depth for a Homogeneous Alloy

where $\mathcal{W}_{u,u\pm1}$ is the jump probability factor of the solute atoms, $\mathcal{V}_u$ the solute atom oscillation frequency in layer u, λ the atomic jump distance, and ΔG_D the free energy of bulk diffusion. The time dependence of the first two atomic layer concentrations, taking into account only diffusion and segregation, is given by

$$\frac{dX^1_A}{dt} = \left(\dot{j}_{21} - \dot{j}_{12} \right) \lambda^2 \qquad (4.10.7a)$$

$$\frac{dX^2_A}{dt} = \left(\dot{j}_{12} + \dot{j}_{32} - \dot{j}_{21} - \dot{j}_{23} \right) \lambda^2 \qquad (4.10.7b)$$

The solute fluxes, as presented for an ideal homogeneous solution at time t=0, can be easily modified for an arbitrary initial concentration profile by redefining G_D to reflect a concentration dependence (if any) or by adding other applicable terms (e.g., radiation-induced segregation).

4.11 Preferential Sputtering

Sputtering (erosion) of the alloy surface region caused by energetic ion bombardment results in a loss of component (A and B) atoms. Unless the alloy elements have relatively equal masses, atomic numbers, and sublimation energies,

preferential sputtering occurs, i.e. unequal erosion loss rates due to different sputtering coefficients. According to the JL model, the sputtered surface recession rate can be calculated by [151]

$$\frac{d\delta}{dt} = \phi\Omega\left(Y^A X_A^S + Y^B X_B^S\right)$$

(4.11.1)

where δ is the thickness of the surface layer removed by sputtering, ϕ is the incident ion flux, Ω is the average atomic volume, and Y^A and Y^B are the sputtering coefficients of the A and B coefficients, respectively. Equation 4.11.1 is based upon the inherent assumptions that the components are of relatively equal size, that the sputtering coefficients are those of the pure elements and not dependent on the alloy composition, and that the sputtering is exclusively a surface layer phenomenon. Relaxing the equal size condition, the erosion rate takes the form

$$\frac{d\delta}{dt} = \phi\left(Y^A X_A^S V_A + Y^B X_B^S V_B\right)$$

(4.11.2)

where V_A and V_B are the component (atomic) alloy volumes.

TRIM results of 1 keV Ar+ on targets of pure copper, of a monolayer of lithium adsorbed on copper, and of a homogeneous Cu-2.6%Li solid solution (Figure 4.7 a,b,c) show that sputtering is a multilayer phenomenon. The fractional
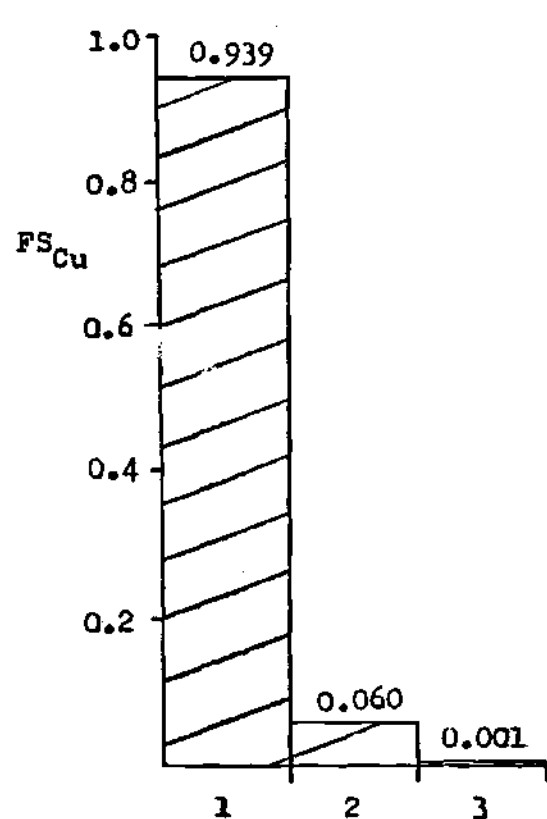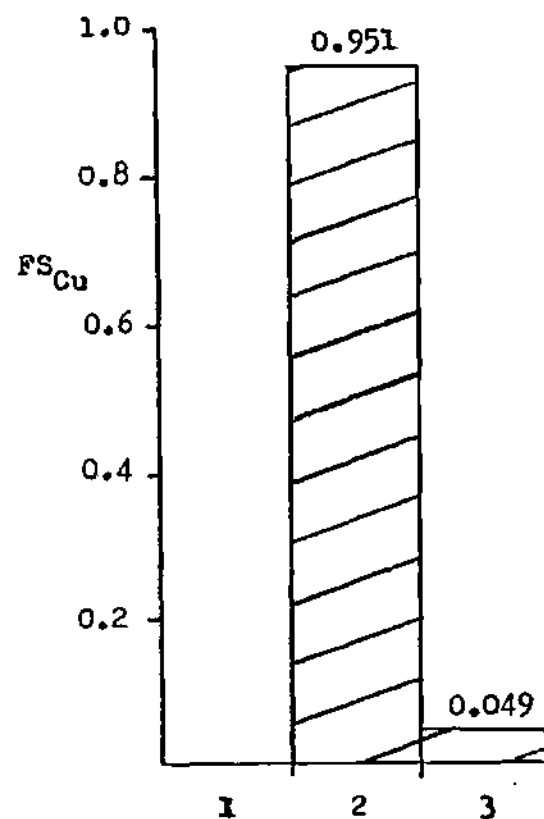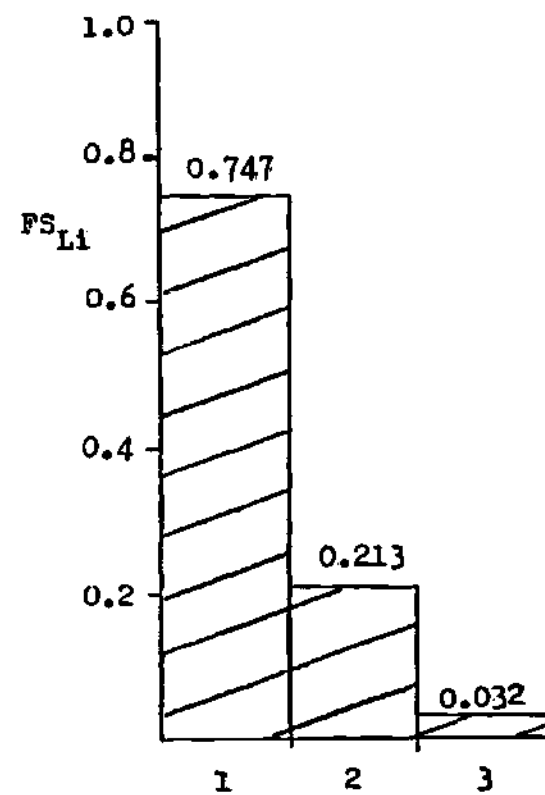
Figure 4.7   Fractional Sputtering Coefficient as a Function of the Atomic
Layer of Origin for (a) Elemental Cu (b) A Monolayer of Li on
Elemental Cu (c) Cu-2.6%Li

sputtering coefficient, FS, denotes the probability that a sputtered species atom originates from layer u. While the fractional sputtering coefficient as a function of the atomic layer of origin for pure copper approximates single layer sputtering, clearly for the adsorbed lithium and for the alloy cases, FS is layer dependent. Likewise, the sputtering coefficients are composition dependent such that the modified erosion rate is

$$\frac{d\delta}{dt} = \sum_u \frac{d\delta_u}{dt}$$

(4.11.3)

where u is the layer index and

$$\frac{d\delta_u}{dt} = \phi\left(FS_{A,u} Y^A V_A + FS_{B,u} Y^B V_B\right)$$

(4.11.4)

The sputtering coefficients are determined from TRIM calculations as a function of the u=1,2 atomic layers; i.e., $Y^A = Y^A(X_A^1, X_A^2)$ and $Y^B = Y^B(X_B^1, X_B^2)$.

4.12 Sinks

The annealing process of defects randomly diffusing to inexhaustible fixed sinks varies according to the time dependent relation [200]

$$L_j = \frac{\partial c_j}{\partial t} = -\beta c_j \quad ; \quad j = i, v \tag{4.12.1}$$

where β is a rate constant independent of c_j and is proportional to the defect diffusion coefficient, D_j. Thus,

$$\beta = \alpha D_j \tag{4.12.2}$$

such that the proportionality factor, α, is defined as a geometrical/boundary condition dependent constant. If the crystal contains no sinks other than the external surface, then the coefficient α is expressed as [200]

$$\alpha = \pi^2 \sum_n (SL_n)^{-2} \tag{4.12.3}$$

where SL_n is the nth dimension scale length. The scale length(s) in a finite system is(are) defined in terms of the smallest dimension(s). For a semi-infinite solid, where $SL_n \rightarrow \infty$ (for all n) and $\alpha \rightarrow 0$, the surface defect concentrations become time independent (boundary conditions)

$$\lim_{SL_n \rightarrow \infty} \frac{\partial c_j^s}{\partial t} = 0 \tag{4.12.4}$$

where the alloy surface is a perfect sink for defects.

The value of α for internally distributed sinks (dislocations, jogs, microvoids, etc.) is determined by either assuming spherical or cylindrical sink geometry. By assuming a random distribution of spherical sinks [195,200],

$$\alpha = 4 \pi r_0 c_\rho \qquad (4.12.5)$$

where r_0 is the sink radius and c_ρ is the sink concentration. The above prescription is analogous to the MFA model previously described for interstitial-vacancy recombination at low "sink" concentrations.[195]

If instead the sinks are thought of as a random distribution of edge dislocations, cylindrical geometry is necessary. Letting ρ equal the sink areal density and r_0 equal the sink radius about the dislocation line, then α is approximated as [200]

$$\alpha = 2\pi\rho \bigg/ \ln\left\{\left(\pi\rho r_0^2\right)^{-\frac{1}{2}}\right\} \qquad (4.12.6)$$

If it is assumed that r_0 is equivalent to two atomic diameters, equation 4.12.6 simplifies to

$$\alpha \cong \rho \qquad (4.12.7)$$

over a wide range of ρ magnitudes.[200] Because dislocations

tend to be the predominant sink for defects in the bulk material, the annealing process of sinks equates to

$$\frac{\partial c_j}{\partial t} = -\rho D_j c_j \qquad (4.12.8)$$

However, a necessary correction must take into account the thermal equilibrium defect concentration which is present simultaneously along with the sink density, ρ . Such a modification results in [201]

$$L_j = -\rho D_j \left(c_j^{eq} - c_j \right) \qquad (4.12.9)$$

where c_j^{eq} is the thermal equilibrium defect concentration.

4.13 Summarization of Surface Kinetics Development

An overview providing insight into and clarification of the relevant atom-defect mechanisms for the near-surface region of irradiated alloys within the Johnson-Lam formalism has been presented in conjunction with an "importance" analysis of the atom-defect mechanisms upon the Cu-Li alloy system under current investigation. Furthermore, generalizations, extensions, substitutions of several defect phenomena have been prescribed and incorporated within a modified JL formalism.

Specifically, contributions to the JL kinetic alloy prescription include the following concepts.

(1) An alternative and more accurate model for the recombination of interstials and vacancies based upon atomistic and continuum calculations has been substituted into the JL mechanics. Recombination is approximated by the mean field approximation concept and is a function of the defect ("sink") concentration and lattice configuration.

(2) An inclusion of a surface segregation energy model is provided based upon the empirical prescription of Miedema. The Meidema model has been substantiated experimentally for a large number of binary alloys.

(3) Preferential sputtering has been generalized to be functionally dependent upon the sputtered layer of origin and the surface concentration of the alloying elements. TRIM calculations have shown that for alloy systems with a large mass disparity, sputtering becomes nonlinear; i.e., sputtering of an alloy cannot be approximated as the concentration weighted average of the elemental sputtering yields.

(4) Self-deposition source terms have been incorporated into the kinetic (solute) equations. One means of providing the self-deposition profile may be accomplished by TRIM calculations.

(5) BCC generalizations to atom-defect diffusivity and vacancy-interstitial recombination have been incorporated

within the JL formalism; however, these generalizations alone are insufficient to allow the proper modeling of bcc alloy systems.

The relative importance of the major atom-defect mechanisms for the Cu-Li alloy is summarized.

(1) For a copper solvent based upon entropy arguments, vacancy diffusion is representative of monovacancies. (Divacancy and trivacancy mechanisms are ignorable.)

(2) No vacancy-solute complexes will be formed in the Cu-Li alloy.

(3) The interstitial configuration of solute lithium in a copper solvent will be identical to the copper self-interstitial configuration.

(4) Interstitial-solute complexes are unlikely in the Cu-Li alloy.

Thus, atom-defect migration in Cu-Li is constituted in terms of simple vacancy and interstitial migration, Gibbsian segregation, sinks (if any), and athermal mechanisms (sputtering, damage, and self-deposition).

4.14 Preliminary Application of the Kinetics Model

Inherent within the JL kinetic formalism is the premise that preferential sputtering determines the surface concentrations of the alloy constituents at steady state. In

other words, compositional changes in an alloy will reflect the preferential loss of the component with the higher sputtering yield or, correspondingly, the component with the weaker chemical bonds and/or with the smaller mass.[202-205] Upon the equilibration of the compositional depth profile for an alloy under particle bombardment, the alloy component ratios within the sputtered flux approximate those of the bulk alloy. Coupling this fact to the knowledge that sputtering is a near-surface phenomenon provides the means of describing the total sputter probabilities in terms of the surface and bulk concentrations of the alloy constituents. The ratio of the total sputter probabilities for a binary alloy is given by [202,204]

$$\frac{Y^A}{Y^B} \frac{\langle c_A^s \rangle}{\langle c_B^s \rangle} = \frac{c_A^b}{c_B^b} \tag{4.13.1}$$

where the sputter probabilities and the surface concentrations have been averaged over the depth of origin of the sputtered atoms. Futhermore, the averaged surface concentrations represent those of steady state as determined by preferential sputtering.

The thickness of the surface layer has been shown theoretically [206], experimentally [147], and via current TRIM calculations to be a first and second layer atom effect. In fact for transition metals, TRIM calculations indicate

that 85-95% of all sputtered atoms originate from the first atomic layer for heavy-ion sputtering, in agreement with experiment.[147] For light-ion sputtering calculations, TRIM results show that 90-98% of all sputtering originates from the first atomic layer. Hence, as a first approximation, the surface layer over which sputtering and surface concentrations are defined can be equated to the first atomic layer (except as noted in Section 4.11).

Rather than conceptually defining the surface layer in terms of the sputtering layer of origin, Ho et al. [204,205] defines the surface layer as an "altered" layer. The altered layer is that depth where the composition is significantly altered by sputtering and is comparable to the escape distance of low energy Auger electrons. Typically, low energy Auger escape distances for most metals are on the order of 3 to 4 Angstroms, i.e., the equivalent of one to two atomic layers.

If the JL model (on a preliminary basis) is applied correctly to the Cu-Li alloy under investigation, then regardless of the initial conditions and the ensuing transients, the equilibrium concentrations must reflect those of preferential sputtering. Indeed, as shown in Figure 4.8, a common equilibrium convergence (as determined by preferential sputtering) has been obtained for two different sets of initial conditions: a homogeneous Cu-2.6%Li solution and a Cu-2.6%Li solution with a 99.98% Li overlayer as
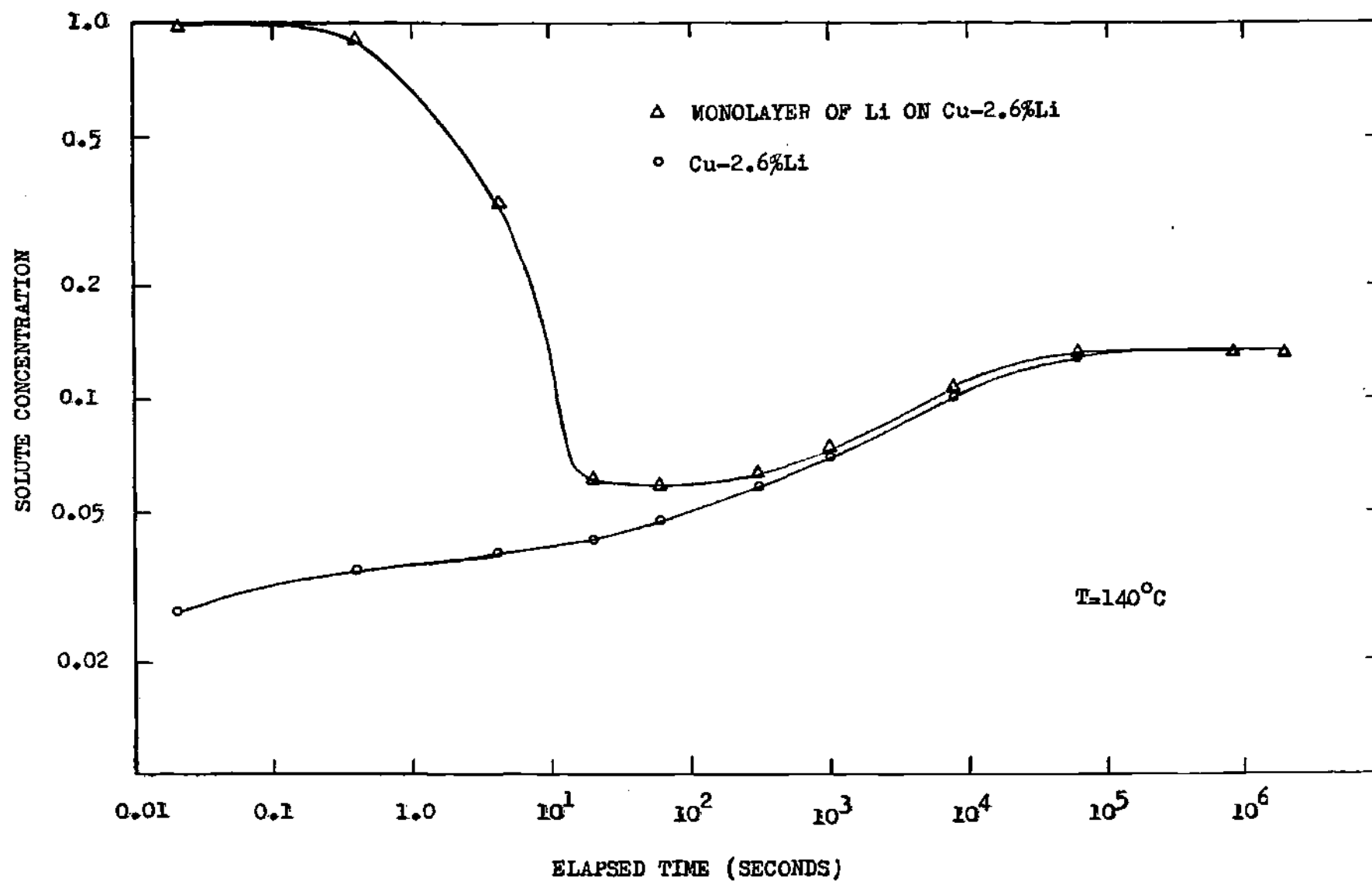
Figure 4.8 Kinetic Time Dependence of the First Atomic Layer Li Concentration
for a Homogeneous Cu-2.6%Li Solid Solution and a Li Overlayer on
Cu-2.6%Li under 3 keV Ar+ (Normal Incidence) Bombardment

predicted by the Miedema segregation model at 140 °C. A common convergence of the entire Li composition profile as a function· of depth has been obtained (but not shown) for both sets of initial conditions. The transient first-layer concentration of lithium depicted in Figure 4.8 is based upon the assumption that sputtering is an elemental yield and a first atomic layer of origin phenomenon. When Equation 4.13.1 is applied enforcing the condition that the surface layer is equal to one atomic layer, the predicted lithium surface concentration, applying the JL model to the Cu-2.6%Li system, is $X_A^I = 13.5 \pm .2\%$.

Sputtering and fractional sputtering (layer of origin) coefficients calculated using TRIM have shown .to be dependent upon the alloy species as well as the alloy species concentration. When there exists a significant mass disparity between the binary alloy components (e.g., Cu-Li or W-Be), preferential sputtering concentrations at steady state cannot be predicted by employing elemental sputtering yields. Indeed, Ho et al. [207] have observed the mass disparity effect on the preferential sputtering concentrations as predicted by Equation 4.13.1 when using elemental yields for the alloys of Al-Pd and Si-Pd. Experimentally, the alloy sputtering ratios of $Y_{Al}/Y_{Pd} = .5$ and $Y_{Si}/Y_{Pd} = .25$ are observed in comparison to the elemental sputtering ratios of $Y_{Al}/Y_{Pd} = 3.0$ and $Y_{Si}/Y_{Pd} = 3.9$. [207] Lighter components introduce a "mass effect" sputtering phenomenon whereby the

lighter component aquires a larger fraction of the energy dissipated by the slowing down process of the incident (target) flux.

For substitutional lithium at 2.6 atomic percent in copper, the effective component (Li) sputtering yield increases four-fold (a result to be presented in Chapter 5). Employing the effective sputtering coefficient of lithium in Cu-2.6%Li and the elemental yield for copper plus assuming single layer sputtering for the same irradiation conditions (as in Figure 4.8), the predicted lithium surface concentration is 3.65%. Thus, the "mass effect" of Li sputtering for Cu-Li alloys is quite significant; however, to accurately predict the surface layer (Li) concentration, the yields must incorporate kinetic (transient) concentration effects as well as the extension to bi-layer sputtering. As shown previously, more than 90% of sputtered copper atoms originate from the first atomic layer, while for elemental lithium (not shown) only 50% of the sputtered atoms originate from the first atomic layer. Application of a dynamic Li sputtering yield in the JL model produces a surface lithium concentration of 4.0±.1%.

As a further validation that the JL model is being applied correctly, the total fluence (dose) necessary to achieve steady state for a given set of temperature and damage profile conditions must be independent of the ion flux magnitude.[151] Shown in Figure 4.9 is the Li surface
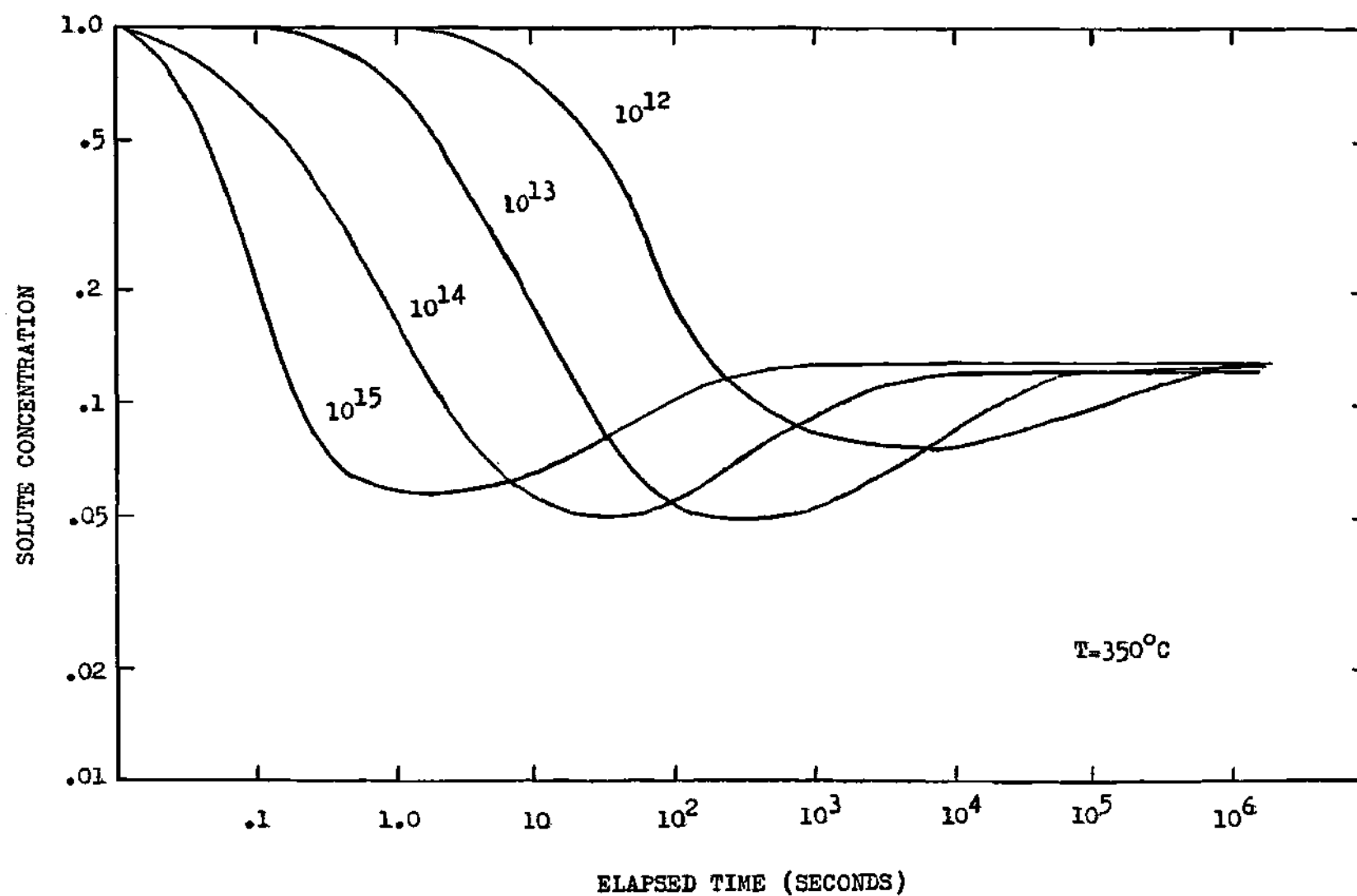
Figure 4.9   Kinetic Time Dependence of the First Atomic Layer Li Concentration
as a Function of 3 keV Ar+ Flux (Normal Incidence)

concentration as a function of elapsed time for varying (3 keV Ar+) flux magnitudes. The same steady state is obtained for all fluxes, except that the time required to attain steady state conditions decreases with increasing ion flux.

Experimental ion-flux data of the transient Li concentration [208] verify the general calulated trends observed in Figure 4.9. A higher flux magnitude initially depletes the first layer Li concentration more rapidly than a lower flux magnitude [208], and at a later time a "crossover" is observed where the higher flux magnitude exhibits a greater first layer Li concentration than the lower flux magnitude. After a sufficiently long period of time, the first layer Li concentration equilibrates asymptotically to the same limit regardless of the flux conditions.[209]

In the application of any kinetics formalism to a specified target geometry, the dimensions must be chosen sufficiently large to extend beyond the maximum thickness of the compositionally altered layer.[202] Shown in Figure 4.10 is the comparitive effect of choosing two different 1-D target thicknesses, r_f, on the steady state compositional profile. If r_f is too small, the solute source (Li) is insufficient at the boundary $x=r_f$ to sustain the solute diffusion to the surface. Moreover, if the target thickness were substantially smaller, no subsurface Li enrichment would be observed; rather, a severe depletion of lithium would result.
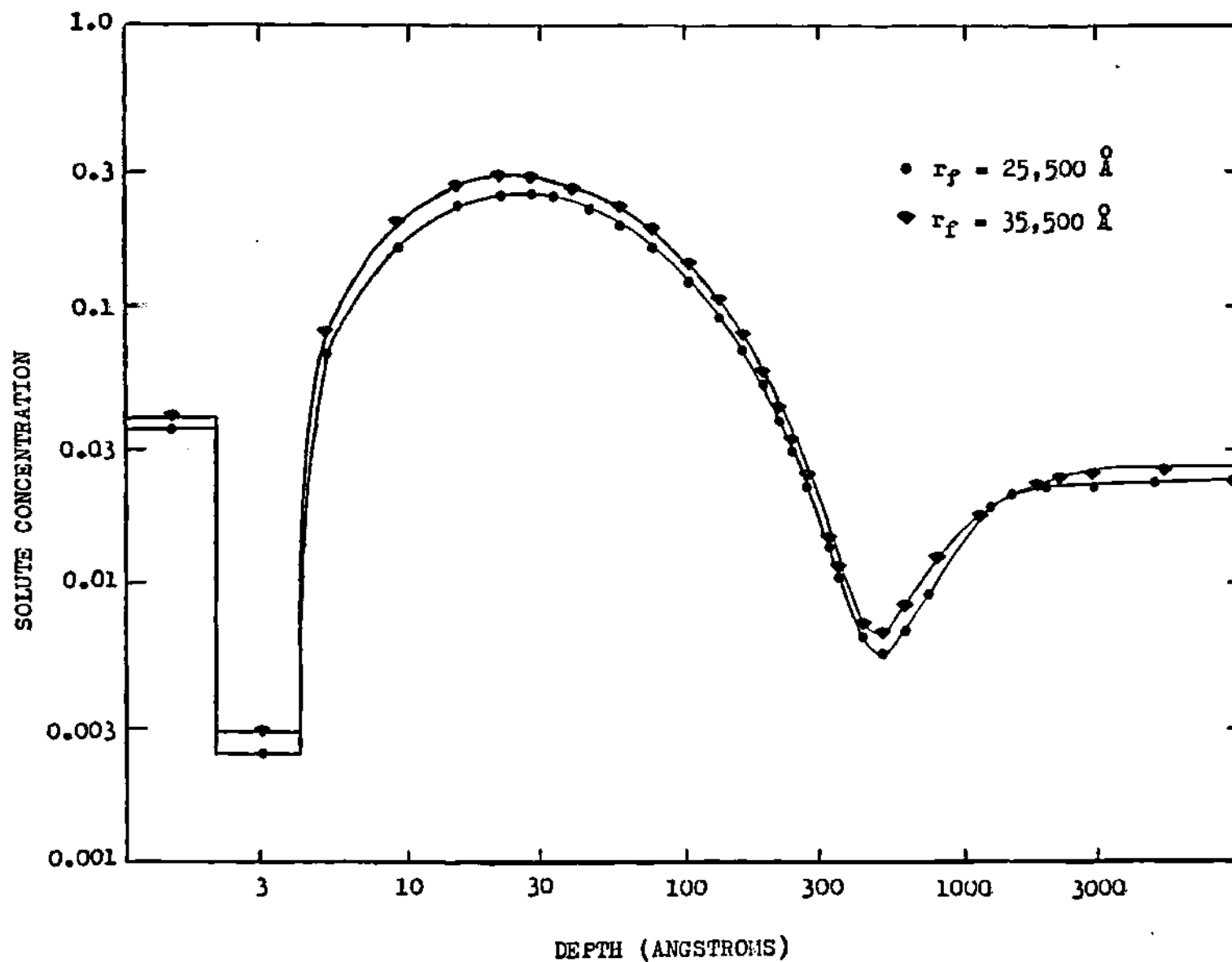
Figure 4.10 Steady State Solute (Li) Concentration Profile as a Function of Target (Cu-2.6% Li Bulk Alloy) Thickness under 3 keV Ar+ Bombardment (Normal Incidence) Material Temperature @ 140°C

The target thickness is not a fixed quantity since r is dependent upon the target temperature and the transient diffusion processes. From thermal diffusion considerations alone, the average depth of diffusion is given by

$$\overline{x} = \left(2Dt \right)^{1/2}$$

(4.13.2)

Here, D is the diffusion coefficient of the form $D \propto \exp(-\Delta G_{D}/kT)$, and t is the time required for the diffusing component to penetrate $\overline{x}$. For a surface undergoing significant sputter erosion, the altered layer thickness can be expressed as [202]

$$d = D/v$$

(4.13.3)

where v is the recession velocity of the alloy surface. These relationships (thermal and erosion) provide a means for determining r_f as a function of temperature. However, it has been observed that the transient altered layer during the time between t=0 and steady state may be much larger than the steady state altered layer. Thus, the choice of D must be made by coupling simple temperature arguments to an understanding of the transient thermal/radiation diffusion processes.

CHAPTER V

Model Application to the Alloy Systems

5.1 Introduction

Model applications to the Cu-Li as well as the V-Al and the W-Be alloy systems are based upon the expected fusion reactor operating conditions of a plasma-edge density, $n_e \gtrsim 0(10^{18} \, m^{-3})$, and a plasma-edge temperature, $T_e \lesssim 0(10^2 \, eV)$. These conditions are representive of a plasma-edge Debye length that is smaller than the plasma-edge ion gyroradii. As a limiting condition, based upon the impact angle results from the sheath potential modeling (Chapter 2), light-ions are assumed to impact at 60 degrees and heavy-ions impact at an angle of 20 to 30 degrees. Because the sputtering yield for impact angles less than 45 degrees varies approximately as $(\cos\theta)^{-m}$ where $1 < m < 5/3$ [210], the sputtering yield for heavy-ions at 25 degrees will exceed that of normal incidence by roughly 20%, which is well within experimental error. Hence, heavy-ion sputtering can be assumed a result of normal incidence impact.

The V-Al and the W-Be alloys have been investigated only in regard to erosion analysis since the JL model mechanics are insufficiently generalized to kinetically model bcc alloy

systems. Some preliminary (bcc) modifications have been made to the current JL model; however, it is beyond the scope of the current research to verify and to apply defect-atom kinetics to bcc alloy systems.

5.2 Cu-Li Sputtering Behaviour

For the Cu-Li alloy system at the limiter/divertor and a grazing magnetic angle, D, T, He, and Li impact at 60 degrees and Cu impacts at normal incidence. The copper sputtering yields, as a function of energy for these impact conditions (TRIM calculation), are displayed in Figure 5.1. Of significance is the energy at which copper self-sputtering exceeds unity. For the lithium overlayer on copper, the "unity" self-sputtering energy is 1350 eV which greatly exceeds the "unity" self-sputtering energy of pure copper, 350 eV (TRIM result). Such a reduction in the copper self-sputtering yield allows the comparison of copper to refractory metals such as W and Mo, that have "unity" self-sputtering energies approaching 1000 eV due to their greater masses and higher sublimation energies. Besides a reduction in the copper self-sputtering yield, a similar reduction in the light-ion yields is provided by the lithium overlayer. At low energies $\sim O(100$ eV), sputtering is reduced by an order of magnitude, while at higher impact energies

Figure 5.1   Partial Sputtering Yields of Copper from a Li
              Overlayer on Elemental Cu for D, T, He, Li, and
              Cu Projectiles
              (TRIM Calculation)

~O(1000 eV), sputtering is reduced by 2.5 (Figures 5.2 a,b). Experimentally, a copper sputtering reduction of 3.0 is observed for 3 keV Ar+ at normal incidence on the Cu-Li alloy system [208] in accordance with the calculated TRIM sputtering reduction factor of 2.5 for copper self-sputtering. If, copper were to impact at oblique angles, self-reflection would diminish the shielding action of the lithium overlayer although an appreciable erosion reduction exists even at oblique angles.

Another measure of sputtering is to look at the cumulative yield of all impact species of the alloy system as a function of energy. The cumulative yield is defined as the summation over all projectile sputtering yields for the identical impact energy. The inclusion of the copper sputtering due to lithium reduces the energy (to 650 eV) at which copper sputtering exceeds unity. Thus, a lithium overlayer on copper system is less favorable than refractory metals based on a cumulative sputtering perspective. However, the cumulative sputtering yield is not a true measure of the erosion as a function of energy for the reasons: (1) a differential sheath potential acceleration as a function of the ion species charge (Z) in which the impact energy scales as $Z_k e\phi$; and (2) the neglect of the lithium secondary-ion fraction which if sufficiently large (and in the presence of a sheath potential and/or a grazing magnetic field angle) would prevent plasma-edge lithium recycling.
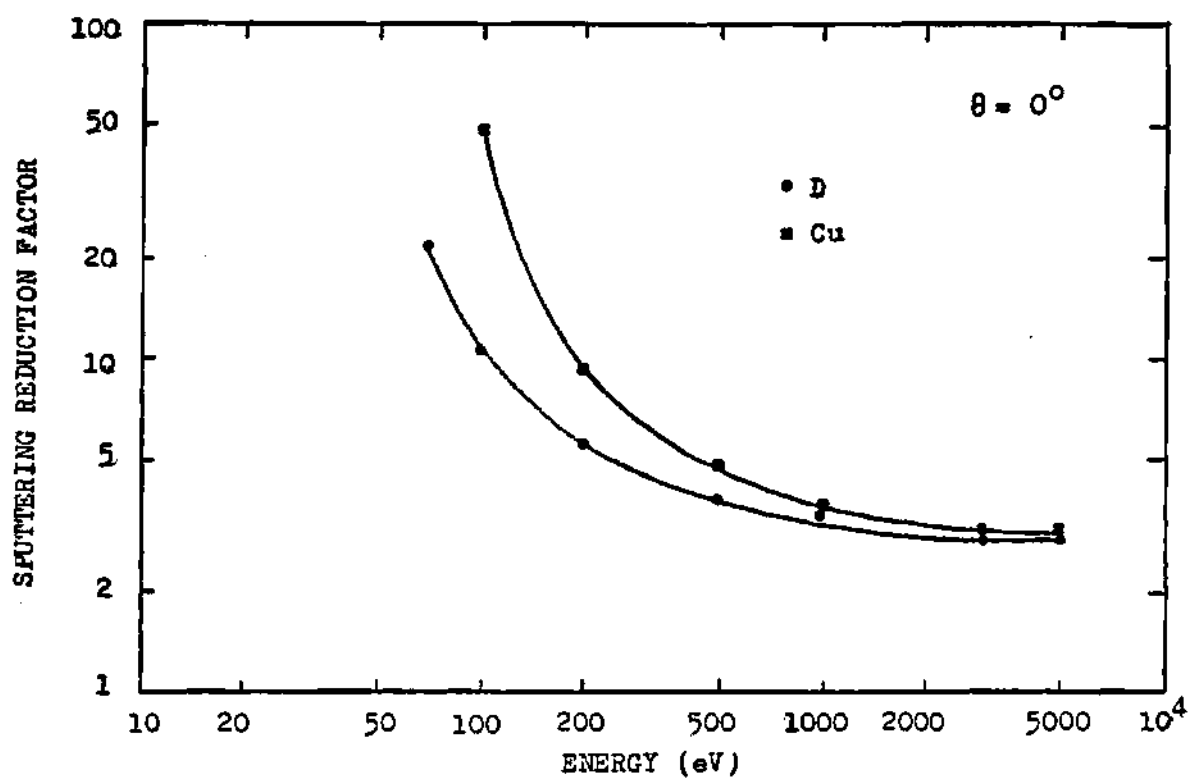
Figure 5.2a
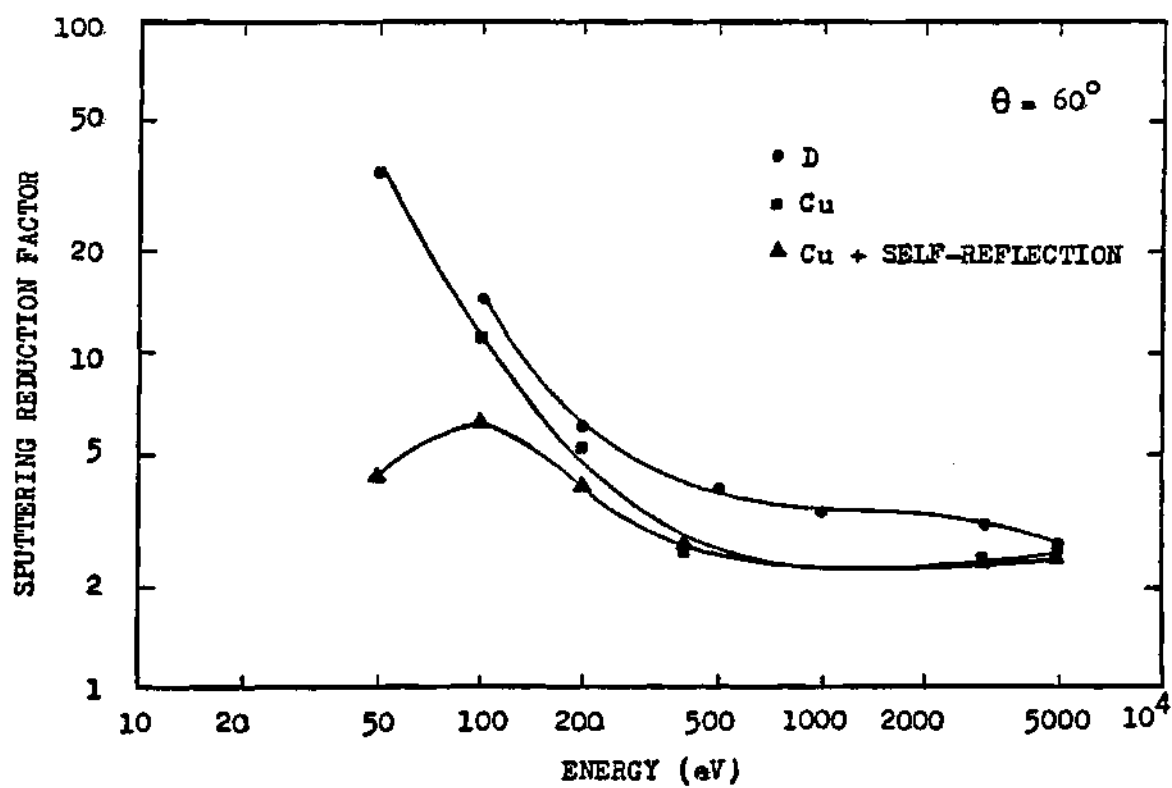
Figure 5.2b

Shown in Figure 5.3 is the energy dependence of the lithium sputtering yield. For light-ion sputtering (D,T,He) alone, the erosion yield for energies in excess of 50 eV ranges from 0.6 to 0.85, and the inclusion of Li and Cu sputtering indicates that a overlayer of lithium on copper would be intolerable if lithium were to primarily sputter as neutral atoms. Indeed, in a previous self-consistent analysis in which the sputter erosion was coupled to the sheath potential [42], the lithium overlayer on copper system was proven inferior to pure copper if the secondary-ion fraction was assumed negligible for all eroded species. However, experimental evidence of the Cu-Li alloy system indicates that a secondary-ion fraction approaching 95% is observed for a self-sustaining atomic overlayer of lithium.[211] Furthermore, the Auger electron surface analysis of the Cu-Li alloy appears to be more representative of 1.5 to 2.0 monolayers of epitaxial lithium coverage rather than one self-sustaining monolayer.[209,211]

If the dilute Cu-Li alloy is protected by 1.5 atomic layers of lithium, the "unity" self-sputtering energy for copper extends to 3100 eV, far superior to any pure metal system. Futhermore, at high energies $\sim O(1000 \text{ eV})$, the light-ion sputtering is reduced by a factor of four to five. In the presence of a sheath potential that roughly scales as $3kT_e$ and where the plasma-edge ion temperature approximates the electron plasma-edge temperture, the maximum plasma-edge
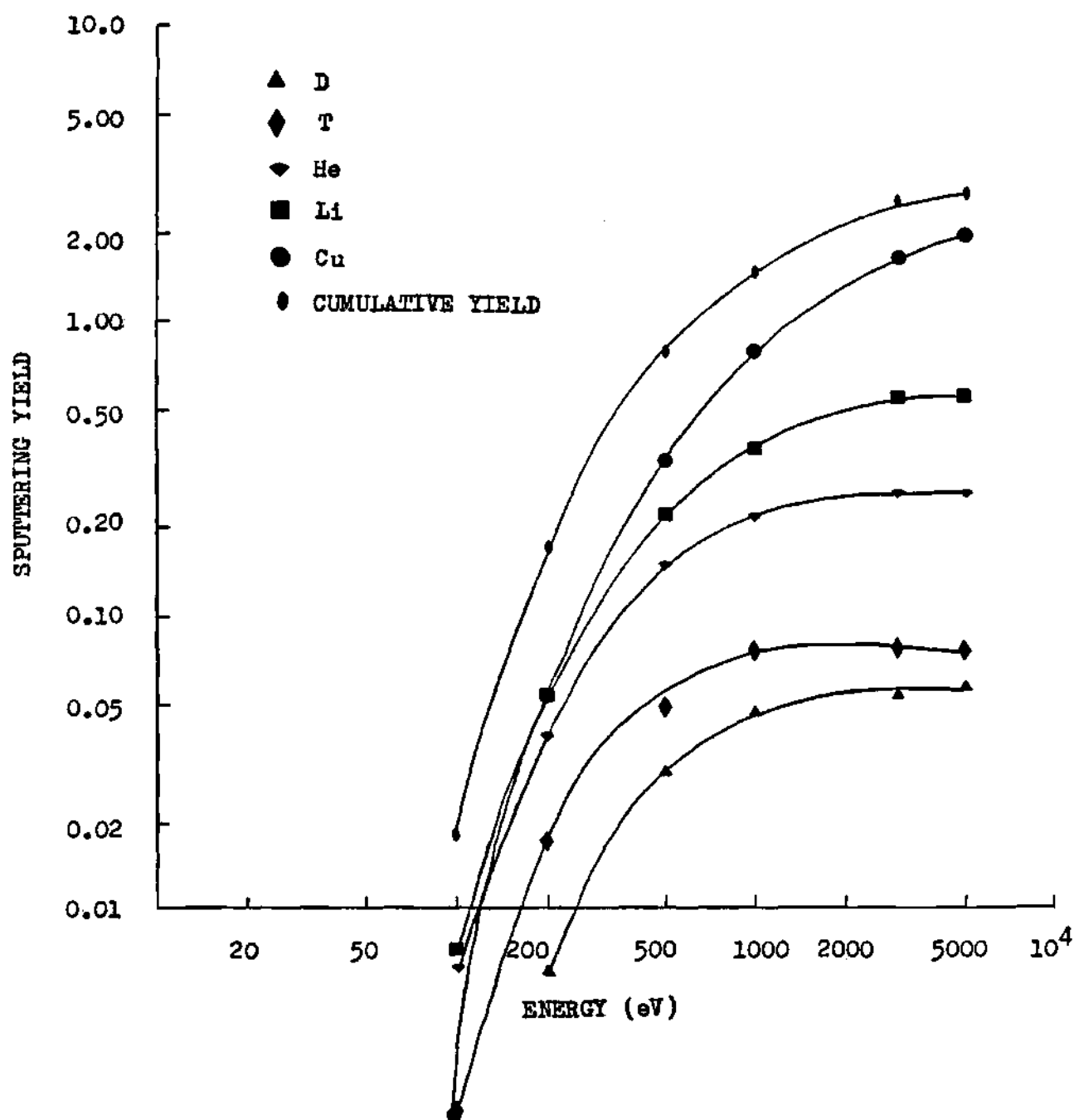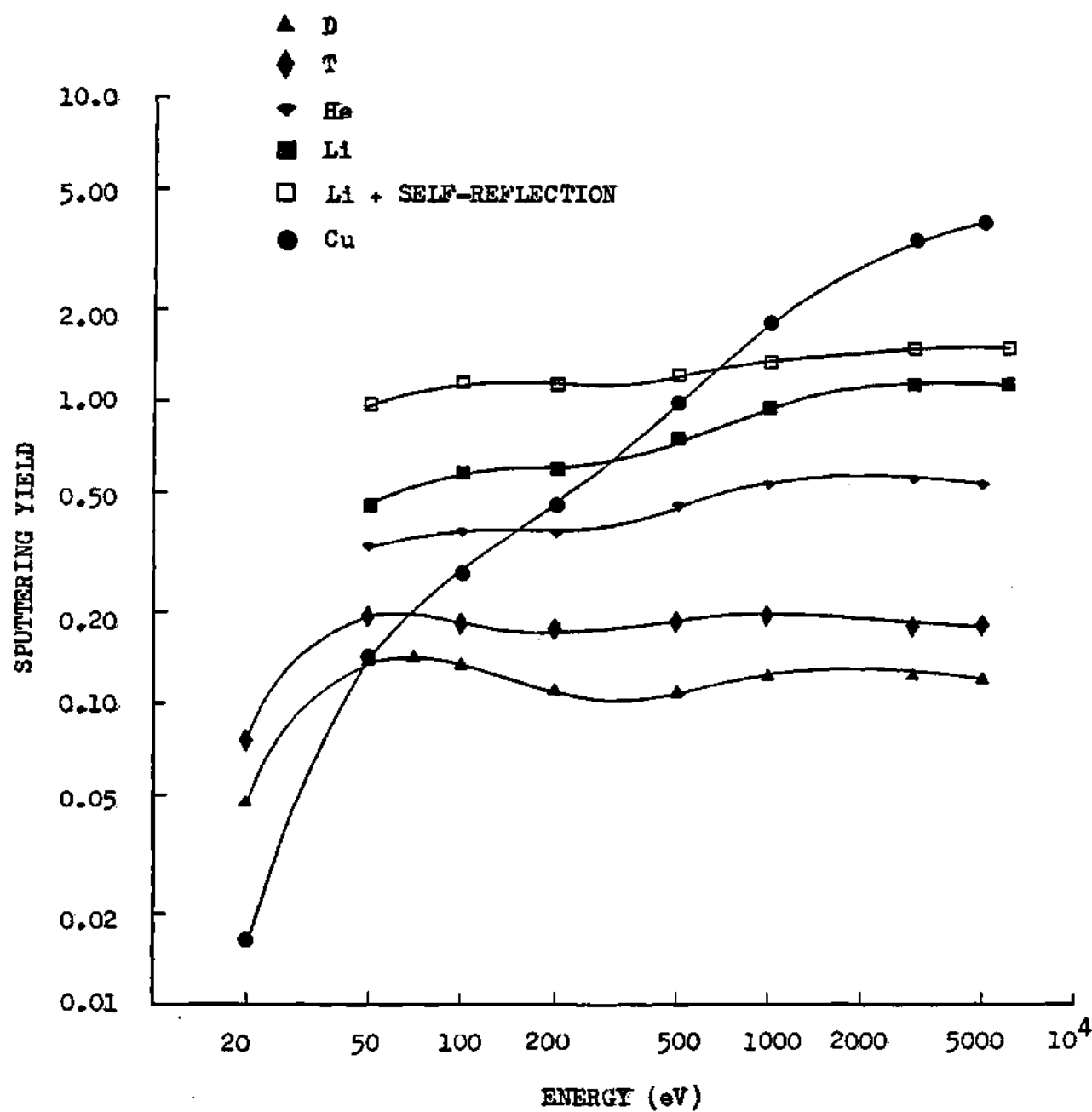
Figure 5.3   Partial Sputtering Yields of Lithium from a Li
            Overlayer on Elemental Cu for D, T, He, Li, and
            Cu Projectiles   (TRIM Calculation)

temperature of the solvent species which maintains a self-sputtering yield less than unity can be estimated by

$$T_e = \frac{E_{ss}}{(1 + 3Z_k)} \qquad (5.2.1)$$

where E_{ss} is the "unity" self-sputtering energy. For the Cu-Li alloy, a 3100 eV copper self-sputtering energy would easily allow for plasma-edge temperatures in excess of 100 eV for Cu charge states less than Z=5.

5.3 Evaluation of the Lithium Activation Energy

Migration and formation energies by which the lithium solute diffuses within the Cu-Li alloy remain unknown; however, from the overview of defect mechanisms presented in Chapter 4 and from other experimental defect data on pure copper and copper alloys, conclusions may be drawn as to which defect mechanism(s) is(are) dominant in determining the lithium (solute) flux. As previously cited, interstitial-solute and vacancy-solute complexes are unlikely to be formed (or important) in a Cu-Li alloy system. Furthermore, thermal equilibrium data for pure copper [212,213] and for the copper alloys of Cu-Zn [214], Cu-Ge [215], Cu-Al [212], and Cu-Ni [212] are suggestive of a monovacancy dominant defect mechanism for both solvent and

solute diffusion. Hence, for the current application of the JL model to Cu-Li, all defect types other than monovacancies will be treated as secondary effects (if at all). A thermal equilibrium activation energy of lithium diffusion via monovacancies in Cu-Li has never been measured although thermal equilibria diffusion studies of Li in a Cu-Al-Li alloy have been performed, yielding a lithium activation energy of 1.24 eV.[216] High temperature irradiation of Cu-Li alloys has produced a lithium activation energy equal to 1.16 eV.[154] Such a value, though, cannot be equated to the Li thermal activation energy value, because it incorporates radiation transport mechanisms which may act to accelerate lithium (solute) diffusion. Hence, the thermal activation energy of lithium in Cu-Li probably is greater than 1.16 eV.

To specify the lithium activation energy, a parametric study employing the JL model has been conducted to reproduce incipient compound formation that has been observed experimentally for Cu-Li alloy temperatures less than $140°C$.[211] Compound formation of Cu_4Li precipitants is initiated when the local lithium concentration exceeds ~18%.[217] Morever, it has been assumed that the lithium activation energy replicates the behaviour of fcc metals such that $H_v^f / Q_v = .55$ (Equation 4.4.4). Shown in Figures 5.4 and 5.5 are the parametric "fittings" of a monovancy lithium activation energy, Q_v^{Li}, for single and bi-layer sputtering, respectively. Activation energies of $Q_v^{Li} = 1.55$ eV for
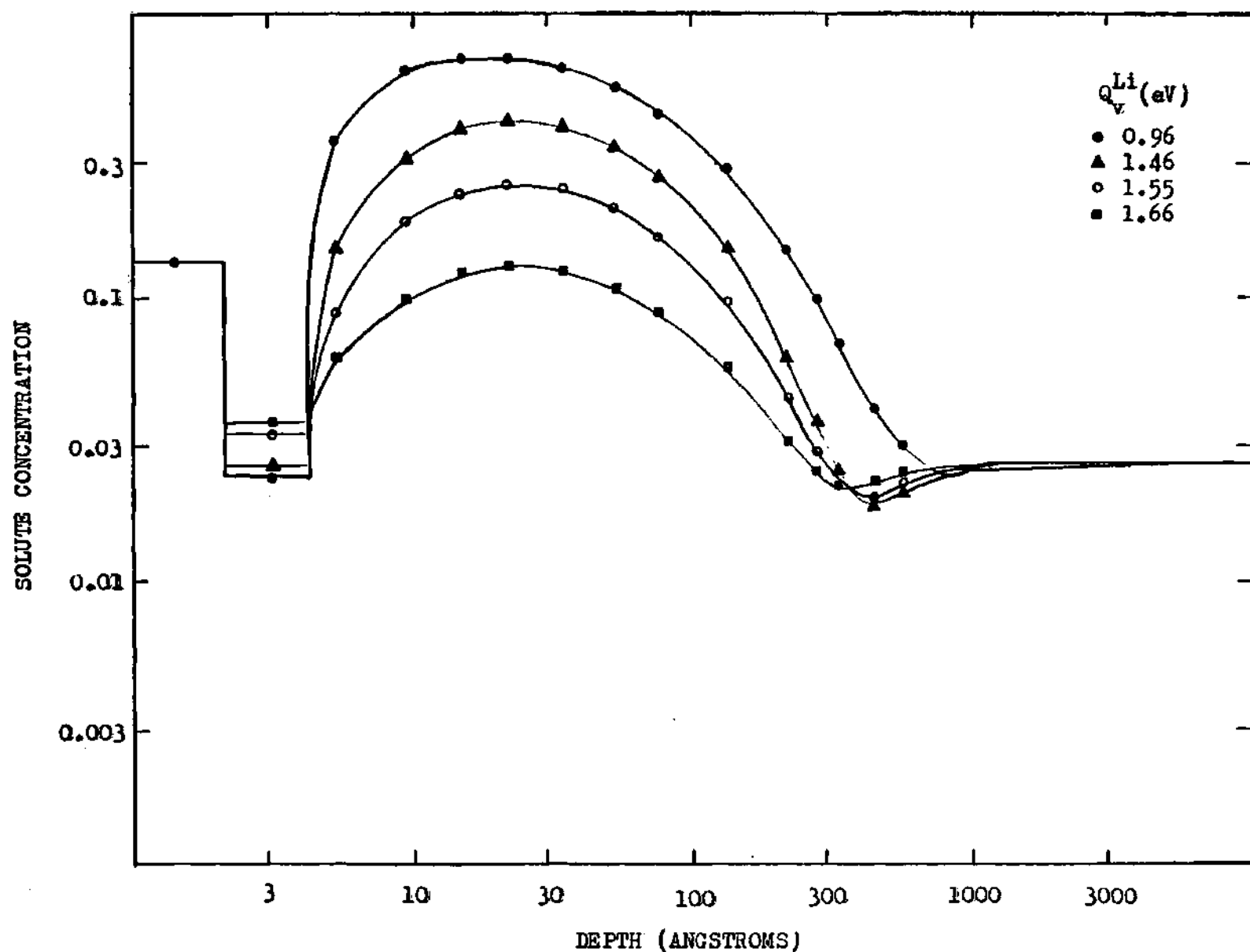
Figure 5.4   Steady State Lithium Concentration Depth Profile for Elemental
Single-Layer Sputtering of Cu-2.6%Li as a Function of Lithium
Activation Energy at an Alloy Temperature of 140°C
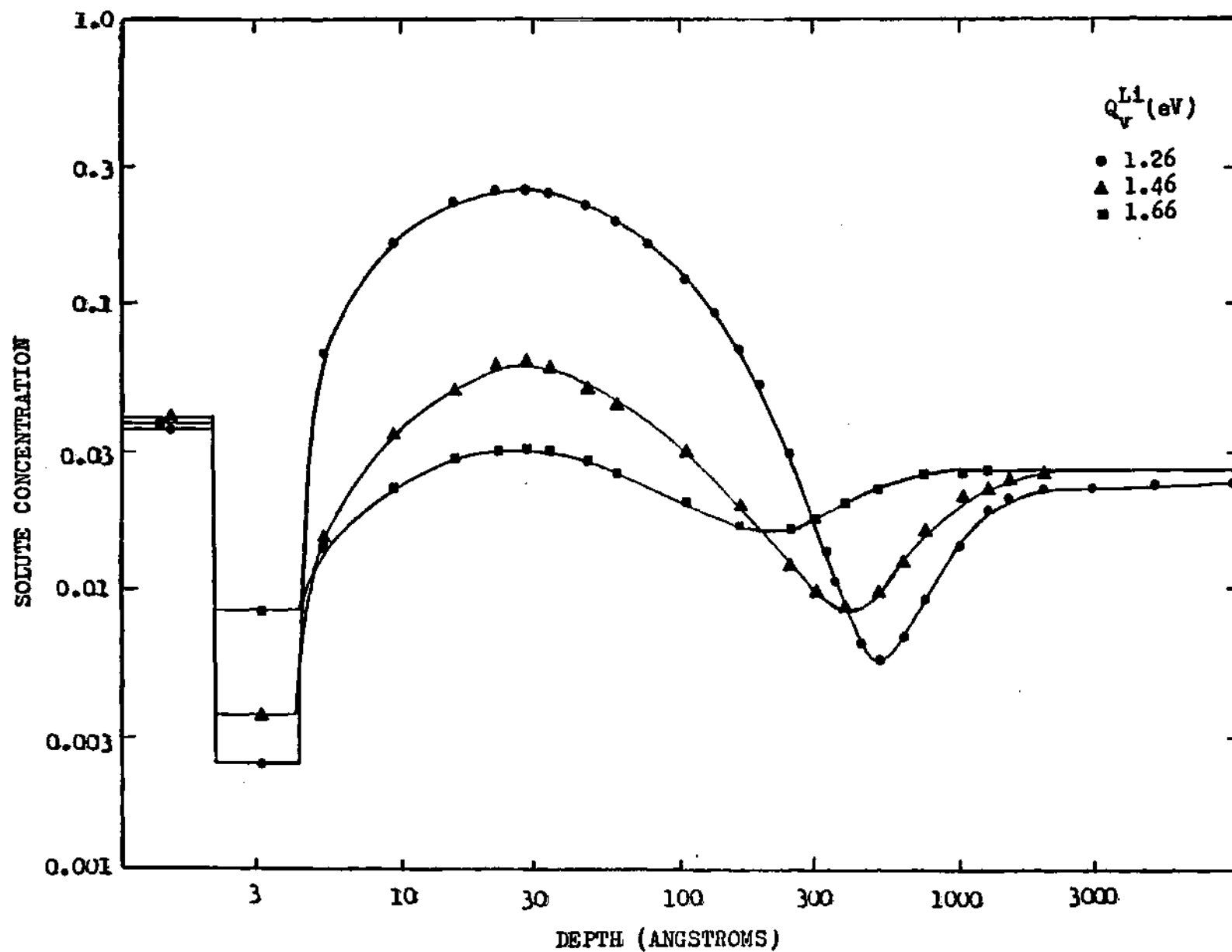
Figure 5.5 Steady State Lithium Concentration Depth Profile for Alloy
Bi -Layer Sputtering of Cu-2.6%Li as a Function of Lithium
Activation Energy (Alloy Temperature of 140°C)

elemental single-layer sputtering and Q_v^{Li} =1.31 eV for alloy bi-layer sputtering appear to best fit the experimental Cu-Li alloy data at 140°C where small precipitant quantities probably exist within the subsurface, indicative of a 20-25% Li concentration.[209,211] The difference between the activation energies for one-layer versus bi-layer sputtering is primarily due to the differential sputtering (erosion) rates. Increasing the solute sputtering yield necessarily requires a corresponding increase in the solute diffusion rate, hence, a lowering of the solute activation energy in order that the bulk solute concentration profile remains a relative constant.

The general characteristics of the lithium (concentration) depth profile are qualitatively similar for both pure elemental one-layer and bi-layer sputtering. The first atomic layer concentration is determined by preferential sputtering. Suppression of the solute concentration within the second atomic layer is an artifact of Gibbsian segregation (Equation 4.10.2). Subsurface enrichment is a direct result of vacancies flowing out of a damage region coupled to an opposing flux of solute atoms into the damage region. Because the dpa damage profile (for the displayed conditions) is peaked near the surface, the lithium enrichment would be expected to be skewed toward the surface direction. Conservation of lithium solute requires that a region of enrichment have a corresponding region of

depletion. The depletion region for bi-layer sputtering is more severe since the erosion rate is greater than that of elemental one-layer sputtering.

An understanding of the transient kinetics is obtained by tracking the time evolution of four selected depths within the Cu-Li alloy as shown in Figures 5.6 a-d. The four lithium concentration traces correspond to (1) the first atomic layer, (2) the second atomic layer, (3) a near-surface layer within the Li enrichment zone, and (4) the depth at which maximum depletion of lithium occurs at steady state. Upon comparison of elemental one-layer sputtering to bi-layer sputtering, a similar first atomic layer behaviour is observed where, initially, preferential sputtering rapidly depletes the lithium overlayer concentration. However, the second atomic layer behaviour is initially quite different. Because elemental one-layer sputtering fails to accurately describe the actual Li sputtering magnitude and the sputtered layer of origin, an initial Li enrichment of the second atomic layer is predicted (Figures 5.6 a,c) rather than the actual (sputtered) depletion (Figures 5.6 b,d). An initial enrichment of the subsurface is primarily due to radiation enhanced diffusion. The initial behaviour of the fourth trace remains unchanged since deeper atomic layers are "unaware" of surface irradiation effects on "short" time scales. As the near-surface lithium reservoir (enrichment region) broadens (shifts to greater depths), the first and
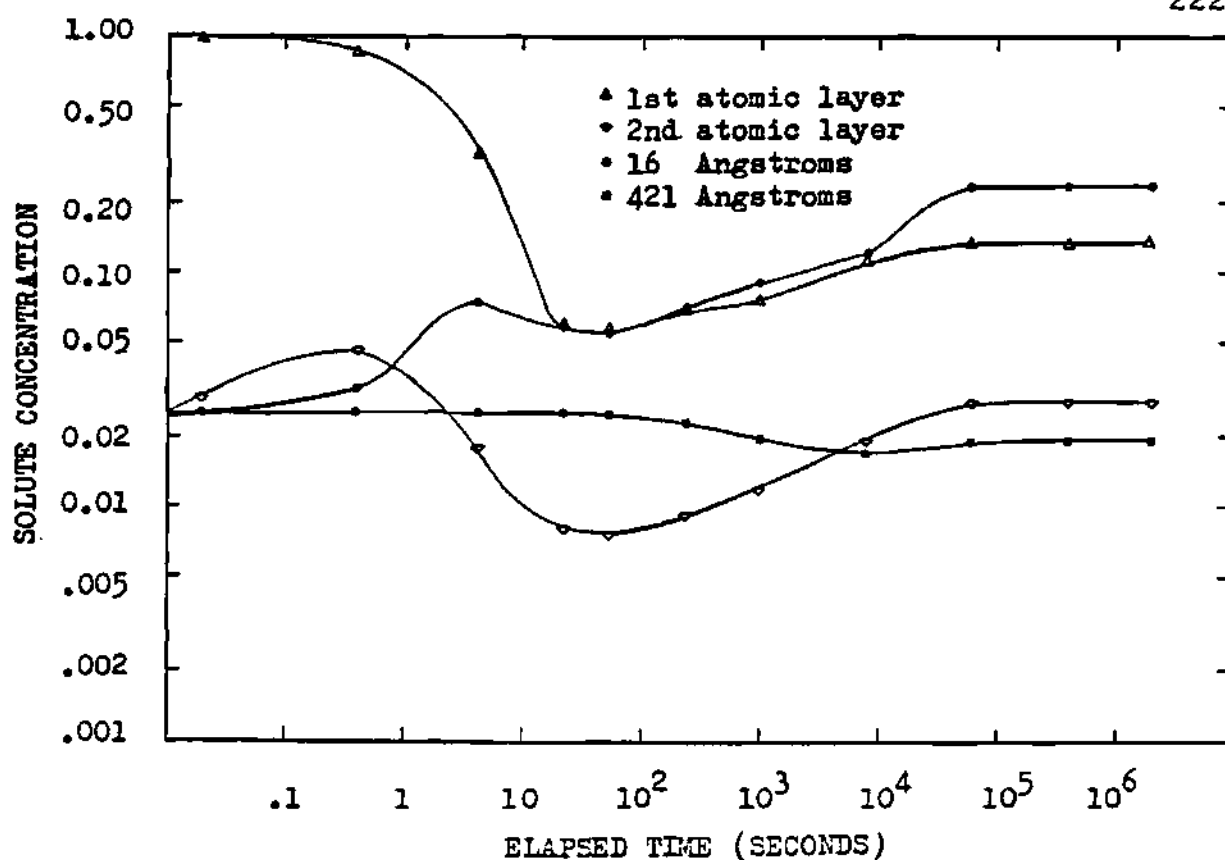
Figure 5.6a   Kinetic Time Dependence for Elemental
Single-Layer Sputtering (T=140°C)
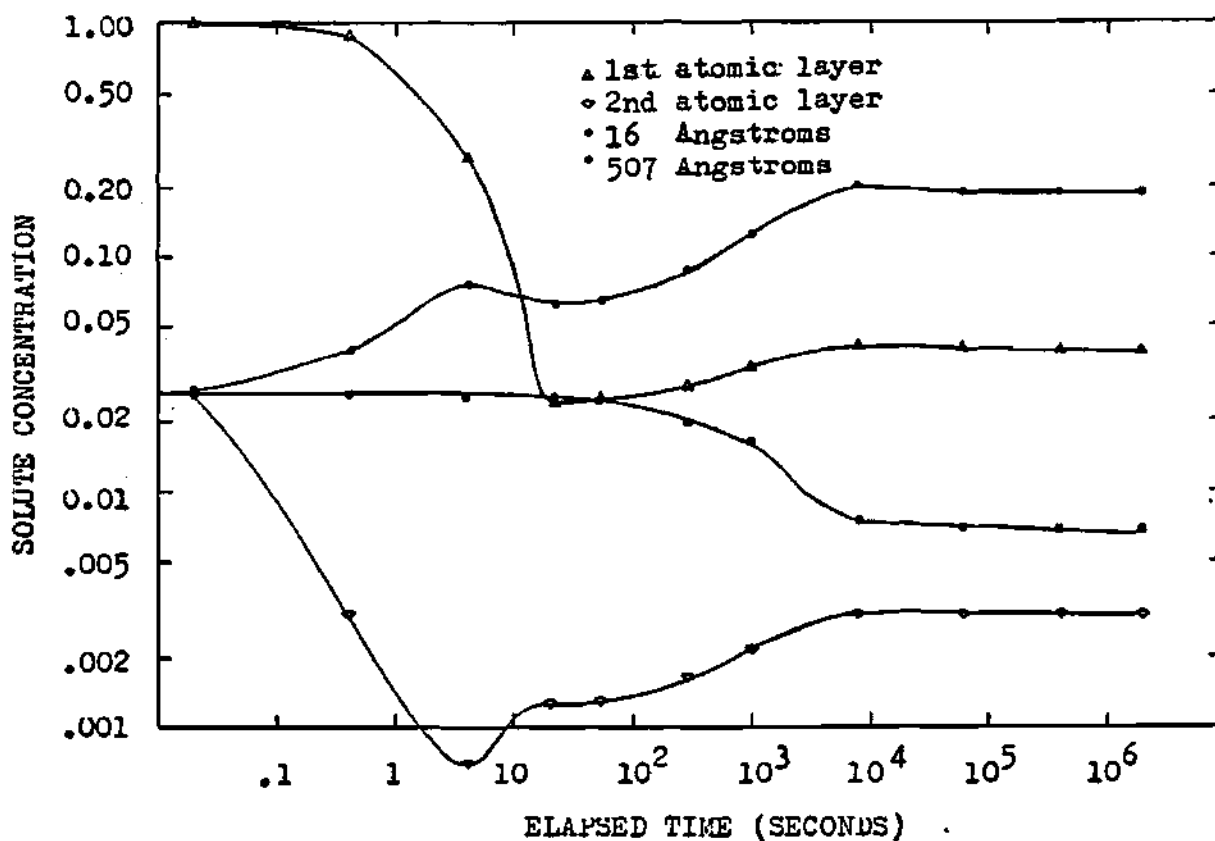
Figure 5.6b   Bi-Layer Sputtering (140°C)
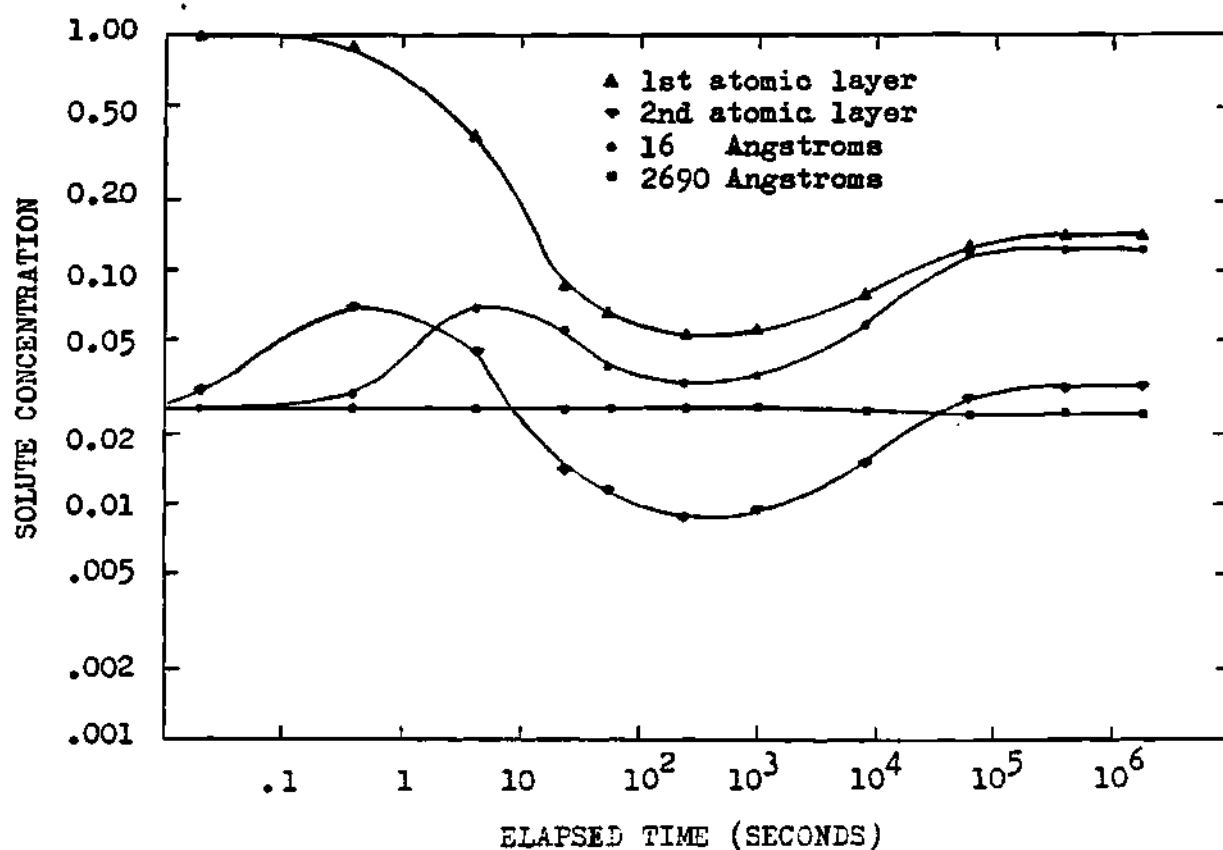
Figure 5.6c Elemental Single-Layer Sputtering (350°C)
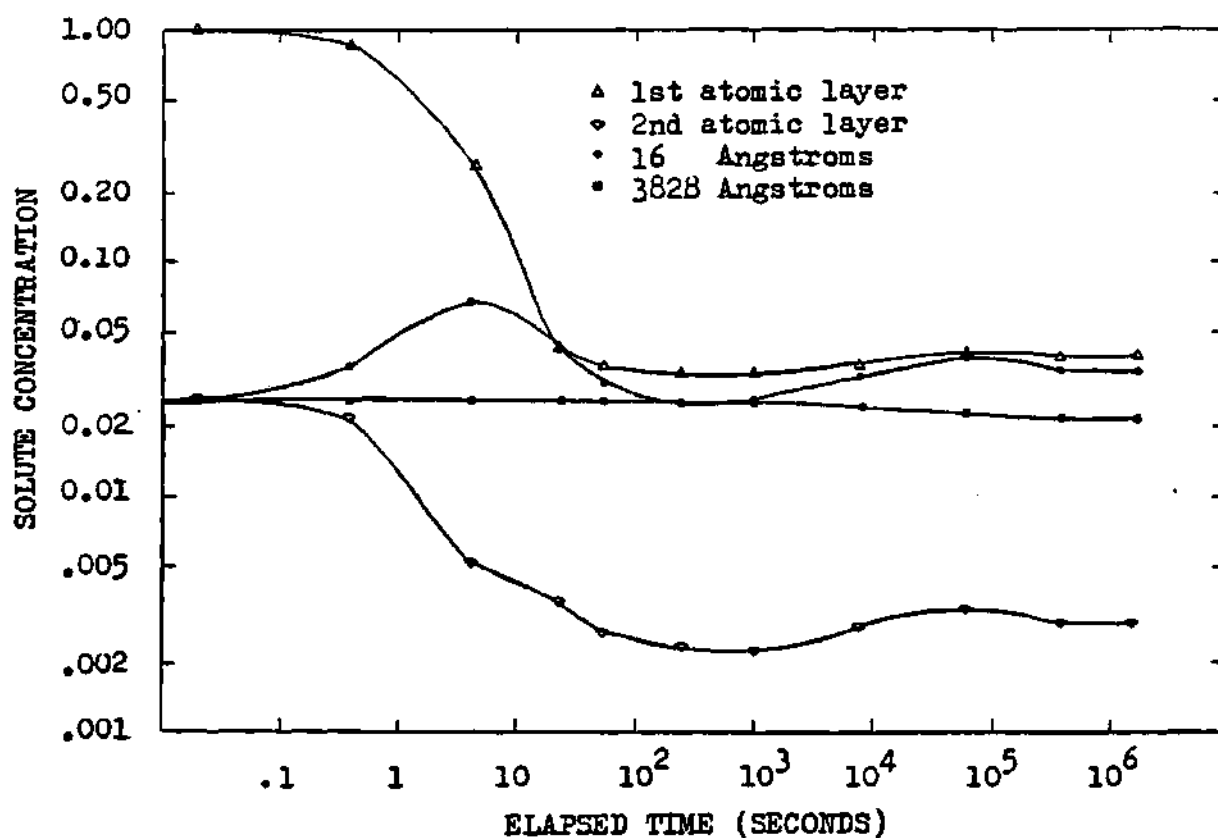
Figure 5.6d Bi-Layer Sputtering (350°C)

second atomic layers become replenished. The enhanced diffusion of lithium to the surface due to radiative processes requires a corresponding depletion at deeper depths (fourth trace). All four depth traces approach a steady state as determined by the coupling of preferential sputtering to the damage profile.

The transient trends for all trace layers at 350°C are similar to those observed at 140°C, except that the traces are "smoother" due to an increased solute transport rate ($D \propto \exp(-\Delta G_D/kT)$). Also, the concentration profile at higher temperatures broadens as indicated by the position of the fourth trace. The expansion of the lithium rservoir results in lower concentrations within the near-surface. Thus, at higher temperatures, the subsurface enrichment is insufficient to allow incipient Cu_4Li compound formation, a result that is verified by experiment in which no precipitation of Cu_4Li is observed for temperatures approaching 300°C.[218]

Experimentally, the depletion of the surface lithium concentration at low temperatures (140°C) is observed to be more severe than that at higher temperatures [218] as predicted by the JL kinetic model. However, no depletion is observed experimentally for temperatures greater than 260°C; rather an enrichment occurs, in direct contrast to the predicted kinetic transient employing the JL model (Figure 5.7).[218] In fact, a stable lithium surface layer with
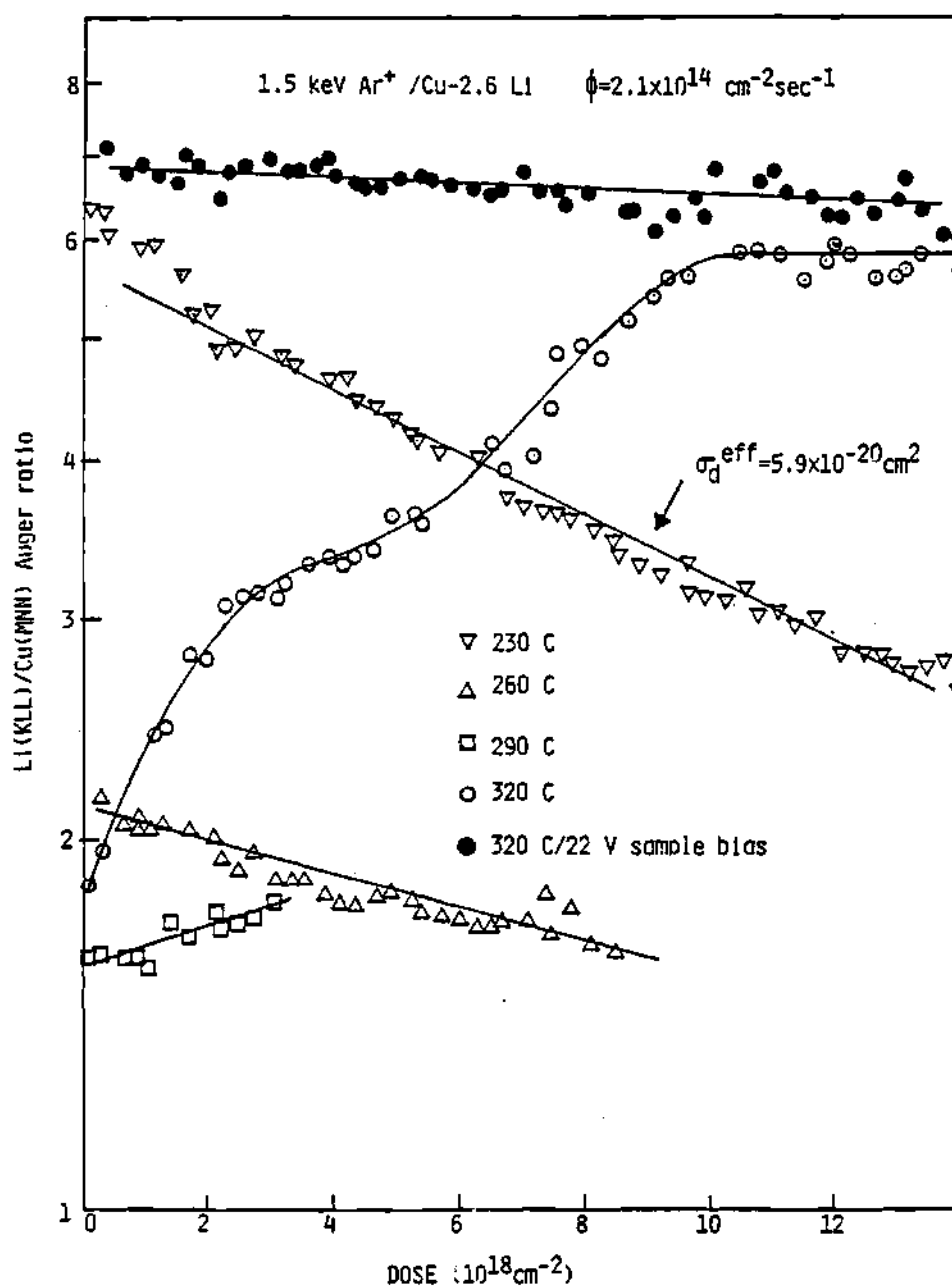
Figure 5.7 Experimental Li/Cu Auger Ratio as a
Function of Fluence and Cu-Li Alloy
Temperature

negligible bulk ·Li reduction has been observed experimentally for the same flux conditions at an alloy temperature of 430°C over a continuous 3 week irradiation period $(1.8 \times 10^{6}$ seconds).[219] The discrepancy between the experimental and model results is such that the concept of preferential sputtering determining the steady state surface solute concentration becomes questionable if, indeed, uncertainties in the model application and the experimental procedure are negligible.

A kinetic analysis, assuming a 50% deviation in the elemental sputtering yields and in the damage rate for a given set of temperature/irradiation conditions, has been performed to determine if model (TRIM) parameters can partially explain experiment/model disagreement. Using the elemental one-layer sputtering yields (underestimation of erosion), the maximum surface Li concentration predicted is 26%, followed by a depleted (Gibbsian) second layer of lithium. A ±50% deviation in the damage rate served only to increase or to decrease the local enrichment region concentration by 10%. These combined effects are insufficient to explain the self-sustaining lithium overlayer observed experimentally for the Cu-2.6Li% alloy at high temperatures.

It has been postulated that a "small" potential (a couple of volts) between the target and the vacuum chamber existed during the irradiation and data collection of the

Cu-Li alloy. Because a high fraction of the sputtered lithium is through secondary ion emission, the presence of a potential would drive back to the surface low energy sputtered ions and effectively reduce the sputtering yield. Lithium concentration profiles for various sputtered ion fractions are shown in Figure 5.8 for elemental one-layer sputtering. A high secondary-ion emission of lithium from the Cu-Li alloy sustains not only a lithium overlayer but provides an extensive subsurface Li reservoir. However, the subsurface enrichment significantly exceeds the lithium solubility limit of 18% such that extensive Cu_4Li compound formation is prevalent. Experimentally, lithium tends to diffuse out of regions of precipitation; hence, the accumulation of lithium within the subsurface, as exhibited in Figure 5.8, should not be as great.[217] An investigation of the experimental procedure indicates that no "noticeable" potential exists between the target (Cu-Li) holder and the vacuum chamber. Even if such a potential had existed, a negative bias of -2 V would simulate only a ion fraction of 28% for 3 keV Ar+ on a lithium overlayer on Cu-2.6%Li (TRIM calculation). Potentials of -10 V and -35 V correspond to 74.5% and 90% ion fractions, respectively, for the same bombardment conditions. The experimental application of a negative bias, -22 V, to the Cu-Li alloy has been found to sustain a first layer Li concentration regardless of the irradiation and temperature conditions (if
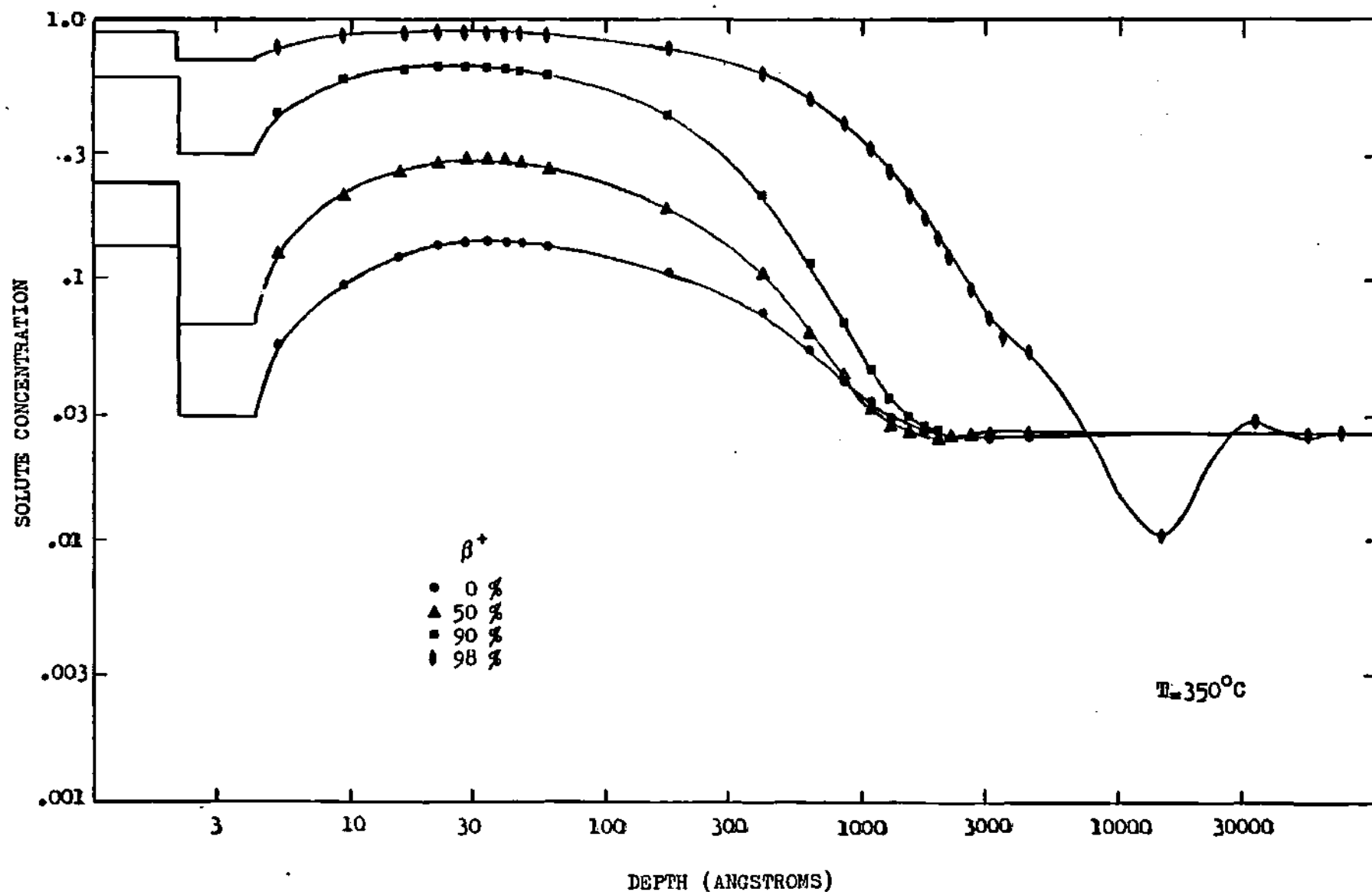
Figure 5.8 Steady State Lithium Concentration Depth Profile Dependence upon the Secondary-Ion Fraction of Lithium for 3 keV Ar+ at Normal Incidence

$120°C<T<430°C$).[208,218,219] Thus, the presence of a sheath potential will maintain the lithium overlayer for heavy-ion impact.

5.4   DPA Profile Effects

An inherent feature within the JL model is the assumption that the dpa profile, $K_o(x)$, is time independent. The dpa profile approximation of Cu-2.6%Li is that of pure copper for the identical bombardment conditions (Figure 5.9). The dpa profile is peaked and heavily weighted towards the first atomic layer. TRIM calculations for 3 keV Ar+ on pure lithium (Figure 5.10) show a much broader dpa damage profile. The disparity between the pure copper and the pure lithium damage profiles is a mass ratio effect of Ar/Cu and Ar/Li as well as a chemical bond effect since the copper binding energy is twice that of the lithium binding energy. Thus, during irradiation of the Cu-Li alloy, the dpa profile may change significantly in response to the transient Li concentration profile. A time dependent dpa profile will not only alter the time evolution of the alloy composition but may alter the steady state component profiles as well. Specifically, a broader profile should reduce the vacancy driving force of the solute to the surface.

Within the time independent (dpa) framework of the JL
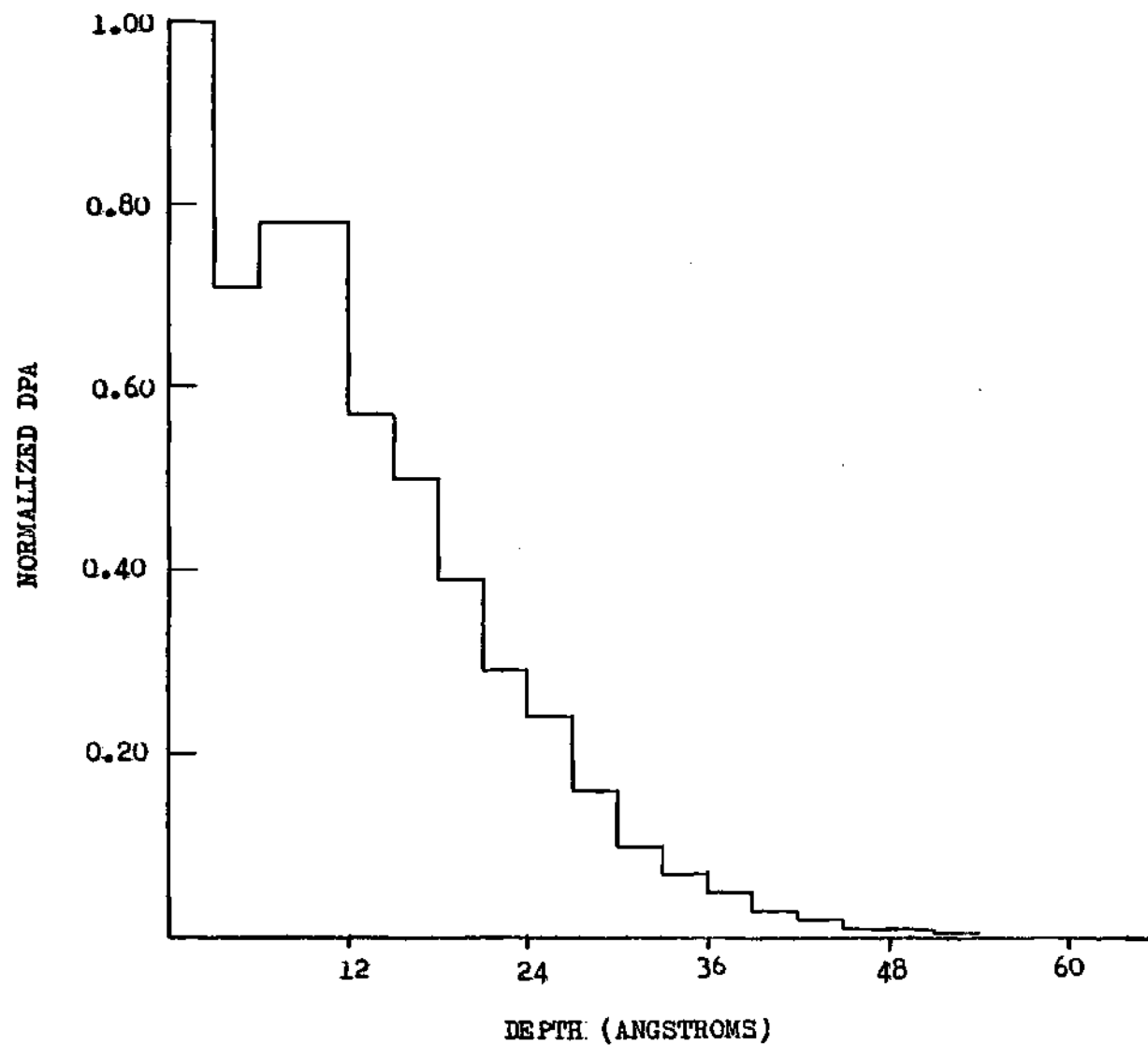
Figure 5.9   Normalized DPA Depth Profile for Copper as a
Result of 3 keV Ar+ at Normal Incidence
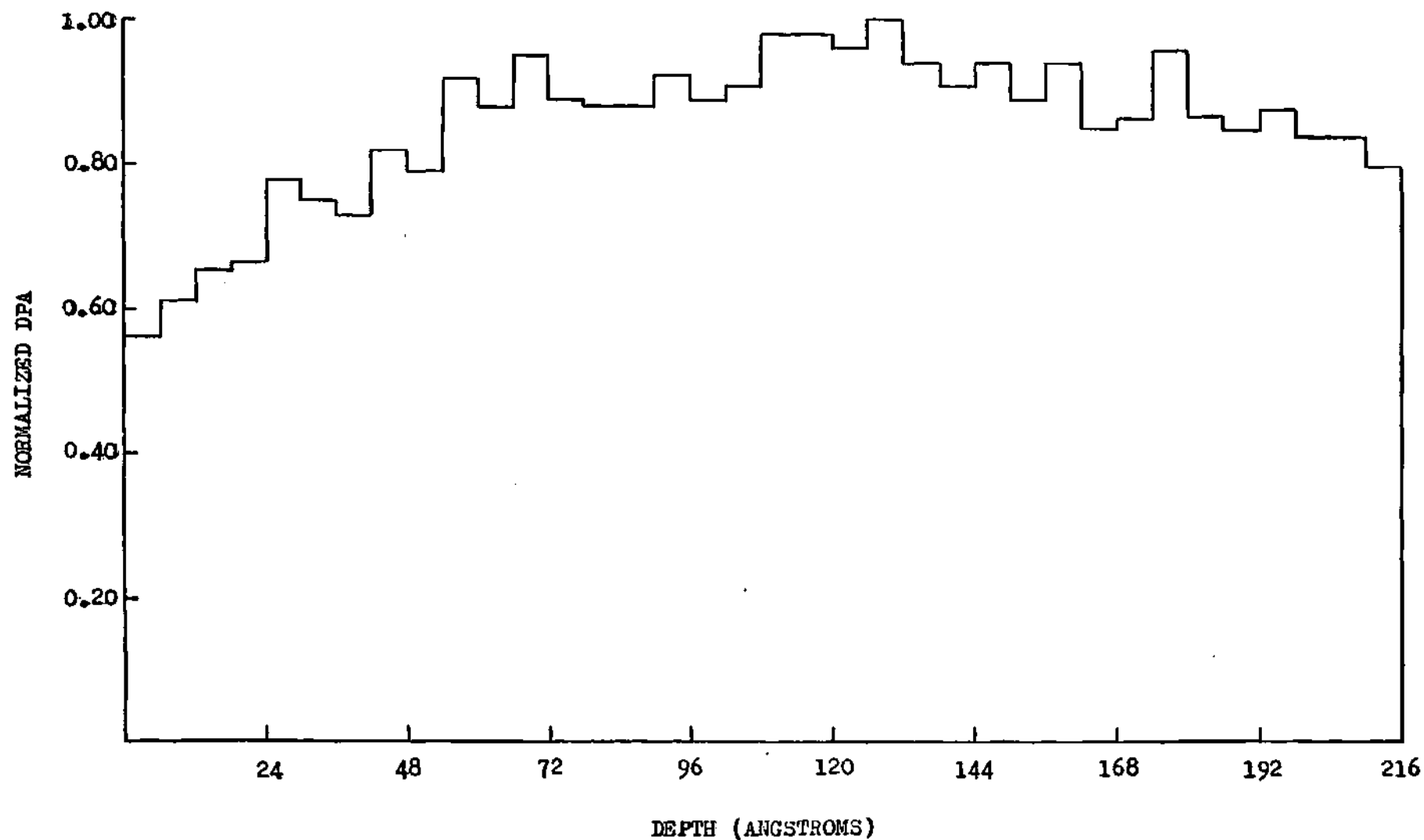
Figure 5.10   Normalized DPA Depth Profile on Lithium as a Result of 3 keV Ar+ at
Normal Incidence

model, an investigation of an altered dpa profile on the steady state Li concentration has been performed. The alloy has been described as a "sandwich" of Li-Cu-Li-Li atomic overlayers on a pure copper substrate. The dpa profile for the sandwich has been calculated by TRIM (Figure 5.11.a), and the resultant Li concentration profile calculated by the kinetics model is shown in Figure 5.11.b. A suppression of the near-surface Li enrichment occurs due to the small broadening of the sandwich dpa profile relative to the pure copper dpa profile.

5.5 Cascade Mixing Effects

An inherent feature within the JL model (not previously discussed) is the effect of collision cascade mixing which is defined in terms of an effective "diffusion" process. The bombardment of an alloy with a significant mass disparity will lead to the implantation of the lighter component in the beam direction, while a compensating flux of the heavier component(s) in the opposite direction occurs(occur) if the atomic density of the alloy is to be preserved.[202] Thus, the cascade mixing diffusion coefficients for a binary alloy are equal across any parallel marker plane with respect to the surface and are defined as [220]
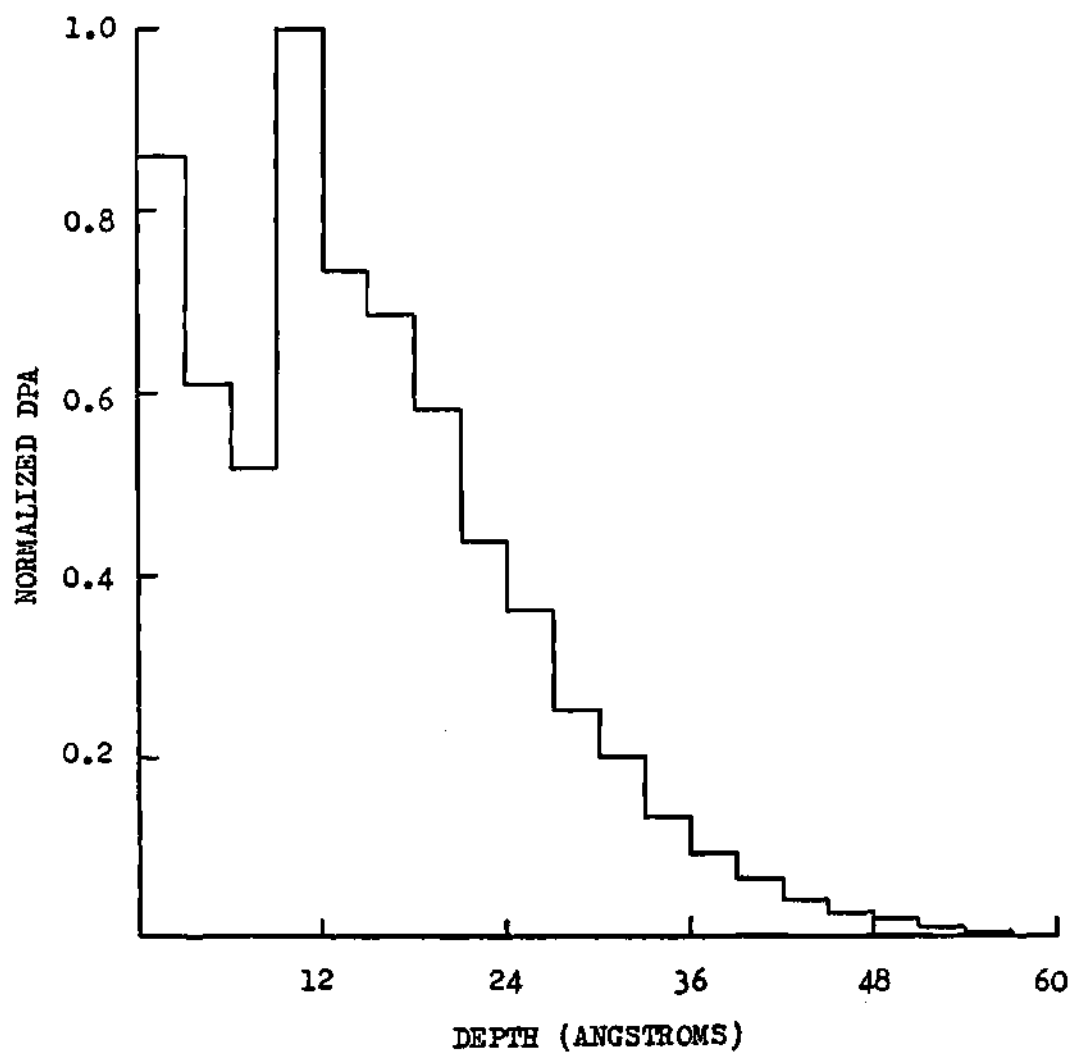
Figure 5.11a Normalized DPA Depth Profile for a
Li-Cu-Li-Li Overlayer Sandwich on
Copper as a Result of 3 keV Ar+
Bombardment at Normal Incidence
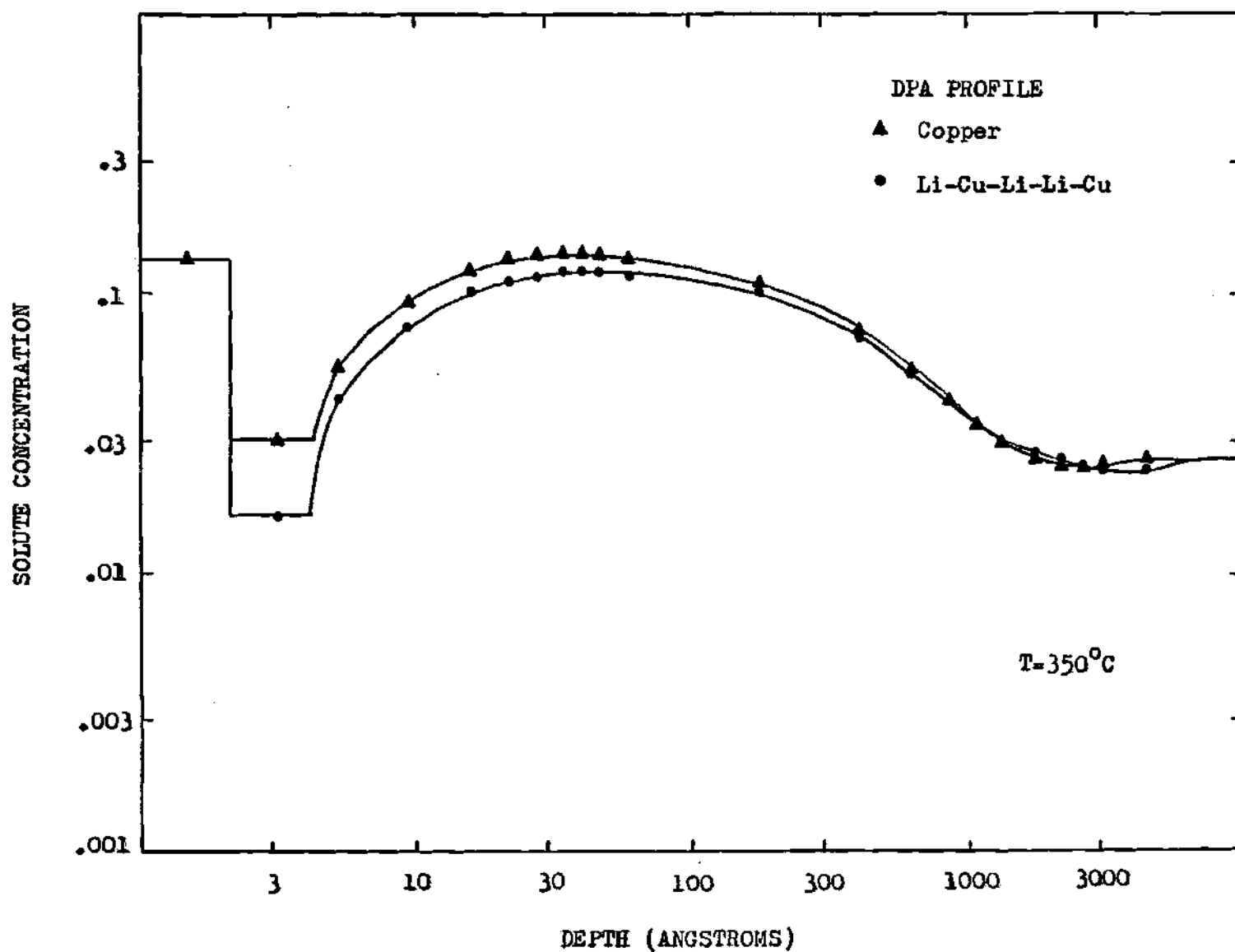
Figure 5.11b Steady State Lithium Concentration Depth Profile for
Cu-2.6% Li Employing a Li-Cu-Li-Li Overlayer on Cu
(Sandwich) DPA Depth Profile

$$D = \lambda^2 K_o \eta/6 \qquad (5.5.1)$$

where η is the number of local replacements (atomic interchange events) per displacement (surviving defect pair).[202]

A phenomenon that may be occurring within the Cu-Li alloy is that the local atomic density within the surface is not time independent. Also, an interstitial matrix may be produced as a result of anisotropic collision cascade mixing. Hence, the interchange coefficient η may conceivably be spatially (concentration) dependent, where the net flux of atoms due to energetic atomic mixing would be nonzero. For a lithium overlayer on Cu-2.6%Li interface, mixing would consist of (1) implantation of the 1st layer lithium into the second layer, accompanied by a significant backscatter effect; (2) the simple mixing of lithium from the second layer into the first layer; and (3) an increased mixing effect of the copper from the second layer into the first layer as compared to mixing in pure copper due to the mass disparity of Cu/Li. While no such investigations of differential cascade mixing factors have been made for the Cu-Li system, TRIM calculations performed for 800 keV Xe+ for the recoil implantation of Yt on Ni (mass disparity of 50%) appear to indicate that atomic mixing across a marker plane

is anisotropic by as much as 25 to 200%.[221] Currently, the only means of investigating changes in cascade mixing is by adjusting the magnitude of η on a uniform basis (Figure 5.12). An increase in the cascade mixing factor leads to further near-surface enrichment as a direct result of Equation 5.2 since the cascade mixing diffusion coefficient is proportional to the damage, K_o.

5.6 Projectile Mass/Energy Effects

Heavy-ion impact of the Cu-Li alloy is indicative of lithium surface enrichment; however, to fully examine the alloy kinetics, light-ion impact effects must be considered as well. In general, light-ions have a deeper and broader implantation profile depth (and a corresponding damage profile) than heavy-ions of the same energy. A TRIM damage profile calculation of 3 keV D^+ on copper used to simulate the damage in the Cu-2.6%Li alloy (Figure 5.13a) shows a much broader dpa profile. The deuterium damage extends 500 Angstroms into the bulk copper (not shown); whereas, the argon damage extends only 50 Angstroms from the surface. On an equal incident flux basis, though, the damage magnitude per Angstrom and the sputtering yield are 70 times smaller for deuterium than for argon. Alloy kinetics will be heavy-ion dependent if the ion species flux magnitudes are of
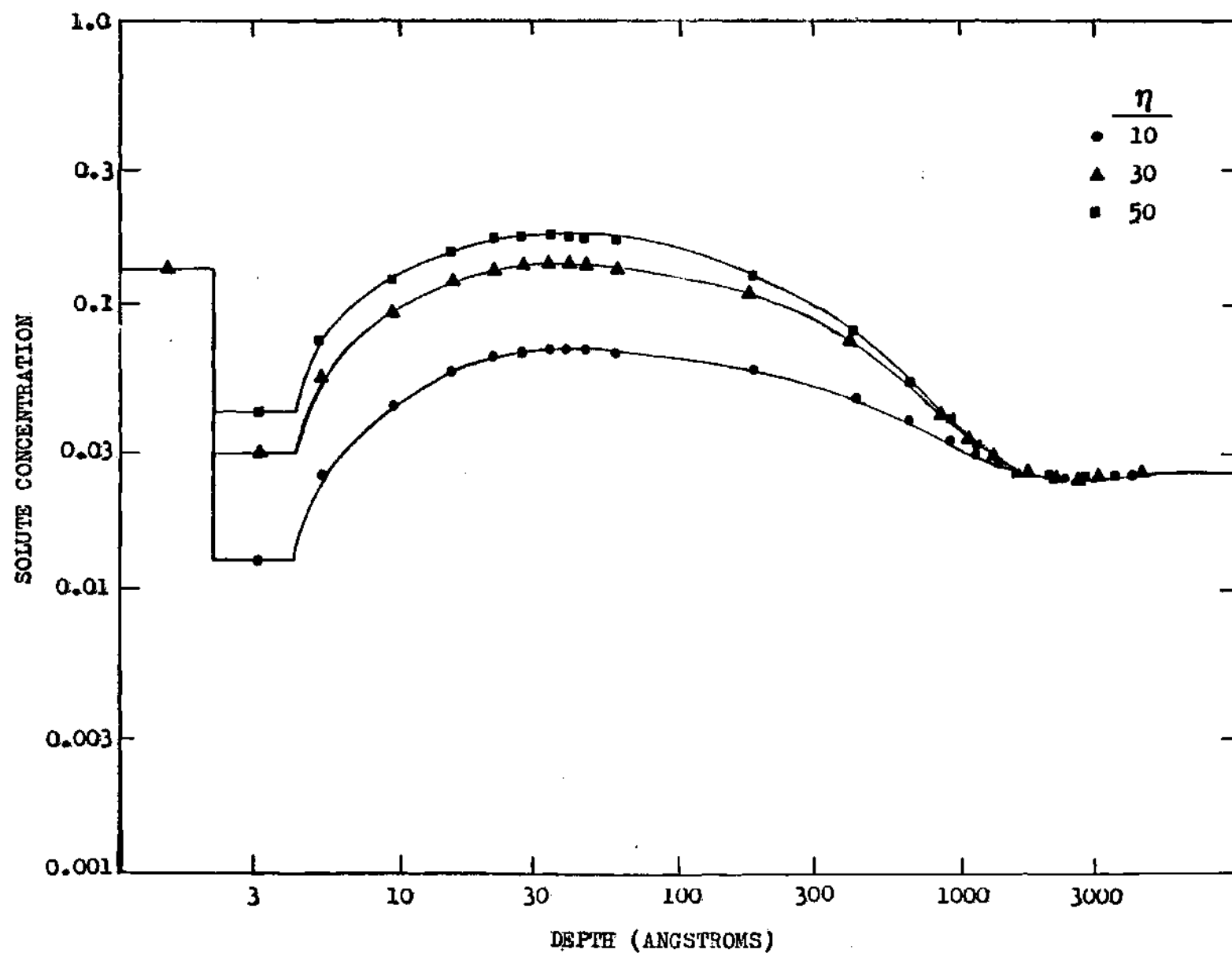
Figure 5.12   Steady State Lithium Concentration Depth Profile as a Function
of the Cascade Mixing Coefficient for 3 keV Ar+ (Normal Incidence)
and a Alloy Temperature of 350°C
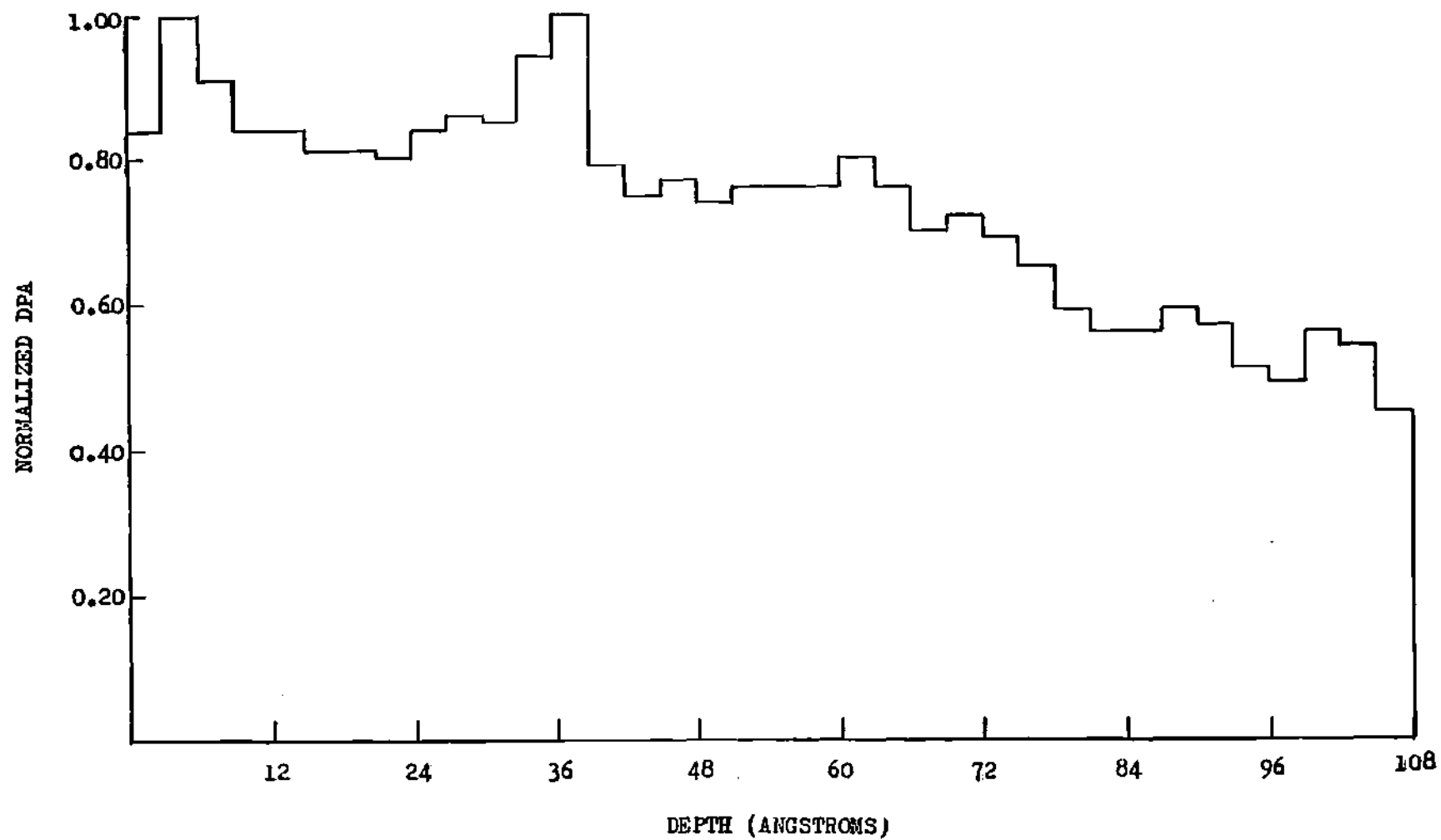
Figure 5.13a   Normalized DPA Depth Profile for 3 keV D+ on Copper at Normal Incidence

the same order. If the deuterium flux approximates the erosion rate and the damage rate of argon, then the light-ion effects on the Cu-Li alloy could be significant as shown by Figure 5.13b. The lithium solute within the Cu-Li alloy is driven towards the damage "center" (peak) regardless of the incident flux species; hence, for deuterium bombardment, lithium diffuses away from the surface. Preliminary experimental evidence (for light-ion impact) is suggestive of a non-self-sustaining lithium overlayer [222,223] qualitatively confirming the kinetic calculations.

For fusion operating conditions, the above comparison of 3 keV D to 3 keV Ar ions, while informative, fails to model the expected light-ion, plasma-edge energy conditions. In the presence of a sheath potential, primary light-ions have average energies of 4 to 6 kT_e while heavy-ions have average energies of 10 to 15 kT_e for edge temperatures on the order of T_e=100 eV. Thus, while the 3 keV Ar+ kinetic calculations approximate the expected accelerated heavy-ion erosion/damage, further coupled TRIM/JL model simulations are necessary for incident deuterium. If an average deuterium impact energy of 500 eV (and Θ=0°) is assumed, the resultant damage profile (Figure 5.14a) is calculated (TRIM) to be peaked towards the surface in contrast to the broad 3 keV D^+ damage profile. Because the 500 eV deuterium damage profile is broader and more removed from the surface than the 3 keV Ar+ damage profile, the near-surface lithium enrichment due
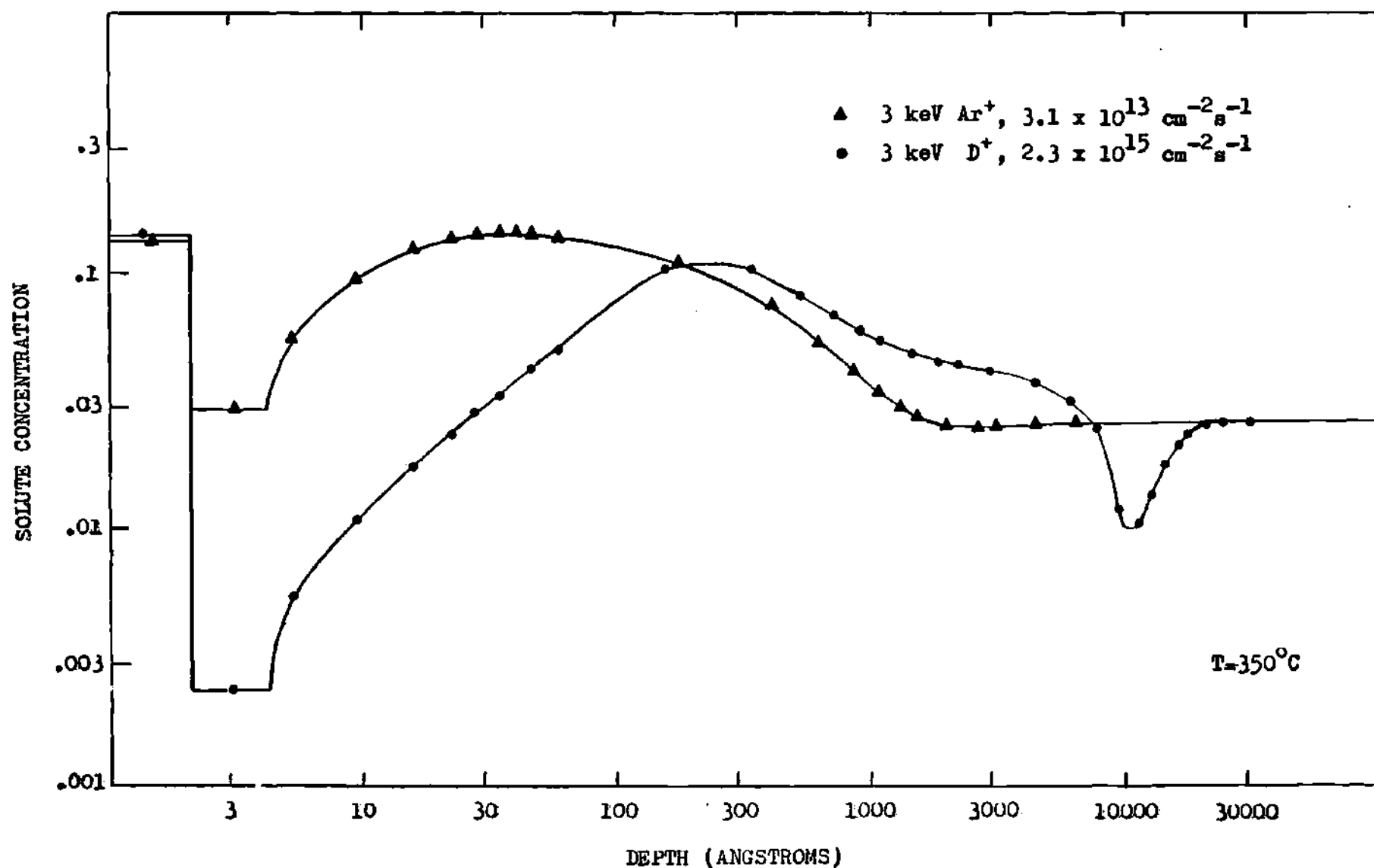
Figure 5.13b   Comparison of the Steady State Li Concentration of Cu-2.6%Li for 3 keV Ar+
and 3 keV D+ at NormalIncidence and the Identical DPA Rate per Angstrom at
the Position of Peak Damage
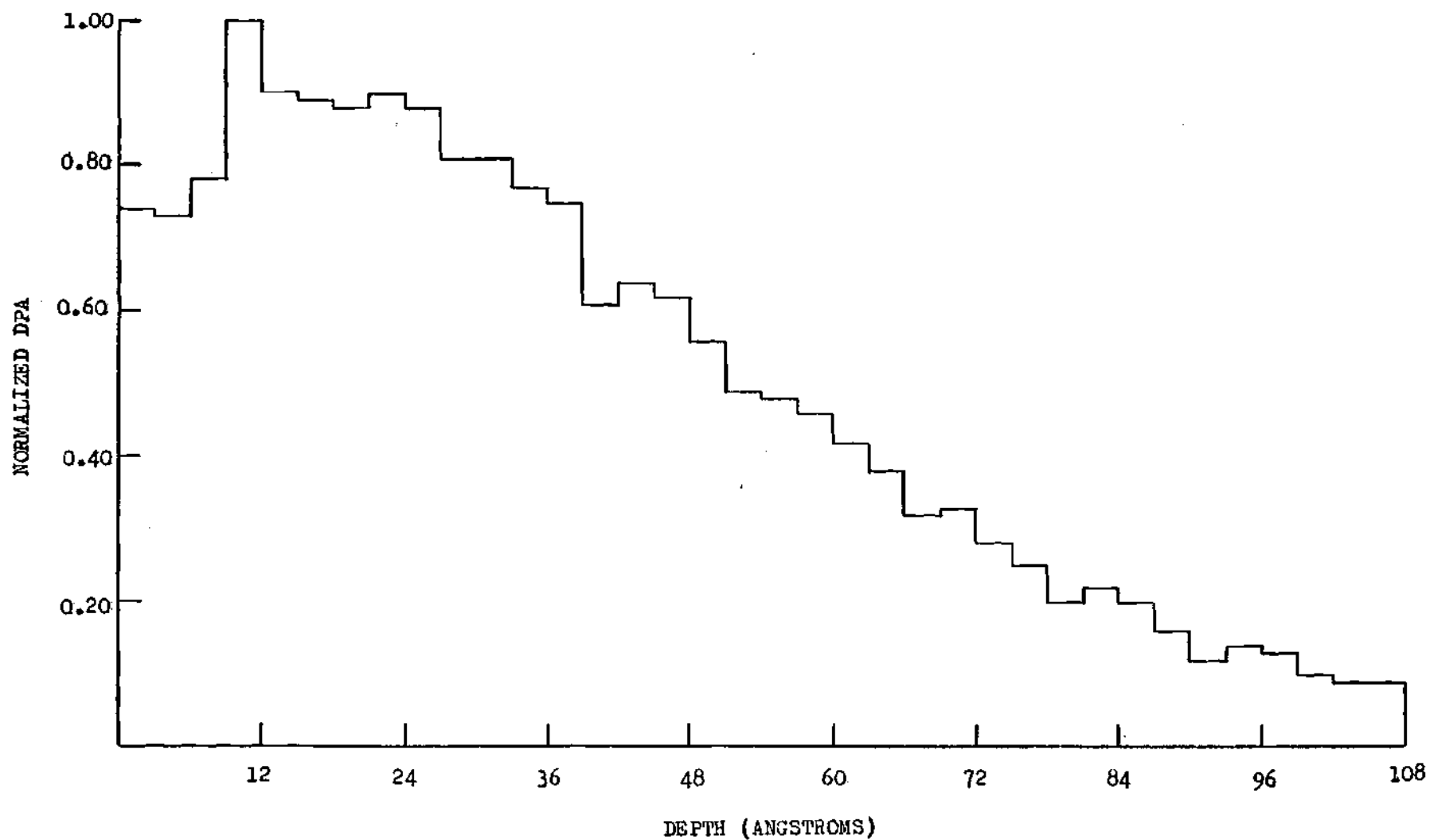
Figure 5.14a   Normalized DPA Depth Profile for Copper as a Result of 500 eV D+ Bombardment at Normal Incidence

to deuterium bombardment should be less than for argon bombardment. These results still fail to model the deuterium erosion/damage since light-ions are more likely to impact at oblique angles if the magnetic angle is oblique as well (Chapter 2). Displayed in Figure 5.14b is the damage profile for 500 eV deuterium impacting a copper surface at 60 degrees. The resultant damage profile is similar to to that of heavy-ion impact hence, the positioning of the subsurface lithium enrichment (if any) due to deuterium impact should correspond to heavy-ion (argon) impact.

Kinetic alloy calculations for 500 eV D^+ at normal incidence for a fusion wall temperature of $350°C$ indeed show that the subsurface Li "peaking" is translated closer to the surface in correspondence with the general heavy-ion impact behaviour (Figure 5.15). However, quantitatively, the Li surface concentration is lower for low energy deuterium bombardment, and a depletion of subsurface lithium rather than an enrichment of subsurface lithium exists. The 500 eV incident deuterium, in contrast to the 3000 eV deuterium, results in less damage to the Cu-Li alloy; hence, the magnitude of the lithium (damage) "sink" is reduced such that the corresponding lithium (subsurface) enrichment magnitude is reduced as well. Also, at lower deuterium incident energies, a greater relative depletion of the lithium in comparison to the copper occurs due to sputtering yield differences. For 500 eV D+, the elemental copper to lithium
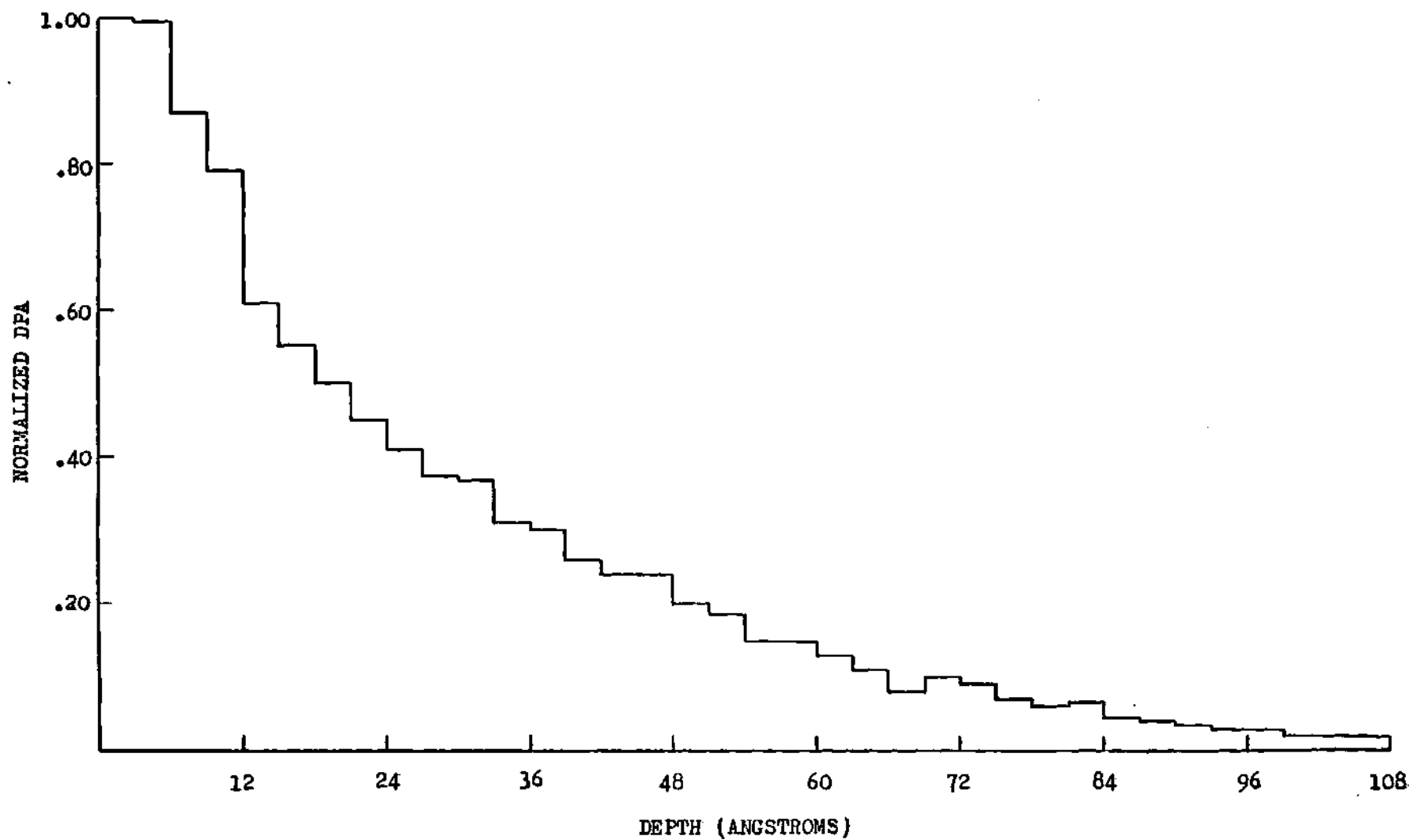
Figure 5.14b - Normalized DPA Depth Profile for Copper as a Result of 500 eV D+ Bombardment at 60 Degrees Incidence
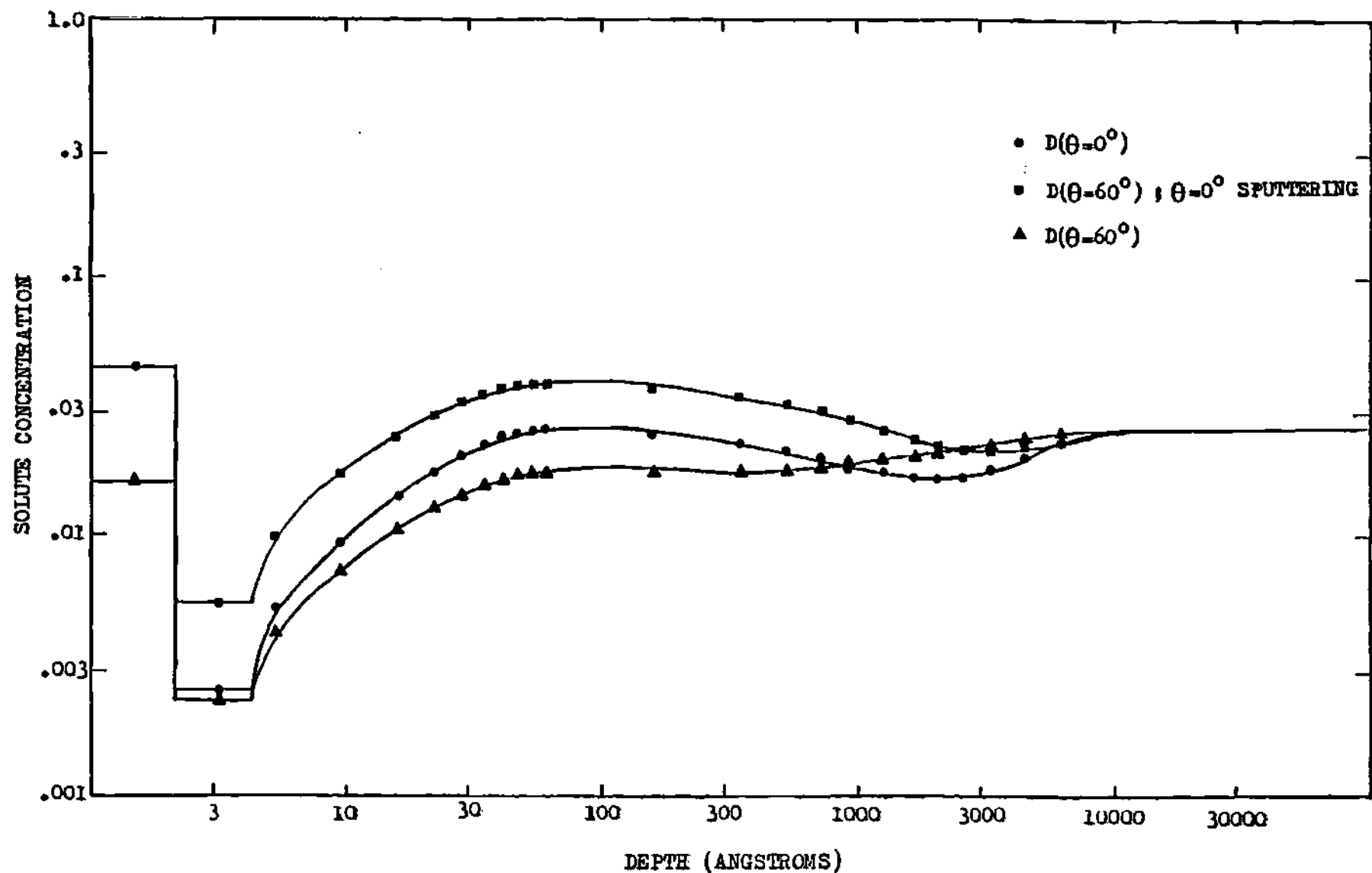
Figure 5.15   Steady State Lithium Concentration Depth Profile of Cu-2.6%Li for 500 eV D+
for Different Angular Conditions with Alloy Temperature 350°C

sputtering yield ratio is 5.9, while for 3000 eV D+, the ratio is only 1.8 if the secondary-ion fraction is assumed nonexistent in both cases.

If the 500 eV D+ were to impact the surface obliquely resulting in the damage displayed in Figure 5.14b, and if the sputtering coefficients of normal incidence are assumed, a small lithium subsurface enrichment region results. However, the incorporation of the oblique elemental sputtering yields shows no evidence of surface and subsurface enrichment, rather lithium depletion occurs over the first 5000 Angstroms of the surface. The damage sink for lithium is overcome by the preferential sputtering of lithium to that of copper since the sputtering ratio of elemental copper to elemental lithium is less than unity (equal to 0.6). Definitely, these results show that light-ion impact will not act to replenish the lithium overlayer to the same extent as that provided by heavy-ion bombardment (if at all). However, the deuterium results suggest a trend, at best, since for heavy-ion (argon) impact, experimental results indicate considerable lithium surface enrichment (at 350°C) in disagreement with the kinetic calculations which are representative of a lower (preferential sputtering) Li surface concentration.

Mixed beam results for 500 eV D+ and 3 keV Ar+ for the same peak damage rate per Angstrom are shown in Figure 5.16. To insure an equivalent peak (spatial) damage rate, requires that a deuterium flux magnitude approximately two orders
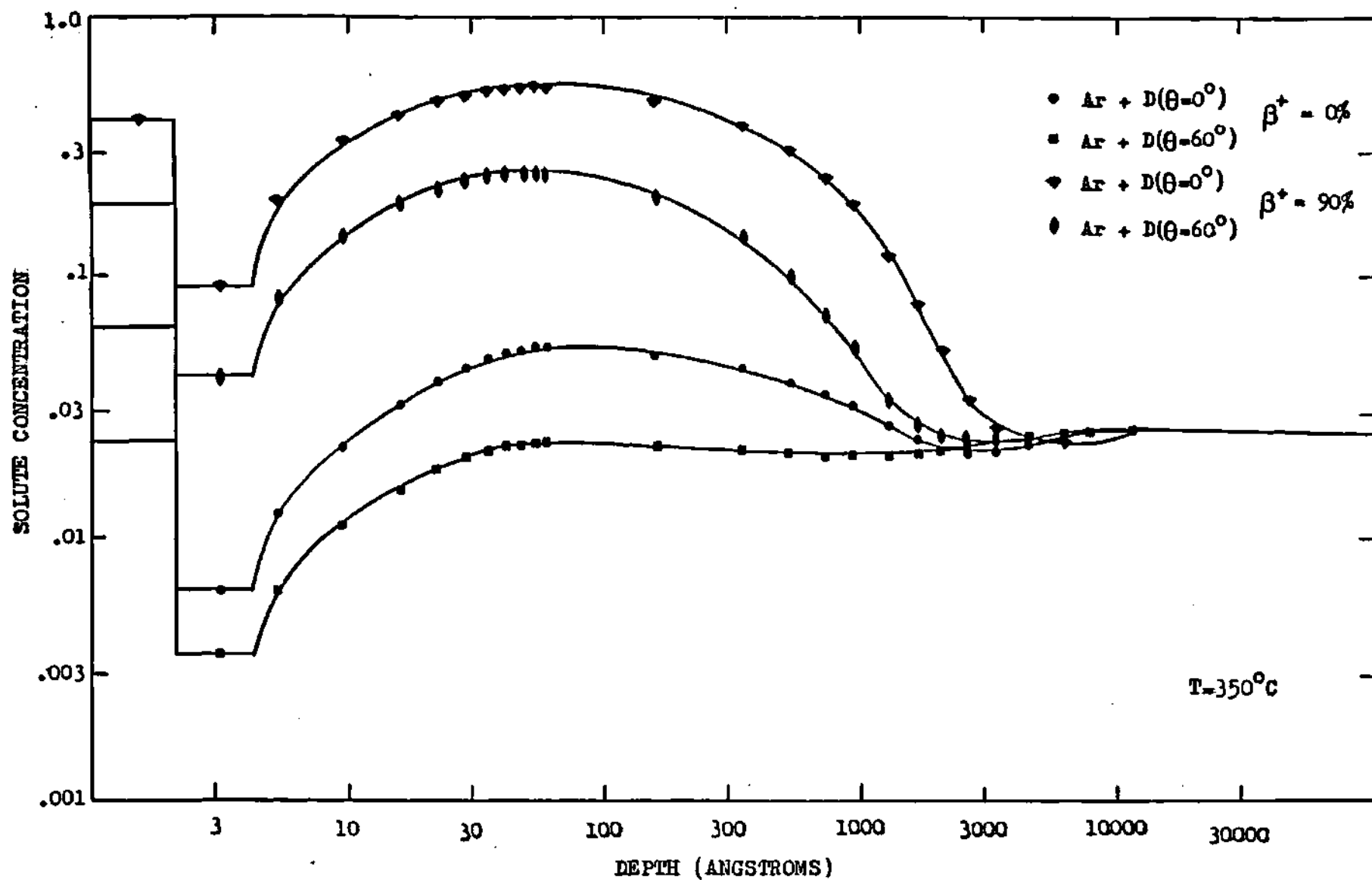
Figure 5.16 Lithium Concentration Depth Profile at Steady State (Cu-2.6%Li Bulk Alloy) Under a Mixed Beam Bombardment of 3 keV Ar+ and 500 eV D+

greater than the argon flux magnitude is selected. Hence, the deuterium impact "detracts" from the lithium surface and subsurface enrichment due to the greater sputtering depletion of lithium via 500 eV deuterium in contrast to the 3 keV argon. If a secondary-ion fraction of 90% is assumed, substantial lithium enrichment is observed for the mixed beam; however, the self-sustainment of a lithium overlayer for preferential sputtering driven kinetics would probably require a β^+ value of 98% for the mixed beam to self-sustain the lithium overlayer. The mixed beam result behaviour definitely shows the general trend that oblique deuterium impact causes less enrichment (if any, depending upon β^+) due to the greater relative sputter depletion of lithium in comparison to copper.

At the first wall (away from the limiter/divertor), no significant sheath potential effects exist; thus, the impact energies of light and heavy ions (as well as neutrals) approximate the Maxwellian 3/2 kT_e. The Cu-Li alloy kinetics are driven entirely by surface erosion/damage phenomena, thus providing the driving forces necessary to self-sustain a highly enriched lithium surface layer. However, because the average impact angle is representative of the isotropic Maxwellian (approximately 45 degrees), the relative depletion of lithium to that of copper for all species (heavy and light) is significantly greater than the normal incidence Li losses. If the secondary-ion yield is O(>90%) as observed

experimentally, then the Cu-Li alloy should be self-sustaining since most secondary-ions are returned via gyromotion within close proximity of their point of origin.

5.7   V-Al Sputtering Behaviour

As with the Cu-Li alloy system, the limiting impact angle conditions in the presence of a sheath potential assume that light-ions (D, T, and He) impact at 60 degrees and heavy-ions at normal incidence. Aluminum which is an "intermediate" mass ion is treated as a heavy-ion and impacts at normal incidence. If a monolayer coverage of Al on pure vanadium is assumed to simulate an Al enriched surface layer for a dilute V-Al alloy, the vanadium (partial) sputtering yields as determined by TRIM are given by Figure 5.17. The vanadium self-sputtering of V-Al does not appear to exceed unity, and, if at all, self-sputtering occurs for an energy in excess of 10 keV. In contrast, the "unity" self-sputtering energy for pure vanadium occurs at 975 eV (TRIM result). Thus, an aluminum overlayer substantially reduces the erosion of vanadium (Figure 5.18 a,b) such that at low energies (100 eV), light-ion sputtering is reduced by a factor of 40 and heavy-ion sputtering is reduced by a factor 20 while at high energies (1000 eV), sputtering for all species is reduced by a factor of four to five. As with
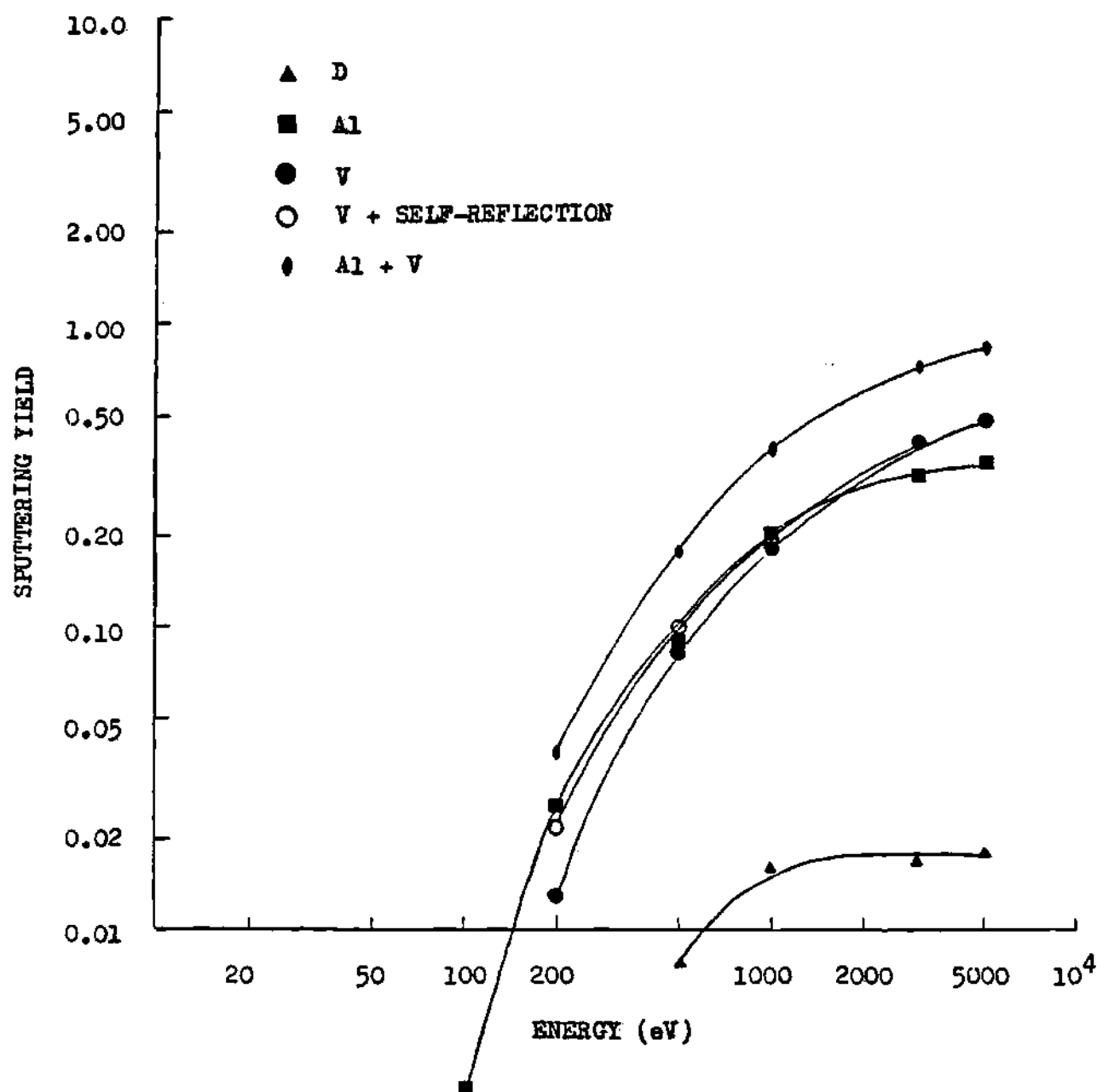
Figure 5.17   Partial Sputtering Yields of Vanadium from a Al
             Overlayer on Elemental V for D, Al, and V Projectiles
             (TRIM Calculation)
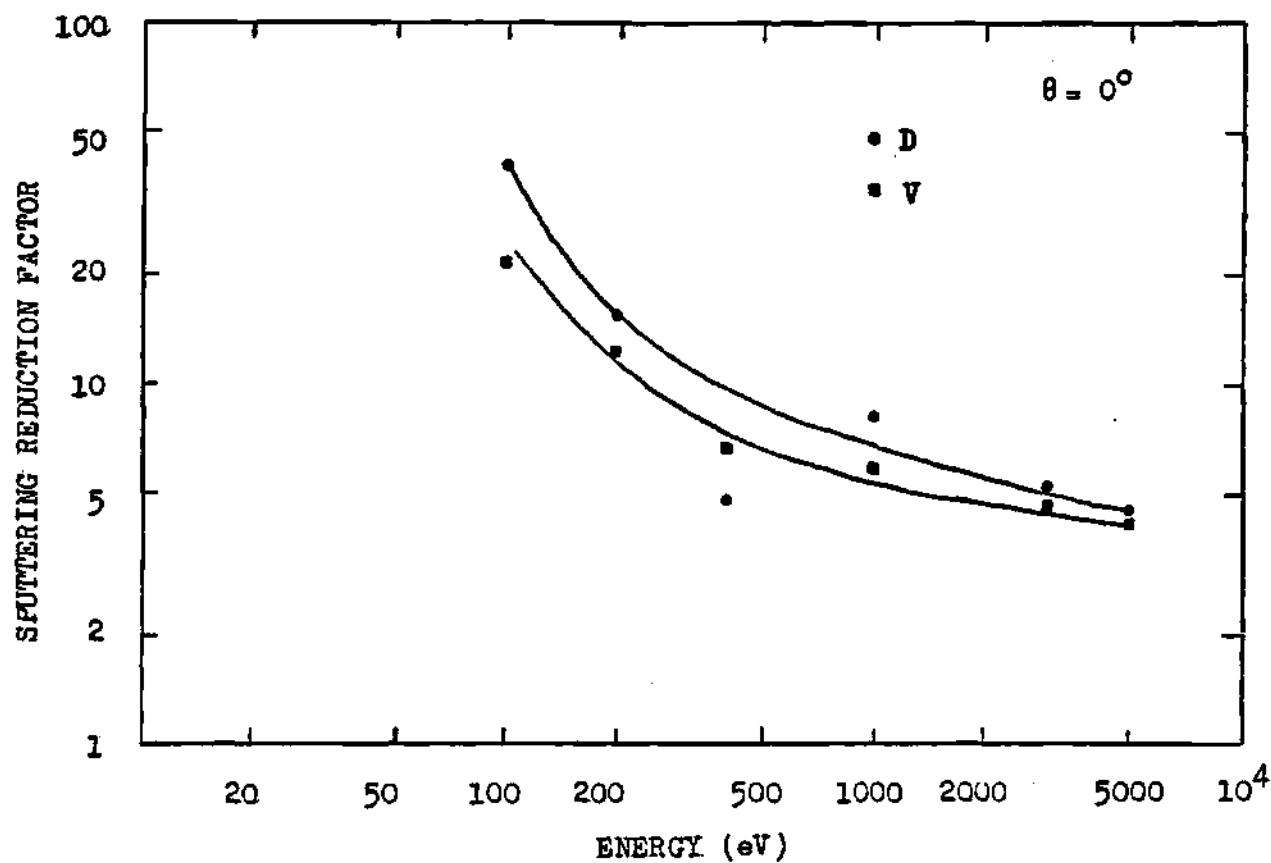
Figures 5.18 a,b
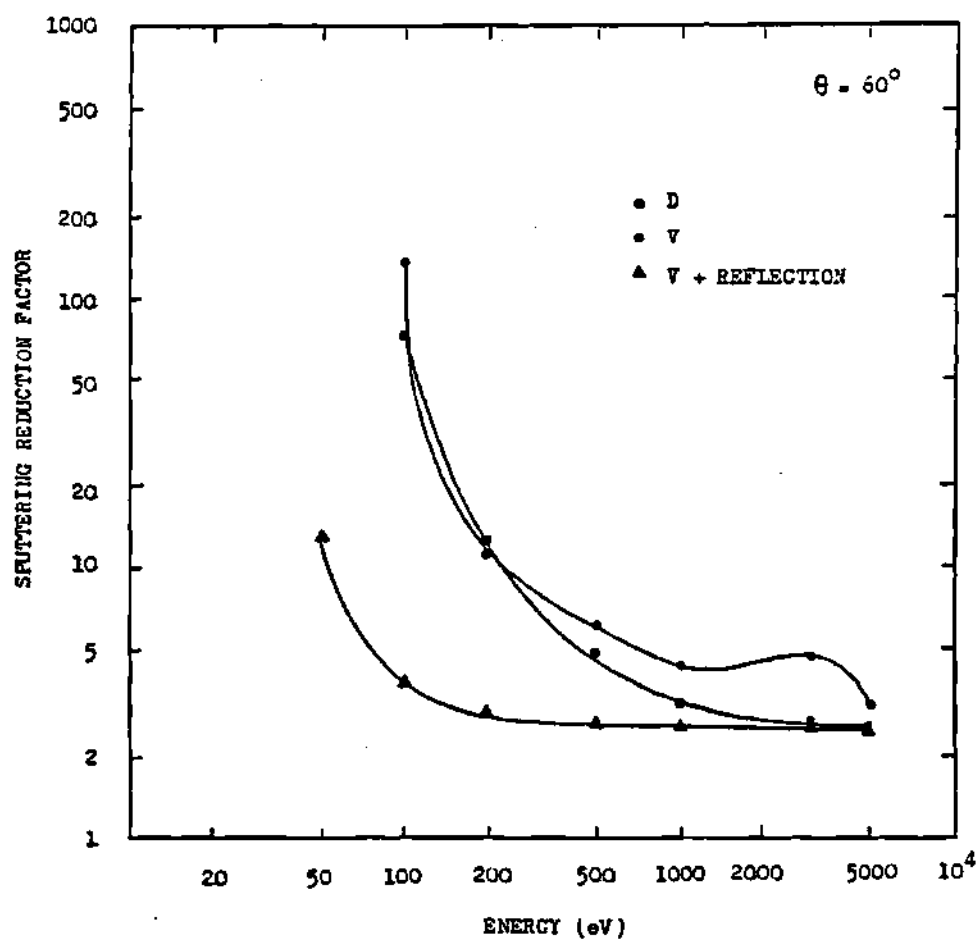
all thin-film systems, the solute metal contribution to the solvent sputtering must be considered as well. With the coupling of the Al and the V sputtering yield dependences (Figure 5.17), the "unity" self-sputtering energy occurs in the 8 to 9 keV range. Hence, even with the inclusion of the solute vanadium erosion yield, a factor of 10 gain is obtained in the energy limitation of vanadium sputter erosion.

The sputtering yield behaviour of the aluminum from the V-Al alloy is bracketed in terms of the surface binding energy assumed for an aluminum atom residing on a vanadium matrix. At the low end, an aluminum atom is treated as having a surface energy equal to that of elemental aluminum (3.32 eV), and at the high end, an aluminum atom is treated as having a surface energy comparable to elemental vanadium (5.28 eV). From the phase diagram for dilute V-Al alloys [224], the melting temperature is not affected by the aluminum concentration; hence, the binding energy of aluminum in the vanadium matrix approximates the vanadium binding energy. Therefore, an aluminum atom residing on a vanadium surface probably has a surface binding energy representative of the vanadium surface binding energy.

Both the low end and the high end (surface binding energy) aluminum sputtering yield dependences are given by Figures 5.19 a,b for the V-Al alloy. The aluminum sputtering (if predominantly neutral atoms) severely limits the maximum
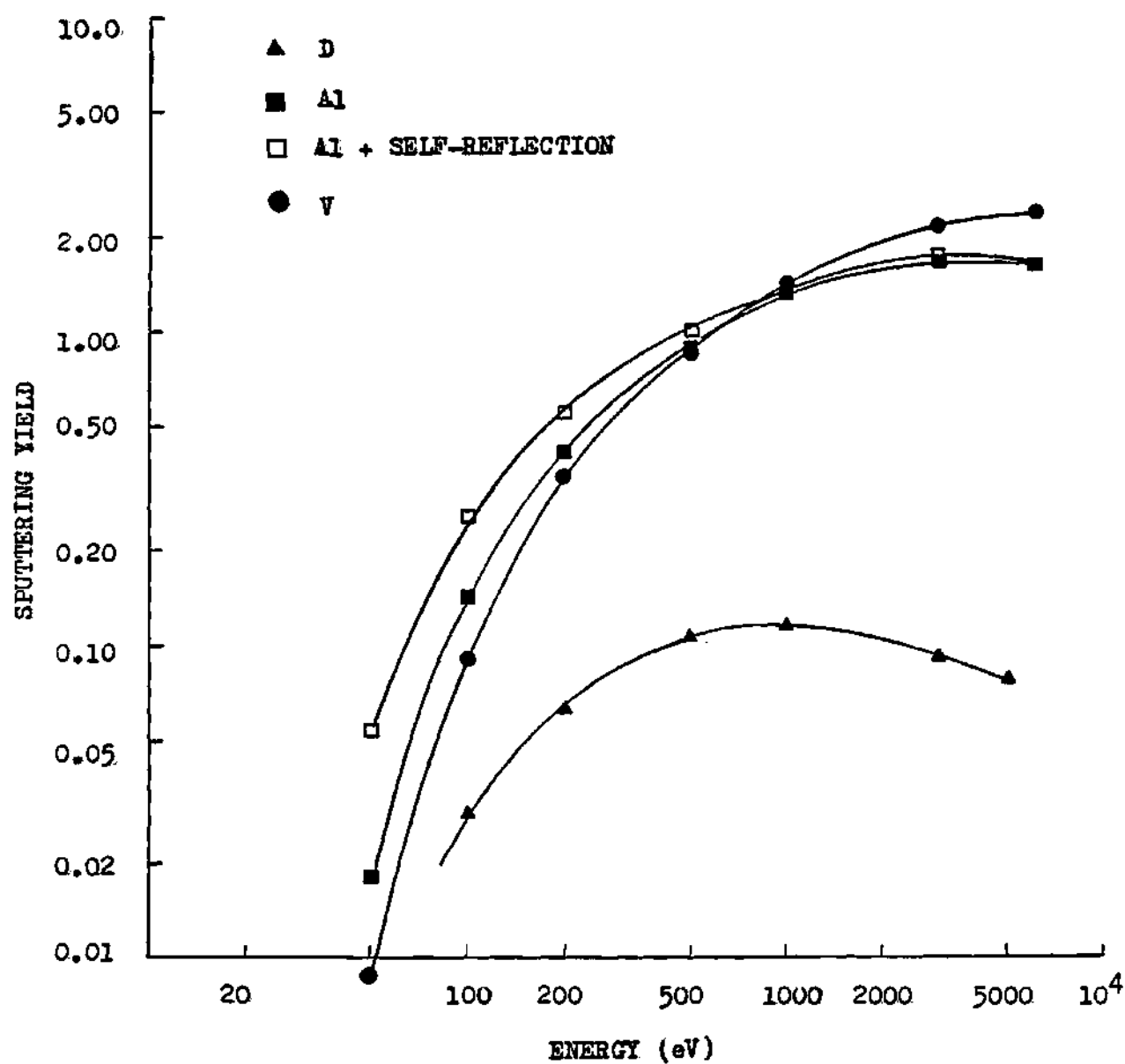
Figure 5.19a   Partial Sputtering Yields of Aluminum from an Al
              Overlayer on Elemental V for D, Al, and V Projectiles
              with Al Surface Binding Energy of 3.32 eV
              (TRIM Calculation)
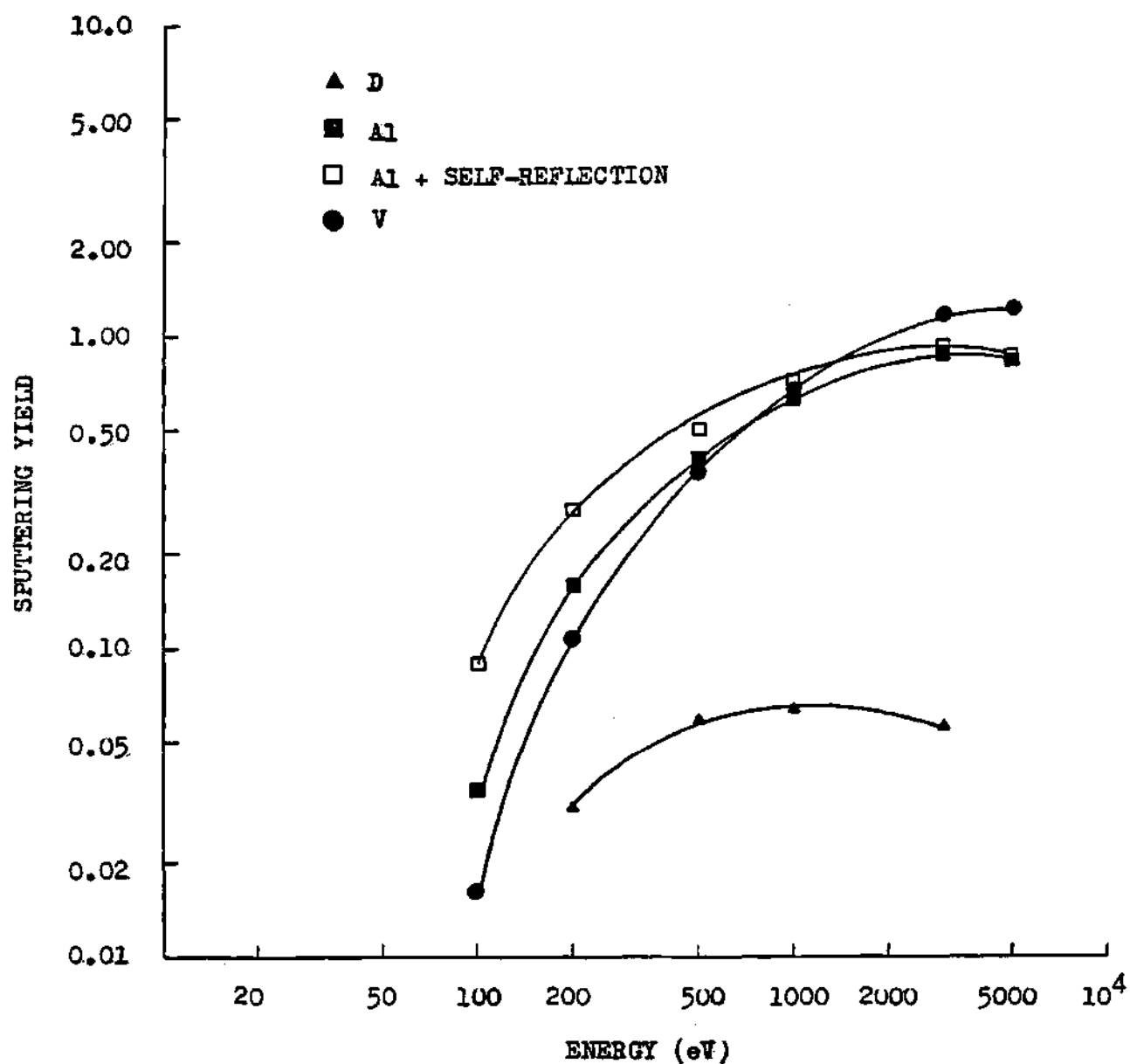
Figure 5.19b   Partial Sputtering Yields of Aluminum from an Al
Overlayer on Elemental V for D, Al, and V Projectiles
with Al Surface Binding Energy of 5.28 eV
(TRIM Calculation)

allowable heavy-ion (Al and V) impact energy. The cumulative Al+V sputtering yield dependence for the low binding energy results in a unity sputtering threshold energy of 250 eV. With the inclusion of aluminum self-reflection, the limiting impact energy drops to 200 eV; in addition, inclusion of light-ion sputtering would further reduce the unity threshold sputtering energy. At the high end surface binding energy, the cumulative Al+V aluminum erosion yield results in a unity threshold energy of 650 eV. Hence, even if the aluminum binding energy approximates vanadium, the V-Al alloy system is sputter-erosion limited by an impact energy less than that of pure vanadium. The secondary-ion fraction for an aluminum atom sputtered from a vanadium surface is experimentally unknown; however, from an optimistic extrapolation of theoretical/experimental considerations, the fraction is not expected to exceed 20 to 30 percent. If a 30% secondary-ion fraction is assumed for aluminum, the high end Al sputtering energy threshold is comparable to elemental vanadium, being equal to 1000 eV. However, both the sputtering of vanadium and aluminum must be considered in the estimation of a threshold energy, and such a consideration at best yields an upper impact energy of 700 eV for both species. A calculation of the maximum plasma-edge temperature for the V-Al alloy in the presence of a sheath (based on Equation 5.2.1) yields a limiting value of 60 eV; whereas, for elemental vanadium, a limiting value of 90 eV results.

While the V-Al alloy performs worse than elemental vanadium (in terms of erosion considerations), the benefit is that aluminum erosion has been substituted for vanadium erosion within a tolerable plasma-edge temperature limitation. Lowering the atomic number of the sputtered species, correspondingly, reduces plasma radiation losses. The hypothetical one-for-one substitution of aluminum for vanadium would account for a reduction of the bremmstrahlung radiation by 70%.

5.8 W-Be Sputtering Behaviour

The sputtering coefficients of the W-Be alloy are defined in terms of the limiting sheath potential conditions where light-ions (D, T, He, and Be) impact at 60 degrees and the solvent metal (W) impacts at normal incidence. Again modeling the solute enriched surface of a dilute W-Be alloy as a monolayer of Be on a W substrate, the solvent sputtering yield dependences, as calculated by TRIM, are presented in Figure 5.20. The tungsten self-sputtering threshold energy of the Be overlayer on W system alone is 4400 eV, and when the Be contribution to W sputtering is included, the threshold energy is lowered to 3800 eV. The light-ion sputtering yields are relatively insignificant for the current system. In contrast to the Be overlayer on W, the

Figure 5.20   Partial Sputtering Yields of Tungsten from a Be
Overlayer on Elemental W for Be and W Projectiles
(TRIM Calculation)

elemental tungsten "unity" self-sputtering energy is 1000 eV (TRIM result); thus, the addition of only one atomic layer of beryllium on tungsten significantly lowers the tungsten erosion. A reduction of heavy-ion sputtering (W) by a factor of 150 is observed at low energy (200 eV), while at high energies ~O(1000 eV), a sputtering reduction in the range of four to eight is obtained (Figure 5.21 a). If tungsten were to impact at an oblique angle (e.g., 60 degrees), the self-reflection yield negates any beneficial shielding effect of the beryllium (Figure 5.21 b) at low energies. For light-ions (modeled by Be), the reduction in normal incidence sputtering varies over the range of five to ten for impact energies in the range of 1000 eV to 200 eV.

The beryllium sputtering behaviour of the Be overlayer on W system is a bleak proposition at best in comparison to elemental tungsten. If only Be impact erosion is considered, the "unity" sputtering threshold energy is 350 eV, and when self-reflection is included, the threshold energy reduces to 85 eV (Figure 5.22). The TRIM yields as presented are based upon the assumption that a beryllium atom on a tungsten surface behave similarily to that of an elemental beryllium surface. Information on dilute W-Be alloys is "sketchy," and no basis exists for extrapolating a surface binding energy that would greatly exceed elemental beryllium. Also, secondary-ion data (experimental or theoretical) are lacking for the W-Be alloy. From the sputtering behaviour of the Be
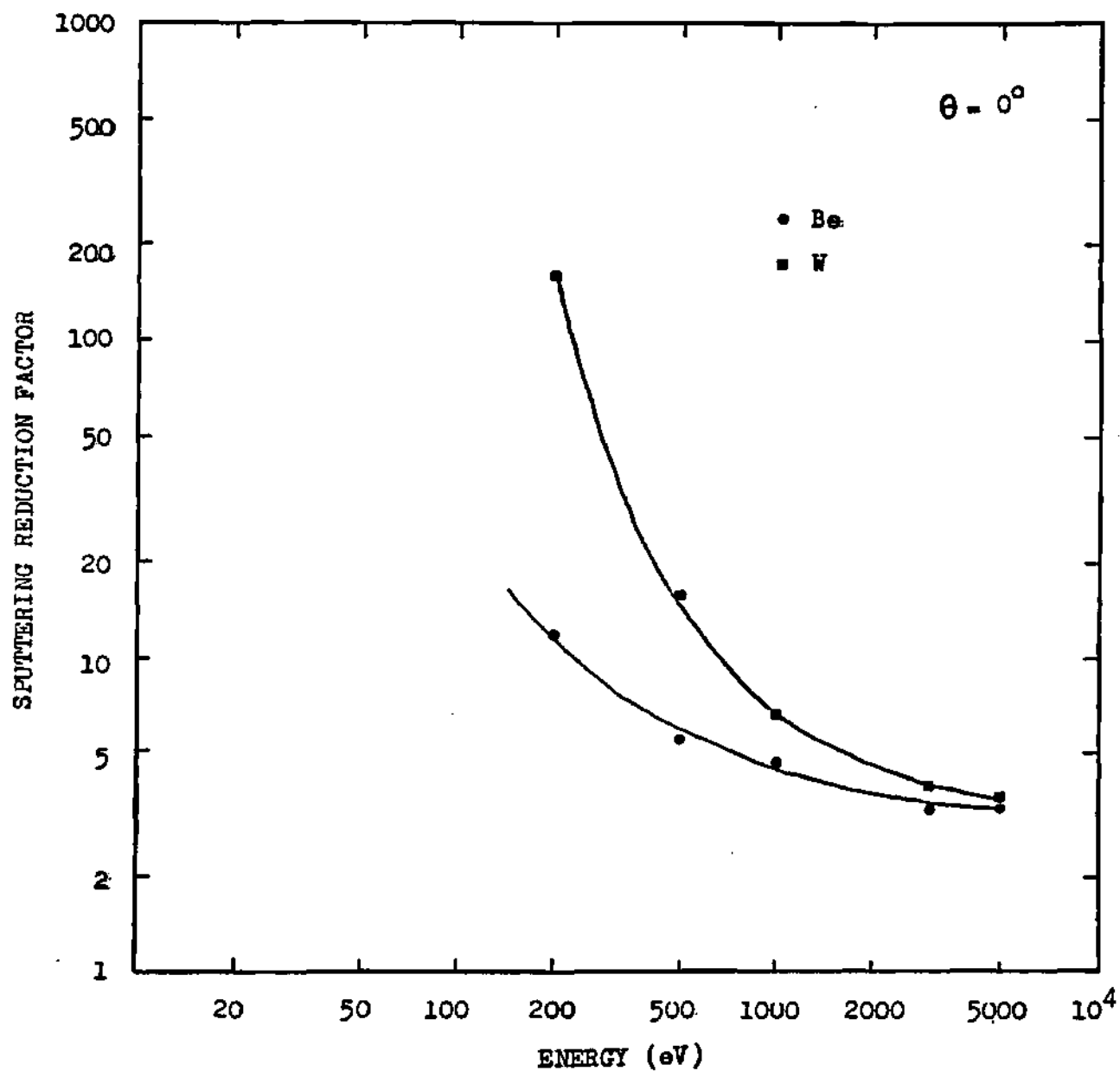
Figure 5.21a   Sputtering Reduction Factor of a Be Overlayer on Elemental W in Comparison to Elemental W for Tungsten Sputtering at Normal Incidence (TRIM Result)
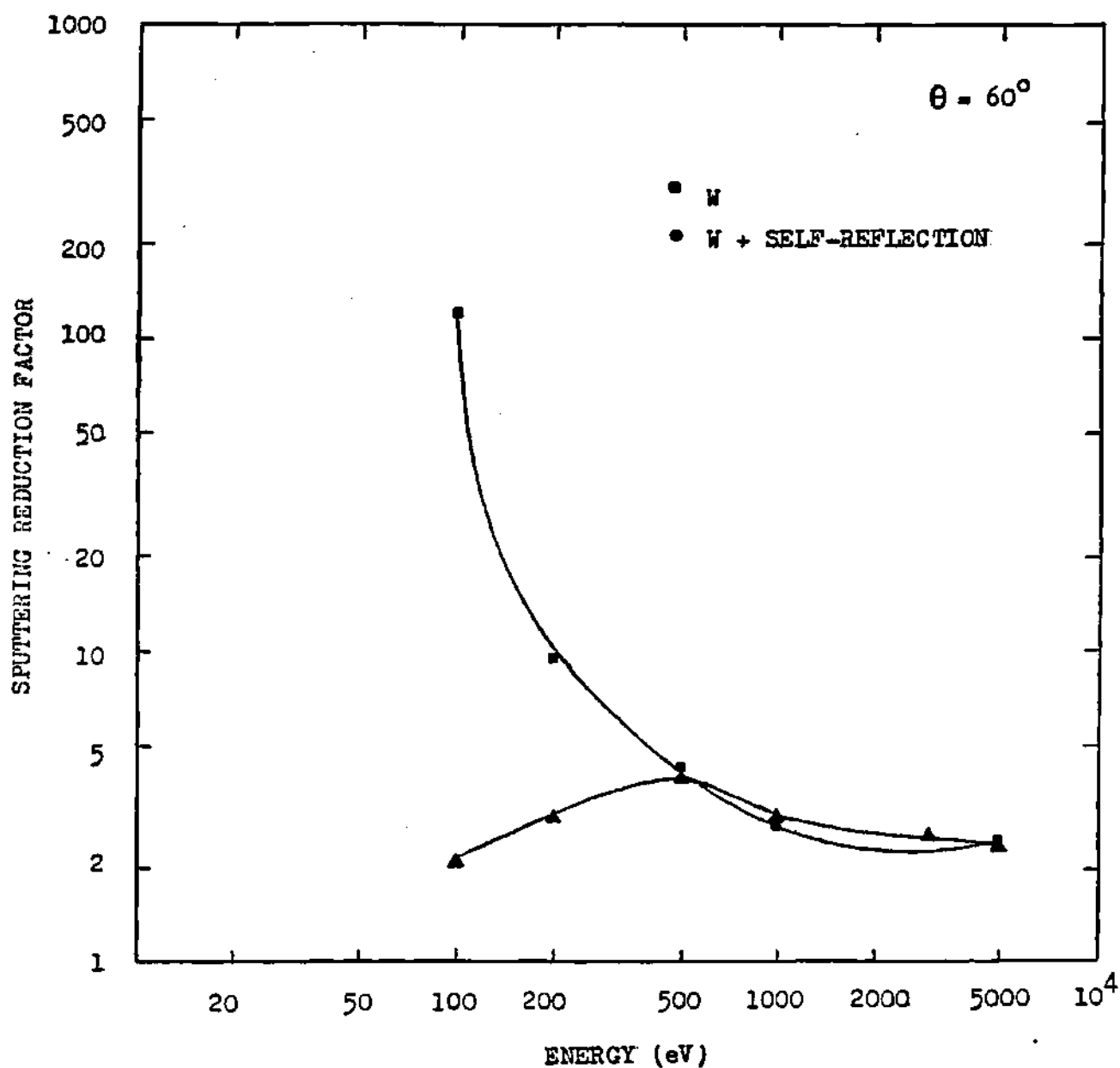
Figure 5.21b Sputtering Reduction Factor of a Be Overlayer
              on Elemental W in Comparison to Elemental W
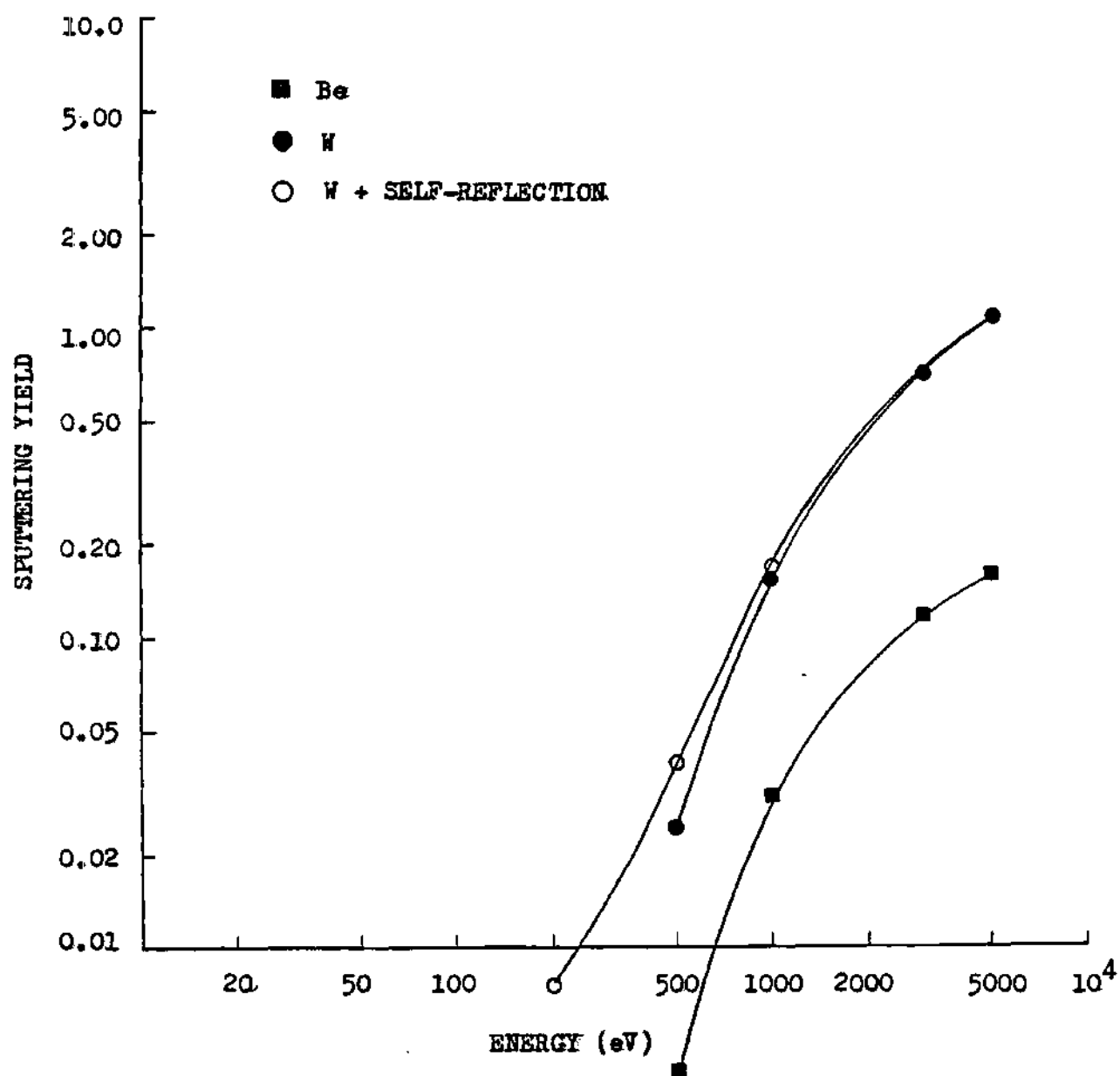   for Tungsten Sputtering at 60 Degrees Impact
              (TRIM Result)
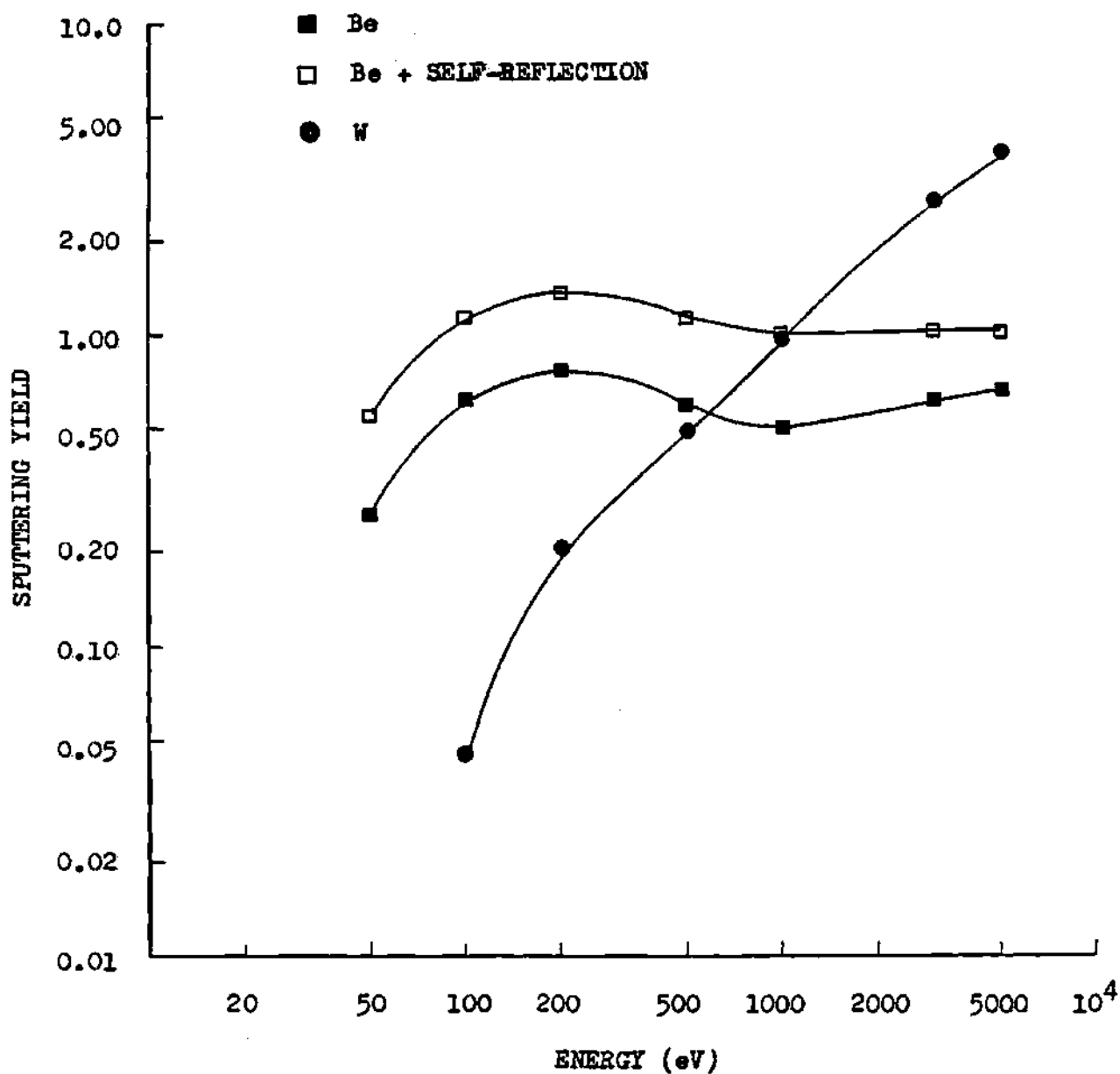
Figure 5.22   Partial Sputtering Yields of Beryllium from a Be
Overlayer on Elemental W for Be and W Projectiles
(TRIM Calculation)

overlayer on W system, though, it is clear that a high secondary-ion (Be) fraction is necessary if the system is to be viable from an erosion standpoint.

CHAPTER VI

Conclusions and Recommendations

The analysis of self-sustaining (low-Z) "thin-films" as a means of fusion plasma impurity and wall erosion control has required the development and/or extension of potential sheath, sputtering mechanics, and metal kinetics models. The application of these models inherently has assumed a "worst case" scenario, namely, that of a potential field with a grazing magnetic field angle. Angular impact behaviour as determined from the plasma-edge sheath modeling has provided the parameterization necessary for calculating the sputtering yields of thin-film alloys (Cu-Li, V-Al, W-Be). The sputtering and damage characteristics (for the Cu-Li alloy alone) either on on an elemental basis or an alloy component concentration basis have been used to determine the alloy (atom-defect) kinetics for (expected) fusion reactor operating conditions. Thus, in an heuristic manner, the model simulation of the thin-film (monolayer) concept may be analyzed within a coupled plasma-wall framework.

A self-consistent kinetic sheath model has been developed for arbitrary plasma-edge and magnetic angle conditions. It has been proven that potential is not a function of magnetic angle in contrast to Chodura's results

[51]; hence, the primary particle impact energy is independent of magnetic angle. However, the impact angle of the primary particles functionally is dependent upon the magnetic angle, thereby qualitatively verifying the results of Chodura for hydrogen impact.[68] Resulting from the current research, the impact angle is a function not only of the magnetic angle but also of particle mass, plasma-edge density, and plasma-edge temperature. It has been concluded that if the plasma-edge Debye length is larger than the ion gyroradius, all ion species will impact at oblique angles for grazing magnetic angles. If the ion gyroradius is larger than the plasma-edge Debye length, the impact angle for heavy-ions is aligned closer to the surface normal even at oblique magnetic angles, while for light-ions, the impact angle closely coincides to the magnetic angle. For the fusion edge conditions of $n_e \gtrsim O(10^{19} m^{-3})$ and $T_e \lesssim O(10^2 eV)$, heavy-ions may be assumed to impact normally, while light-ions may be assumed to impact at angles of 60° or less for magnetic angles of 80 degrees or less.

Elemental sputtering behaviour for light and heavy ion/atom impact, as calculated by the modified TRIM model, has been experimentally confirmed. The agreement between experiment and the modified TRIM model has not required the adjustment of the underlying scattering physics (such as modifying the interatomic potential, electronic energy losses, or atomic binding energies) unlike previous TRIM and

MARLOWE model prescriptions. Generalization of the TRIM framework to multi-component and multi-layer systems has provided the means for simulating heterogeneous materials under energetic particle bombardment. The calculated sputtering yields determined for Al-Li and Cu-Li alloys are within 25% of the measured experimental values. Due to approximations made in the collision energy dissipation, the validity of the absolute sputtering yields for elemental and alloy systems becomes questionable for heavy-ion impact energies less than 200 eV. However, the sputtering reduction factor of a self-sustaining overlayer on a solvent element in comparison to the elemental solvent is found to be relatively independent of approximations employed within the TRIM mechanics.

In the sputtering analysis of the thin-films systems, Cu-Li exhibits an extremely high self-sputtering threshold of 3100 eV in comparison to elemental copper of 350 eV, with the assumption that lithium is predominately (> 90%) sputtered as a secondary-ion. Such a high self-sputtering threshold energy makes the Cu-Li alloy potentially advantageous in comparison to elemental refractory metal systems such as tungsten and vanadium which have "unity" self-sputtering energies of 1000 eV. Simple plasma-sheath considerations suggest that plasma-edge temperatures in excess of 100 eV should be attainable for a Cu-Li alloy. Indeed, in a postscript to the thesis research, recycling/redeposition

calculations using the sputtering coefficients for the Cu-Li alloy assuming 60 degree light-ion impact and normal heavy-ion impact confirm that Cu-Li is not restricted by a short erosion lifetime for medium edge temperature operation ($\sim$150 eV).[225]

The sputtering analysis of the V-Al system shows that no gain can be made in plasma-edge temperature, rather the benefit is one of reducing radiation losses by substituting sputtered aluminum for sputtered vanadium. The quantitative projections of the V-Al alloy are limited due to the unknown secondary-ion emission coefficient of Al from V-Al and the surface behaviour of Al in terms of binding energy and self-sustaining overlayer thickness.

A sputtering analysis of the W-Be alloy suggests that unless the secondary-ion fraction of Be from the Be/W surface is significant (>50%), then the W-Be alloy is unfeasible as a fusion reactor plasma contact material. If beryllium sputters from the W-Be alloy as a neutral atom only, the Be self-sputtering energy is only 85 eV, thus limiting the plasma-edge temperature to 10-15 eV in the presence of a plasma sheath. Again, projections for the W-Be system are hampered by the experimental unknown secondary-ion emission behaviour of Be from a Be/W surface and any unknown surface characteristics that may positively impact the present bleak outlook for a W-Be "thin-film" system.

In general, the calculated sputtering yields indicate

that low-Z self-sustaining monolayer systems must be secondary-ion emitting if wall erosion control is to be sustained. Furthermore, without significant secondary-ion emission, the plasma-edge temperature for the thin-film systems is lower than those for the elemental solvents and, at best, provide a benefit in terms of reduced plasma-edge radiation losses. A better (proposed) system than Cu-Li is that of a high-Z self-sustaining monolayer for maximum erosion protection in conjunction with a high secondary-ion fraction (if possible) to attain the maximum allowable plasma-edge operating conditions.

The application of the atom-defect kinetics to the Cu-Li alloy verifies that lithium enrichment of the surface can be sustained although not to the degree observed experimentally. The discrepancy between experiment and the metal kinetics model suggests that preferential sputtering is not the determinant mechanism for alloy surface concentrations at equilibrium as is normally assumed for irradiated alloy systems. Hence, other atom-defect mechanisms must "play" an important role in the kinetic evolution as well as the equilibrium conditions of alloys, especially where there exists a large mass disparity between the alloying components as in Cu-Li.

Lithium subsurface enrichment which acts as a reservoir "feeding" the self-sustainment of a surface Li monolayer is dependent upon the displacement damage profile. The damage

region is analogous to a lithium "sink"; hence, if the damage region is removed from the surface, the subsurface lithium enrichment, likewise, is removed from the surface. Heavy-ion impact guarantees surface damage, whereas light-ion impact may result in subsurface damage sufficiently removed from the surface so as to prevent the self-sustainment of a Li overlayer. Low-energy light-ion impact guarantees a near-surface damage region; however, the relative depletion of solute to solvent due to preferential sputtering increases for decreasing impact energy. For current (anticipated) fusion plasma-edge conditions, the light-ion impact damage will be within the near-surface. Kinetic model simulations indicate a substantial lithium surface and subsurface enrichment for high secondary-ion yields in agreement with Cu-Li irradiation experiments. Thus, the overall inference from plasma sheath, sputtering mechanics, and metal kinetics arguments in conjunction with available experimental Cu-Li data and recent plasma-edge recycling calculations, suggests that a Cu-Li thin-film system may provide an alternative means of controlling the fusion plasma impurity and wall erosion problems for high secondary-ion (Li) yields.

In the conclusions presented, a number of simplifications and assumptions have been made in the underlying physics of sheath potential, sputtering, and atom-defect migration phenomena in order to analyze the self-sustaining "thin-film" systems. Kinetic electrons have

been ignored in the sheath modeling, empirical approximations have been made within the TRIM simulations, and preferential sputtering has been assumed to be the dominant mechanism for determining surface concentrations for an irradiated alloy (kinetics approach). An outline for recommended (future) research follows that is based on the removal of the limiting constraints and conditions within the present modeling.

If kinetic electrons are included in the sheath potential formalism, a "truer" response of the electrons to all processes (primary/secondary) affecting the sheath space-charge region would result. Hence, secondary emission of electrons due to electron impact and high secondary-ion emission effects upon the sheath profile and/or magnitude could be analyzed. Furthermore, some of the numerical/computational schemes devised to insure a stable sheath development, perhaps, could be "lifted" since an assumption of Boltzmann electrons fixes the background behaviour (rigidity of the solution). The inclusion of kinetic electrons, ultimately, allows for the direct coupling of the wall material to the plasma. In short, secondary processes affect the primary-particle distributions that have been assumed as constant boundary conditions. Thus, if the boundary conditions evolve in time due to wall effects, a corresponding effect upon the sheath potential evolution would occur that may alter the potential profile and potential magnitude behaviour and may even affect

primary-particle impact quantities.

Within the TRIM development, the most serious defect is the inaccuracy of low-energy sputtering yields for heavy-ion impact. Refinement of the empirical approximations made to the inelastic energy losses and the interatomic potential may provide the means of rectifying current discrepancies. The importance of cascade mixing for alloys of significant mass disparity (Cu-Li and W-Be) could be modeled with TRIM, thereby providing a means of investigating cascade mixing (as a funtion of solute concentration) upon the metal kinetics of irradiated materials. Also, TRIM investigations of the DPA profile as a function of solute concentration would be of importance in further understanding the kinetic evolution of irradiated alloys.

The identification of atom-defect mechanisms to explain the surface concentration in lieu of preferential sputtering for alloys with a significant mass disparity is necessary so that the behaviour for various fusion operating conditions may be predicted. Surface effects, precipitation, a time-dependent DPA profile, a time-dependent cascade mixing factor, and uncertainties in the material parameters, if accounted for, probably provide the means for accurately simulating irradiated alloys. Also, the kinetic modeling as presented with some minor modifications can and should be extended to model bcc alloys.

Finally, a comprehensive analysis of all possible binary

alloy combinations compatible with the bulk property constraints of fusion reactor materials should be carried out to identify other (if any) "thin-film" systems comparable or better than those presented within the current research.

Appendix A

Plasma-Edge Primary-Ion Velocity Coordinates

The half-Maxwellian distribution in the x-direction and the full Maxwellian distribution in the plane perpendicular to the x-direction of primary ions streaming into the presheath region are represented by the probability functions

$$p\left(\nu_1\right) = \frac{2}{\sqrt{\pi}}\, e^{-\nu_1^2} \quad ; \quad 0 < \nu_1 < \infty \tag{A.1a}$$

$$p\left(\nu_2\right) = \frac{1}{\sqrt{\pi}}\, e^{-\nu_2^2} \quad ; \quad -\infty < \nu_2 < \infty \tag{A.1b}$$

where ν_1^2 and ν_2^2 are defined as

$$\nu_1^2 \propto \left(V_x - V_{s.}\right)^2 \tag{A.2a}$$

$$\nu_2^2 \propto V_y^2,\ V_z^2 \tag{A.2b}$$

The Monte Carlo technique employed to pick values of ν from the function $p(\nu)$ is prescribed by [A1]

$$\nu = \left\{ - \ln(r) \right\}^{1/2} \tag{A.3}$$

where r is a random number selected uniformily over the interval $[0,1]$.

Furthermore, the velocities in the plane perpendicular to the magnetic axis, v_y and v_z, must uniformily represent all phase angles over the interval $[0,2\pi]$. The phase angle is simply given by

$$\vartheta = 2\pi p \tag{A.4}$$

where p is randomly selected over the interval $[0,1]$.

Rearranging equations A.2 and making use of the expressions for ν and ϑ, the velocity coordinates v_x, v_y, and v_z yield

$$V_x = \beta_{\parallel} \left\{ - \ln(r_{\parallel}) \right\}^{1/2} + V_s \quad ; \quad r_{\parallel} \left[0,1 \right] \tag{A.5a}$$

$$V_y = \beta_{\perp} \left\{ - \ln(r_{\perp}) \right\}^{1/2} \cos \vartheta \tag{A.5b}$$

$$V_z = \beta_\perp \left\{ -\ln(r_\perp) \right\}^{1/2} \sin \vartheta \; ; \; r_\perp[0,1] \qquad \text{(A.5c)}$$

The velocity constants $\beta_{\shortparallel}$ and $\beta_\perp$ satisfy the conditions that the primary-ion Maxwellian energy is partitioned kT/2 parallel to the magnetic axis and kT perpendicular to the same axis.

$$\beta_{\shortparallel} = \left(\frac{kT}{m} \right)^{1/2} \qquad \text{(A.6a)}$$

$$\beta_\perp = \left(\frac{2kT}{m} \right)^{1/2} \qquad \text{(A.6b)}$$

Prescription of the flow velocity, v_s, setup by the "weak" electric field over the physical space preceding the sheath should reflect a quasi-collisional regime; that is, the flow velocity lies between the collisional (sound speed) and the collisionless (kinetic) limits. In the mechanics outlined by Emmert et al. [48], collisionality effects within the plasma are replaced by source terms to kinetically model the collisionless flow velocity limit preceding the sheath. If all ions are assumed to be born thermally at the

sheath edge $(x'=0)$, then the flow velocity would be defined as [48]

$$V_s = \left(2 \, \Psi_s T_e / m_i \right)^{1/2} \qquad \text{(A.7a)}$$

where $\Psi_s = e \, \phi_s / kT$ and ϕ_s is the potential at the plasma side of the sheath. In reality, the ion flow velocity is randomly developed upstream from the sheath-edge such that

$$V_s = \left\{ 2 \left(\Psi_s - \Psi \right) T_e / m_i \right\}^{1/2} \qquad \text{(A.7b)}$$

where Ψ varies randomly in a nonuniform fashion over the interval $[0, 0.85]$.[48] The above treatment of the flow velocity is kinetically consistent across the sheath boundary $(x'=0)$ as opposed to the commonly used sound speed approximation to the flow velocity where a coupling of fluid theory to kinetic theory is assumed at the sheath boundary.[A2] The sound speed is formulated as

$$V_s = \left\{ \left(\gamma_i T_i + \gamma_e T_e \right) / m_i \right\}^{1/2} \qquad \text{(A.8)}$$

where γ_i and γ_e are temperature constants of the ion species and the electrons, respectively. Chodura employs the ion sound speed approximation, choosing $\gamma_i = 5/3$ and $\gamma_e = 1$.[68] Much

of the current research represents a compromise between the collisional and collisionless limits where the flow velocity is equated to the ion thermal velocity such that

$$V_S = \left(\gamma_i \, T_i / m_i \right)^{1/2}$$

(A.9)

and $\gamma_i = 5/3$.

Appendix B

Electronic Excitation Integral

The inelastic energy loss per unit velocity integral, Y_{ek}, of the Karpusov model is defined as [115]

$$Y_{ek} = \int_{r_0}^{\infty} \frac{(1 - V(r)/E_c)}{\left[1 - V(r)/E_c - p^2/r^2\right]^{1/2}} f(r_k)\, dr \qquad (B.1)$$
$$; \quad k = 1, 2$$

It is computationally convenient to evaluate Y_{ek} in reduced units (dimensionless distance and energy). Thus, the transposition of the integral into reduced terms yields

$$\frac{V(r)}{E_c} = \frac{\phi(x)}{\epsilon X} \quad ; \quad \epsilon = \frac{Z_1 Z_2 e^2}{a_s E_c} \qquad (B.2a)$$

$$b = p/a_s \qquad (B.2b)$$

$$f(r_k) = f(c_k x) \quad ; \quad c_k = \alpha_k Z_k^{1/3} \frac{a_s}{a_0} \qquad (B.2c)$$

such that

$$Y_{ek}(\varepsilon, b) = a \int_{X_0}^{\infty} \frac{\left(1 - \frac{\phi(x)}{\varepsilon x}\right)}{\left\{1 - \frac{\phi(x)}{\varepsilon x} - \left(\frac{b}{x}\right)^2\right\}^{1/2}} f(c_k x)\, dx \qquad \text{(B.3)}$$

The evaluation of the screening potential integral, $f(c_k x)$, is well approximated by the integral exponential function where

$$Ei(z) = -\int_{z}^{\infty} t^{-1} \exp(-t)\, dt \qquad \text{(B.4)}$$

if the potential is of an exponential behaviour as is the universal Moliere function. The square of the Moliere potential necessitates the evaluation of a six term exponential integral; however, it is sufficient to approximate $\phi^2(x)$ as a truncated three term series such that

$$f(r_k) = \sum_{j=1}^{4} D_j\, Ei(d_j r_k) \qquad \text{(B.5)}$$

where the coefficients D_j and d_j have the values (.1225,.385,.3085) and (.6,1.5,2.4), respectively.

Appendix C

Atom and Defect Fluxes

For any multicomponent (k=1,2,...,N) alloy system having j=1,2,...,M defect types, the total atom/defect fluxes can be partitioned into partial fluxes such that

$$\overline{J}_k = \sum_j \overline{J}_k^j \qquad (C.1)$$

$$\overline{J}_j = \sum_k \overline{J}_j^k \qquad (C.2)$$

Assuming that multiple and complex defect types can be adequately defined in terms of single interstitial and monovacancy concentrations (j=i,v), the partial fluxes are defined as

$$\overline{J}_k^i \equiv \overline{J}_i^i = -D_k^i \, \alpha \, \nabla c_k - D_i^k \nabla c_i \qquad (C.3)$$

$$\overrightarrow{J}_k^v \equiv \overrightarrow{J}_v^k = - D_k^v \alpha \nabla c_k + D_v^k \nabla c_v \qquad \text{(C.4)}$$

The thermodynamic factor, α, is a measure of the chemical potential gradient difference of the alloy constituents in a nonideal solution $(0 < \alpha < 1)$.

Substituting the above definitions into the total flux equations yields

$$J_k = - \left(D_k^v + D_k^i \right) \alpha \nabla c_k + D_v^k \nabla c_v - D_i^k \nabla c_i \qquad \text{(C.5a)}$$

$$J_i = - \sum_k \left(D_k^i \alpha \nabla c_k + D_i^k \nabla c_i \right) \qquad \text{(C.5b)}$$

$$J_v = \sum_k \left(D_k^v \alpha \nabla c_k - D_v^k \nabla c_v \right) \qquad \text{(C.5c)}$$

For a binary $(k=A,B)$ alloy the total flux equations simplify to

$$J_A = - D_A \alpha \nabla c_A + D_v^A \nabla c_v - D_i^A \nabla c_i \qquad \text{(C.6a)}$$

$$J_i = \left(D_B^i - D_A^i \right) \propto \nabla c_A - D_i \nabla c_i \qquad \text{(C.6b)}$$

$$J_v = \left(D_A^v - D_B^v \right) \propto \nabla c_A - D_v \nabla c_v \qquad \text{(C.6c)}$$

where definitions of the total diffusion coefficients (Equations 4.2.6a,b) and of $\nabla c_B = -\nabla c_A$ have been incorporated.

Appendix D

Substitutional Lithium (in Cu) Geometry Dependences

According to phase diagram data for Cu-Li [D1], lithium is substitutional in copper for atomic concentrations less than 20% after which compound precipitation of Cu_4Li initiates. The density of substitutional alloys (atoms of similar size) is normally prescribed as

$$\rho = \frac{\langle wt \rangle}{(.602 \times 10^{24}\ amu/g)\ a_{LC}^3} \tag{D.1}$$

where $\langle wt \rangle$ is the effective mass of the unit cell and a_{LC} is the alloy lattice parameter. Specifically, these quantities are defined as

$$\langle wt \rangle = BS\left\{ X_A M_A + X_B M_B \right\} \tag{D.2}$$

where BS is the basis of the unit cell (e.g., BS=4 for a fcc lattice), X and M are the atom fraction and mass, respectively, of solvent A or solute B;

$$a_{LC} = f_g \langle r \rangle \qquad\qquad (D.3)$$

where f_g is the lattice geometrical basis factor (e.g., $f = 4/\sqrt{2}$ for fcc) and $\langle r \rangle$ is the average alloy atomic radius (the concentrated weighted sum of the pure solvent and solute atomic radii).

However, experimental data do not justify the proceeding approach; for example, the predicted alloy density for Cu-18.6%Li (equation D.1) is 6.75 g/cm^3 while the experimental value is 7.24 g/cm^3.[D1] The experimental behaviour of the alloy lattice parameter and the average alloy volume versus the substitutional lithium concentration (Figures D.1,D.2) clearly indicates that a concentrated weighted atomic radius determined from the pure Cu and Li atomic radii is erroneous. In order to achieve a fit to the experimental data (assuming that solvent lattice atomic radius (1.278 Å) and volume (7.11 cm^3) remain constant), the lithium "atoms" must contract to an atomic radius of 1.335 Å and an atomic volume of 8.3 cm^3 compared to the pure lithium values of 1.51 Å [D2] and 12.8 cm^3.[D3] Such a reduction in the lithium atomic radius is indicative of a partial electron transfer (ionic lithium has a radius of .69 Å [D2]) which should be expected from a substitutional electropositive atom (Li) into an electronegative solvent (Cu) lattice. Thus, on
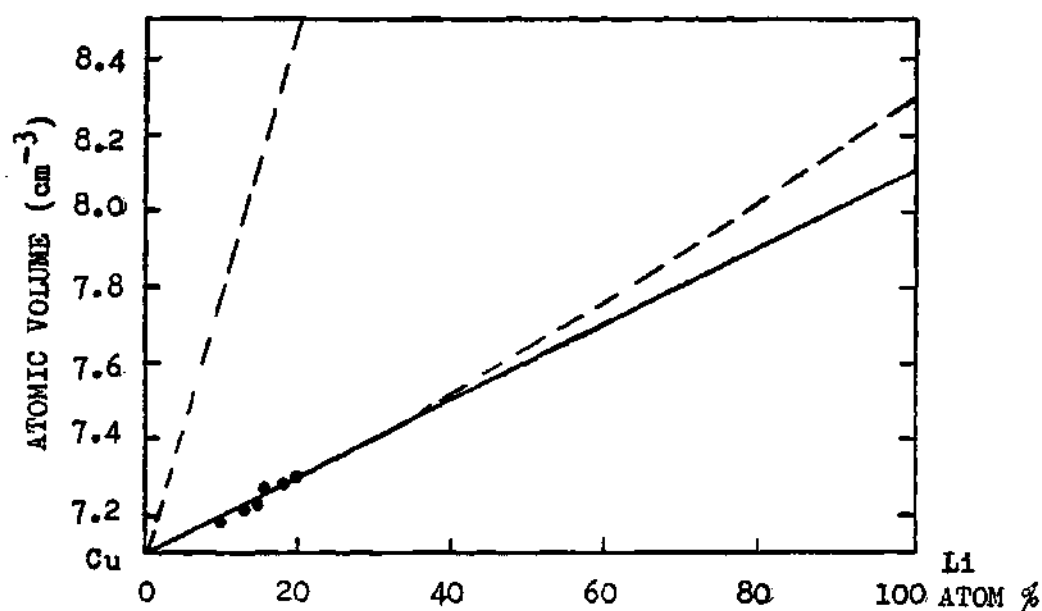
Figure D.1   Cu-Li Atomic Volume Dependence
upon the Atomic Concentration
of Lithium
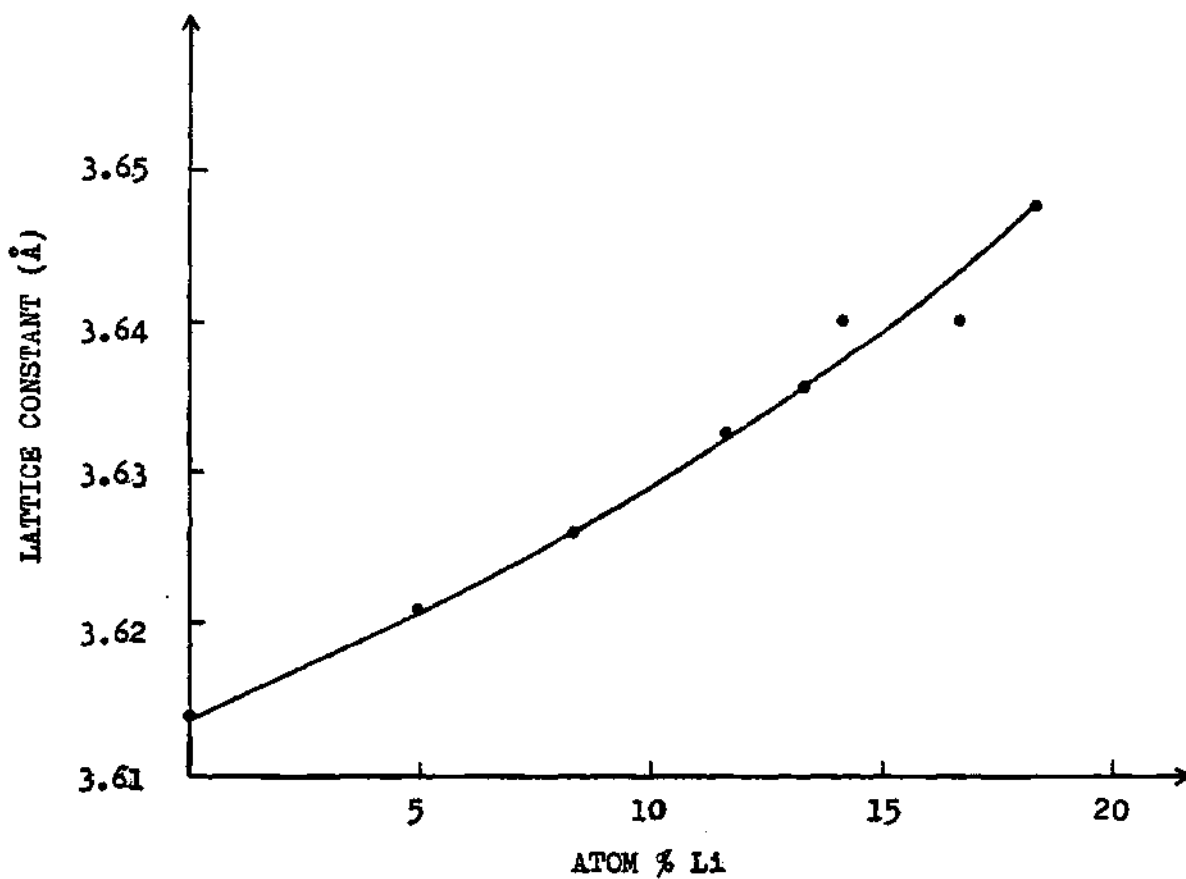
Figure D.2   Lattice Constant of Cu-Li as a Function
of the Substitutional Lithium (^{a}/o)

an atom per atom basis, the size mismatch between lithium and copper in the copper lattice is relatively small.

REFERENCES

[1] E. Teller, "Magnetic Confinement," Volume 1, Part A, published by the Academic Press, New York, NY, 1981.

[2] W.M. Stacey, Jr., "Fusion Plasma Analysis," published by John Wiley & Sons, New York, NY, 1981.

[3] G.M. McCracken and P.E. Stott, Nuclear Fusion 19(1979)889.

[4] R.J. Hawryluk, et. al., Nuclear Fusion 19(1979)1307.

[5] T. Tazima, Y. Nakamura, and K. Inoue, Nuclear Fusion 17(1977)419.

[6] M. Keilhacker, et. al., Eighth Conference Proceedings on Plasma Physics and Controlled Nuclear Fusion Research, July 1980.

[7] R.V. Jensen, D.E. Post, W.H. Grasberger, C.B. Tarter, and W.A. Lokke, Nuclear Fusion 17(1977)1187.

[8] M. Nagami, et. al., Eighth Conference Proceedings on Plasma Physics and Controlled Nuclear Fusion Research, July 1980.

[9] Y. Shimomura, Nuclear Fusion 17(1977)1377.

[10] D.E. Roberts, Nuclear Fusion 21(1981)215.

[11] A.V. Bortnikov, N.N. Brevnov, S.N. Gerasimov, V.G. Zhokovskij, N.V. Kuznetsov, S.M. Naftulin, V.I. Pergament, and L.N. Khimchenko, Eighth Conference Proceedings on Plasma Physics and Controlled Nuclear Fusion Research, July 1980.

[12] D.E. Post, "Data Requirements for Theory and Modeling of Impurity Control Techniques in Large Fusion Experiments," Proc. 6th Intl. Conf. on Plasma-Surface Interactions, Nagoya, Japan, May 14-18, 1984.

[13] INTOR Phase Two A Part I, IAEA, Vienna, STI/PUB/638, 1983.

[14] A.B. DeWald, GTFR-30, January 1982.

[15] M. Auweterming and H.O. Schrade, J. Nucl. Mater. 93/94(1980)799.

[16] P. Mioduszewski, R.E. Clausing, and L. Heatherly, J. Nucl. Mater. 91(1980)297.

[17] S.K. Sethuraman, P.A. Chatterton, and M.R. Barrault, J. Nucl. Mater. 111/112(1982)510.

[18] R. Kelly and O. Auciello, Surface Science 100(1980)135.

[19] V. Alexander, H.J. Lippold, and H. Niedrig, Rad. Eff. 56(1981)241.

[20] R. Behrisch, et al., J. Appl. Phys. 48(1977)3914.

[21] M. Kaminsky, Argonne National Laboratory, private communication 1982.

[22] TFR Group presented by P. Deschamps, J. Nucl. Mater., 76/77(1978)587.

[23] H.F. Dylla, J. Nucl. Mater. 93/94(1980)61.

[24] Y. Sakamoto et al., J. Nucl. Mater. 111/112(1982)485.

[25] N. Noda et al., J. Nucl. Mater. 111/112(1982)498.

[26] G.M. McCracken, J. Nucl. Mater. 93/94(1980)3.

[27] R.E. Clausing, L.C. Emerson, and L. Heatherly, J. Nucl. Mater. 93/94(1980)81.

[28] K. Hothker, W. Bieger, H. Hartwig, E. Hintz, and K. Koizlik, J. Nucl. Mater. 93/94(1980)785.

[29] W. Poschenrieder, G. Staudenmaier, and P. Staib, J. Nucl. Mater. 93/94(1980)322.

[30] W.M. Stacey, Jr. et al., "Impurity Control in Tokamak Reactors," Argonne National Laboratory, ANL/FPP/TM-91, August 1977.

[31] J.N. Brooks, Nuclear Technology/Fusion 4(1983)33.

[32] R. Yamada, K. Nakamura, K. Sone, and M. Saidoh, J. Nucl. Mater. 95(1980)278.

[33] J.M. Ogden, C.E. Singer, D.E. Post, R.V. Jensen, and F.G.P. Seidl, IEEE Trans. Plas. Sci. 9(1981)274.

[34] K. Nakamura, R. Yamada, M. Saidoh, and Y. Murakami, J. Nucl. Mater. 111/112(1982)852.

[35] R. Yamada, K. Nakamura, M. Saidoh, and Y. Murakami, J. Nucl. Mater. 111/112(1982)856.

[36] L. Keller, L. Oren, R.J. Taylor, F. Schwirzke, and R.F. Bunshah, and C.N.J. Wagner, J. Nucl. Mater. 111/112(1982)493.

[37] J. Cecchi, Proc. 6th Intl. Conf. on Plasma-Surface Interactions, May 14-18, 1984, Naygoya, Japan, J. Nucl. Mater. (in press).

[38] D.M. Mattox and M.J. Davis, J. Nucl. Mater. 111/112(1982)819.

[39]   A.R.   Krauss and D.M.   Gruen, J.   Nucl.   Mater. 93/94(1980)686.

[40] A.R.   Krauss, D.M.   Gruen, and A.B.   DeWald, 9th Symposium   of   Engineering   Problems   of   Fusion   Research, Chicago, Illinois, October 26-29, 1981, p.   1633.

[41]   A.R.   Krauss and D.M.   Gruen, J.   Nucl.   Mater. 103(1982)239.

[42]   A.B.   DeWald, J.N.   Davidson, A.R.   Krauss, and D.M. Gruen, J.   Nucl.   Mater.   111/112(1982)448.

[43]   A.R.   Krauss and D.M.   Gruen, J.   Nucl.   Mater. 85/86(1979)1179.

[44] L. Tonks and I. Langmuir, Phys. Rev.   34(1929)876.

[45] D. Bohm, "Minimum Kinetic Energy for a   Stable   Sheath," in   the   Characteristics of Electrical Discharges in Magnetic Fields,   edited   by   A.   Guthrie   and   R.K.   Wakerling, McGraw-Hill, New York 1949, pgs.   77-86.

[46] J.D. Cobine,   "Gaseous Conductors," Dover   Pub.   Inc., New York 1958, pgs.   134-142.

[47] A.E.   Robson and P.C.   Thonemann, Phys.   Soc.   of London Proc.   73(1959)508.

[48] G.A.   Emmert,   R.M.   Weiland,   A.T.   Mense,   and   J.N. Davidson, Phys.   Fluids 23(1980)803.

[49] J.G.   Laframboise   and   J,   Rubenstein,   Phys.   Fluids 19(1976)1900.

[50] U. Daybelge and B. Bein, Phys.   Fluids 24(1981)1190.

[51] R. Chodura, Phys. Fluids 25(1982)1628.

[52] P. Sigmund, Phys. Rev. 184(1969)383.

[53] D.A. Thompson, Radiation Effects 56(1981)105.

[54] H.E. Roosendaal and J.B. Sanders, Radiation Effects 52(1980)137.

[55] N. Matsunami et al., Radiation Effects Letters, 57(1980)15.

[56] T.J. Hoffman, H.L. Dodds, M.T. Robinson, and D.K. Holmes, Nucl. Sci. and Eng. 68(1978) 204.

[57] M.T. Robinson and I.M. Torrens, Phys. Rev. B, 9(1979)5008.

[58] J.P. Biersack and L.G. Haggmark, Nucl. Instr. Meth. 174(1980)257.

[59] D.L. Smith, J.N. Brooks, and D.E. Post, 9th Symposium of Engineering Problems of Fusion Research, Chicago, Illinois, October 26-29, 1981.

[60] Interim Report to the INTOR Workshop, Phase 2A, Session V, July 1982, USA Contribution, FED-INTOR/ICFW/82-13.

[61] J. Roth, J. Bohdansky, and W. Ottenberger, "Data on Low Energy Light Ion Sputtering," European Contributions to the 3rd Meeting of the INTOR Workshop, October 1-26, 1979.

[62] J. Roth, "Sputtering with Light Ions," Symposium on Sputtering, SOS, Wien (28.4-1.580) Osterreich (1980).

[63] P. Gierszewski, P. McKenty, J. McCullen, and, R. Morse, Phys. Rev. Lett. 49(1982)650.

[64] C.D. Boley, J.N. Brooks, and Y.K. Kim, Argonne National Laboratory, ANL/FPP/TM-171 (March 1983).

[65] David Potter, "Computational Physics," John Wiley & Sons Ltd., New York, 1973.

[66] C.K. Birdsall and A.B. Langdon, "Plasma Physics via Computer Simulation," Part I, Course Notes for UCLA, December 1978. Permagon Press, 1967.

[67] R. Chodura in European Community Contributions of the INTOR Phase-Two-A Workshop, Rep. Commission of the European Communities, Brussels (1982).

[68] R. Chodura, J. Nucl. Mater. 111/112(1982)420.

[69] G.D. Hobbs and J.A. Wesson, Plasma Phys. 9(1967)85.

[70] G. Fuchs and A. Nicolai, Nuclear Fusion, 20(1980) 1247.

[71] H. Bruining, "Physics and Applications of Secondary Electron Emission," Permagon Press, 1954.

[72] D.J. Gibbons, in "Handbook of Vacuum Physics," Vol. 2, Permagon Press, 1966.

[73] I.M. Bronshtein, B.S. Karasik, I.L. Krainskii, and I.I. Khinich, Soviet Phys. Solid State 16(1975)2248.

[74] R.A. Baragiola, E.V. Alonso, J. Ferron, and A. Oliva-Florio, Surface Science 90(1979)240.

[75] N. Benazeth, Nucl. Instr. Meth. 194(1982)405.

[76] L.M. Kishinevsky, Radiation Effects 19(1973)23.

[77] Homer D. Hagstrum, Phys. Rev. 96(1954)325.

[78] R.J. Beuhler and L. Friedman, J. Appl. Phys. 48(1977)3928.

[79] E.V. Alonso, R.A. Baragiola, J. Ferron, M.M. Jakas, and A. Oliva-Florio, Phys. Rev. B 22(1980)80.

[80] R.C. Abbott and H.W. Berry, J. Appl. Phys. 30(1959)871.

[81] W. Eckstein, "Springer Series in Chemical Physics," Vol.17, Editors: E. Taglauer and W. Heiland, Springer-Verlag Berlin Heidelberg, 1981.

[82] R.S. Bhattacharya, W. Eckstein, and H. Verbeek, Surface Science 93(1980)563.

[83] H. Verbeek, W. Eckstein, and S. Datz, J. Appl. Phys. 47(1976)1785.

[84] W. Eckstein, H. Verbeek, and R.S. Bhattacharya, Surface Science 99(1980)356.

[85] K. Wittmaack, Surface Science 53(1975)626.

[86] A. Benninghoven, Surface Science 53(1975)596.

[87] K. Komori and J. Okano, Inter. J. Mass Spect. and Ion Phys. 27(1978)379.

[88] M.A. Rudat and G.H. Morrison, Surface Science 82(1979)549.

[89] W.O. Hofer, H.L. Bay, and P.J. Martin, J. Nucl. Mater. 76/77(1978)156.

[90] A.R. Krauss and D.M. Gruen, J. Nucl. Mater. 63(1976)380.

[91] J.N. Brooks, "Plasma Sheath Region Near a Boundary with Positive Ion Backscattering", Argonne National Laboratory, ANL/FPP/TM-142 (April 1981).

[92] L.G. Haggmark and W.D. Wilson, J. Nucl. Mater. 76/77(1980)149.

[93] A.T. Macrander, "Modifications to the TRIM Monte-Carlo Simulation Program," DOE Report 4234 (unpublished) Contract no. DE-AS02-76ER03158.

[94] H. Goldstein, "Classical Mechanics," Addison-Wesley Pub. Co., Reading, Mass. 1950.

[95] O.B. Firsov, Soviet Physics JETP 7(1958)308.

[96] L.G. Haggmark and J.P. Biersack, J. Nucl. Mater. 93/94(1980)664.

[97] O.B. Firsov, Soviet Physics JETP 6(1958)534.

[98] J. Linhard, V. Nielsen, and M. Scharff, K. Dan. Vidensk Selsk. Mat. Fys. Medd. 36(1968)no.10.

[99] J.P. Biersack and J.F. Ziegler, Nucl. Instr. Meth. 194(1982)93.

[100] O.B. Firsov, Soviet Physics JETP 5(1957)1192.

[101] W.D. Wilson, L.G. Haggmark, and J.P. Biersack, Phys. Rev. B 15(1977)2458.

[102] reference (call up R.B. Wright)

[103] A.A. Abrahamson, Phys. Rev. 178(1969)76.

[104] L.G. Haggmark and J.P. Biersack, J. Nucl. Mater. 103(1982)345.

[105] S.A. Cruz, E.V. Alonso, R.P. Walker, D.J. Martin, and D.G. Armour, Nucl. Instr. Meth. 194(1982)659.

[120] J.O. Schiffgen, D.W. Schwartz, R.G. Ariyasa, and S.E. Cascadden, Radiation Effects 39(1978)221.

[121] F. Seitz, Faraday Soc. Discussions 5(1949)271.

[122] P. Vajda, Rev. Mod. Phys. 49(1977)481.

[123] A.S.A. Karim, M.E. Whitehead, M.H. Loretto, and R.E. Smallman, Acta. Met. 26(1978)975.

[124] R.S. Averback, R. Benedek, K.L. Merkle, J. Sprinkle, and L.J. Thompson, J. Nucl. Mater. 113(1983)211.

[125] M.W. Thompson, Phil. Mag. 18(1968)377.

[126] M. Hou and M.T. Robinson, Appl. Phys. 18(1979)381.

[127] D.P. Jackson and D.V. Morgan, Can. J. Phys. 53(1975)1513.

[128] M.J. Pellin, R.B. Wright, and D.M. Gruen, J. Chem. Phys. 74(1981)6448.

[129] D.P. Jackson, Radiation Effects 49(1980)233.

[130] D.P. Jackson and J.B. French, Advan. Appl. Mech. Suppl. 5(1969)1119.

[131] D.M. Gruen, A.R. Krauss, M.H. Mendelsohn, and S. Susman, J. Nucl. Mater. 111/112(1982)831.

[132] M.J. Pellin, C.E. Young, M.H. Mendelsohn, D.M. Gruen, R.B. Wright, and A.B. DeWald, J. Nucl. Mater. 111/112(1982)738.

[133] J. Bohdansky, J. Nucl. Mater. 93/94(1980)44.

[106] V.I. Shulga, Radiation Effects 62(1982)237.

[107] M.T. Robinson, J. Appl. Phys. 54(1983)2650.

[108] O.S. Oen and M.T. Robinson, Nucl. Instr. Meth. 132(1976)647.

[109] O.S. Oen and M.T. Robinson, J. Nucl. Mater. 76/77(1978)370.

[110] O.B. Firsov, Soviet Physics JETP 9(1959)1076.

[111] J. Linhard, M. Scharff, and H.E. Schiott, K. Dan. Vidensk. Selsk. Mat. Fys. Medd. 33(1963)no.14

[112] J. Linhard and M. Scharff Phys. Rev. 124(1961)128.

[113] L.M. Kishinevskii, Sov. Phys.-Bull. Acad. Sci. USSR (Phys. Ser.) 26(1962)1433.

[114] P. Bertrand and M. Ghalim, Physica Scripta, T6(1983)168.

[115] D.S. Karpusov, Appl. Phys. 24(1981)121.

[116] M.T. Robinson: "Theoretical Aspects of Monocrystal Sputtering," in Sputtering by Particle Bombardment I, ed. R. Behrisch, Topics in Applied Physics, Vol. 47 (Springer, Berlin, Gottingen, Heidelberg) pg. 73.

[117] P. Jung, 1973.

[118] M.J. Norgett, M.T. Robinson, and I.M. Torrens, Nucl. Eng. Design 33(1975)50.

[119] D.M. Schwartz, J.O. Schiffgens, D.G. Doran, G.R. Odette, and R.G. Ariyasa, Nucl. Metall. 20(1976)75.

[134] N. Matsunami et al., "Energy Dependence of the Yields of Ion-Induced Sputtering of Monatomic Solids," Institute of Plasma Physics, Nagoya University, IPPJ-AM-32, 1983.

[135] N. Laegreid and G.K. Wehner, J. Appl. Phys. 32(1961)365.

[136] V.K. Koshkin, J.A. Rysov, I.I. Shkarban, and B.M. Gourmin, Proc. 9th Int. Conf. Phenomena of Ionized Gases, Bucharest, Hungary, 1969, p. 62.

[137] W. Eckstein and H. Verbeek, J. Appl. Phys. 51(1980)1194.

[138] Y. Yamamura, Y. Itikawa, and N. Itoh, "Angular Dependence of Sputtering of Monatomic Solids," Institute of Plasma Physics, Nagoya University, IPPJ-AM-26, 1983.

[139] H. Oechsner, Z. Phys. 37(1973)261.

[140] M.R. Weller and T.A. Tombrello, Rad. Eff. 49(1980)239.

[141] H.L. Bay, B. Schweer, P. Bogen, E. Hintz, J. Nucl. Mater. 111/112(1982)732.

[142] F. Bernhardt, H. Oechsner, and E. Stumpe, Nucl. Instr. Meth. 132(1976)329.

[143] G.K. Wehner and D. Rosenberg, J. Appl. Phys. 31(1960)177.

[144] M. Mannami, K. Kimura, and A. Kyoshima, Nucl. Instr. Meth. 185(1981)553.

[145] J. Bohdansky, G.L. Chen, W. Eckstein, J. Roth, B.M.U. Scherzer, and R. Behrisch, J. Nucl. Mater. 111/112(1982)717.

[146] P. Sigmund, A. Olivia, G. Falcone, Nucl. Instr. Meth. 194(1982)541.

[147] M.F. Dumke, T.A. Tombrello, R.A.· Weller, R.M. Housley, and E.H. Cirlin, Surface Science 124(1983)407.

[148] H.H. Andersen, V. Chernysh, B. Stenum, T. Sorensen, H.J. Whitlow, Surface Science 123(1982)39.

[149] R.A. Johnson and N.Q. Lam, Phys. Rev. B 13(1976)4364.

[150] N.Q. Lam, G. Leaf, and R.A. Johnson, J. Nucl. Mater. 74(1978)277.

[151] N.Q. Lam, G.K. Leaf, H. Wiedersich, J. Nucl. Mater. 88(1980)289.

[152] N.Q. Lam, A. Kumar, and H. Wiedersich, "Effects of Radiation on Materials: Eleventh Conference," ASTM STP782, Eds. H.R. Brager and J.S. Perrin, American Society for Testing Materials, 1982, pp. 985-1007.

[153] D.A. Mervyn, R.J. Baird, and P. Wynblatt, Surf. Sci. 82(1979)79.

[154] D.M. Gruen, A.R. Krauss, S. Susman, M. Venugopalan, and M. Ron, J. Vac. Sci. Technol. A 1(1983)924

[155] N.Q. Lam, P.R. Okamoto, and R.A. Johnson, J. Nucl. Mater. 78(1978)408.

[156] N.Q. Lam, K. Janghorban, and A.J. Ardell, J. Nucl. Mater. 101(1981)314.

[157] N.Q. Lam and H. Wiedersich, Rad. Eff. Lett. 67(1982)107.

[158] N.L. Peterson, J. Nucl. Mater. 69/70(1978)3.

[159] J.R. Manning, Nucl. Metall. 20(1976)109.

[160] H. Bakker, N.A. Stolwijk, L. van der Meij, and T.J. Zuurendonk, Nucl. Metall. 20(1976)96.

[161] A. Seeger, Crystal Lattice Defects, 4(1973)221.

[162] R.W. Siegel, J. Nucl. Mater. 69/70(1978)117.

[163] B.T.A. McKee, W. Triftshauser, and A.T. Stewart, Phys. Rev. Lett. 28(1972)358.

[164] J.K. MacKenzie and P.C. Lichtenberger, Appl. Phys. 9(1976)331.

[165] K. Maier, H. Metz, D. Herlach, and H.E. Schaefer, J. Nucl. Mater. 69/70(1978)589.

[166] H.M. Gilder and D. Lazarus, Phys. Rev. B 11(1975)4916.

[167] J. Ortega, Z. Metallkunde 73(1982)665.

[168] J.L. Campbell, C.W. Shulte, and J.A. Jackman, J. Phys. F Metal Phys. 7(1977)1985.

[169] B.D. Sharma and G.P. Tiwari, Acta. Met. 15(1967)1551.

[170] S.A. Cho, Z. Metallkunde 71(1980)47.

[171] K. Mukherjee, Phil. Mag. 12(1965)915.

[172] P.R. Couchman, and C.L. Reynolds, Jr., Z. Metallkunde 66(1975)121.

[173] H.B. Huntington, G.A. Shirn, and E.S. Wajda, Phys. Rev. 99(1955)1085.

[174] R.D. Hatcher, R. Zeller, and P.H. Dederichs, Phys. Rev. B 19(1979)5083.

[175] J.J. Burton , Phys. Rev. B 5(1972)2948.

[176] P. Wynblatt, J. Phys. Chem. Solids 30(1969)2395.

[177] P.A. Varotsos, J. Phys F: Metal Phys. 8(1978)1373.

[178] M. Doyama, J. Nucl. Mater. 69/70(1978)350.

[179] J.A. Wert, Acta. Met. 28(1980)1361.

[180] R.A. Swalin, Acta. Met. 5(1957)443.

[181] P.H. Dederichs, C. Lehmann, H.R. Schober, A. Scholz, and R. Zeller, J. Nucl. Mater. 69/70(1978)176.

[182] F.W. Young, Jr., J. Nucl. Mater. 69/70(1978)310.

[183] N.Q. Lam, L. Dagens, and N.V. Doan, J. Phys. F: Met. Phys. 13(1983)2503.

[184] J.W. Corbett, R.B. Smith, and R.M. Walker, Phys. Rev. 114(1959)1460.

[185] R. Lennartz, F. Dworschak, and H. Wollenberger, J. Phys. F: Metal Phys. 7(1977)2011.

[186] M.L. Swanson, L.M. Howe, and A.F. Quenneville, Rad. Eff. 28(1976)205.

[187] M.P. Macht, V. Naundorf, R.P. Wahi, and H. Wollenberger, "The Third Topical Meeting on Fusion Reactor Materials," September 19-22, 1982, Albuquerque, New Mexico, USA.

[188] F. Dworschak, C. Dimitrov, and O. Dimitrov, J. Phys. F: Metal Phys. 8(1978)L153.

[189] C. Dimitrov, O. Dimitrov, and F. Dworschak, J. Phys. F: Metal Phys. 8(1978)1031.

[190] H. Wiedersich, P.R. Okamoto, and N.Q. Lam, J. Nucl. Mater. 83(1979)98.

[191] T. Leffers and B.N. Singh, J. Nucl. Mater. 91(1980)336.

[192] N.Q. Lam, private communication 1983.

[193] T. Leffers and B.N. Singh, Rad. Eff. 59(1981)83.

[194] R.H.J. Fastenau, Phys. Stat. Sol.(a) 53(1979)K39.

[195] R.H.J. Fastenau, C.M. van Baal, P. Penning, and A. van Veen, Phys. Stat. Sol.(a) 52(1979)577.

[196] F.F. Abraham and C.R. Brundle, J. Vac. Sci. Tech. 18(1981)506.

[197] A.R. Miedema, Z. Metallkunde 69(1978)455.

[198] S. Hofmann and J. Erlewein, Surface Science 77(1978)591.

[199] P. Wynblatt and R.C. Ku, Surface Science 65(1977)511.

[200] A.C. Damask and G.J. Dienes, "Point Defects in Metals," Gordon and Breach, New York, 1963.

[201] N.Q. Lam, G.K. Leaf, and M. Minkoff, J. Nucl. Mater. 118(1983)248.

[202] H. Wiedersich, H.H. Andersen, N.Q. Lam, H.W. Pickering, and L.E. Rehn, in "Surface Modification and Alloying,", eds. J.M. Poate and G. Foti, NATO Series on Material Science, Plenum Press, New York, N.Y., 1983.

[203] R. Kelly, Surface Science 100(1980)85.

[204] P.S. Ho, J.E. Lewis, H.S. Wildman, and J.K. Howard, Surface Science 57(1976)393.

[205] P.S. Ho, J.E. Lewis, and J.K. Howard, J. Vac. Sci. Technol. 14(1977)322.

[206] G. Falcone and P. Sigmund, Appl. Phys. 25(1981)307.

[207] P.S. Ho, J.E. Lewis, and W.K. Chu, Surface Science 85(1979)19.

[208] A.R. Krauss, D.M. Gruen, and A.B. DeWald, J. Nucl. Mater. 121(1984)398.

[209] A. R. Krauss, Argonne National Laboratory, private communication 1984.

[210] P. Sigmund, Rev. Roum. Phys. 17(1972)1079.

[211] A.R. Krauss, D.M. Gruen, and M. Venugopalan, J. Nucl Mater. 122/123(1984)1425.

[212] K. Kuribayashi, S. Tanigawa, S. Nanao, and M. Doyama, Solid State Communications 12(1973)1179.

[213] R.R. Bourassa and B. Lengeler, J. Phys. F: Metal Phys. 6(1976)1405.

[214] E. Lang and W. Schule, Z. Metallkunde 61(1970)866.

[215] M. Doyama, K. Kuribayashi, S. Nanao, and S. Tanigawa, Appl. Phys. 4(1974)153.

[216] K. Schneider and M. von Heimendahl, Z. Metallkunde 64(1973)430.

[217] C.F. Old and P. Trevena, Metal Sci. 15(1981)281.

[218] A.R. Krauss, A.B. DeWald, D.M. Gruen, and N.Q. Lam, Workshop on Synergistic Effects in Surface Phenomena Related Plasma-Wall Interactions, Nagoya, Japan, May 21-23, 1984, Rad. Eff. (in press).

[219] A.R. Krauss, D.M. Gruen, N.Q. Lam, and A.B. DeWald, Proc. 6th Intl. Conf. on Plasma-Surface Interactions, Nagoya, Japan, May 14-18, 1984, J. Nucl. Mater. (in press).

[220] N.Q. Lam and H. Wiedersich, Proc. of the Symposium on Metastable Materials Formation by Ion-Implantation, Boston, Mass, Nov. 16-19, 1981.

[221] A.B. DeWald and M. Kaminsky, unpublished 1983.

[222] J. Bohdansky, unpublished preliminary experimental data, 1984.

[223] A.R. Krauss, unpublished preliminary experimental data, 1984.

[224] R.P. Elliott, "Constitution of Binary Alloys," First Supplement, published by McGraw Hill, 1965.

[225] J.N. Brooks, A.R. Krauss, A.B. DeWald, and R.F. Mattas, "Performance of a Copper-Lithium Alloy as an Impurity Control System Surface Material for a Fusion Reactor," Argonne National Laboratory, ANL/FPP/TM-194 (October 1984).

[A1] C.J. Everett and E.D. Cashwell, "A Second Monte Carlo Sampler," USAEC Report LA-5723-MS, Los Alamos Scientific Laboratory, 1974.

[A2] A. Bailey, private communication, Georgia Institute of Technology, December 1983.

[D1] V.W. Klemm and B. Volovsek, Z. Anorg. Allg. Chem. 296(1958)184.

[D2] V. Vlack, "Elements of Materials Science and Engineering," Addison-Wesley Pub. Co., Inc., Reading, Mass., 1975, p. 468.

[D3] A.R. Miedema and P.F. Chatel, "Theory of Alloy Phase Formation," ed. L.H. Bennett, American Institute of Mining, Metallurgy, and Petroleum Engineers, Inc., New York, N.Y., 1980, p. 344.